THÈSE EN COTUTELLE PRÉSENTÉE
POUR OBTENIR LE GRADE DE

DOCTEUR DE

L'UNIVERSITÉ DE BORDEAUX

ET DE L'UNIVERSITÉ CATHOLIQUE DE LOUVAIN

ÉCOLE DOCTORALE DES SCIENCES CHIMIQUES
ÉCOLE POLYTECHNIQUE DE LOUVAIN
SPÉCIALITÉ : Docteur en Sciences de l'Ingénieur

Par **Sergey BASOV**

Nouvelles approches pour le design de composites multiferroïques nanostructurés de type (1-3)

Sous la direction de Catherine ELISSALDE
et de Luc PIRAUX

Soutenances le 14 décembre 2017 (privée), 30 janvier 2018 (publique)

Membres du jury :

Mme. VIART, Nathalie	Professeur des Universités, Université de Strasbourg	Rapporteur
M. BOUSQUET, Eric	Chercheur qualifié, Université de Liège	Rapporteur
Mme. VIGNERAS, Valérie	Professeur des Universités, Université de Bordeaux	Examinateur
M. NYSTEN, Bernard	Professeur des Universités, UCL Louvain	Examinateur
M. TEMST, Kristiaan	Professeur des Universités, KU Leuven	Examinateur
M. ROULLAND, François	Maître de Conférence, Université de Strasbourg	Examinateur
M. MAGLIONE, Mario	Directeur de Recherche, Université de Bordeaux	Invité
Mme. PAYAN, Sandrine	Maître de Conférence, Université de Bordeaux	Invité
M. PIRAUX, Luc	Professeur des Universités, UCL Louvain	Directeur
Mme. ELISSALDE, Catherine	Directeur de Recherche, Université de Bordeaux	Directeur

Erasmus Mundus Joint Doctorate

Education and Culture DG
ERASMUS MUNDUS

Preamble

This PhD had been performed within the framework of IDS FunMat joint doctoral Programme. IDS-FunMat is “International Doctoral School in Functional Materials” funded by the ERASMUS MUNDUS Programme of the European Union.

IDS FunMat PhD School offers PhD projects in Functional Materials Science which has to be carried out in co-supervision between universities from two different countries. In most projects, an industry partner is also involved. As one of the criteria, the PhD candidate must spend at least 6 months in each university and ideally 1.5 year in each of the university.

In this PhD project, two partner universities were Université catholique de Louvain (UCL, Belgium) and Université de Bordeaux (UB, France).

IDS FUNMAT
Erasmus Mundus Joint Doctorate
International Doctoral School
in Functional Materials
for Energy, Information Technology and Health

European Commission
ERASMUS
MUNDUS

Acknowledgements

This dissertation is to all those people who have helped me, both scientifically and personally, along my way to this point. This thesis would not have been possible without the guidance and support I received from several individuals throughout my time at Université catholique de Louvain and Université de Bordeaux. I want to extend my deepest gratitude to my supervisors, Prof. Luc Piraux and Dr. Catherine Elissalde, for providing the resources and comprehensive support without which my research, doctoral program, and Ph.D. thesis would not have been possible. You have been good friends and your advices over the years has been priceless. I would also like to extend my sincerest thanks to my invited committee members president of our institute Prof. Mario Maglione and Dr. Sandrine Payan at Université de Bordeaux, for their help collecting dielectric measurements and offering access to the impedance analyser and magnetron sputtering system as well as all their time, decisive guidance, and necessary support. Prof. Maglione has provided a great deal of insight and perspective for both ferroelectric and dielectric aspects of my work. I must also thank my committee member president of our institute Prof. Bernard Nysten at Université catholique de Louvain for his guidance and support with piezoresponse force microscopy. I want to express my profound gratitude to committee member Prof. Kristiaan Temst at KU Leuven for his help with conducting magnetoelectric measurements and offering access to the PPMS as well as his guidance and support. I must also express my sincere gratitude to my committee members, Prof. Nathalie Viart and Dr. François Roulland at IPCMS-CNRS, Prof. Valérie Vigneras at Bordeaux INP, and Dr. Eric Bousquet at Université de Liège for their invaluable feedback and mentorship.

I have had the distinct privilege of working with many amazing and talented people during my time at Université catholique de Louvain and Université de Bordeaux. In particular, I would like to thank Dr. Quentin Simon at ICMCB, aka Prof. Quentin, for his help with magnetron sputtering, dielectric measurements, GIXRD analysis as well as his mentorship and encouragement, not only were you a good mentor, but you were a good friend. I would like to thank Dr. Vlad Andrei Antohe at Université catholique de Louvain for his support with magnetron sputtering, anodization and pulsed electrodeposition as well as countless hours of scientific discussion. To Dr. Vera Lazenka at KU Leuven for the magnetoelectric measurements, it was a distinct honour and wonderful learning experience to have worked with you in the field of multiferroics.

I would also like to extend my deep gratitude to Dr. David Sallagoity for his invaluable assistance with sol-gel synthesis, performing TEM analysis, overall supervision, and encouragement throughout my time at ICMCB. I cannot thank you enough for your conversations, your efforts, and dedication to our combined work and the science presented in this thesis. I wish you and your family the best in future. To Dr. Pedro de Sá at Université catholique de Louvain for his mentorship and assistance with magnetic, PFM, and SEM measurements as well as magnetic nanopillar arrays preparation. I have thoroughly enjoyed discussing, debating, and working with you and my experience at Université catholique de Louvain would not have been the same without your friendship. I would also like to thank Dr. Thomas Herrison and Christopher Castro-Chavarria for their help with dielectric measurements magnetron sputtering, targets sintering and hours of scientific discussion. I want to thank Pascal Van Velthem for his help with E-beam deposition, sputtering, anodization and electrodeposition. I would also like to thank Delphine Magnin and Cécile D'Haese for the SEM and AFM training. I am grateful to Eric Lebraud for collecting GIXRD measurements as well as many enlightening discussions and analysis of XRD results.

I would like to acknowledge Dr. Jérôme Majimel, Dr. Michäel Josse, Dr. Aline Rougier, Dr. Andres Cano, Prof. Thierry Toupance, Dr. Bernhard Zeimetz, Dr. Laurent Servant, Prof. Karine Glinel, Prof. Alain Jonas. I would like also to acknowledge Marianne Delmas, Christopher Niesen, Audrey Sidobre, Nathalie Augoyard, Cathie Lachapelle at UBordeaux and Anne Bouchat, Aurore Becquevort, Emilie Brichart, Laurence Bertrand for their organizational assistance. Thank you for always taking time to answer my questions, no matter how simple they might be.

To my colleagues at UCLouvain Vivien, Flavio, Yenni, Guillaume, Claire, Jeremy, Joaquin, Juan Manuel, Shashi, Tristan, Florian, LuShi, Ronggang, Moira, Catherine, Diana, Laurence, Varun, Haresh, Abdel, Bruno, Mirasbek and at UBordeaux Ruihao, Shun, Sheavon, Giljoo, Vusala, Mehdi, Cong, Pengyun, Hairui, Clio, Clement, Tadhg, Mathias, Alice, Lorenzo. You have been good friends and your advices over the years have been priceless. I still look happily on our fun times.

Finally, this thesis would have not be possible without the love and encouragement of my family. I very much appreciate the unconditional support, encouragement, and patience of my parents Marina and Aleksander Basovy through the good and challenging times. I am grateful to my grandma Sazida and uncle Ruslan Gilyaevy for the wisdom and love. Throughout all the achievement and difficulties of the last several years, you have been by my side offering your constant support and encouragement.

The IDS-FunMat European doctoral school is acknowledged for financial support. This work was partly supported by the Fédération Wallonie-Bruxelles (ARC 13/18-052, Supracryst) and by the Fonds de la Recherche Scientifique – FNRS under Grant n° T.0006.16. Work at KU Leuven was supported by the Fund for Scientific Research – Flanders (FWO) and the KU Leuven Concerted Action (GOA/14/007).

Table of Contents

Chapter 1

Introduction

Multiferroics are materials possessing two or more ferroic order parameters (*Eerenstein et al., 2006*). Multiferroic materials are called magnetoelectric if they show coupling between magnetic and ferroelectric (FE) order parameters. The possibility of magnetically switchable electric polarization or electric field induced magnetization rotation in multiferroics, ideally ferroelectric and ferromagnetic (FM) at room temperature, makes them very appealing for technology application with lower power/energy consumption, such as nanoscale multi-state data storage, spintronic devices, magnetic reading heads, field sensors, actuators, and other microwave devices (*Fiebig, 2005*). The emergence of magnetoelectric behaviour in single-phase multiferroics by means of coupled lattice, orbital, spin, and charge is typically restricted to low temperatures (*Cheong & Mostovoy, 2006*). In addition, the requirements of empty d^0 shell for ferroelectrics and partially field d^n shell for ferromagnetics limit the number of single-phase multiferroic magnetoelectrics operating at room temperature (*Hill, 2000*). To overcome these limitations, artificial nanocomposites consisting of ferroelectric and ferromagnetic phases were designed (*Ramesh & Spaldin, 2007*).

The magnetoelectric coupling in multiferroic nanocomposites could be observed in different forms (*Nan et al., 2008*). The two most common forms are the electric field control of exchange bias in ferromagnet-multiferroic nanostructure and the mechanical strain-stress interaction in piezoelectric-magnetostrictive heterostructure. In the first type in order to provide the magnetoelectric coupling based on antiferromagnetic-ferromagnetic exchange bias the thickness of ferro/ferrimagnetic layer is typically limited to few nm. This is not the case for the second type of nanocomposite, where the magnetoelectric coupling is based on the strain interaction in two-phase nanocomposites. The main advantage of the second type of multiferroic nanocomposite is a larger variety of ferroelectrics with strong piezoelectric properties and ferromagnetics with strong magnetostrictive characteristics that can be used in nanostructures. Large magnetoelectric coupling was demonstrated at room temperature in multiferroic epitaxial thin films and multilayers, but a key limitation of the planar

architecture of multilayer nanocomposite is a substrate imposed clamping effect, which reduces the strain in nanocomposites due to the heteroepitaxial bonding. Designing innovative architectures is a challenge in the field of multiferroic nanocomposites. To reduce the clamping effect in nanocomposites, recently a vertically aligned architecture was developed in multiferroic thin-film nanocomposites (*Zheng et al., 2004*), where vertically aligned ferrimagnetic $CoFe_2O_4$ nanopillars were self-assembled in three-dimensional $BaTiO_3$ matrix by pulsed laser deposition. The main advantages of the (1-3) thin-film nanocomposites are the reduced clamping effect in magnetic nanopillars, increased interfacial surface area between magnetic and ferroelectric phases, and easy direction of magnetization along the pillars axis, what is appealing for technology applications in data storage.

Our work is focused on vertically aligned architecture multiferroic nanostructures, where one-dimensional ferrimagnetic $CoFe_2O_4$ (CFO) nanostructures (i.e. vertically aligned nanopillar and nanowire arrays) are embedded into three-dimensional $PbZr_{0.52}Ti_{0.48}O_3$ (PZT), $BaTiO_3$ (BTO), and $Ba_{0.7}Sr_{0.3}TiO_3$ (BSTO) layers. New routes were considered to design three kinds of nanocomposites: i) vertically aligned CFO nanowire arrays surrounded by PZT nanotubes inside commercial alumina membranes; ii) vertically aligned CFO nanopillar arrays embedded in thin BTO, BSTO and PZT layers on silicon substrates; ii) 3D interconnected CFO nanowire (NW) networks embedded into thick PZT matrix.

The objectives of the present work include: (1) The control of the thermal oxidation of metallic $CoFe_2$ nanowire and nanopillar arrays into insulating metal oxide CFO spinel phase. In order to carry out the macroscopic dielectric, ferroelectric and magnetoelectric measurements of multiferroic nanocomposites, the oxidation of metallic $CoFe_2$ nanowires and nanopillars must be complete to ensure high resistivity of multiferroic nanocomposites and no shortcut of devices under applied voltage. (2) Control of the morphology and density of CFO nanowires and nanopillars. Thermal oxidation of the $CoFe_2$ nanowire and nanopillar arrays inside alumina templates at high temperature can facilitate the interdiffusion between two adjacent materials leading to the Al diffusion into CFO phase. While thermal oxidation of free-standing $CoFe_2$ nanopillar arrays and 3D nanowire networks leads to the thermal expansion and corresponding variation of nanowires diameter, morphology, surface roughness, and deformation. In particular, increase of nanopillars diameter results in highly dense nanopillars arrays, so that the deposition and penetration of ferroelectric matrix on nanopillars becomes more difficult. (3) Control of the resistivity and dielectric losses of the nanocomposites at the interface region. Low resistivity and high dielectric losses in multiferroic nanocomposites can lead to a smaller spontaneous polarization in ferroelectric layers leading to lower magnetoelectric voltage response (induced voltage) to the applied magnetic field. (4) Increase of the magnetoelectric coupling in multiferroic nanocomposites by using strongly ferroelastic constituents with large permittivity and low dielectric losses. The materials with large piezoelectric coefficient

used in the present work are PZT and BTO layers, with large permittivity are BSTO layers, and the CFO nanostructures were used due to their large magnetostriction coefficient. (5) Increase of the magnetoelectric coupling at the interface in multiferroic nanocomposites by extending the interfacial surface area between two ferroic phases (i.e. height of nanopillars and nanowires) and by controlling the density of interfaces (i.e. ratio between FM nanopillars height and FE layers thickness).

In Chapter 2 the definitions and historical background of multiferroic materials is presented including phenomenology of single-phase multiferroics and types of multiferroic nanocomposites. The main types of ferroic order parameters, i.e. magnetism, ferroelectricity and ferroelasticity, in multiferroic nanocomposites are discussed. The classification of magnetoelectric mechanisms in single-phase magnetoelectric materials is shown with respect to the problem of coexistence of magnetism and ferroelectricity in a single material. The mechanisms of magnetoelectric coupling in multiferroic composites and heterostructures through the exchange of magnetic, electric, and elastic energy across interfaces between different constituent materials are presented. Preparation of artificial multiferroic nanocomposite with three types of architecture including planar, particulate, and vertical is reviewed. In particular, alternative strategies for the growth of vertically aligned multiferroic nanocomposites are discussed. The recent progress on the understanding of magnetoelectric coupling mechanisms, designing of magnetoelectric nanocomposites, relatively comprehensive experimental dataset on the magnetoelectric coupling in thin-film nanocomposites with three types of architecture and brief theory and computation for vertically aligned thin-film nanocomposites are presented in Chapter 2, offering a perspective on the design of magnetoelectric nanocomposites with enhanced magnetoelectric properties.

In Chapter 3 we describe in detail the preparation of multiferroic nanocomposites, experimental techniques, and samples characterizations. We must emphasise that Chapter 3 is not the standard and straightforward “experimental chapter” including only the experimental tools used in our study. It also contains all the details on the fabrication of the samples, which somehow justifies the large size of the chapter. In the section devoted to the preparation of PZT-CFO core-shell magnetoelectric system, the sol-gel based chemical solution deposition technique is discussed. The sol-gel dip-impregnation synthesis of PZT nanotube arrays inside commercial anodic alumina membranes, pulsed electrochemical electrodeposition of $CoFe_2$ nanowire arrays are explained. In the sections devoted to BSTO/BTO/PZT-CFO magnetoelectric nanocomposites with vertical architecture, preparation of supported AAO templates using anodization technique, radio-frequency magnetron sputtering of BSTO and BTO layers, and sol-gel dip-coating deposition of PZT layers are described in detail. The basic working principals of characterization techniques including structural and microstructural characterization (i.e. HR-SEM, EDX, TEM, and XRD) and performance evaluation on both macro- and micro-scale (i.e. alternating gradient

magnetometer, impedance analyser, piezoelectric force microscopy, and magnetoelectric susceptometer) are explained in detail.

In Chapter 4 we present the results for the synthesized dense arrays of multiferroic PZT-CFO core-shell nanocables with high interfacial area between the ferroelectric and the magnetic phases via a combination of low-cost impregnation and electrodeposition processes within the ordered nanochannels of a porous AAO templates. We show that the thermal annealing steps required for phase's crystallization and oxidation of metallic $CoFe_2$ phase into spinel CFO phase are critical with respect to interdiffusion phenomena through the interfaces. The impact of the processing temperature on the morphological and structural features of the nanocables is discussed. We demonstrate that an optimization of process variables in the system of PZT-CFO nanocables allows a significant improvement in their microstructure and ensures the chemical integrity of the two-phase materials. Microscopic ferroelectric properties of the optimized PZT nanotubes, PZT-$CoFe_2$ and PZT-CFO nanocables analysed using Piezo-Response Force Microscopy (PFM) technique are discussed.

In Chapter 5 we present a new strategy to elaborate multiferroic nanocomposites with controlled dimensions and vertical alignment using supported nanoporous alumina layer as a template for growth of free-standing and vertically aligned $CoFe_2$ nanopillars via pulsed electrodeposition process. The characterization of vertically aligned multiferroic nanocomposites using various techniques for their structural and physical properties is discussed. The efficiency of *in situ* simultaneous oxidation of $CoFe_2$ nanopillars into CFO phase during direct deposition via radio-frequency sputtering on the top surface of the pillar structure of BSTO and BTO films is discussed. Measurements of direct magnetoelectric coupling in the grown vertically aligned BSTO-CFO and BTO-CFO nanocomposites are presented and the dependences of ME coefficient as a function of geometrical factors, density of interfaces, and effective permittivity are discussed. The simple method to prepare vertically aligned PZT-CFO multiferroic nanocomposites using thermal oxidation of free-standing $CoFe_2$ nanopillar arrays and sol-gel based dip coating of PZT layers is discussed. We show that through optimization of PZT coating solution and crystallization thermal conditions a uniform and continuous PZT layer on top of the CFO nanopillars without microcracks. The preliminary results for the magnetoelectric voltage response in PZT-CFO nanocomposites are shown.

In Chapter 6 we show future perspective in designing vertically aligned multiferroic nanocomposite. The preliminary results for the synthesis of PZT-CFO nanocomposite based on 3D interconnected $CoFe_2$ nanowire networks include microstructure and magnetic properties. We demonstrate an original synthesis technique of PZT-CFO vertically aligned multiferroic nanocomposite with large interfacial surface area between magnetic CFO 3D NW networks and ferroelectric PZT matrix and near-zero clamping effect. The efficiency of *in situ* oxidation of metal $CoFe_2$ 3D NW networks

into the CFO spinel phase is demonstrated using XRD and magnetic measurement techniques.

Finally, the main results of the present work are summarized in the conclusion Chapter 7.

Chapter 2

Background and History of Multiferroics and Magnetoelectric Effect

Modern electronics and hardware are operating mainly using electronic and magnetic materials. For instance, the regions with opposite direction of magnetization in ferromagnets (magnetic materials with a spontaneous magnetization retaining their magnetization in the absence of a field and switchable by a magnetic field) are often used as bits of information in data storage devices. Related electric materials called ferroelectrics (materials with a spontaneous electric polarization that can be switched by an applied electric field) are widely used in the sensor industry. Many ferroelectrics and ferromagnetics are also ferroelastics (materials with a spontaneous strain that is switchable by an applied stress) because their deformation leads to a change of electric polarization and magnetization and vice versa. Thus, using these ferroic materials the sound waves can be converted into electric signals in sonar detectors, electrical impulses can be converted into motion in actuators and magnetic fields can be converted into currents. Recently the ferrotoroidics have been proposed to complete the main classes of ferroics (*Fiebig et al., 2016; Yadav et al., 2016*). Materials combining magnetic order parameter with other two kinds of ferroic order parameters in the same phase – ferroelectricity and ferroelasticity (**Figure 2.1**) are often called multiferroics (*Spaldin & Fiebig, 2005; Khomskii, 2009*). Material displaying two or more primary ferroic orderings simultaneously are formally defined as multiferroic (*Schmid, 1994*).

Combining electronic and magnetic properties in a single multifunctional material or a single multitask device is appealing for the development of electronic industries in terms of device miniaturization. Moreover, besides the combination of magnetic and electronic properties in a ferromagnetic ferroelectric multiferroics, interactions between the magnetization and electric polarization brings additional functionality. For

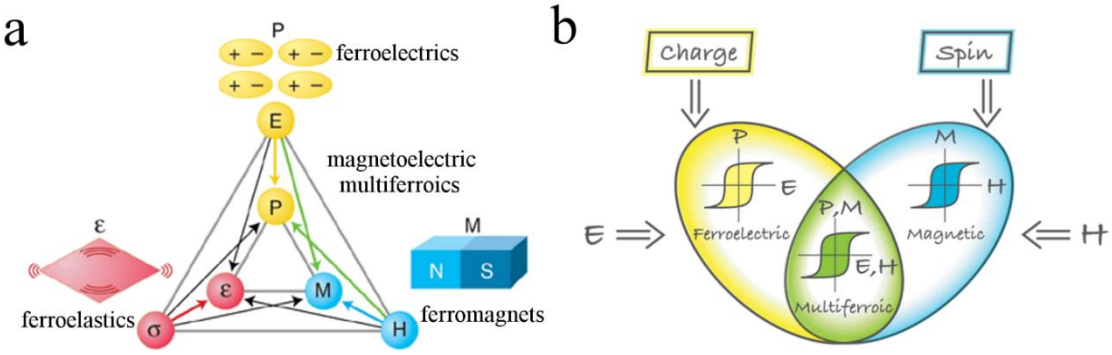

Figure 2.1: (a) Phase control in ferroics and multiferroics. The electric field *E*, magnetic field *H*, and stress σ, control the electric polarization *P*, magnetization *M*, and strain ε, respectively. In a ferroic material, *P*, *M*, or ε, are spontaneously formed to produce ferromagnetism, ferroelectricity, or ferroelasticity, respectively. In a multiferroic, the coexistence of at least two ferroic forms of ordering leads to additional interactions. In a magnetoelectric multiferroic, a magnetic field may control *P* or an electric field may control *M* (pink arrows) (from *Spaldin & Fiebig, 2005*). **(b)** In the ideal case, the magnetization of a ferromagnet in a magnetic field displays the usual hysteresis (blue), and ferroelectrics have a similar response to an electric field (yellow). In principle it is the basis for making a 4-state logic state: (*P*+ *M*+), (+−), (−+), (−−). From *Khomskii, 2009*

instance, this refers to the magnetoelectric (ME) coupling, that is, the control and tuning of electric polarization using magnetic field, or of a magnetization by an electric field. The magnetoelectric effect is attractive due to a possibility of designing new devices, such as magnetic data storage controlled via electric field and 4-state logic states. However, many attempts in implementing this concept into practice using a single multiferroics have shown to be challenging.

Theoretical studies have revealed that the ferromagnetism and ferroelectricity generally does not coexist in a single phase because their mechanisms contradict each other. They require empty and partially filled d orbitals of transition metals, respectively (*Hill, 2000*). This is why many researches have proposed alternative ferroelectric mechanisms, which could be suitable with the existence of ferromagnetic ordering leading to the discovery of new multiferroic materials. Large indirect magnetoelectric coupling was achieved in perovskite manganites in terms of magnetically induced ferroelectric phase transition (*Kimura et al., 2003*) and in hexagonal manganites with respect to electrically induced ferromagnetism (*Lottermoser et al., 2004*). However, none of the discovered single-phase multiferroics is able to retain both large and robust electric polarization and magnetization at room temperature, which limits them from real application in the short term.

The issues associated with ferroelectric and ferromagnetic ordering coexistence and limited polarization or magnetization in a single phase materials have been avoided by designing two-phase multiferroic composites including a ferroelectric constituent, such as $Ba_{1-x}Sr_xTiO_3$ (BSTO, $BaTiO_3$, $x = 0$), $PbZr_{1-x}Ti_xO_3$ (PZT, PTO, $x = 1$), $(PbMg_{1/3}Nb_{2/3}O_3)_{1-x}$-$(PbTiO_3)_x$ (PMN-PT), $(PbZn_{1/3}Nb_{2/3}O_3)_{1-x}$-$(PbTiO_3)_x$ (PZN-PT), copolymer PVDF:TrFE, and a ferromagnetic constituent, such as metallic $Tb_{1-x}Dy_xFe_2$

(Terfenol-D), Metglas, CoFeB, FeGaB, FeBSiC, Co, Ni, Fe, $Fe_{1-x}Co_x$, $Fe_{1-x}Ni_x$, perovskite $La_{1-x}A_xMnO_3$ (L*A*MO, $A = Ca, Se, Ba, Co$), and spinel Fe_3O_4, $CoFe_2O_4$ (CFO), $NiFe_2O_4$ (NFO). In these composites, the magnetoelectric effect is a product property of the interfacial interaction of the elastic components of the ferromagnetic and ferroelectric constituents. Briefly, a magnetic field generates deformation in the ferromagnetic; then this deformation is transferred into the mechanically coupled ferroelectric, where it causes polarization. The magnetoelectric effect can be enlarged by increasing the coupling at the interface using nanocomposites with large surface area (such as multilayers thin films or pillars embedded into matrix) with strongly ferroelastic constituents (such as piezoelectric coefficient, magnetostrictive coefficient etc).

The composite multiferroic materials allow to tune the magnetoelectric response through the nature, ratio, and microstructure of the constituents. Their magnetoelectric coupling coefficients at room temperature exceed the low-temperature values obtained in single-phase magnetoelectrics by three to five orders of magnitude (*Fiebig et al., 2016*; *Dong et al., 2015*; *Hu et al., 2017*; *Nan et al., 2008*). Composite magnetoelectric multiferroics are currently entering the technological application markets as transducers converting between electric and magnetic fields. Among other potential applications are attenuators, filters, field sensors, and data storage devices such as magnetoelectric random access memories, multiple-state logic device based on magnetization reversal via an applied electric field, where the direction of either ferroelectric polarization or magnetization represents the "1" or "0" of the data bit (*Scott, 2007; Bibes & Barthélémy, 2008; Heron et al., 2014b; Shen et al., 2016; Nan et al., 2008; Palneedi et al., 2016*).

The main challenges remaining in composites and single-phase multiferroics are:

- For composites: (1) a better understanding of ferromagnetic-ferroelectric-ferroelastic coupling between the constituents; (2) the need for new theory since linear elasticity models cannot be used to interpret phenomena at the atomic level; (3) experimentally, the design of composite multiferroics with novel architectures such as pillars embedded into matrix with reduced clamping to substrate effect (*Zheng et al., 2004*), which is relatively large in classic multi-layered thin film multiferroics, offering particularly efficient coupling between two phases and probably even magnetoelectric switching of polarization and magnetization; (4) the use of cost-effective and scale-up preparation techniques with low energy consumption as alternative to the self-assembly of vertically aligned nanocomposites via pulsed laser deposition (*Zheng et al., 2004*);

- For single-phase multiferroics: (5) to explore the origin of the ferroelectricity in some specific multiferroics (*Kimura et al., 2003*); (6) to develop robust room-temperature ferromagnetic ferroelectrics which are good insulators and able to uphold a large macroscopic polarization; (7) to design new multiferroic epitaxial thin films that may drive the single-phase materials toward technological application; (8) to develop new fundamental theoretical concepts to integrate ferrotoroidicity, represented by a

spontaneous ferromagnetic and ferroelectric vortexes, into the group of primary ferroics (*Schmid, 2001*; *Damodaran et al., 2017*), which should bring a more comprehensive understanding of the possible forms of ferroics order parameters and the relation between them.

2.1 Types of Ferroic Ordering in Multiferroics

2.1.1 Magnetic Materials

Magnetic materials are either ferromagnetic or ferrimagnetic when magnetic flux density Φ inside (e.g. magnetic induction $B = \Phi/A$) is very much greater than Φ outside (e.g. magnetic field $H = \Phi/A$), where A is an area that magnetic flux passing through. When a magnetic field H is applied to a material, the response of the material is called its magnetic induction, B. The relationship between B and H is a property of the material. The equation relating B and H is (in cgs units)

$$B = H + 4\pi M, \tag{2.1}$$

where M is the magnetization of the medium. The magnetization is determined as the magnetic moment per unit volume,

$$M = \frac{m}{V}\,\frac{emu}{cm^3}, \tag{2.2}$$

M is a property of the material, and depends on both the individual magnetic moment of the constituent ions, atoms, or molecules, and on the interaction between the dipole moments. The cgs units of magnetization M, magnetic induction B, and magnetic field H are the emu/cm^3, gauss, and oersted, respectively. In SI units the relation between B, H, and M is

$$B = \mu_0(H + M), \tag{2.3}$$

where μ_0 is the permeability of free space. The units of M and H are the same (A/m), and those of μ_0 are weber/(A/m), or henry/m. Thus, the units of B are weber/m^2, or tesla, where 1 tesla = 10^4 gauss.

In ferromagnets, the magnetic dipoles of the atoms are likely to align in the same direction. Ferrimagnets are in part similar to antiferromagnets since the dipoles are ordered antiparallel, but some of the dipole moments are larger than others, thus the materials have net long-range magnetic moments. Ferromagnetic and ferromagnetic materials have a tendency to concentrate magnetic flux intrinsically. **Figure 2.2** illustrates schematically antiferromagnetic, ferrimagnetic and ferromagnetic magnetic materials.

The variation of the magnetization, or the magnetic induction with the applied magnetic field is also one of the main properties of a magnetic material. The ratio between M and H is called the susceptibility:

$$\chi = \frac{M}{H}\,\frac{emu}{cm^3 Oe}. \tag{2.4}$$

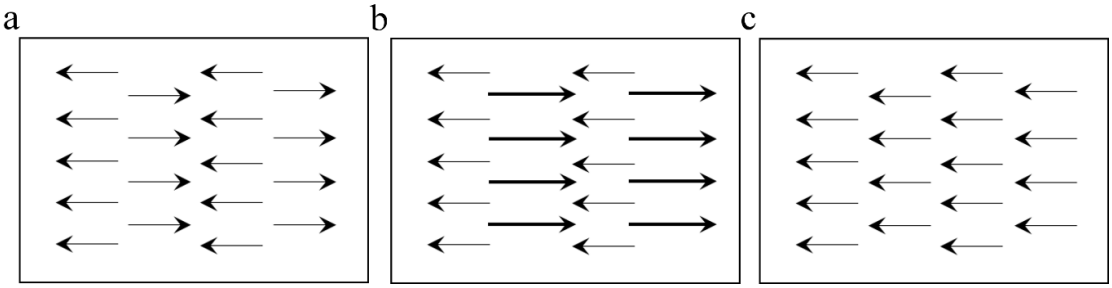

Figure 2.2: Ordering of the magnetic dipoles in **(a)** antiferromagnetic, **(b)** ferrimagnetic, (c) ferromagnetic materials

The susceptibility shows how responsive a material to an applied magnetic field. The ratio of B to H is called the permeability:

$$\mu = \frac{B}{H}\frac{gauss}{Oe}, \tag{2.5}$$

μ shows how permeable the material is to the magnetic field. A magnetic material that accumulates intrinsically a large ammount of flux density features a high permeability. Adopting the equation $B = H + 4\pi M$ gives us the relationship (in cgs units) between permeability and susceptibility:

$$\mu = 1 + 4\pi\chi. \tag{2.6}$$

In SI units the susceptibility is dimensionless, and the permeability is in units of henry/m. The equivalent equation for permeability and susceptibility in SI units is

$$\frac{\mu}{\mu_0} = 1 + \chi. \tag{2.7}$$

Figures 2.3 illustrates schematic general hysteresis loop of M over H with applied field sweeping from zero to positive values, then reversed to negative values and returned to positive values, graphs, for ferrimagnets and ferromagnets. The magnetization M saturates above a particular applied field when increasing field results

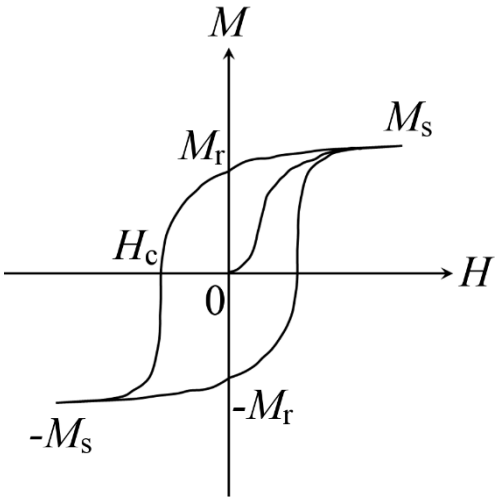

Figure 2.3: Schematic illustration of hysteresis loop for ferri- and ferromagnetics

only in a very small change of magnetization, whereas decreasing the field to zero after saturation does not turn the magnetization back to zero. This effect is called hysteresis, and is used for technological applications such as permanent magnets. To return the magnetization into zero value, a field must be applied in reversed direction.

Initially the magnetic material is in an unmagnetized state, and the magnetization follows the curve going along the curve from 0 to M_s with the field increasing in the positive direction. The M value at M_s is called the saturation magnetization, and the curve of M from the demagnetized state to M_s is called the normal magnetization curve. When applied field is returned to zero after saturation, the magnetization decreases from M_s to M_r – the remanent, or residual magnetization. The reversed field needed to reduce the magnetization to zero is called the coercivity, H_c. Ferromagnetic materials are categorised as hard or soft, depending on the value of the coercivity. When a large field is required to reduce the magnetization to zero or to saturate the magnetization, a magnet is called hard ferromagnet, on the contrary easily saturated and demagnetized ferromagnets are soft. When H is reversed and increased further, the magnetization saturates in the reverse direction. The loop that is traced out is called the major hysteresis loop.

The condition for the appearance of magnetism is that in ferromagnets the composing electrons must have a net angular momentum. This can be originated either in the orbital component of the angular momentum, or the spin component (when there is different number of "up"- and "down"-spin electrons) or one and the other. So, the quantum-mechanical exchange energy is causing a strong motive force for electrons to order their spins parallel generating different number of up- and down-spin electrons. Then if a couple of electrons have spins with opposite directions, they are permitted to share the same atomic or molecular orbital, thus they will intersect spatially, and the electrostatic repulsion will increase. Although if they have parallel spins with the same direction, then they are obliged to populate different orbitals and will have smaller electrostatic repulsion. In other words, the direction of the spins modifies the spatial part of the wavefunction, which successively defines the electrostatic repulsion between the electrons. A small change of electron distribution will strongly affect the total energy of the system. On the hole, the energy difference per magnetic ion between ferro- and antiferromagnetically ordering are of the order of electron volts, while the magnetic dipolar energy between a couple of electrons distant by a few Å is ~10^{-6} eV. Depending on either ferromagnets are magnetic insulators or metals, two phenomenological theories can be used to describe the properties of ferromagnetism – the localized moment theory of Curie and Weiss and the Stoner band theory, respectively.

In the localized momentum theory, above some specific temperature ferromagnetic materials become paramagnetic, and their susceptibility follow the Curie-Weiss law; the specific temperature is called Curie temperature, T_C (*Weiss, 1907*). The magnetization decreases smoothly to zero at $T = T_C$, indicating the ferromagnetic to

paramagnetic transition of a second-order. Below the Curie temperature, T_C, the molecular field (the short-range quantum-mechanical exchange interaction) is strong enough to magnetize the material even in the absence of an applied field. At temperatures higher then Curie temperature, the thermal energy, kT, and corresponding entropic effects overcome the ordering energy of the molecular field, leading to random orientation of magnetic moments and paramagnetic behaviour. The experimentally observed Curie-Weiss law for the susceptibility χ of the ferromagnets and ferrimagnets is

$$\chi = \frac{C}{T - T_C}. \tag{2.8}$$

The Weiss theory is not suitable for ferromagnetic metals due to two discrepancies, firstly, the magnetic dipole moment on each atom and ion is not the same in both the ferromagnetic and paramagnetic phases, and secondly, the magnetic dipole moment on each atom or ion does not correspond to an integer number of electrons. Therefore, the Stoner band theory of ferromagnetism is used to explain the properties of metals (*Stoner, 1933*), in which the general motive force for ferromagnetism is also the exchange energy, which is minimized when all the electrons have the same spin. Opposing the ordering of spins is the increased band energy involved in transferring electrons form the lowest band states (populated equally by up- and down-spin electrons) to band states with higher energy. This band energy forbids some metals to be ferromagnetic. In the basic ferromagnetic transition metals, Fe, Ni and Co, the Fermi energy lies in a region of overlapping 3d and 4s bands. Since the 4s bands are broad and have a low density of states at the Fermi level, the energy required to move a 4s electron to a vacant state reversing its spin is higher than the energy acquired from the decrease in exchange energy. As for the 3d band, the larger number of density of states or electrons at the Fermi level reduces the band energy required for a spin reversal, so the exchange energy is larger. The exchange interaction forms an exchange potential that shifts the energy of the 3d band for electrons with the same direction of spin relative to the band for electrons with opposite spin direction. The magnetic moment accordingly does not relate to an integer number of electrons, since the electrons are shared between partially filled 4s, 3d up- and 3d down-spin direction bands.

In 1937 and 1938, Slater and Pauling estimated the saturation magnetization as a function of the number of 3d and 4s valence electrons per atom for the first set of transition metals and their alloys (*Slater, 1937*; *Pauling, 1938*). They reported a linear increase in M_s from Cr to Fe, followed by a linear decrease, reaching zero M_s at an electron density between Ni and Cu. The calculated results fit well with the experimentally measured magnetizations of the metal Fe, Co ad Ni, as well as alloy $CoFe_x$, $CoNi_x$ and $CuNi_x$ ferromagnets (see **Figure 2.4**). The saturation magnetic moment depends on the number of valence electrons almost linearly.

To minimize the total energy of the ferromagnet, domains form. Although a single ferromagnetic domain, in which all the magnetic moments were aligned, would

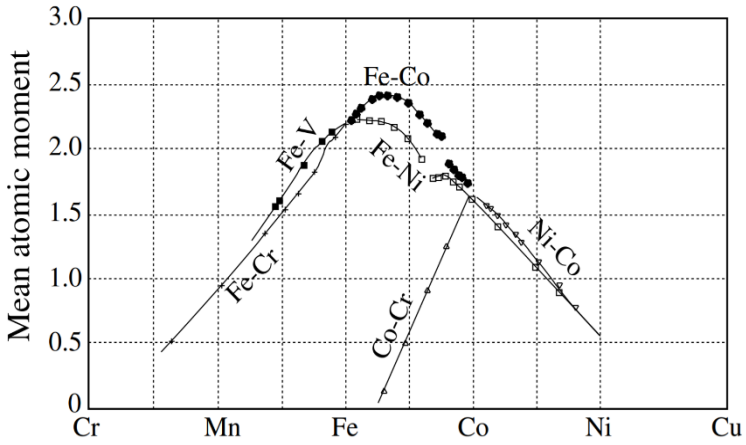

Figure 2.4: Slater-Pauling curve which is a plot of magnetic moment measurements of several TM alloys, where the maximum saturation magnetisation was found for $Fe_{65-70}Co_{35-30}$ alloys with $\mu_0 M_s =$ 2.45 T ($M_s \sim 2.45 \times \frac{10^4}{4\pi} = 1950$ emu/cm^3) – the Slater-Pauling limit. From *Sourmail, 2005*

minimize the exchange energy, it also maximizes the magnetostatic energy, which is the main motive force for domain formation. The size and shape of the domains are also defined by magnetocrystalline and magnetostrictive energies. **Figure 2.5** illustrates the reduction of magnetostatic energy by domain formation (*Spaldin, 2010*). The single-domain sample in **Figure 2.5a** has a large magnetostatic energy, which is reduced in **Figure 2.5b** by the creation of parallel domains. At the domain boundaries the magnetic moments are no longer oriented parallel to each other resulting in an increase in exchange energy. **Figure 2.5c** shows the fully cancelled magnetic moments. However, if the ferromagnet has strong magnetostriction (which induces the specimen to deform, contract or expand, in the direction of magnetization) or a strong magnetocrystalline anisotropy (which induces the magnetization to align preferentially along a single crystallographic lattice axis), the perpendicular domains shown in **Figure 2.5c** can be disadvantageous. In this situation an ordering with very small perpendicular domains (see **Figure 2.5d**), is normally the lowest in energy.

The width of the boundary between magnetic domains (the domain wall) is determined by a balance between the exchange energy (which prefers wide walls, so

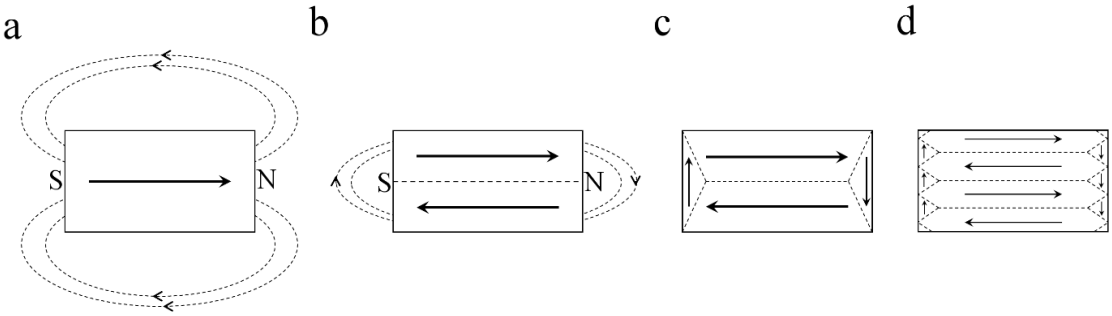

Figure 2.5: Reduction of the magnetostatic energy by domain formation in a ferromagnet. The single domain shown in **(a)** optimizes the exchange, magnetocrystalline and magnetostatic energies. Often, the arrangement shown in **(d)** has the lowest total energy (from *Spaldin, 2010*)

that adjacent magnetic moments are not too far from being parallel to each other) and the magnetocrystalline energy (which prefers narrow walls, so that the magnetization is aligned most closely to an easy axis). For typical transition metals, domain walls are a few hundred angstroms thick (or consist of a few hundred planes of atoms).

2.1.2 Ferroelectrics

The part “ferro” in “ferroelectric” does not correspond to the use of iron in ferroelectrics. It just underscores that there are many similarities in behaviour between ferroelectrics, that show spontaneous electric polarization and ferromagnetics showing spontaneous magnetization. The spontaneous electric polarization is switchable by an applied electric field similarly with the ferromagnetic, whose spontaneous magnetization can be realigned by a magnetic field. Another similarity is that the electric polarization switching process is associated with the hysteresis (see **Figure 2.6**). Most of the time a change in the polarization direction leads to a deformation of ferroelectric, or strain. In both ferromagnets and ferroelectrics the macroscopic net magnetization and electric polarization can be cancelled by the presence of domains with oppositely oriented parallel magnetization and polarization within the specimen. Both the magnetization and polarization decrease with increasing temperature and become close to zero when a phase transition to a paramagnetic or paraelectric state takes place at high temperature. Ferroelectrics undergo a structural phase transition from the prototypical high symmetry phase to a low temperature non-centrosymmetric phase that has a spontaneous polarization whose direction can be switched by an electric field. Also, the coupling between magnetization, or polarization, and the lattice strain results in the piezomagnetism in ferromagnetics and piezoelectricity in ferroelectrics. The piezoelectric effect is stronger than in piezomagnetics, therefore ferroelectrics are typically used in transducer and actuator applications, whereas

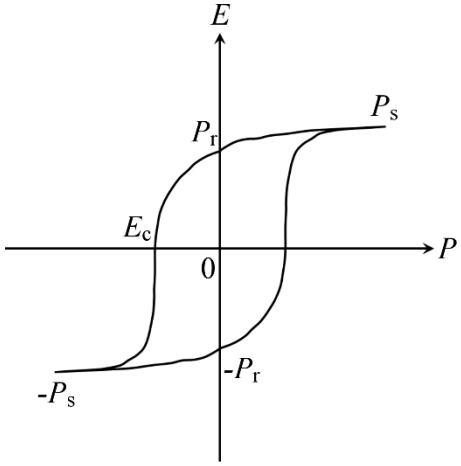

Figure 2.6: Schematic illustration of a typical ferroelectric hysteresis loop

ferromagnetics are more commonly used for data storage applications where the direction of spontaneous magnetization represents the "1" and "0" of the data bit, although ferroelectrics are currently also approaching for data storage technology application.

However, the microscopic effects that cause ferroelectricity and ferromagnetism are different; polarization requires lattice distortion, magnetization does not. Another requirement for a material to be a ferroelectric is that the spontaneous polarization must be switchable between two stable states of opposite polarization when the electric field is applied. In the following paragraph the origin of cationic off-centering in the classic ferroelectrics is explained.

In general, ferroelectric materials can be defined as polar non-centrosymmetric phase, of which the most common is the perovskite structure ABO_3 shown in **Figure 2.7**. Ferroelectricity manifests as a symmetry-breaking structural distortion from the perfect cubic perovskite structure. The A or B cations shift off-centre with respect to the oxygen anions, so the spontaneous polarization occurs from the electric dipole moment caused by the shift. Most of ferroelectrics undergo a phase transition from a high-temperature paraelectric phase to a low-temperature ferroelectric phase. The phase transition takes place at the Curie temperature, T_C. In barium titanate the transition from the parent paraelectric cubic phase to the ferroelectric tetragonal phase occurs at ~390 K. Although long-range electrostatic forces favour the ferroelectric state, the short-range repulsion between the electron clouds of adjacent ions are minimized for nonpolar, cubic structure (*Cohen, 1992*; *Cohen, 2000*). Either the ferroelectricity is present or absent is determined by a balance between these short-range repulsions, which favour the non-ferroelectric symmetric structure, and additional chemical bonding factors, which act to stabilize the distortion needed for the ferroelectric phase (*Megaw, 1952*). The Curie temperature is related to chemical bonding especially in

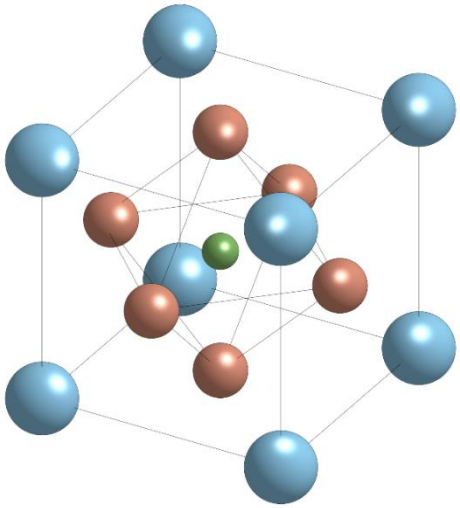

Figure 2.7: The centrosymmetric cubic perovskite structure. The small B cation (in green) is at the centre of an octahedron anions (in red). The large A cations (blue) occupy the unit-cell corners

corner-linked octahedron structure phases, taking into account steric, charge, covalency, electronic configuration, and Jahn-Teller effects.

First-principles density functional theory calculations have provided significant insights in the understanding of ferroelectric behaviour in perovskite oxides, in particular $PbTiO_3$ and $BaTiO_3$. It was shown that the Ti 3d-O 2p hybridization is essential for the stabilization of the ferroelectric distortion. The mixing of atomic orbitals allows to soften the short-range repulsions which tend to cancel the ferroelectric distortion (It is the lone-pair of Pb). The hybridization between Pb 6s and O 2p leads to a high polarizability and a strain that stabilizes the tetragonal phase over the rhombohedral one (*Cohen & Krakauer, 1992b*).

The constituent ions in ferroelectrics are normally off-centred, but below the Curie temperature the directions of off-centring which does not align cooperatively; similar behaviour taking place in the ferromagnetic materials was mentioned above. The analogy is to the band theory of ferromagnetism, in which the Curie temperature is coincident with equal number of up- and down-spin electrons and no macroscopic magnetic moment. However, the large difference between ferroelectric and ferromagnetic lays in the size of domain walls. Ferromagnetic domain walls are wide, but those of ferroelectrics have a thickness of only a few lattice constants as was reported in $PbTiO_3$ both experimentally by HR-TEM (*Stemmer et al., 1995*) and theoretically using ab-initio calculations (*Meyer & Vanderbilt, 2002*). In turn, the domain-wall energies in ferroelectrics are considerably larger than those in typical ferromagnets. Comparison of lattice parameters determined using HR-TEM with predictions based on Landau–Ginzburg theory to extract a value of 50 $mJ \cdot m^{-2}$ for a 90° domain wall in $PbTiO_3$ (*Stemmer et al., 1995*). For comparison, first-principles calculations give a value of 35 $mJ \cdot m^{-2}$ for a 90° domain wall and ∼150 $mJ \cdot m^{-2}$ for a 180° domain wall (with the exact value depending on the details of the symmetry used in the calculation). The same first-principles study also showed that the change in polarization in ferroelectric domains is accommodated by a reduction in the magnitude of the local atomic displacements at the domain wall (*Meyer & Vanderbilt, 2002*). This is in contrast to the situation in magnetic domains, where the local moments are not significantly reduced, but instead rotate their orientation through the width of the wall.

Different size dependencies and different domain wall widths in ferroelectrics and ferromagnets can be understood to result from the different mechanisms driving ferromagnetism and ferroelectricity, for ferroelectrics: electric dipoles - lattice distortion mechanism; for ferromagnetics: spins – electronic excitations mechanism. Ferromagnets prefer wide domain walls, in which adjacent magnetic moments are oriented close to each other, because the exchange coupling between magnetic moments is strong, and the magnetocrystalline anisotropy energy, which couples the spin to the lattice, is driven by spin-orbit coupling, which is comparatively weak. In ferroelectrics the situation is quite different in that the energies of the “anisotropy” and “exchange” effects are comparable. For example, the calculated energy difference in

$BaTiO_3$ between the rhombohedral ground state (in which the atoms displace along the [111] direction) and the higher-energy tetragonal phase (in which they displace along [100]) is around 5 meV per 5 atom unit cells (*Cohen & Krakauer, 1992*).

2.1.3 Ferroelastics

The essential parameter of ferroelastics is the spontaneous strain, a deformation of the crystal generated by the phase transition, which has to have at least two orientations between which switching may occur. Strain and ferroelasticity can mediate the coupling between ferroelectric and ferromagnetic properties.

Piezoelectricity

The mechanical deformations in ferroelectrics are caused by the coupling between strain and ferroelectric polarization resulting in the widely applied piezoelectric response of ferroelectrics.

In epitaxial thin films, a lattice mismatch between the lattice parameters of the single crystal substrate, such as $SrTiO_3$ (STO), $LaAlO_3$ (LAO), and MgO, and epitaxially grown thin films can induce either compressive or tensile in-plane (i.e. horizontal) strain in these films, which will align electric polarization along vertical or horizontal directions, respectively. The "incipient ferroelectric" $SrTiO_3$, which is generally behaving like a paraelectric material down to $T = 0$ K and never becoming a ferroelectric, can be obtained as a classic ferroelectric in highly epitaxially strained STO materials (*Haeni et al., 2004*).

Magnetostriction

When a magnetic material is magnetized, a small change in the dimensions takes place. The relative change is on the order of several parts per million (ppm) and is called magnetostriction. It works in both ways, which means if a magnetic material is deformed, depending on the magnetic material the direction of magnetization will be aligned either parallel to the direction of stress or at right angled to it. The magnetostriction energy depends on the amount of stress and on a constant characteristic of the magnetic material called the magnetostriction constant, λ, as $E = 3/2\lambda_s\sigma$, where σ is applied stress and λ_s is saturation magnetostriction. If the sign of the magnetostriction constant is positive, then the magnetization is increased by tension and also the material expands when the magnetization is increased. On the other hand, if the magnetostriction is negative, the magnetization is decreased by tension and the material contracts when it is magnetized. The anisotropy in magnetostriction can be explained by incomplete orbital quenching and the so-called spin-orbit coupling.

For good quality soft magnetic materials, a low magnetostriction is required. Whereas in magnetostrictive transducers for such applications as ultrasonic generators, the mechanic motion generated by the magnetic excitation through magnetostriction is used, and thus a high magnetostriction is desirable in this case. Since both anisotropy and magnetostriction are intrinsic properties of a magnetic material, by tuning the chemistry and crystal structure, the magnetic properties can be adjusted for a specific application.

2.2 Single-Phase Magnetoelectric Materials

2.2.1 The Scarcity of Magnetic Ferroelectrics

The competition between energy-lowering covalent bonding and energy-raising repulsions decides if a cation will shift from the centre of the coordination octahedral and form an electric dipole moment. In the next paragraphs the problem of scarcity of magnetic ferroelectrics is discussed (*Hill, 2000*). The first requirement for a material to be ferroelectric is that it must be insulating, if not an applied electric field will induce a current before its polarization is reversed. Considering the partially filled d shells in ferromagnets, the top of the valence band and the bottom of the conduction band are occupied with transition-metal d states resulting in the same symmetry of the ground and low-lying excited states. So, the absence of energy-lowering bond formation prevents off-centering. As a result, in transition metals with partially filled d shells, the repulsive electrostatic interactions are stronger than the energy gaining from chemical bonding formation, and ferroelectric off-centring does not take place. This is the reason why the common (ferro- or antiferro-) magnetic perovskites structure oxides [e.g. $LaMnO_3$ (LMO), $SrRuO_3$ (SRO), $GdFeO_3$ (GFO)] do not show ferroelectric behaviour.

2.2.2 Mechanisms Supporting the Coexistence of Magnetism and Ferroelectricity

The presence of d electrons (favourable for magnetism) does not favour a hybridization with oxygen and thus the cationic displacement required for ferroelectricity, therefore new ways of combining magnetism and ferroelectricity are needed to overcome this limitation. So as for ferroelectricity and magnetism to coexist in a single phase, either an alternative (non-d-state electron) mechanism for magnetism or an alternative mechanism for ferroelectricity is required.

The alternative mechanism for ferromagnetism could be in using f-electron magnetism. For example, GFO can be used due to the divalent Eu^{2+} having large

magnetic moment from the seven f electrons and the Ti^{4+} ion having a non-magnetic d^0 electron configuration favourable for ferroelectric off-centring. Bulk $EuTiO_3$ is not ferroelectric, but the similarity between a large permittivity increasing rapidly at low temperature and ferroelectric phase transition revealed that the small size of the Eu^{2+} ion and the related small lattice parameter do not allow for the large Ti^{4+} ion to off-centre (*Rushchanskii et al., 2010*). Therefore, via increasing the lattice parameter artificially, through tensile and compressive strains (*Fennie & Rabe, 2006*) or by replacing A-site ions with a larger ion such as Ba (*Rushchanskii et al., 2010*) the ferroelectric state can be induced. However, the main disadvantage of f-electron magnetism is that the tightly bound f electrons have quite low ordering temperature, for example $EuTiO_3$ aligns antiferromagnetically at 5 K. Multiferroicity in bulk Ba-$SrMnO_3$ (SMO) was also obtained through the strain exerted chemically by the large size of Ba^{2+} ions (*Sakai et al., 2011; Bhattacharjee et al., 2009*).

Four main types of the ferroelectric materials belonging to the nondisplacive class that enable the coexistence of ferroelectric and magnetic orders can be distinguished (*Fiebig, 2005; Cheong & Mostovoy 2007; Fiebig et al., 2016; Bousquet & Cano, 2016; Johnson & Radaelli, 2014; Barone & Picozzi, 2015*) considering the mechanism inducing the multiferroicity (**Figure 2.8**). Ferroelectricity may be driven by electronic and steric effects, charge order or magnetism. In the first three types, the magnetic and ferroelectric orders occur independently, and the magnetoelectric material is classified as type I. In the last type, the ferroelectric and magnetic transitions are induced together, wherein the magnetoelectric material is classified as type II.

In magnetic perovskite oxides, multiferroicity is typically formed by using so-called lone-pair stereochemical activity of the large (A-site) cation to induce the ferroelectricity, while keeping the small (B-site) cation magnetic. The spatial asymmetry is generated by the anisotropic distribution of unbonded valence electrons around the host ion (**Figure 2.8a**). The lone pair on the Bi^{3+} ion is the mechanism responsible for the room-temperature ferroelectricity in the Bi-based magnetic ferroelectrics, the most commonly studied of which is bismuth ferrite, $BiFeO_3$ (*Wang et al., 2003*). The pair of Bi^{3+} valence electrons in the 6s orbital is not involved in sp hybridization and generates a local dipole, inducing a spontaneous polarization (*Lebeugle et al., 2007; Li et al., 2004; Wang et al., 2003*) of ~60-100 $\mu C/cm^2$ below Curie temperature (*Teague et al., 1970*), T_C = 1103 K. A long-range order antiferromagnetic arrangement arises below the Néel temperature (*Fischer & Polomska, 1980*), T_N = 643 K. Among the lone-pair systems, $BiFeO_3$ is the only room-temperature single-phase multiferroic material, which has large and robust electric polarization and magnetoelectric coupling at T = 300 K (*Kumar et al., 2011*), α = 10 ps/m in 100-nm-thick film (~ 15 mV cm^{-1} Oe^{-1} considering ε = 50). Besides, in the epitaxially grown $BiFeO_3$ thin films of the giant electric polarization beyond 150 $\mu C/cm^2$ was obtained by straining them and leading to the tetragonal crystal structure where the polarization is aligned along [001] direction (*Moreau et al., 1971*; *Yun et al.*,

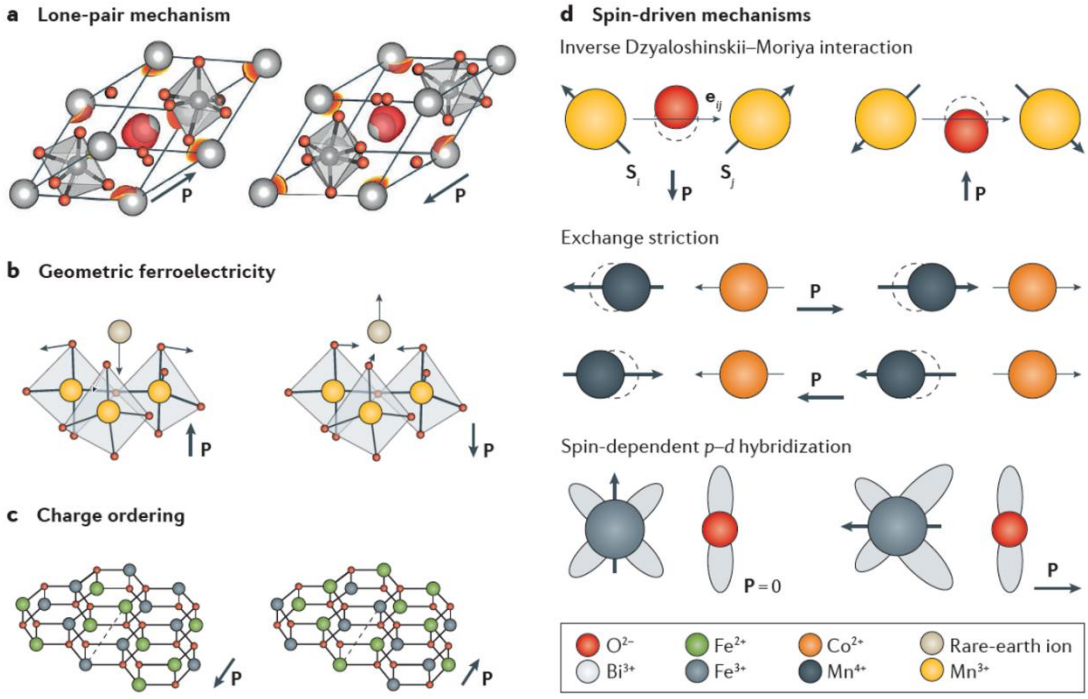

Figure 2.8: Mechanisms promoting the coexistence of magnetic and electric long-range order. **(a)** Lone-pair ferroelectricity in $BiFeO_3$. Ferroelectricity originates from two Bi^{3+} electrons that shift away from the Bi^{3+} ion and towards the FeO_6 octahedra, giving rise to a spontaneous polarization P along the [111] direction. The lone pair is visualized by the isosurface (red) of the electron localization function of ferroelectric $BiFeO_3$. **(b)** Geometrically driven ferroelectricity in hexagonal (h-) $R MnO_3$ emerges from a tilt and deformation of MnO_5 bipyramids, which displace the rare-earth ions as indicated by the arrows, leading to a spontaneous polarization along the [001] axis. **(c)** Charge ordering in $LuFe_2O_3$ creates alternating layers with Fe^{2+}/Fe^{3+} ratios of 2:1 and 1:2. This was argued to create a spontaneous polarization between the two layers, which is oriented parallel to the arrow. **(d)** Mechanisms for spin-induced ferroelectricity. Polar displacement is induced by antisymmetric spin exchange interactions (inverse Dzyaloshinskii–Moriya interaction; top panel) as observed, for example, in orthorhombic (o-) $R MnO_3$: the polarization vector is $P \propto e_{ij} \times (S_i \times S_j)$, where e_{ij} is the unit vector connecting neighbouring spins and $S_{i,j}$ are the spins at *neighbouring* sites i and j. Ferroelectricity arises from symmetric spin exchange in Ca_3CoMnO_6 (*Choi et al., 2008*) shown in the middle panel, with $P \propto R_{ij}(S_i \cdot S_j)$, where R_{ij} denotes the direction along which the magnetostriction occurs. Spin-driven modulations of the chemical bond between magnetic 3d orbitals and ligand 2p orbitals (indicated by grey clouds) yield a spontaneous polarization along the bond direction in delafossites, such as $CuFeO_2$, as expressed by the relation $P \propto (S_i \cdot e_{ij})2e_{ij}$ (bottom panel). From *Fiebig et al., 2016*

2004). So that Fujitsu Co. announced the application of the $BiFeO_3$ ferroelectric material in Ferroelectric Random-Access Memory (FRAM) technology (*Maruyama et al., 2007*).

A second type of multiferroism is provided by so-called "geometrically-driven" ferroelectricity, which is a different type of off-centering that does not depend on covalent bond formation and thus is consistent with the coexistence of magnetism. Space-filling phenomena and geometrical constrains can generate structural instabilities in materials. When these steric effects, instead of chemical bonding

consideration, cause ionic shifts that result in the formation of polar state, the term geometrically-driven ferroelectricity can be used (**Figure 2.8b**). In this case the ferroelectric phase transition is caused by a rotation instability of the coordination polyhedral and correspondent displacement of the A-site cations. This system requires an absence of tree-dimensional connectivity of the polyhedra, if not when one polyhedron rotates in one direction its connected neighbour rotates as well in the opposite direction resulting in zero net polarization. For instance, in h-RMnO$_3$ (R=Sc, Y, In, or Dy-Lu), unit cell tripling causes the formation of a ferroelectric order (*Van Aken et al., 2004; Fennie & Rabe; 2005; Lilienblum et al., 2015*) at $T_C \geq 1200$ K with a polarization 5.6 μC/cm^2 (*Coeuré et al., 1966*), whereas magnetic ordering at $T_N \leq 120$ K (*Fiebig et al., 2000*). A similar effect is demonstrated in h-LuFeO$_3$ thin films, that shows a larger magnetic moment and ambient temperature magnetic order (*Wang et al., 2013a*). The layered antiferromagnetic ferroelectric BaNiF$_4$ (*Ederer & Spaldin, 2006*) also falls into geometrically-driven ferroelectricity, in which an asymmetry between Ba^{2+} and F^- sites leads to a spontaneous polarization. A comprehensive first-principles calculations study of the existence and origin of the ferroelectric instability in the ABF_3 fluoroperovskites was reported, which revealed the existence of many fluoroperovskites that have a ferroelectric instability in their high-symmetry cubic structure, which originates from ionic size effects (*Garcia-Castro et al., 2014*). Although the value is low ~0.01 μC/cm^2, it couples to a weak ferromagnetic moment enabling its reversal with the electric polarization. Another example is the cooperation between two nonpolar lattice modes generating an electric polarization in $Ca_3Mn_2O_7$ (*Benedek & Fennie, 2011*).

When materials contain magnetic ions of the same element but with different valence charges, such as Fe^{2+} and Fe^{3+}, valence electrons can be distributed non-uniformly around their host ions in the crystal lattice to from a periodic superstructure in a non-centrosymmetric arrangement. Here, the Fe atoms in $LuFe_2O_4$ may form a superstructure with an alternating sequence of Fe^{2+} and Fe^{3+} ions (*Ikeda et al., 2005*). The ordering arrangement should be switchable by an electric field, resulting in an electric polarization and ferroelectricity (*Van der Brink & Khomskii, 2008*) (**Figure 2.8c**), however, the occurrence of ferroelectricity in this material has not been shown yet (*De Groot et al., 2012*). Charge polarized state is also observed in mixed manganite, such as $Pr_{1-x}Ca_xMnO_3$ that are also included in this class of multiferroics (*Jooss et al., 2007*).

Magnetic ordering can break inversion symmetry and cause directly the polarization. The interaction of spins and charges may transfer the non-centrosymmetry from the magnetic to the electric lattice, directly generating a polar state. These magnetically induced, improper ferroelectric materials represent the ultimate change from displacive ferroelectrics, in which magnetic ordering is inhibited, towards materials in which ferroelectric polarization is induced by the formation of a symmetry-

lowering magnetic ground state, such as a magnetic spiral that lacks of inversion symmetry.

Currently three main microscopic models were developed to better understand multiferroics in which ferroelectricity is magnetically induced (**Figure 2.8d**) (*Kimura, 2007*).

The most widely studied mechanism is the so-called inverse Dzyaloshinskii-Moriya (DM) interaction. The DM interaction is an antisymmetric exchange coupling between two spins on a non-centrosymmetric crystallographic structure (*Dzyaloshinskii, 1958*). In the inverse DM interaction, an acentric spin structure drives a non-centrosymmetric shift of charges (*Katsura et al., 2005*; *Mostovoy, 2006*). Spin-orbit coupling is crucial in both DM and inverse DM interactions. The electric polarization originated in the inverse DM interaction is determined by the optimization of the spin configuration by means of antisymmetric exchange, expressed by the antisymmetric product $S_i \times S_j$ of neighbouring spins S_{ij}. It yields a one-to-one correlation between (antiferro-)magnetic order and electric polarization. This mechanism occurs in Cr_2BeO_4 (*Newnham et al., 1978*), o-$TbMnO_3$ (*Kimura et al., 2003*) and $CaMn_7O_{12}$ (*Terada et al., 2016*). However, DM interaction does not account for systems in which ferroelectricity is induced by collinear spin arrangements.

In contrast to the DM interaction, the Heisenberg-like exchange striction (**see Figure 2.8d**) defines an acentric displacement of charges derived from the optimization of the symmetric spin product $S_i \cdot S_j$ (*Sergienko & Dagotto, 2006; Fiebig et al., 2016*). The mechanism was first discovered in perovskite $TbMn_2O_5$ (*Hur et al., 2004*). The dominance of the non-relativistic symmetric mechanism ($|S_i \cdot S_j| > |S_i \times S_j|$) is demonstrated in (o-) $TbMnO_3$, in which an increase in the polarization is achieved when a cycloidal order (parameterized by $S_i \times S_j$) transforms into a collinear antiferromagnetic order ($S_i \cdot S_j$) under pressure (*Aoyama et al., 2014*). Among the spin-driven ferroelectrics, symmetric Heisenberg-like exchange striction leads to a larger polarization that antisymmetric DM exchange. This is reflected by (o-) $TbMnO_3$, which experiences a transition from a spiral order ($P_s \leq 0.1$ μC cm^{-2}) to a collinear antiferromagnetic order ($P_s \sim 1$ μC cm^{-2}) under pressure (*Sergienko & Dagotto, 2006*). The largest spin-spiral-driven polarization has been claimed for $CaMn_7O_{12}$ ($P_s \sim 0.3$ μC cm^{-2}) (*Johnson et al., 2012*).

In delafossite system, such as Cu*M*O_3 (*M*=Fe, Cr), $CuFe_{1-x}Al_xO_2$ (*Arima, 2007*; *Nakajima et al., 2007*; *Frontzek et al., 2011*), a spontaneous polarization $P \leq 0.03$ μC/cm^2 is induced by a screw-like spin structure with $S_i \times S_j = 0$. This polarization is driven by a variation in the metal-ligand hybridization as a function of spin-orbit coupling (*Arima, 2007*).

2.3 Artificial Magnetoelectric Nanostructured Composites

Until now, the focus has been primarily on the mechanisms permitting the combination of ferroelectric and magnetic order in a single-phase material. The alternatives are hybrid systems, such as composite multiferroic materials. Magnetoelectric composites made by combining ferroelectric and magnetic phases are a novel class of next generation multifunctional materials that have drawn significant interest in recent years (*Nan et al., 2008*; *Martin et al., 2008*; *Schileo, 2013*; *Srinivasan, 2010*; *Spaldin & Fiebig, 2005*; *Eerenstein et al., 2006*). In particular, the indirect strain mediated coupling interaction between piezoelectric and magnetostrictive constituents could produce large ME responses. For example, magnetoelectric thin-film cantilever made of AlN and FeCoSiB showed a ME coefficient as large as ~20 kV cm^{-1} Oe^{-1} at 152 Hz (*Kirchhof et al., 2013*), and ($BaTiO_3$-$BiFeO_3$)×15 ultrathin multilayer composite showed α~55 V cm^{-1} Oe^{-1} at 1 kHz (*Lorenz et al., 2017*). The highest low-frequency ME coupling in bulk thin-film composite ~52 V cm^{-1} Oe^{-1} at 1 kHz was observed in Metgals/PZT (fiber)/Metglas composite (*Wang et al., 2011*). The composites show 3-6 orders of magnitude higher α than for single-phase ME materials such as Cr_2O_3 α~4.14 ps m^{-1} or 22.4 mV cm^{-1} Oe^{-1} at 260 K (*Wiegelmann et al., 1994; Pyatakov & Zvezdin, 2012*), which can be attributed to the large intrinsic polarization (e.g. BTO, PZT & BFO), piezoelectric coefficient (e.g. AlN, PZT, PZN-PT & PMN-PT), magnetostrictive constant (Metglas, CFO & Terfenol-D), and magnetization (e.g. Co_xFe_{1-x}, CoFeB, FeGaB, FeCoV, FeCoSiB & FeBSiC) in these systems (*Nan et al., 2008).* The ME effect in composite materials is known as a product tensor property which results from the cross interaction between piezoelectric and magnetostrictive ordering of the two phases.

ME composite architectures have been elaborated in several geometries (**Figure 2.9**) like horizontal multilayer structures (*Ryu et al., 2012*; *Mori & Wuttig, 2002*; *Fang et al., 2009*), particles embedded in a matrix (*Van Run et al., 1974*; *Islam & Priya, 2009*), as well as low-dimensionality heterostructures such as laminated and epitaxial self-assembled vertically aligned heterostructures (*Zheng et al., 2004*; *Yan et al., 2009*; *Zheng et al., 2006*; *Li et al., 2005a*) including the sub-class coaxial nanocables (*Yao et*

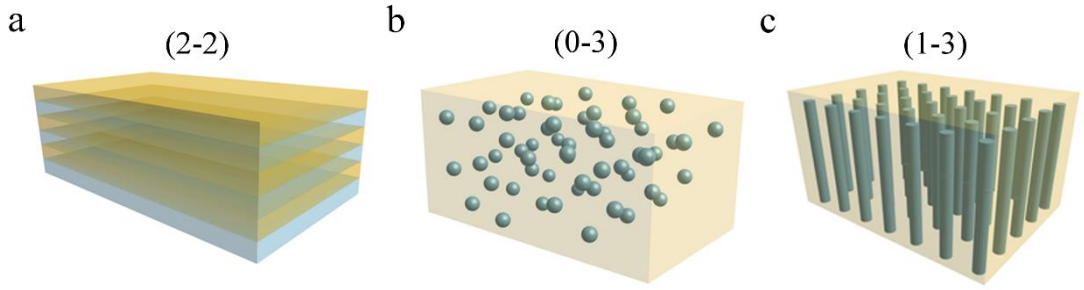

Figure 2.9: Schematic diagrams of the three types of multiferroic composites. **(a)** Horizontal multilayer heterostructures, which is (2-2) connectivity system, **(b)** particulate composites, which is (0-3) connectivity system, and **(c)** vertically aligned heterostructures, which is (1-3) connectivity system.

al., 2010; *Xie et al., 2011*; *Zhu et al., 2014*). However, to precisely control the strain value as well as to miniaturise the composites for future application technology in nanodevices, the development of the thin-film architectures corresponding to these three geometries is required, which is discussed in the present Section.

2.3.1 Multilayer (2-2) Thin-Film Nanocomposites

Ferromagnetic and ferroelectric oxide thin films can be grown epitaxially either on single crystal or even on Pt/Si substrates layer by layer with atomic-scale precision, with much better control than for bulk crystals. In the beginning, these techniques were mostly used to reproduce multiferroic bulk phases in thin films, and this was done in compounds such as o-$TbMnO_3$, h-$RMnO_3$, $BiFeO_3$, and $EuTiO_3$ (*Wang et al., 2003; Glavic et al., 2013; Marti et al., 2006; Fennie & Rabe, 2006*). The most successful multiferroic candidates were $BiFeO_3$ thin films, which were grown in a large range of structural configurations (e.g. tetragonal lattice) that are inaccessible in bulk crystals. The comprehensive reviews for these structures have been reported previously (*Yang et al., 2015; Heron et al., 2014a; Sando et al., 2014*). This section is dedicated to the classification of magnetoelectric effects in multiferroic heterostructures. In particular, the effects of strain, heteroepitaxy and interfaces in horizontal and vertical heterostructures. The interfaces between different phases can transfer the strain-stress mechanical interaction between the constituents (e.g. strain-stress deformation).

A general problem of the single-phase multiferroics is their antiferromagnetic order, because the cancelation of a macroscopic net magnetization makes them technologically unsuitable. This limitation of the antiferromagnet can be overcome by growing it on the ferromagnetic materials (bilayers, multilayers). Exchange bias occurs when the antiferromagnet is in contact with the ferromagnet and gives shift and hardening of the ferromagnetic hysteresis resulting from interfacial exchange interaction with adjacent antiferromagnet. Similar mechanism is used in the read-write heads in hard disk technology. Coupling an electrically-tuneable antiferromagnet with a ferromagnetic layer could enable the control of the magnetic exchange bias with an applied electric field and to shift the ferromagnetic hysteresis loop via voltage. The current operation principle could be used for low-energy magnetoelectric memories (*Scott, 2007a; Bibes & Barthélémy, 2008*). In this regard, a theoretical prediction of magnetoelectric coupling shown in $BiFeO_3$ (*Ederer & Spladin, 2005*) was followed by the experimental proof of a modification of the exchange bias at room temperature in $BiFeO_3$-CoFe (*Allibe et al., 2012*). Another significant breakthrough was achieved through the observation of an electrically induced rotation of the magnetization in a microscopic $BiFeO_3$-CoFe dot (*Chu et al., 2008*), wherein a repeatable magnetization reversal by an electric field was demonstrated at room temperature (*Heron et al.,*

2014b); that is the main requirement for the memory application of magnetoelectric multiferroics.

Another mechanism for the magnetoelectric coupling of multiferroic thin films is epitaxial strain. By choosing a substrate with specific lattice constant, wide range of tensile and compressive strains can be obtained. The corresponding change of the lattice constant can induce a transition to new material phases or modify the present one. Strain was used to confirm the correlation between ferroelectric and magnetic spiral order in $BiFeO_3$ (*Sando et al., 2013*). Strain can generate ferroic order in non-ferroic compounds, such as $SrTiO_3$ (*Haeni et al., 2004*), $SrMnO_3$ (*Becher et al., 2015*) and $EuTiO_3$ (*Lee et al., 2010*); in the last one the polar order coexists with magnetic order. Finally, strain can be used to couple ferroelectric and ferromagnetic domains across an interface through piezoelectric-magnetostrictive coupling, or strain-stress mediated magnetoelectric coupling (*Duan et al., 2006; Molegraaf et al., 2009*). This effect was experimentally shown in $BaTiO_3$-CoFe system, where it was revealed that the anisotropy and ordering temperature of interfacial magnetism can be changed by electric field (*Lahtinen et al., 2012*). However, this interaction is mainly a product of epitaxial interfaces rather than a magnetoelectric response in magnetostrictive-piezoelectric composites with unspecified, rough interfaces that serve as strain mediators (*Nan et al., 2008*).

Magnetoelectric effect can also be produced at the interface between two constituent phases. New properties may be generated at the interface due to low local symmetry, confinement effects, strain gradients and chemical anisotropy. Indeed, the multiferroic nature of the interface between Fe, or Co, and a $BaTiO_3$ was shown, wherein the multiferroicity is maintained within several atomic layers around the interface (*Valencia et al., 2011*). Interestingly, interfaces break space- but not time-inversion symmetry. Therefore, the magnetization axis at the interface can be changed by an applied electric field, but the direction along this axis remains stable unless an external magnetic field is applied.

2.3.2 Particulate (0-3) Thin-Film Nanocomposites

Particulate multiferroic thin-film nanocomposites are typically fabricated by self-assembly. By simply mixing the precursors of the ferroelectric and ferromagnetic materials, which cannot form a solid solution, such as $BaTiO_3$ and $NiFe_2O_4$, self-assembled (0-3) nanocomposite thin films can be prepared. The surface energy of the materials was found to play a critical role in determining the microstructure of the (0-3) thin-film nanocomposites. The self-assembled two-phase thin-film nanocomposites, combining perovskite ferroelectrics (e.g. BTO, PZT, and BFO) with spinel ferromagnetic materials (e.g. CFO and NFO), showed large magnetoelectric coefficient at room temperature. In a previously reported polymer-assisted deposition of the BTO-

CFO particulate nanocomposites, four separate solutions with Ba, Ti, Co, and Fe bound to polymer were prepared, respectively (*Yan et al., 2011*). Ba and Fe were bound as an ethylenediaminetetraacetic acid (EDTA) complex to polyethyleneimine (PEI). Co was bound to PEI directly. The Ti solution was made by adding the mixture of 30% peroxide and titanium chloride in water to the solution mixed with PEI and EDTA. The prepared solutions were purified and concentrated in a filtration unit. Inductively coupled plasma optical emission spectrometer was used to analyse the final concentration of Ba, Ti, Co, and Fe ions in the four solutions, respectively. These solutions were mixed to the final solution with the molar ratio of Ba:Ti:Co:Fe=1:1:1:2. The resulting solution was spin-coated on the $LaAlO_3$ (LAO) substrate. The thermal crystallization was then performed with oxygen. First the polymer was pyrolyzed by initially slowly heating it to 550 °C at the rate of 1-5 °C/min. Then the samples were annealed by heating at 900 °C for 1 h to induce crystallization. XRD analysis showed that the $BaTiO_3$ thin film is epitaxial, while CFO is c-axis oriented. The magnetic properties of CFO were characterized using Magnetic Force Microscopy (MFM), wherein the magnetic domains were observed showing that the CFO phase is dispersed uniformly in the BTO film. The microstructure of the BTO-CFO particulate composite was characterized using the cross-section TEM, revealing that BTO phase is epitaxially grown on the substrate forming the matrix in the nanocomposite, while CFO nanoparticles were embedded in the BTO matrix.

Correspondingly, the BTO-NFO particulate thin-film nanocomposites were prepared using the polymer-assisted deposition technique (*Luo et al., 2007*). However, in contrast to the BTO-CFO system, the BTO nanoparticles were embedded into the NFO matrix. This difference between self-assembly of the BTO-CFO and BTO-NFO nanocomposites was ascribed to the surface energy. It was found that the surface energy of (001) CFO (1.486 J/m^2) is larger than (001) BTO (1.26 J/m^2), whereas the surface energy of (001) BTO is larger than (001) NFO (1.161 J/m^2). The material with lower surface would like to wet the one with a higher surface energy, forming a matrix surrounding the material with larger surface energy. Therefore, for the BTO-CFO nanocomposites, the BTO is the matrix, meanwhile for the BTO-NFO nanocomposite, the NFO is the matrix.

2.3.3 Vertically Aligned (1-3) Thin-Film Nanocomposites

Intensive research in the field of multiferroic nanocomposites has opened new routes such as the fabrication of vertically aligned thin-film nanocomposites, i.e. nanopillars embedded in a matrix, the so called (1-3) connectivity nanocomposite. As compared to the conventional multilayer (2-2) thin-film nanocomposites, these types of nanocomposites offer the advantage to reduce the substrate imposed clamping effect, which is known to suppress both the piezoelectric response as the magnetoelastic

coupling mediated by lattice deformation (*Nan et al., 2005; Nagarajan et al., 2004*), and to enhance the interfacial surface area between the two phases, so that large magnetoelectric (ME) coupling can be expected (*Nan et al., 2008; Bichurin et al., 2003*). This approach using vertically aligned multiferroic nanocomposites is relatively new, and extensive research is still needed to describe the nature of the heteroepitaxy as well as the coupling mechanisms, the interfacial and ferroelectric-ferromagnetic domain boundary effects.

Up to now, large number of (1-3) thin-film nanocomposites from spinel and perovskite systems, including $BaTiO_3$-$CoFe_2O_4$ (BTO-CFO) (*Zheng et al., 2004*), $BiFeO_3$-$CoFe_2O_4$ (BFO-CFO) (*Zavaliche et al., 2005*), $PbTiO_3$-$CoFe_2O_4$ (PTO-CFO) (*Levin et al., 2006*), $PbZr_{0.52}Ti_{0.48}O_3$-$CoFe_2O_4$ (PZT-CFO) (*Wan et al., 2007*), $Bi_5Ti_3FeO_{15}$-$CoFe_2O_4$ (BTFO-CFO) (*Imai et al., 2013*), $PbMg_{1-x}Nb_xO_3$-$PbTiO_3$-$CoFe_2O_4$ (PMN-PT-CFO) (*Wang et al., 2014a*), $BiFeO_3$-$NiFe_2O_4$ (BFO-NFO) (*Benatmane et al., 2010*), and $BiFeO_3$-$Co_xNi_{1-x}Fe_2O_4$ (BFO-CNFO) (*Ojha et al., 2016*) were fabricated using pulsed laser deposition (PLD) technique.

Under appropriate growth conditions, nanopillar arrays of the magnetic component form in a ferroelectric matrix; due to the close oxygen sublattice parameters, both phases grow epitaxially, both in-plane and perpendicular to the substrate. For $BaTiO_3$ –$CoFe_2O_4$ multiferroic nanocomposites, a sizeable change in the magnetic properties that arises from strain-induced magnetoelastic interaction between the $BaTiO_3$ and the $CoFe_2O_4$ nanopillars is observed as the system passes through the ferroelectric critical temperature, (*Zheng et al., 2004*; *Nan et al., 2005*; *Ryu et al., 2006*) as shown in **Figure 2.10**. (*Zheng et al., 2004*) The vertical disposition of the nanopillars is more favourable for magnetoelectric coupling, (*Ryu et al., 2006*) as it minimizes the clamping effect due to strong in-plane elastic coupling to the substrate. Room temperature magnetization reversal induced by an electric field was demonstrated in $BiFeO_3$ – $CoFe_2O_4$ multiferroic nanocomposites (*Zavaliche et al., 2005*; *Zavaliche et al., 2007*).

In terms of nanocomposite assembly, controlling the degree of ordering in the array of nanopillars is one of the most challenging tasks. The formation of self-assembled, vertical nanocomposites with long-range ordering will have great impact in the field of artificial multiferroic nanocomposites. Particularly active research has been focused in improving the nanopillars ordering. In order to control the long-range ordered vertical interface, anodic aluminium oxide (AAO) membranes were used as a hard mask to fabricate PZT-CFO and BFO-CFO (1-3) nanocomposites (*Gao et al. 2010; Stratulat et al., 2013*). The PZT-CFO (1-3) nanocomposites were prepared via PLD deposition through an ultrathin AAO membrane of the CFO dots, followed by the mechanical removal of the AAO mask and then another constituent, PZT, in form of dots or film was deposited by PLD as well (*Gao et al. 2010*). To grow BFO-CFO (1-3) nanocomposites, first, CFO nanodots were deposited by PLD technique through AAO masks as nucleation centres with hexagonal symmetry (*Stratulat et al., 2013*). Then the BFO-CFO (1-3) vertically aligned system was grown by PLD technique from a mixed

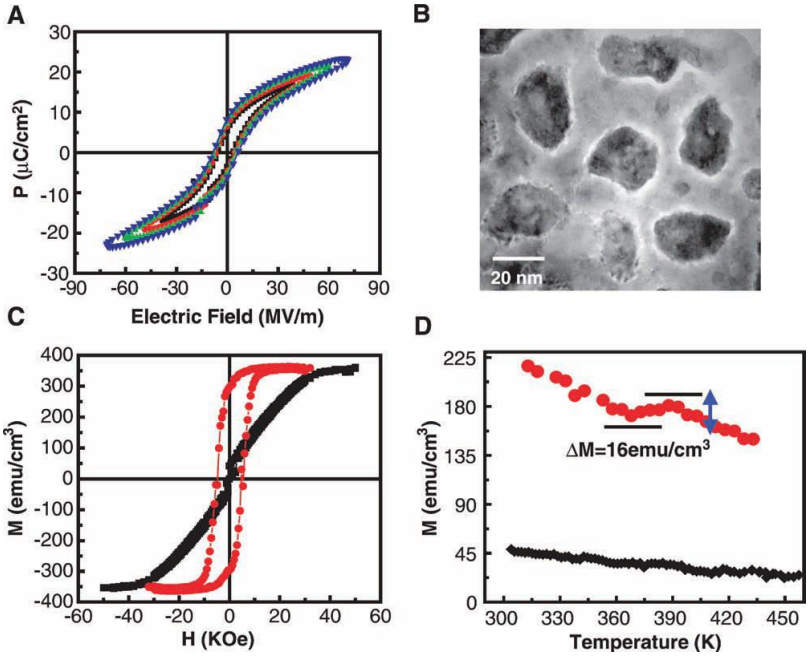

Figure 2.10: Multiferroic $BaTiO_3$-$CoFe_2O_4$ nanocomposite: **A,C**: classical ferroic behavior showing the coexistence of ferroelectric and magnetic order. **B**: Planar transmission electron micrograph of the sample structure, showing the $CoFe_2O_4$ nanopillars embedded in the $BaTiO_3$ matrix. **D**: Magnetization *vs.* temperature response of the system, showing a change in the magnetic response of the system with the onset of ferroelectric order (red symbols) compared with the signal from a simple multilayered structure showing negligible change in magnetism. From *Zheng et al., 2004*

target resulting in a thicker BFO-CFO nanocomposite as compared to the mentioned earlier PZT-CFO system, in which the PZT film was grown on top of the CFO dots from an individual target.

As alternative to AAO masks to prepare BFO-CFO (1-3) nanocomposites a triblock copolymer was used as a mask to etch the square array of holes on STO substrate, followed by the CFO nuclei PLD growth in the patterned pits. (*Choi et al. 2014*) Then a thin BFO layer was deposited by PLD to cover the mesas, and finally, a thick BFO/CFO nanocomposite was grown from BFO and CFO targets by PLD. Another approach to etch the Nb-doped STO substrate with shallow pits was reported by the same group using a Ga focused ion beam (FIB). Then similar strategy was used to grow BFO-CFO (1-3) nanostructure. First, the CFO islands were grown selectively by PLD at the substrate template sites, then a thin BFO film was grown by PLD, which covered the rest of the substrate. Finally, the few-nm-thick well-ordered BFO-CFO composite layer was used as a guide for the directed growth of a thick self-assembled nanocomposite from two separate BFO and CFO targets.

Another work demonstrated the preparation of the BFO-CFO (1-3) nanocomposites using pulsed electron deposition and e-beam lithography (*Comes et al., 2012*). Briefly, the CFO film was deposited using pulsed electron deposition (PED), then the as-deposited CFO film was etched using Ar ion, followed by the deposition of 1-nm-thick BFO film using PED. Finally, CFO and BFO were co-deposited using PED to form a thick epitaxial nanocomposite.

2.3.4 Alternative Strategies for the Growth of Vertically Aligned (1-3) Multiferroic Nanocomposites

The main problems of the PLD based self-assembly are low reproducibility of the pillars, high-cost, low scale, and high complexity in fabrication. Alternatively, vertically aligned (1-3) multiferroic nanocomposites can be prepared in two steps: (i) preparation of the free-standing vertically aligned nanopillar arrays and (ii) deposition of the constituent matrix, film, or layer on top of the nanopillars using different Physical Vapour Deposition (PVD) and Chemical Vapour Deposition (CVD) techniques.

Recently free-standing and vertically aligned BTO and PZT nanocomposites were prepared using low-cost and large scale chemical methods (*Yao et al., 2017; Zhang et al., 2016*). Highly-oriented BTO nanorod arrays were fabricated using hydrothermal reaction on the glass substrate (i.e. alkaline treatment of the TiO_2 nanorod arrays) (*Yao et al., 2017*). Whereas, the PZT nanocups were prepared by dipping a PZT solution into the AAO template, followed by annealing (*Zhang et al., 2016*). Then the residual PZT film on the AAO membrane was removed by Ion Beam Etching. After the Ion Beam Etching process, the remaining AAO was chemically dissolved revealing the arrays of PZT nanocups.

On the other hand, the ferromagnetic metal nanopillar arrays can be grown by electrochemical deposition into nanoporous templates. The geometric parameters of the grown nanopillars can be tuned by adjusting the morphological features of the hosting template (e.g. pore diameter, height, pores density, and porosity). The templating method can be implemented using three main host materials, which are block copolymers (*Tang et al., 2008*), track-etched polymer membranes (*Ferain et al., 2003*), and porous oxide templates. The magnetic nanowires can be subsequently electrodeposited into the nanochannels of those oxide or polymer membranes (*Piraux et al., 1994*). Recently, a new type of vertically aligned magnetic nanocomposites was developed, the 3D interconnected magnetic nanowire networks using the track-etched polymer membranes containing porous 3D nanochannel networks (*Araujo et al., 2015*).

In the second step of multiferroic nanocomposites preparation, the deposition of nanoscale matrix (or top layer) on of the nanopillar (or nanowire) arrays could be conducted by either top-down processing – using bulk ceramic targets as a source for the nanomaterials formation, including physical vapour deposition (e.g. sputtering deposition and pulsed laser deposition), focused ion-beam and electron beam writing, or bottom-up processing – using self-organization of atoms and molecules in aqueous and gas phases to built-up the nanomaterials, including molecular beam epitaxy, atomic layer deposition, metal-organic chemical vapour deposition, and chemical solution deposition (e.g. sol-gel, co-precipitation, and hydrothermal syntheses). The possibility of the integration of functional PZT films with the on-chip copper foil using sol-gel spin-coating has been reported (*Kingon & Srinivasan, 2005*). High-quality PZT films were deposited on Si substrates using Metal-Organic Chemical Vapour Deposition

(*Yokoyama et al., 2003*), PLD (*Dekkers et al., 2009*), sol-gel (*Fe et al., 2001*; *Taylor and Damjanovic, 2000*; *Gong et al., 2003*) and RF magnetron sputtering (*Adachi et al., 1987*; *Kalpat & Uchino, 2001*). Among them, sol-gel is a flexible, facile, and inexpensive chemical synthesis method to deposit polycrystalline or textured films with preferential orientation providing possibility to fabricate large-scale thick films. However, to grow the epitaxial oxide thin films with excellent crystal structure, atomic thickness control, and good interface matching, the conventional chemical solution deposition is replaced by the PVD techniques (e.g. PLD, molecular beam epitaxy [MBE] and magnetron sputtering) on the oxide substrates such as $SrTiO_3$.

There is also a significant interest in the use of template-assisted synthesis methods due to their proven reliability, flexibility and reproducibility in order to build well-ordered three-dimensional arrays of nanocables (NCs) with high aspect ratio and high surface areas (*Andrew et al., 2014*; *Liu et al., 2012a*; *Liu et al., 2012b*; *Liu at el., 2007*; *Johnson et al., 2011*; *Narayanan et al., 2012*). In a previous work (*Sallagoity et al., 2015a*), the two-step elaboration of $BaTiO_3$-Ni (BTO-Ni) NC arrays within porous anodic aluminium oxide (AAO) templates was reported, and the limitations inherent to annealing temperature was pointed out (*Yang et al., 2003*; *Xiao et al., 2002*; *Sallagoity et al., 2016*). Thermal treatment performed at too high temperature: (i) may affect the ferroelectric BTO shell microstructure through defects-driven surface rearrangement and diffusion inside the AAO pores, or it (ii) may induce the template curvature and hence hinder the subsequent Ni electrodeposition into the BTO-coated AAO pores. Meanwhile, composites made of $PbZr_{0.52}Ti_{0.48}O_3$-$CoFe_2O_4$ (PZT-CFO) are very appealing, as PZT with composition near the morphotropic phase boundary (MPB) exhibits excellent FE and piezoelectric properties, whereas CFO displays large magnetocrystalline anisotropy, high coercivity, and moderate saturation magnetization (*Nan et al., 2008*). Most of the studies devoted to coaxial PZT-CFO were based on electrospinning (*Xie et al., 2008*; *Xie et al., 2011*; *Xie et al., 2013*) and sol-gel deposition into AAO pores (*Hua et al., 2008*; *Tang et al., 2017*).

Co-axial electrospinning is a flexible technique based on the sol-gel deposition, which can be used to synthesize a large variety of multiferroic core-shell nanocables, including BFO-CFO (*Zhu et al. 2014*) and BTO-CFO (*Baji, et al., 2014*; *Fu et al., 2015*). Additionally, the core-shell multiferroic NCs can be prepared using a combination of sol-gel deposition and crystallization of FE shells into porous AAO and subsequent electrodeposition of ferromagnetic (FM) cores into the as-deposited FE shells, as was previously demonstrated for BFO-Co, PZT-Co (*Johnson, S. H., 2011*), BFO-Ni (*Shi et al., 2014*) and BTO-Co (*Narayanan et al., 2012*) core-shell nanowires. After the electrodeposition of FM core inside FE shell, a thermal oxidation can be conducted in order to transform metallic core into insulating spinel magnetic oxide, as was demonstrated for the vertically aligned PZT-NFO core-shell NC arrays (*Liu, et al., 2007*).

2.4 Magnetoelectric Coupling

The independent coexistence of two or more ferroic orderings in one material could result in the coupling between magnetic and electric degrees of freedom and additional phenomena (*Hill, 2002*). The linear and quadratic magnetoelectric effects are already well defined (*Fiebig et al., 2004*). Wherein a magnetization linear or quadratic in the applied field strength is induced by an electric field (or vice versa, an electric polarization is induced by a magnetic field). The free energy, *F*, can be expended in terms of the electric field *E* and magnetic field *H* as:

$$F(E,H) = F_0 + P_i E_i + M_i H_i + \frac{1}{2}\varepsilon_0 \varepsilon_{ij} E_i E_j + \frac{1}{2}\mu_0 \mu_{ij} H_i H_j + \alpha_{ij} E_i H_j + \frac{1}{2}\beta_{ij} E_i H_j H_k + \frac{1}{2}\gamma_{ijk} H_i E_j E_k + \cdots . \quad (2.9)$$

Here, P_i and M_i are the spontaneous polarization and magnetization in direction i, ε_{ij} and μ_{ij} are the relative permittivity and permeability, $\varepsilon_0 = 1/(c^2\mu_0)$ and $\mu_0 = 4\pi \cdot 10^{-7}$ are free space permittivity and permeability, α is the linear magnetoelectric susceptibility tensor, and β and γ are the bilinear magnetoelectric susceptibility tensors describing the *EHH* and *HEE* effects. The symmetry group that allows the existence of the linear and bilinear magnetoelectric effects, and the form of the corresponding tensors have been tabulated (*Ascher, 1968; Grimmer, 1994*). Note that the linear magnetoelectric effect can only take place in crystals with ferromagnetic or antiferromagnetic point groups, although bilinear effects can occur in diamagnetic and paramagnetic materials.

Magnetoelectric Effect Measuring Units

There are three systems of units for the coefficient of the linear ME effect which have been used by different authors (*Schmidt, 2003*): the "Gaussian system in conventional form", the "Gaussian system in rationalized form" and the "SI-system". The relation between the three kinds of unit is the following: $4\pi\alpha_{ij}^r = \alpha_{ij}' = 3 \times 10^8 \alpha_{ij}$, where α_{ij}^r is expressed in rationalized Gaussian units, α_{ij}' in Gaussian (conventional, non-rationalized) units and α_{ij} in SI units. The SI unit is [s/m].

Typically, the electrical response can be measured in terms of either current or voltage, and accordingly two types of technical units are used in literature (*Eerenstein et al., 2006*). The technical voltage units [V cm^{-1} Oe^{-1}] and [V A^{-1}] are often used in the literature, where the conversion relation between two units is 1 [V A^{-1}] = 0.796 [V cm^{-1} Oe^{-1}], where the voltage is detected via lock-in amplifier. The corresponding ME coefficient, α_{ij}^E, expressed as a voltage unit is determined as $\alpha_{ij}^E = \partial E/\partial H_{ac}$, where ∂E is a ME voltage generated in response to the applied *ac* magnetic field ∂H_{ac}. The non-standard technical charge unit is [C m^{-2} Oe^{-1}]. The corresponding ME coefficient,

α_{ij}^{P}, is expressed as a charge unit $\alpha_{ij}^{P} = \partial P/\partial H_{ac}$, where ∂P is a change of polarization induced by *ac* magnetic field ∂H_{ac}, which is directly represented by the time-integrated current per unit area. The modulated charges instead of voltages could be measured using a high-impedance charge amplifier. This makes the amplified signal independent of film thickness but proportional to electrode area, and the charge noise corresponds to a voltage noise of $\Delta Q/C_s$ (C_s – sample capacitance). The α_{ij}^{P} could be expressed as a voltage unit α_{ij}^{E} using the relationship $\alpha_{ij}^{P} = \varepsilon_0 \varepsilon_{ij} \alpha_{ij}^{E}$, where ε_{ij} is the permittivity of a specimen. Thus, to convert the determined technical unit the value of permittivity of the specimen is required: 1 [C m^{-2} Oe^{-1}] = 10^{-2} $\varepsilon_0 \varepsilon_{ij}$[V cm^{-1} Oe^{-1}].

Linear Magnetoelectric Effect

The basic physics behind the linear magnetoelectric effect was described in detail elsewhere (*Fiebig, 2005*). The term "magnetoelectric" was first given in 1957 by Landau and Lifshitz in their classic *Electrodynamics of Continuous Media* (*Landau & Lifshitz, 1984*), where they assumed that applied electric field should in principle induce magnetization in certain magnetically ordered crystals. The first practical proposal was made two years later by Dzyaloshinskii (*Dzyaloshinskii, 1960*) who demonstrated, using symmetry arguments and thermodynamics, that the effect should occur in Cr_2O_3 and not long time after it was showed experimentally by Astrov (*Astrov, 1960*).

The linear magnetoelectric effect is described as the first-order magnetic response of a system to an applied electric field, or the electrical polarization induced by an applied magnetic field (*O'Dell, 1970*; *Fiebig, 2005*):

$$P_i = \alpha_{ij} H_j \tag{2.10}$$

$$M_i = \alpha_{ij} E_j, \tag{2.11}$$

where α is the magnetoelectric tensor (in Gaussian units). An electric field both displace the magnetic cations relative to the anions and modifies the electronic wavefunctions resulting in a change in the magnetic interactions, mediated mostly by the spin-orbit coupling.

There are three restrictions on α that have to be taken into account while designing news magnetoelectric systems. Firstly, certain symmetry requirements must be fulfilled for α to be non-zero. Secondly, for the case with allowed symmetry there are defined bonds on the magnitude of its component. The material must be electrically insulating so that it is able to sustain an electric polarization. α_{ij} can only be non-zero when materials are neither time-reversal nor space-inversion symmetric (i.e. time-asymmetric and without a centre of symmetry) (*O'Dell, 1970*). The linear magnetoelectric effect is defined by a term in the thermodynamic potential Φ that is linear in both the magnetic and electric fields:

$$\Phi = -\alpha_{ij} E_i H_j. \tag{2.12}$$

Therefore, since E is a polar vector and H an axial vector, α must be odd under both space inversion and time reversal, and symmetric under the product of the two operations, for the free energy to be invariant. In other words, to have a non-zero linear magnetoelectric response a material must be both magnetically ordered (to lift the time-reversal symmetry) and must lack an inversion centre (to lift the space-inversion symmetry). As a result, all magnetic ferroelectrics have a linear magnetoelectric response; in addition, this requirement can be met in cases where a non-centrosymmetric magnetic ordering lifts the inversion centre.

The magnitude of all elements of the magnetoelectric tensor are bounded by the product of the geometrical means of the corresponding elements of the magnetic and electric susceptibilities, χ^m and χ^e (*Brown et al., 1968*). Here,

$$\alpha_{ij} < \sqrt{\chi^e_{ii}\chi^m_{jj}}. \tag{2.13}$$

An analogous relation can be obtained on the basis of thermodynamic theory (*Brown et al., 1968*)

$$\alpha_{ij} < \sqrt{\varepsilon_{ij}\mu_{ij}}. \tag{2.14}$$

This shows the advantage of multiferroic magnetoelectric nanocomposites over the single-phase materials, since the magnitude of linear magnetoelectric response in single-phase magnetoelectric materials is limited and the occurrence of simultaneously large permeability and large permittivity is chemically contra-indicated (*Hill, 2000*). The possibility for obtaining larger linear magnetoelectric response through optimization of α in single-phase materials is rather limited.

Determination of Magnetoelectric Coupling Constants

The major challenge relating to magnetoelectric measurements is to make samples sufficiently insulating to prevent leakage currents contributing to the measured signal - a widespread problem undermining the measurement of ferroelectric polarization loop (*Eerenstein et al., 2006*; *Dawber et al., 2005*).

Magnetoelectric coupling can be measured indirectly by observing variation in either the magnetization near a ferroelectric phase transition temperature (*Zheng et al., 2004*), or the permittivity near a magnetic transition temperature. The resulting effects are defined as “magnetocapacitance” or “magnetodielectric response”. It was previously shown the frequently reported effects could be also originated in magnetoresistance or Maxwell-Wagner effects alone (*Catalan, 2006*), and that the signature of true magnetocapacitance is high-frequency endurance and low loss. However, even real magnetocapacitance measurements do not determine magnetoelectric coupling constants.

Direct measurements are more challenging (*Eerenstein et al., 2006; Fiebig et al., 2005; Nan et al., 2008*). They record either the magnetic response to an applied electric field or an electrical response to an applied magnetic field. The former scenario, so-

called converse magnetoelectric effect, typically requires electrically addressing the sample in a magnetometer (*Zavaliche et al., 2005*), and the magnetoelectric coefficient, also called magnetoelectric susceptibility, is defined as $\alpha_C = \mu_0 dM/dE$. The Gaussian unit is Oe cm V^{-1} or G cm V^{-1}. However, this reading mode will complicate the device structure because additional layers such as a magnetic tunnel junction is required to detect the change of local magnetization (*Shen et al., 2016*). Therefore, to solve this problem and to read information the latter scenario is more commonly measured, so called direct magnetoelectric effect, where the electrical response can be measured in terms of either current or voltage, and the magnetoelectric coefficient is defined as $\alpha_D = dP/dH$. The time-integrated current per unit area directly represents the magnetically induced change of polarization in equation (2.10), that is magnetoelectric charge coefficient, $\alpha_P = dP/dH$, ignoring higher-order terms. Measurement of voltage, however, results in empirical coupling coefficient commonly denoted as magnetoelectric voltage coefficient or magnetoelectric voltage response, α_E, which assuming linearity take the form $\alpha_E = dE/dH$. In this way, both the writing and reading operations are convenient and efficient.

2.5 Theoretical Computation of Magnetoelectric Effect in Vertically Aligned (1-3) Thin-Film Nanocomposites

The effective coupling properties of magnetoelectric nanocomposites were previously described in a convenient matrix formulation by using the Green's function technique (*Nan, 2012*). This method explains the effect of the composite microstructure (e.g. phase volume composition, phase connectivity, aspect ratio) on the physical properties of multiferroic nanocomposites. In the composites based on piezoelectric and magnetostrictive materials, the magnetoelectric effect is mediated by strain. The strain-mediated magnetoelectric coupling in the nanocomposites can be calculated by the Green's function method.

The magnetoelectric effect in nanocomposites is a product tensor property (*Van Suchtelen, 1972*) resulting from the interfacial mechanic interaction between two phases in the composite. Thus, the magnetoelectric coupling effect is a product of the magnetostriction (magnetic-mechanical effect) in the ferromagnetic phase and piezoelectricity (mechanical-electrical effect) in the ferroelectric phase (*Nan, 1994*), and is a coupled electrical and magnetic phenomenon by elastic interaction. Similarly, a coupled magnetoelectric effect can also be obtained by thermal interaction in a pyroelectric-pyromagnetic composite. For the direct magnetoelectric effect, α_{ij}^{D}, a magnetic field is applied to a composite, the magnetic constituent phase deforms magnetostrictively (i.e. expands or contracts), then the strain is transferred along the adjacent piezoelectric phase leading to an electric polarization switching. The reverse effect with an electric field applied would be called a converse magnetoelectric effect,

α_{ij}^{C}. The magnetoelectric effect in composites is extrinsic and depends on the composite microstructure and coupling interaction across ferromagnetic-ferroelectric interface boundary.

In comparison with bulk composites, the multiferroic (1-3) thin-film nanocomposites provide more degrees of freedom, such as lattice strain or interlayer interaction that changes the magnetoelectric behaviour (*Zheng et al., 2004*). These nanocomposites also offer a way to study the physical mechanism of the magnetoelectric effect in nanoscale. Although the mechanism of the coupling interaction between two oxides in the multiferroic nanocomposites is the same as in the case of bulk composites – an elastic interaction, but the mechanical constraints caused by the film- or matrix-substrate bonding and the bonding between two constituent phases in the nanocomposites could significantly modify the magnetoelectric coupling interaction. Also, the interfacial surface area or density of interfaces in the vertically aligned (1-3) nanocomposites is increased compared to the (1-3) bulk composites.

Similar to the bulk composites shown in **Figure 2.9**, there are three types of connectivity between two phases in the thin-film nanocomposites, i.e. (a) (2-2) type multilayer thin-film nanocomposites, (b) (0-3) type particulate thin-film nanocomposites consisted of magnetic spinel nanoparticles (e.g. CFO or NFO) embedded in the ferroelectric oxide film (e.g. BTO, BFO, PTO or PZT), (3) (1-3) type vertically aligned thin-film nanocomposites, where the magnetic spinel oxide nanopillars are impeded into a ferroelectric matrix.

In theoretical simulation, some characteristics of thin films, e.g. giant residual stress/strain resulting from lattice mismatch between the film and substrate, as well as spontaneous polarization in epitaxial films, have been considered to understand the magnetoelectric response in nanocomposite films (*Nan et al., 2005*). That is

$$\sigma = c\epsilon - d^T E - c\epsilon^{ms} - \sigma_s, \tag{2.15}$$

$$D = d\epsilon + \varepsilon E + \alpha H + P_s, \tag{2.16}$$

$$B = \mu(\epsilon, E, H)H + M_s. \tag{2.17}$$

where σ, ϵ, D, E, B, and H are stress tensor, strain tensor, electric displacement, electric field intensity, magnetic induction (or flux density), and magnetic field intensity, respectively; c, ε, and μ are the elastic stiffness tensor (measured at a constant electrical and magnetic fields) and permittivity and magnetic permeability tensors (measured at a constant strain), respectively; d is the piezoelectric coefficient tensor, and α is the magnetoelectric coefficient tensor. In comparison with the constitutive equation for bulk composites, the residual stress, σ_s, residual strain, ϵ_s, spontaneous polarization, P_s, and magnetization M_s, are incorporated for the multiferroic nanocomposite thin films. Permeability, μ, strongly depends on ϵ and electric and magnetic fields, and ϵ^{ms} is the magnetostrictively induced strain related to the magnetic field dependent magnetostriction constants, λ_{100} and λ_{111}, of the ferromagnetic phase. The subscript T means the transpose of the tensor. The tensors c,

d, ε, μ, and α are (6×6), (3×6), (3×6), (3×3), and (3×3) matrices, respectively, by means of compressive representation. For the composite, all these tensors are local quantities depending of the spatial position *x*.

The magnetically induced polarization was previously calculated for the BTO-CFO (1-3) thin-film nanocomposites using the Landau–Ginsburg–Devonshire phenomenological thermodynamic theory (*Liu et al., 2005*; *Liu et al., 2006*). The calculated results showed that the BTO-CFO (1-3) thin-film nanocomposite exhibit a much larger magnetoelectric coefficient than in the BTO-CFO (2-2) thin-film nanocomposite due to large in-plane constraint (i.e. clamping effect) in the latter nanocomposite (**Figure 2.11a**). All dependence of magnetoelectric coefficient on the volume fraction, ^{m}V, of CFO phase in **Figure 2.11a** showed a monotonical increase up to a peak at $^{m}V = 0.85$ where after it decreased to zero (*Liu et al., 2006*).

The nonlinear thermodynamic theory combined with elastic theory approach was recently employed to evaluate dependence of magnetoelectric coefficient in (1-3) BTO-

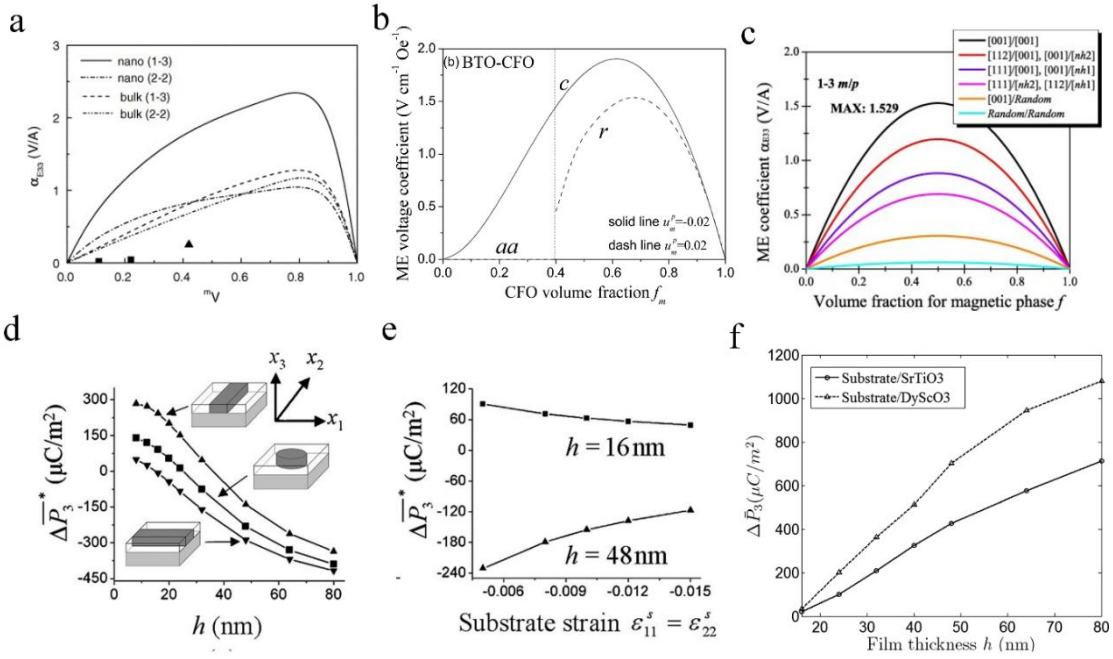

Figure 2.11: Phenomenological thermodynamic simulation of ME coupling in the (1-3) BTO-CFO thin-film nanocomposites. **(a)** Dependence of magnetoelectric coefficient, α_{E33}, on the volume fraction, ^{m}V, of magnetostrictive CFO phase at room temperature for (2-2) and (1-3) BTO-CFO thin-film nanocomposites and bulk composites (from *Liu et al., 2006*). **(b)** Dependence of the magnetoelectric coefficient α_E on the volume fraction, f_m, of CFO phase, where u_m^p is defined as in-plane misfit strain of BTO film (from *Wu et al., 2014*). **(c)** Effect of volume fraction, f, of CFO phase of the magnetoelectric coefficient, α_{E33} (from *Jian et al., 2018*). Phase-field simulation of magnetoelectric polarization response in BTO-CFO (1-3) thin-film nanocomposite. **(d)** Dependence of magnetic field induced electric polarization $\Delta\overline{P_3}^*$ on the film thickness, h (volume fraction of CFO $f = 0.35$ and substrate strains $\varepsilon_{11}^s = \varepsilon_{22}^s = -0.005$). **(e)** Dependence of the magnetic field induced $\Delta\overline{P_3}^*$ on the substrate strains (volume fraction of CFO $f = 0.35$, nanopillar diameter $D_{pillar} = 42.8$ nm, interpillar distance $D_{int} = 64$ nm and two different pillar heights h_{pillar} 16 and 48 nm) (from *Zhang et al., 2007*). **(f)** Dependence of the magnetic field induced electric polarization, $\Delta\overline{P_3}$, on the film thickness, h. From *Chen et al., 2011*

CFO thin-film nanocomposites (*Wu et al., 2014*). According to the nonlinear thermodynamic theory, the polarization terms up to the 8th order in the elastic Gibbs function, *G*, should be included for BTO (*Wu et al., 2014*; *Li et al., 2005b*). The equilibrium thermodynamic states of materials are typically defined by minimizing the potential *G* with respect to polarization components and selecting energetically most favourable phase (*Wu et al., 2014*). **Figure 2.11b** shows the dependence of magnetoelectric coefficient, α_E, of the (1-3) BTO-CFO thin-film nanocomposites on the f_m obtained at $u_m^p = -0.02$ and $u_m^p = 0.02$, where $u_m^p = (a_s - a_p)/a_p$ is defined as the in-plane misfit strain of BTO film (*MacManus-Driscoll et al., 2008; Slutsker et al., 2006*), and related to the substrate lattice parameter, a_s, and the equivalent lattice parameter, a_s, of the free standing BTO film (*Wu et al., 2014*). So, it can be seen from **Figure 2.11b** that α_{E33} increases first and then decreases with the f_m increase for (1-3) BTO-CFO thin-film nanocomposites. They showed that the BTO films are stable in the *c*-phase and the maximum α_{E33} for (1-3) BTO-CFO thin-film nanocomposites is 1.912 V cm^{-1} Oe^{-1} (~2.4 V/A) when $u_m^p = -0.02$ and $f_m \approx 0.6$ (*Wu et al., 2014*), that is quite close the maximum value (~2.25 V/A) obtained in **Figure 2.11a** (*Liu et al., 2006*). For comparison, the maximum value of ME effect for the single-phase Cr_2O_3 at $T \sim 250$ K $\alpha \sim 1.25 \cdot 10^{-3}$ (cgs-units), which can be passed to the value in S.I. units via division by the velocity of light, *c*, thus $\alpha \sim 4.14$ ps m^{-1} or 22.4 mV cm^{-1} Oe^{-1} (S.I. units) (*Wiegelmann et al., 1994; Pyatakov & Zvezdin, 2012*).

Recent study on the crystal orientation dependence of magnetoelectric coefficient, α_{E33}, in (1-3) BTO-CFO thin-film nanocomposites (*Jian et al., 2018*) in arbitrary directions by 3-D coordinate transformation method was carried out. **Figure 2.11c** shows the effects of various orientation selections on the volume fraction, f, dependence of α_{E33} and the maximum value was obtained for [001]-oriented CFO nanopillars inside [001]-oriented BTO matrix, which was 1.529 V/A (~1.217 V cm^{-1} Oe^{-1}), while α_{E33} of the (1-3) BTO-CFO thin-film nanocomposites with randomly oriented CFO pillars embedded in a randomly oriented BTO matrix was about 61.1 mV/A (~48.6 V cm^{-1} Oe^{-1}), which is 4% of the value of [001]/[001] BTO-CFO nanocomposite (*Jian et al., 2018*).

Another powerful method is a phase-field model, in which the elastic energy in the constrained thin film was incorporated including the effect of free film surface and the constraint from the substrate, has been recently developed for studying the ME coupling effect in the 1–3 nanocomposite thin films (*Zhang et al., 2007*; *Chen et al., 2011*). The phase-field simulation illustrates that the magnetic-field-induced electric polarization is highly dependent on the film thickness, morphology of the nanocomposite, and substrate constraint, which provide a number of degrees of freedom in controlling coupling in nanocomposite.

Figure 2.11d shows the previously estimated dependence of magnetic field induced electric polarization on the film thickness of (1-3) BTO-CFO thin-film nanocomposites (*Zhang et al., 2007*). The authors demonstrated that with the increase

of the film thickness, *h*, the effect of stress component $\Delta\sigma_{33}$ becomes more important as the influence of the film surface is less significant. It was shown that $\Delta\overline{P_3}^*$ decreases with the increase of the film thickness, and even becomes negative above a certain critical film thickness, since the decrease of σ_{33} ($\Delta\sigma_{33} < 0$) reduces $\overline{P_3}$. **Figure 2.11e** shows that with the increase of magnitude of compressive strains, the magnitude of $\Delta\overline{P_3}^*$ decreases, which indicates that under large compressive strains, it is rather difficult to change the polarization of ferroelectric phase through elastic coupling (*Zhang et al., 2007*). The results of these calculations were reproduced by another study on the magnetically induced polarization, $\Delta\overline{P_3}$, dependence on the thickness of (1-3) BTO-CFO thin-film nanocomposites (*Chen et al., 2011*). The $\Delta\overline{P_3}$ showed an increase with increasing nanocomposite thickness, *h*, and the increase was larger for $DyScO_3$ substrate then that for $SrTiO_3$ substrate, due to the smaller lattice mismatch between the nanocomposite and substrate (see **Figure 2.11f**).

2.6 Comparison between Magnetoelectric Coupling Experimental Values Reported in (0-3), (2-2) and (1-3) Multiferroic Thin-Film Nanocomposites

2.6.1 Particulate (0-3) Thin-Film Nanocomposites

In 0-3 type of magnetoelectric nanocomposites, most of studies were focused on the physical effects of size and composition of ferromagnetic nanoparticles inside a ferroelectric matrix. **Table 2.1** summarizes the most recent results for the magnetoelectric coupling coefficient in the particulate multiferroic system. It demonstrates the magnetoelectric coefficient ranging from 16 to 3070 mV cm^{-1} Oe^{-1}, which are similar or a bit larger than the one reported in bulk particulate ceramics. The largest low-frequency value of α reported for bulk (1-3) multiferroic nanocomposites is given in the first raw for the comparison.

Particulate $PbZr_{0.52}Ti_{0.48}O_3$-$CoFe_2O$ nanocomposites with $CoFe_2O_4$ nanoparticles embedded in the $PbZr_{0.52}Ti_{0.48}O_3$ matrix were investigated (*Wan et al., 2005*). As shown in **Figure 2.12** the nanoparticles have an average diameter of ~150 nm and they are randomly distributed. The volume fraction of nanoparticles is ~31%. *P-E* measurement showed that the nanocomposite has a high resistivity of ~5×10^9 Ω cm at zero bias**.** **Figure 2.12b** shows a well-defined *P-E* loops. The maximum saturation and remnant polarizations reach 28 μC/cm^2 and 11.0 μC/cm^2, respectively, and the ME coefficient ~220 mV cm^{-1} Oe^{-1} was obtained. The α increases with the increase of magnetic field frequency, f_r, wherein the maximum value α~317 mV cm^{-1} Oe^{-1} was measured at $f_r = 50$ kHz.

Table 2.1: Room-temperature α_{me} in particulate nanostructured composites

Component phases	H_{dc} Oe	f_{ac} Hz	α_{me} mV cm^{-1} Oe^{-1}	Note	Ref.
$0.9PbZr_{0.52}Ti_{0.48}O_3$-$0.1NiFe_{1.9}Mn_{0.1}O_4$ (bulk)	100	1000	140	Longitudinal, (3-0) compos.	*Islam et al., 2006*
$PbZr_{0.52}Ti_{0.48}O_3$ (matrix)-$CoFe_2O_4$ (nanoparticles)	250	1000	3070	Transverse, (3-0) compos., sol-gel	*McDannald et al., 2017*
$PbZr_{0.52}Ti_{0.48}O_3$-$CoFe_2O_4$	450	1000	549	Longitudinal, (3-0) compos., PLD	*McDannald et al., 2013*
$BiFeO_3$–$CoFe_2O_4$	2900	PFM[a]	338[a]	Transverse, (3-0) compos., PLD	*Li et al., 2015a*
$0.69PbZr_{0.52}Ti_{0.48}O_3$ -$0.31CoFe_2O_4$	2000	1000	220	3-0 compos., sol-gel	*Wan et al., 2005*
BTO-Co/100 BTO	500	50000	170	Longitudinal, (3-0) compos., RF sputtering	*Park et al., 2008*
NCZF/0.8PZT-0.2PZN	2600	1000	150	Transverse, (3-0) compos., AD	*Park et al., 2009*
Polycrystalline 65% CFO:BFO/Pt/ TiO2/SiO2/Si	500	PFM[a]	102[a]	Transverse, PLD	*Yan et al., 2013*
$La_{0.6}Ca_{0.4}MnO_3$-$Bi_{0.6}Nd_{0.4}TiO_3$	5000	20000	29.8	(3-0) compos., CSD	*Cheng et al., 2012*
$0.65PbZr_{0.52}Ti_{0.48}O_3$ –$0.35NiFe_2O_4$	2500	194	16	Longitudinal, 3-0 compos., PLD	*Ryu et al., 2006*

NCZF-$(Ni_{0.6}Cu_{0.2}Zn_{0.2})Fe_2O_4$, PZN-$Pb(Zn_{1/3}Nb_{2/3})O_3$, , AD - aerosol deposition, PLD - pulsed laser deposition, CSD -chemical solution deposition

H_{dc} – applied *dc* magnetic field

f_{ac} – frequency of the applied *ac* magnetic field H_{ac}

[a]The α_{me} was obtained indirectly by measuring the piezoresponse displacement loop (using piezoresponse force microscopy) with or without applying an in-plane *dc* magnetic field, and therefore represents the local magnetoelectric response rather than a global one from macroscopic measurements

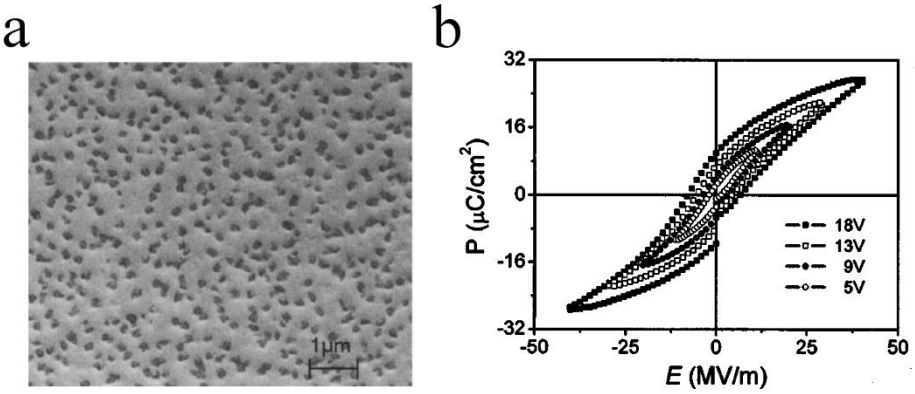

Figure 2.12: (a) SEM image of the $CoFe_2O_4$–PZT composite thin film. **(b)** P–E hysteresis loops of the $CoFe_2O4$–PZT composite thin film. From *Wan et al., 2005*

Particulate PZT-NFO (0-3) nanocomposite with NFO (35%) nanoparticles embedded into PZT matrix was fabricated on Nb:STO substrates, and attributed transverse and longitudinal magnetoelectric coefficients were measured (*Ryu et al., 2006*). After the specimen was poled, the α_{me} values decreased, which is ascribed to charges generated under an *ac* magnetic field at frequency of 194 Hz. The maximum value of α_{E31} was 4 mV cm^{-1} Oe^{-1}, and the value of α_{E33} was 16 mV cm^{-1} Oe^{-1}. In 2013 a PZT-CFO particulate nanocomposite was reported with various composition of CFO nanoparticles (5-8 nm) scattered in PZT matrix (*McDannald et al., 2013*). The solution containing CFO nanoparticles and PZT precursors was spin-coated and annealed at 700 °C. The PZT-CFO

particulate nanocomposite shows good *P-E* hysteresis loop (see **Figure 2.13a**). An *ac* magnetic field, 1 Oe, is superimposed to a *dc* field generated by an electromagnet was used to extract the magnetoelectric coefficient. The nanocomposite containing 0.065 % of CFO nanoparticles (molar ratio) showed the maximum transvers and longitudinal α_{me} of 549 mV cm^{-1} Oe^{-1} and 338 mV cm^{-1} Oe^{-1}, respectively (**Figure 2.13b**). Recently,

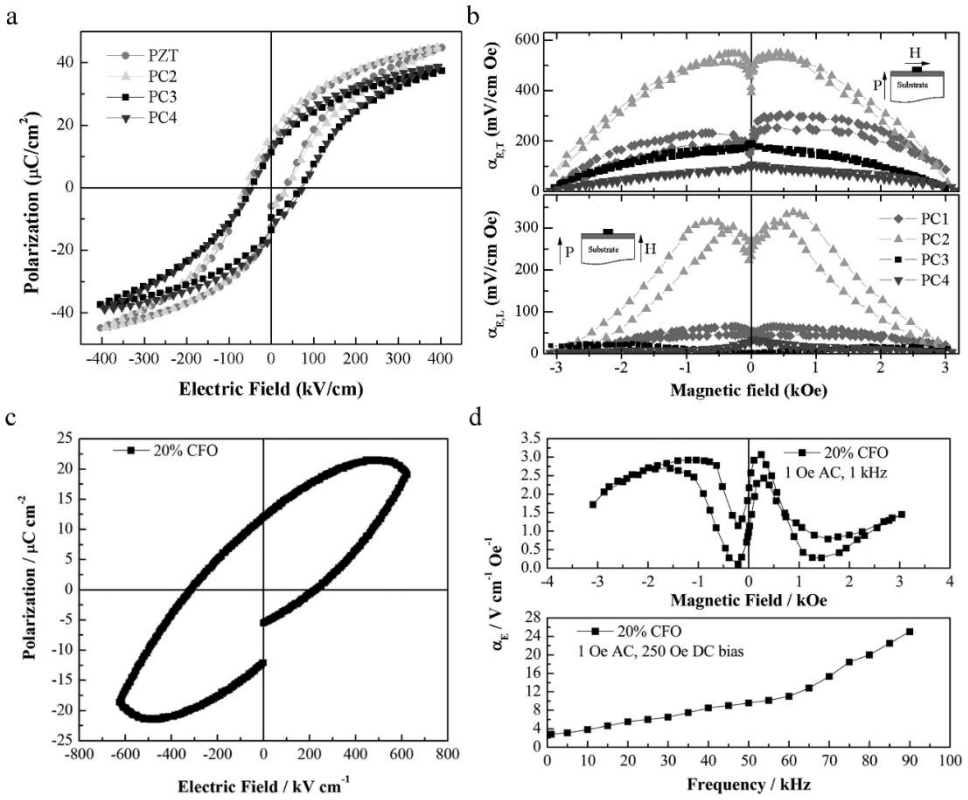

Figure 2.13: (a) Room temperature *P-E* hysteresis loops of pure PZT and ZPT-CFO nanocomposite. (b) The transverse (top) and longitudinal magnetoelectric coefficients of the nanocomposite. The insets depict the field orientation relative to the sample for the respective measurements. (Reprinted from *McDannald et al., 2013*). (c) Ferroelectric *P-E* hysteresis behaviour of PZT-CFO nanocomposite. (d) Transverse magnetoelectric coefficient versus dc bias field (top curve) showing the superposition of remnant magnetoelectric coupling and 180° phase shift between positive and negative DC bias field and versus frequency (down curve) showing monotonic increase in magnetoelectric coupling with increasing frequency. (from *McDannald et al., 2017*)

they reported (0-3) PZT-CFO nanocomposite with 25 nm CFO particles or nanophase distributed in discrete layers through the thickness of the PZT matrix (*McDannald et al., 2017*). Although the ferroelectric, *P-E*, behaviour was a little bit leaky (**Figure 2.13c**), the unique pancake-like distribution of CFO particles in the nanocomposite mimicked a (2-2) type of nanocomposite resulting in α_{me} peaking at a large value of 3.07 V cm^{-1} Oe^{-1} at a *dc* bias of 250 Oe (**Figure 2.13d**).

Recently, a quasi-(0-3) BFO-CFO thin-film nanocomposite was prepared by separately growing (2-2) and (1-3) type nanocomposite layers using PLD. This design is appealing due to a possibility to release the substrate clamping as well as to reduce the overall leakage current (*Li et al., 2015a*). The magnetoelectric coupling, α_{me}, was calculated by $\alpha_{me} = \Delta E/\Delta H$, with the change in the electric field ΔE induced by the magnetic field ΔH, where $\Delta E = \Delta u/(d_{33}D)$, Δu is the average change in the piezoresponse displacement with and without magnetic field, D is the thickness of the BFO-CFO nanocomposite film, and $d_{33}=u/V$ is the converse piezoelectric coefficient calculated from displacement-voltage loop, without the magnetic field (*Li et al., 2015a*), where V is the applied *ac* voltage. The magnetoelectric coupling for the mixed (0-3) - (2-2) type BFO-CFO nanocomposite characterized by this technique was about 338 mV cm^{-1} Oe^{-1}, whereas the α_{me} calculated using the same technique for the classic (0-3) BFO-CFO nanocomposite was around 102 mV cm^{-1} Oe^{-1} (*Yan et al., 2013*).

2.6.2 Bilayer and Multilayer (2-2) Type Nanostructured Composites

Bulk (2-2) type laminate magnetoelectric composites typically show better properties than bulk particulate composites. For example, a transverse α_{me} of about 30 V cm^{-1} Oe^{-1} and 7 kV cm^{-1} Oe^{-1} were observed under H_{dc} = 2 Oe and ω_{ac} of 1 kHz and 23 kHz, respectively, in a 1-1 connectivity horizontal composite consisting of a (011)-oriented Pb(Mg,Nb)O_3-$PbTiO_3$ fiber laminated with Metglas (FeBSiC) fiber (*Chu et al., 2017*). This is due to the insulating ferroelectric layer blocking the leakage current in laminates. However, the magnetoelectric response in (2-2) type nanocomposite is normally similar to the (0-3) type nanocomposite films.

A recent experimental dataset on the magnetoelectric coefficients of direct magnetoelectric coupling in horizontal (2-2) type nanocomposites is shown in **Table 2.2**. The largest low-frequency value of α reported for bulk (1-3) multiferroic nanocomposites is given in the first raw for the comparison. The (2-2) thin-film $I_{r0.3}Mn_{0.7}$/FeCoSiB/AlN and FeCoSiB/AlN nanocomposites showing the largest low-frequency ME coefficients 430 mV cm^{-1} Oe^{-1} and 3.1 mV cm^{-1} Oe^{-1}, respectively, are piezoelectric but not ferroelectric (*Lage et al., 2014; Greve et al., 2010*). Therefore this type of multiferroic nanocomposites are promising for the applications that do not require the presence of room-temperature spontaneous polarization such as field sensors, actuators, transducers, filters, phase shifters, and gyrators.

Table 2.2: Room-temperature α_{me} in (2-2) type thin-film horizontal magnetoelectric nanocomposites

Component phases	H_{dc} Oe	f_{ac} Hz	α_{me} mV cm^{-1} Oe^{-1}	Note	Ref.
Metglas/PMN-PT (fiber)/Metglas (bulk)	8	1000	52000	Longitudinal, (2-1) composite[a]	*Wang et al., 2011b*
$I_{r0.3}Mn_{0.7}$/FeCoSiB/AlN	0	700	430000	Transverse, All-film, Sputtering	*Lage et al., 2014*
$(BaTiO_3–BiFeO_3)\times15$	0	1000	55000	Longitudinal, SLs, PLD	*Lorenz et al., 2017*
$Pb(Zr,Ti)O_3$/Metglas (bulk foil)	22	1000	7000	Transverse, FoS, GSV deposition with laser annealing	*Palneedi et al., 2017a*
$Pb(Zr_{0.52}Ti_{0.48})O_3$/LaNi O_3/HfO_2/Ni (bulk foil)	10	1000	3200	Transverse, CSD	*Palneedi et al., 2017b*
FeCoSiB/AlN	6	100 (753)	3100 (737000)	Transverse, All-film, Sputtering	*Greve et al., 2010*
$Pb(Zr_{0.52}Ti_{0.48})O_3$/Pt/Ni (bulk foil)	86	1000	772	Transverse, FoS, sol–gel	*Feng et al., 2015*
$(La_{0.7}Sr_{0.3}MnO_3$/ $Ba_{0.7}Sr_{0.3}TiO_3)$m	500-100	1000	35-300	Longitudinal and transverse, PLD	*Martinez et al., 2012*
2 μm Py/80 μm PZT/2 μm Py multilayers	50	100	240	Longitudinal, sputtering	*Stognij et al., 2013*
$Pb(Zr_{0.52}Ti_{0.48})O_3$/$CoFe_2O_4$ (bulk ceramic)	600	1000	155	Transverse, FoS, sol–gel	*Wang et al., 2013b*
CFO/BTO	100	1000	104	Longitudinal, PLD	*Zhang et al., 2008*
BTO/Ni (bulk foil)	87	1000	90	Transverse, FoS, CSD	*Liang et al., 2014*
NFO/BTO	100	1000	79	Longitudinal, PLD	*Deng et al., 2008*
CFO/PZT	6000	1000	70	Longitudinal, sol–gel	*He et al., 2009*
PZT film/ CFO ceramic	600	1000	60	Transverse, FoS, sol–gel	*Wang et al., 2013*
300 μm $La_{0.7}Sr_{0.3}MnO_3$/PZT	35	100	60 (120 K)	Transverse, doctor blade	*Srinivasan et al., 2002*
BTO/Metglas/Metglas foil	20	20	55	Transverse, PLD	*Wang et al., 2011a*
BTO/CFO (bulk ceramic)	730	1000	38	Transverse, FoS, PLD	*Wang et al., 2008*
BTO/NFO	100	1000	37	Longitudinal, PLD	*Deng et al., 2008*
$Ni_{0.8}Zn_{0.2}Fe_2O_4$/$Pb(Zr_{0.6}$ $Ti_{0.4})O_3$	0	1000	15	Longitudinal, All-film, PLD	*Ryu et al., 2007*
15 μm NFO/15 μmBTO multilayers	2000	194	18	Longitudinal, tape casting	*Patil et al., 2011*
NFO/BTO	100	1000	12	Longitudinal, PLD	*Deng et al., 2007*
$La_{0.7}Sr_{0.3}MnO_3$/$Pb(Zr_{0.5}$ $_2Ti_{0.48})O_3$	4000	1000	4	Longitudinal, All-film, PLD	*Ma et al., 2007a*
BFO/Ni foil	1	200	3.5	Transvers, PLD	*Yan et al., 2012*

[a]The (2-1) type phase connectivity leads to a significantly enhanced α by magnifying the induced voltage
FeCoSiB - $(Fe_{90}Co_{10})_{78}Si_{12}B_{10}$; SLs – superlattices; FoS – film-on-substrate; GSV – granule stray in vacuum; CSD -chemical solution deposition
H_{dc} – applied *dc* magnetic field; f_{ac} – frequency of the applied *ac* magnetic field H_{ac}

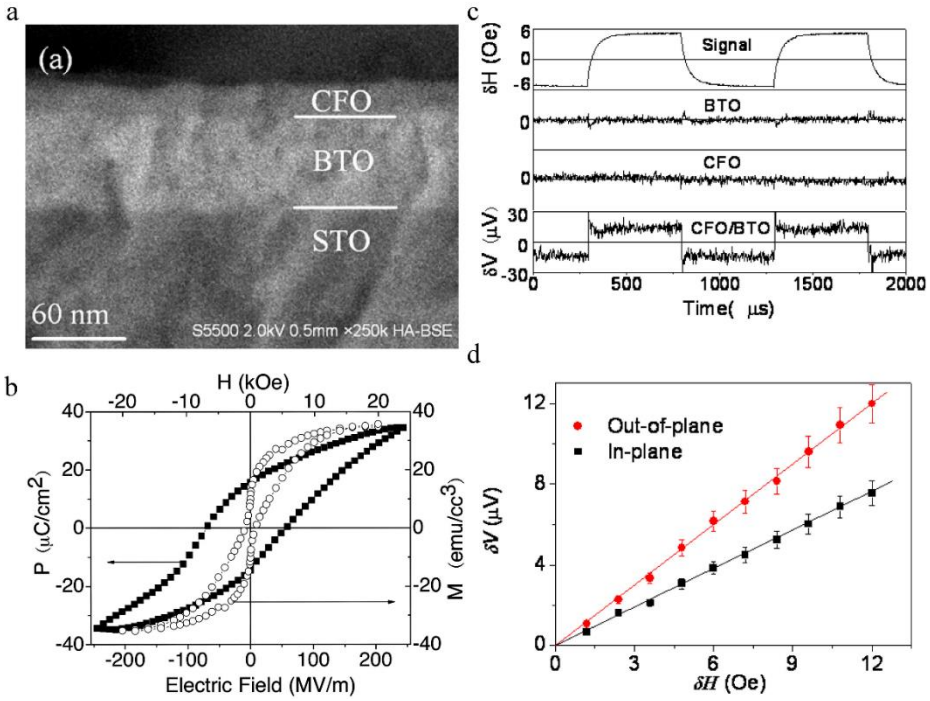

Figure 2.14: (a) A cross-section SEM image of the BTO-CFO nanocomposite. (b) Ferroelectric *P-E* hysteresis loop and in-plane magnetic hysteresis loop of the BTO-CFO horizontal nanocomposite. (c) The magnetoelectric response of the BTO-CFO nanocomposite when the in-plane magnetic field, δ*H*, at 1 kHz with a bias magnetic field of 100 Oe. The in-plane and out-of-plane in (d) represents the measurement modes with the magnetic field parallel and perpendicular to the surface of the nanocomposite, respectively. (from *Zhang et al., 2008*)

In 2008 a (2-2) type bilayer BTO-CFO bilayer nanocomposite was investigated (**Figure 2.14a**) (*Zhang et al., 2008*). The magnetoelectric coefficient of the BTO-CFO nanocomposite ~104 mV cm^{-1} Oe^{-1} under a *dc* magnetic field was reported. **Figure 2.14b** shows the ferroelectric and ferromagnetic hysteresis loops of the BTO-CFO nanocomposite. The magnetoelectric voltage response was measured under an open circuit condition. None magnetoelectric response was observed from the single-phase BTO and CFO films (see **Figure 2.14c**), whereas the (2-2) type BTO-CFO nanocomposite showed a magnetoelectric voltage output following the on-off signal of the *ac* magnetic field ΔH_{ac}. The output ΔV showed a linear increase with the increasing *ac* magnetic field, where the α_{me} can be estimated from the slopes. The reported longitudinal magnetoelectric coefficient of the (2-2) BTO-CFO nanocomposite ~104 mV cm^{-1} Oe^{-1} (*Zhang et al., 2008*) is larger than the one reported for the BTO-NFO bilayer nanocomposite (*Liang et al., 2014*), which was explained by the larger magnetostriction of CFO that that of NFO (*Stognij et al., 2013*). Room-temperature magnetostriction and magnetocrystalline anisotropy constant K_1 of some magnetic ferrite compounds is presented in **Table 2.3**. The ferroelectric constituent also should be chosen carefully. For instance, a large transverse magnetoelectric coefficient of

Table 2.3: Room temperature magnetic and electromechanical properties of bulk oxide magnetic materials (from *Folen, 1970)*

Compound	$a=b, c$ Å	T_C K	ρ $\times10^3$ kg/m^3	ε 1 kHz	K_1 $\times10^4$ erg/cm^3	λ_{100} $\times10^{-6}$	λ_{111} $\times10^{-6}$	λ_s $\times10^{-6}$
Fe_3O_4	8.397	858	5.238	-	-13.0	-20	80	40
$Co_{0.8}Fe_{2.2}O_4$	8.337	-	-	-	290	-590	120	-210
$Co_{0.9}Fe_{2.1}O_4$	-	-	4.82	-	380	-	-	-
$CoFe_2O_4$	8.38	793	5.29	10	260	-	-	-110
$Co_{1.1}Fe_{1.9}O_4$	-	-	-	-	380	-	-	-250
$Ni_{0.8}Fe_{2.2}O_4$	-	-	-	-	-3.9	-36	-4	-17
$NiFe_2O_4$	8.34	858	5.38	21	-6.9	-46	-22	-26

a, b, c – lattice parameters
T_C – Curie temperature
ρ – density
ε – permittivity
K_1 – magnetocrystalline anisotropy constant
λ_{ijk} – magnetostriction coefficient

772 mV cm^{-1} Oe^{-1} was reported for the PZT-Ni nanocomposite on Ni foil (*Feng et al., 2015*), which is possibly due to the large piezoelectric coefficient of PZT and reduced substrate imposed clamping effect. A strong magnetoelectric coupling was also obtained in BSTO/LSMO bilayers and multilayers, in which the longitudinal magnetoelectric coefficient can be as large as 300 mV cm^{-1} Oe^{-1} (*Martinez et al., 2012*). Since the transition temperature of $Ba_{0.7}Sr_{0.3}TiO_3$ is close to room temperature, it is well known that BSTO material with composition $x = 0.7$ shows large permittivity as well as piezoelectric coefficient at room temperature. Room temperature permittivity and piezoelectric coefficient of some bulk ferroelectric materials are summarized in **Table 2.4**.

Table 2.4: Room temperature dielectric and electromechanical properties of bulk oxide ferroelectric materials (from *Mitsui, 1981*)

Compound	$a=b, c$ Å	T_C K	ρ $\times10^3$ kg/m^3	ε 1 kHz	P_r $\times10^{-2}$ C/m^2	P_s $\times10^{-2}$ C/m^2	E_c $\times10^5$ V/m	d_{15} pC/N	d_{31} pC/N	d_{33} pC/N
$BaTiO_3$	3.99 4.03	396	6.02	1350	25	25	3	270	-79	190
$PbTiO_3$	3.90 4.11	743	7.96	230	12	75	-	53	-20	51
PZT 52/48	5.75 14.21	601	7.55	800		36	13.6	494	-93.5	223
BST 70/30	3.96	298	-	20000	-	8	11	-	-	-

P_r – remanent polarization
P_s – saturation polarization
E_c – coercive field
d_{ij} – piezoelectric coefficient

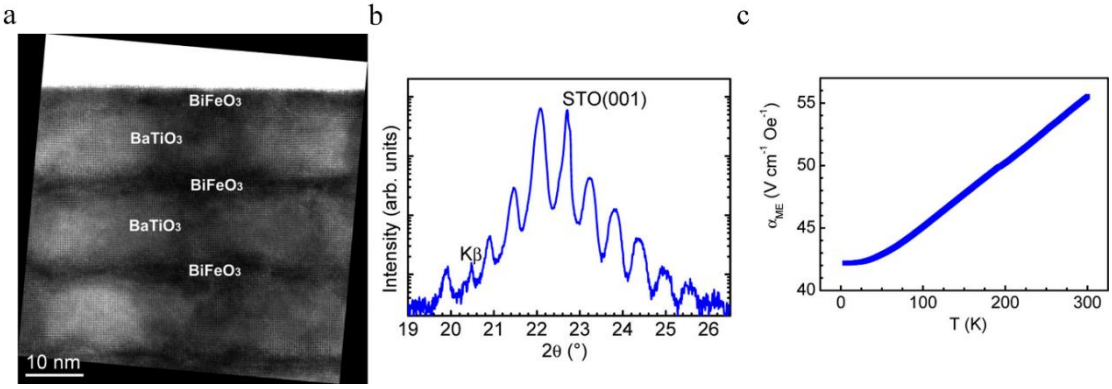

Figure 2.15: (a) HR-TEM image from a cross section of BTO-BFO×15 superlattices near a surface; **(b)** XRD 2θ-ω scan with superlattice fringes. **(c)** Temperature-dependent magnetoelectric coefficient of superlattice BTO-CFO×15. From *Lorenz et al., 2017*

Interestingly, a special type of (2-2) type multilayer nanocomposites called superlattices were reported to have a large magnetoelectric coefficient that can be compared to the highest values obtained in multilayer laminates. In particular, the $BiFeO_3$-$BaTiO_3$ superlattices were built from 15 double layers of BFO-BTO (*Lorenz et al., 2017*). The highest magnetoelectric coefficient of 55 V cm^{-1} Oe^{-1} at room temperature was measured for superlattices. For comparison, one of the largest magnetoelectric coefficients measured in low frequency range (1 kHz) is 52 V cm^{-1} Oe^{-1} obtained in the Metglas/PMN-PT (fiber)/Metgals horizontal composites (*Wang et al., 2011b*). **Figure 2.15a** shows high-resolution TEM image from cross section of the BFO-BTO superlattice revealing the BFO layer thickness varying in the range 2-6 nm and the epitaxial coherence of the different layers, that is the in-plane lattice constants of BTO and BFO math (*Lorenz et al., 2017*). The crystalline structure shown in **Figure 2.15b** revealed the superlattice fringe peaks in the XRD 2θ-ω scans. The BFO-BTO superlattice magnetoelectric coefficient temperature dependence (see **Figure 2.15b**) shows a monotonically increasing α_{me}, which might be related to phase transition of the BTO and BFO constituents.

2.6.3 Vertically Aligned (1-3) Type Nanostructured Composites

Vertically aligned (1-3) type multiferroic nanocomposites are the most attractive among multiferroic nanocomposites in terms of the technology application due to the enlarged vertical interfacial area between ferromagnetic and ferroelectric constituents, reduced substrate imposed clamping effect (i.e. reduced surface area between constituents and substrate), and perpendicular magnetic anisotropy along nanowire axis. As we discussed in **Section 2.5**, it was theoretically predicted that vertically aligned (1-3) type nanocomposites possess larger magnetoelectric coefficient than the multilayer (2-2) type nanocomposites (*Nan et al., 2005*). Also, it was demonstrated that the misfit strain and the volume fraction of ferromagnetic pillars affect the magnetoelectric

coupling in vertically aligned (1-3) type nanocomposites (*Wu et al., 2014*). It was shown that the magnetoelectric coefficient in (1-3) BTO-CFO nanocomposite strongly depends on the in-plane and out-of-plane misfit strains. The magnetoelectric coefficient of (1-3) type BTO-CFO nanocomposite can be increased up to 2 V cm^{-1} Oe^{-1} by using the volume fraction of CFO pillars ~60%.

As was already mentioned in **Section 4.3**, the vertically aligned BTO/CFO (65/35) multiferroic nanocomposites were prepared for the first time by *Zheng et al., 2004*. As shown in **Figure 2.10a**, the BTO-CFO nanocomposite demonstrated a well-shaped ferroelectric hysteresis loop with P_s = 23 μC/cm^2. The HR-TEM image revealed the diameter of CFO nanopillars ~25 nm (**Figure 2.10b**) embedded epitaxially in the BTO matrix. Large magnetic anisotropy with easy axis along [001] direction (or pillars axis) was observed due to the vertical compressive strain in the CFO pillars with negative magnetostriction induced by the BTO matrix (**see Figure 2.10c**) The magnetoelectric coupling between the electric and magnetic order parameters in the self-assembled (1-3) BTO-CFO nanostructure was demonstrated by temperature-dependent magnetization measurements (**Figure 2.10d**). A distinct drop in the magnetization of ~16 emu/cm^3 (~5% of magnetization at a 100 Oe external field) around the ferroelectric Curie temperature (T_C~390 K). It was explained by the fact that, at $T > T_C$, the $CoFe_2O_4$ is compressed due to the lattice mismatch with $BaTiO_3$, whereas for $T < T_C$, the tetragonal distortions in the $BaTiO_3$ lattice decreases this compression in the $CoFe_2O_4$, thus leading to a reduction of the moment due to a negative magnetostriction of $CoFe_2O_4$. For reference, when they measured the temperature dependence of magnetization at 100 Oe (black curve in **Figure 2.10d**) for a (2-2) BTO-CFO multilayer sample with a layer thickness of ~30 nm, only the negligible change around the ferroelectric Curie temperature was observed. This was attributed to the in-plane piezo-deformation in the multilayer structure being clamped by the substrate precluding any deformation in the magnetic layer, which also confirms the dominant elastic interaction for the magnetoelectric coupling in two-phase BTO-CFO nanostructures. Recently, the (1-3) BTO-CFO nanocomposite was also prepared by *Schmitz-Antoniak et al., 2013*. Rectangular-shaped CFO pillars 100-200 nm in size embedded into the BTO matrix were prepared using PLD at 950 °C, while the magnetoelectric coupling was probed using soft X-ray absorption spectroscopy (i.e. XANES and XLD). Vertical (1-3) multiferroic nanocomposite using many other types of ferroelectric and ferromagnetic materials were built using PLD technique, the full list of nanocomposites was mentioned in **Section 4.3**.

Although the first reports on vertically aligned multiferroic nanocomposites were associated with the BTO-CFO system, the BFO-CFO system has attracted much more attention and was widely studied by many researchers. The first investigation of the large magnetoelectric coupling in the (1-3) type BFO-CFO nanocomposite was conducted using Magnetic Force Microscopy to measure the electric-field controlled magnetization reversal (*Zavaliche et al., 2005, 2007*). After the BFO-CFO

nanocomposite was magnetized out-of-plane at a 20 kOe magnetic field, the net magnetization of the CFO pillars was aligned upwards. So, the magnetized BFO-CFO nanocomposite was exposed to an electric field with bias of -12 V and then 12 V, this resulted in the switch of magnetization confirmed by MFM. In the second experiment the quantitative analysis of the BFO-CFO nanocomposite was carried out, namely, the specimen was magnetized in a downward 20 kOe magnetic field and *M-H* hysteresis loops were recorded using Superconducting Quantum Interference Device (SQUID) before and after electric bias was applied to the specimen. The static converse magnetoelectric coefficient, $\alpha_{E33}=\Delta M/\Delta E$ was estimated to be 0.01 Oe cm V^{-1}. Another experiment was conducted to reduce the leakages by deposited (1-3) BFO-CFO nanocomposites on insulation PMN-PT (001) substrate (*Wang et al., 2011c*). Similar experiment with electric filed inducing the magnetization was carried out, and the applied voltage reduced the out-of-plane remnant magnetization and the enlarged the in-plane magnetization. The static converse magnetoelectric effect was estimated by measuring $\alpha_{E33} = \Delta M/\Delta E$, which was around 0.5 Oe cm V^{-1} (*Wang et al., 2011c*).

Direct magnetoelectric effect was studied in the (1-3) type BFO-CFO nanocomposite with different thicknesses (150-2400 nm) grown by PLD on conductive $SrRuO_3/SrTiO_3$ (001) substrates at 700 °C (*Yan et al., 2009*). In particular, a magnetic cantilever technique was used to measure the magnetoelectric coefficient, which was around 20 mV cm^{-1} Oe^{-1}. Such small values were explained by the reduction of piezomagnetic and piezoelectric effect is the nanocomposite due to substrate clamping.

Finally, in 2010 the dynamic magnetoelectric response was measured in a 300-nm-thick BFO-CFO nanocomposite with 1:1 volume ration between CFO pillars and BFO matrix. A small *ac* magnetic (H_{ac} = 4 Oe), which is big enough to move the ferromagnetic domain walls, superimposed on a *dc* magnetic field was used to excite the specimen and the induce charges, or induced polarization (instead of voltages) were recorded. The transverse α_{me} was ~60 mV cm^{-1} Oe^{-1}, and it was five times larger than the longitudinal α_{me}. This enhanced transverse magnetoelectric response was associated with more pronounced transverse magnetostriction of the CFO pillars.

In more recent experiments on the (1-3) type BFO-CFO nanocomposite, the ferromagnetic and ferroelectric constituent phases were switched so that BFO nanopillars would be embedded now in the CFO matrix (*Amrillah et al., 2017*). An alternative strategy of fabricating a self-assembled ferroelectric-ferrimagnetic bulk heterojunction on a flexible muscovite via van der Waals epitaxy was adopted. They investigated the magnetoelectric coupling is a self-assembled by PLD BFO-CFO heterojunctions composed of vertically aligned BFO nanopillars embedded in a ferromagnetic CFO matrix. The weak interaction between the flexible substrate and bulk heterojunction resulted in the reduced substrate clamping and a magnetoelectric coupling of 74 mV cm^{-1} Oe^{-1}, which is larger than the magnetoelectric coefficient reported earlier on flexible substrates.

Another critical point that defined the magnetoelectric coupling in vertically aligned nanostructured composites is the volume fraction of ferromagnetic nanopillar phase as was demonstrated theoretically and the thickness of the (1-3) type nanocomposite film (see **Figures 2.15**, **2.16**, and **2.17**). The largest magnetoelectric coefficient for the vertically aligned nanocomposites was observed in the PZT-CFO vertical nanocomposite ~390 mV cm^{-1} Oe^{-1} with 25% volume fraction of the CFO phase (*Wan et al., 2007*). The PZT-CFO nanocomposite were grown by PLD. It was demonstrated that with increasing CFO contents, the α_{me} decreases significantly. The increased leakages and variation of microstructure were suggested to be responsible for the reduction of magnetoelectric coupling in the PZT-CFO vertical nanocomposites. In **Table 2.5**, the recent results obtained on magnetoelectric coupling in the (1-3) type multiferroic magnetoelectric nanocomposites are outlined. The largest low-frequency value of α reported for bulk (1-3) multiferroic nanocomposites is given in the first raw for the comparison.

Table 2.5: Room-temperature α_{me} in (1-3) type bulk and thin-film vertical magnetoelectric nanocomposites

Component phases	H_{dc} Oe	f_{ac} Hz	α_{me} mV cm^{-1} Oe^{-1}	Note	Ref.
PZT-TDE (bulk)	1500	100	500	Longitudinal, Casting, 1-3 bulk compos.	*Ma et al., 2007b*
$CoFe_2O_4$(core)-PZT(shell) nanofiber	2000	PFM[a]	29500[a]	Transverse, Electrospinning, Core-shell nanofiber	*Xie et al., 2011*
BFO(pillars)-CFO (matrix) on mica	2000	PFM[a]	11000[a]	Longitudinal, PLD	*Amrillah et al., 2017*
25% CFO:PZT/ Pt/Ti/SiO_2/Si	0	10000	390	Transverse, PLD	*Wan et al., 2007*
BFO(pillars)-CFO (matrix) on mica	-	-	74	Longitudinal, PLD	*Amrillah et al., 2017*
BFO(matrix)/ CFO(pillars)	6000	1000	60	Transvers, PLD	*Oh et al., 2010*
35% CFO:BFO/ SRO/STO(001)	100	-	20	Transvers, PLD	*Yan et al., 2009*
35% CFO:BFO/ SRO/STO(001)	100	-	16	Longitudinal, PLD	*Yan et al., 2010*

[a]The α_{me} was obtained indirectly by measuring the piezoresponse displacement loop (using piezoresponse force microscopy) with or without applying an in-plane *dc* magnetic field, and therefore represents the local magnetoelectric response rather than a global one from macroscopic measurements

H_{dc} – applied *dc* magnetic field

f_{ac} – frequency of the applied *ac* magnetic field H_{ac}

TDE - Terfenol-D/Epoxy medium

2.7 Ferrimagnetic $CoFe_2O_4$ Material

Ferrites have the spinel lattice (see **Figure 2.16**) consisting of a close-packed oxygen framework with face-centred cubic structure, wherein metal ions which occupy the tetrahedral sites and octahedral sites are in a ratio of 1:2. Cobalt ferrite is a ferrimagnetic material that has the composition $Co^{2+}Fe_2^{3+}O_4$ in which Fe^{3+} occupies a tetrahedral site, while the other Fe^{3+} and Co^{2+} occupy two octahedral sites. In cobalt ferrite the magnetic moments are parallel to the cube edge directions <100>. The Co^{2+} ions in the octahedral site are responsible for a large anisotropy. Both Fe^{2+} and Co^{2+} in octahedral sites are in $Co_xFe_{3-x}O_4$ have their d_{xy}, d_{yz}, *and* d_{xz} orbitals split into a singlet and a doublet. Fe^{2+} has six 3d electrons which are distributed such that the last electron occupies the singlet; thus the ground state orbital is non-degenerate. On the other hand, Co^{2+} has seven 3d electrons which are distributed such that the last electron occupies the doublet thus the ground state orbital is degenerate. Hence for Fe^{2+}, the singlet lies lower in energy, but for Co^{2+}, the doublet lies lower (*Tachiki, 1960; Chikazumi, 1964*). The consequence of the doublet lying lower in energy is unquenched orbital momentum in Co^{2+}. Since the orbital states are stronger coupled to the crystal lattice, the unquenched orbital momentum due to Co^{2+} in $Co_xFe_{3-x}O_4$ couples strongly to the crystal lattice through the spin-orbit interaction. This results in cobalt-substituted magnetite having higher anisotropy than magnetite (*Slonczewski, 1958*).

The main characteristics of $CoFe_2O_4$ including lattice parameters, Curie temperature, density, magnetocrystalline anisotropy energy, and magnetostriction are summarized and compared to other common oxide spinel ferrites in **Table 2.3**. **Figures 2.17a,b** show *dc* magnetic field and temperature dependence of cobalt ferrite magnetostriction constant, respectively. **Figure 2.17c** shows temperature dependence of magnetocrystalline anisotropy constant of cobalt ferrite.

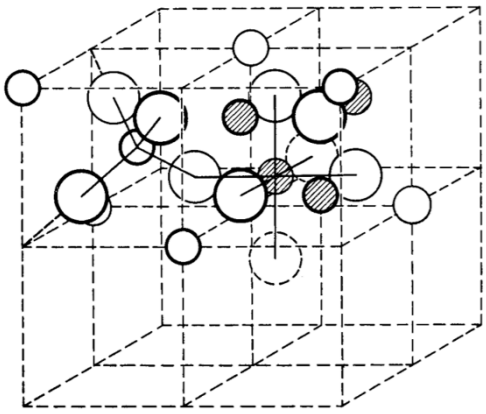

Figure 2.16: Two subsells of a unit cell of the spinel structure. From *Smit & Wijn, 1954.*

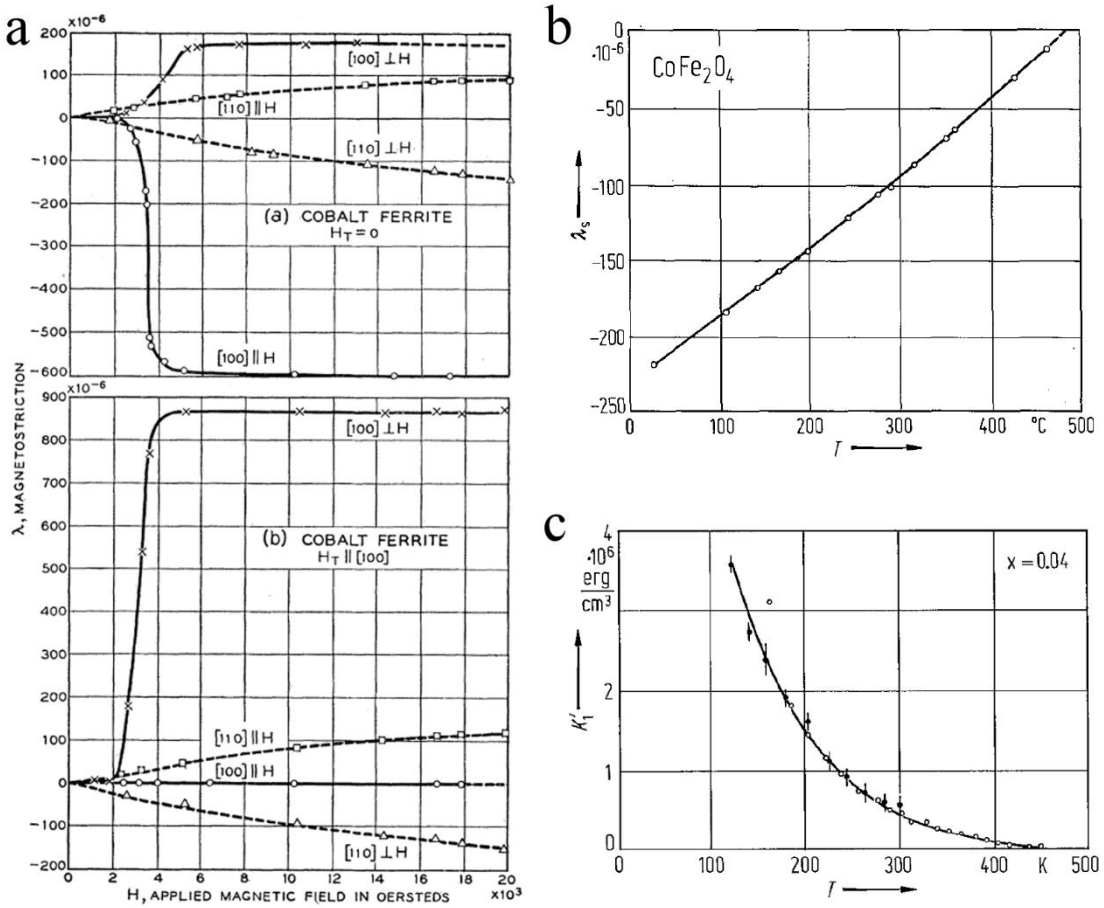

Figure 2.17: Magnetic properties of bulk cobalt ferrite material. **(a)** Magnetostriction of cobalt ferrite without (a) and (b) with magnetic anneal (from *Bozorth et al., 1955*); **(b)** $CoFe_2O_4$ saturation magnetostriction as function of temperature of polycrystalline specimen (from *Murphy & Rao, 1985*); **(c)** $Co_xFe_{3-x}O_4$ effective magnetic anisotropy constant as a funtion of temperature (from *Periklina et al., 1984*).

2.8 Ferroelectric $BaTiO_3$ and $PbZr_{1-x}Ti_xO_3$ Materials

The first perovskite oxide compound identified as being ferroelectric was $BaTiO_3$. The formal valences are +2 for Ba and +4 for Ti, exactly balancing the negative total valence of the oxygens (*Rabe et al., 2007*). At high temperature, it has a paraelectric cubic perovskite structure $Pm\bar{3}m$. At 393 K, it transforms from a cubic phase to a ferroelectric tetragonal phase $P4mm$, as shown in **Figure 2.18**. This phase remains stable until 278 K, where there is a second transformation to a ferroelectric phase of orthorhombic symmetry $Amm2$. The last transition takes place at 183 K. The low-temperature ferroelectric phase is rhombohedral $R3m$. Each transition is accompanied by small atomic displacements, dominated by displacement of the Ti ion relative to the oxygen octahedron network, and a macroscopic strain. In the successive ferroelectric phase, the polar axis is aligned respectively along the <100>, <110> and <111>

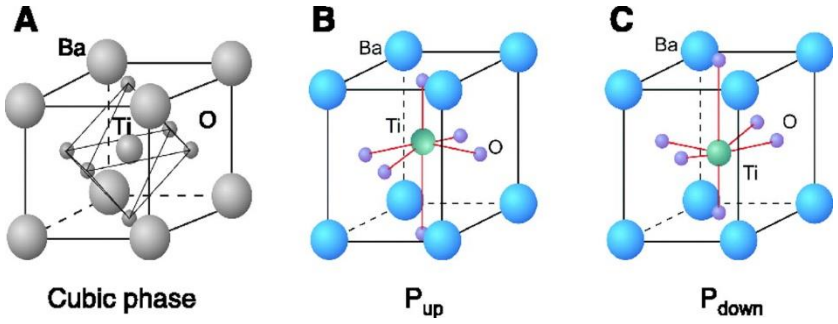

Figure 2.18: Crystal structure of the perovskite ferroelectric $BaTiO_3$. **(A)** High temperature, paraelectric, cubic phase. **(B and C)** Room temperature, ferroelectric, tetragonal phases, showing up and down polarization variants. The atomic displacements are scaled to be clearly visible. From *Ahn et al., 2004*

directions corresponding to the direction of the atomic displacements with respect to their position in the cubic reference structure. The measured polarization in the R, O and T phases are 33 μC/cm^2, 36 μC/cm^2, and 27 μC/cm^2, respectively (*Mitsui et al., 1981*).

Ferroelectricity in the perovskite oxide ferroelectrics can exhibit high sensitivity to changes in strain state, normally produced by external stress (*Rabe et al., 2007*). For $BaTiO_3$, the experimentally determined pressure-temperature phase diagram (*Ishidate et al., 1997*) showed the same R-O-T-C sequence with increasing pressure as with increasing temperature. The phase diagram for epitaxial strain in $BaTiO_3$ thin films is shown in **Figure 2.19**. The epitaxial strain constraint changes the phase sequence (*Tenne et al., 2004*). The orthorhombic phase disappears, and the rhombohedral phase has a monoclinic distortion imposed by matching to the square of the substrate (*Haeni et al., 2004*). The isoelectronic substitutions, for example Ba/Sr and Ti/Zr, are

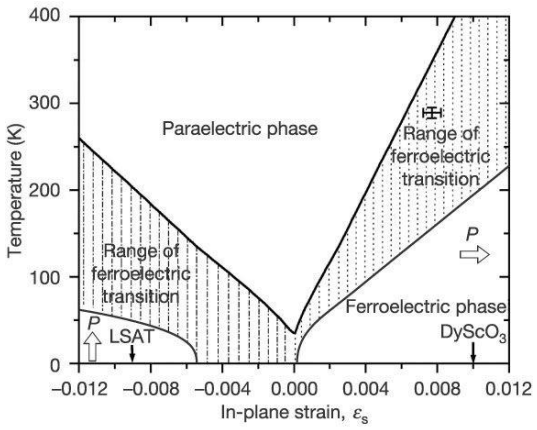

Figure 2.19: Expected T_C of (001) $BaTiO_3$ under biaxial in-plane strain σ, based on thermodynamic analysis. The arrows indicate the predicted direction of the polarization for strained $SrTiO_3$: in-plane for biaxial tensile strain and out-of-plane for biaxial compressive strain. The e s values for $SrTiO_3$ fully constrained (commensurate) to the lattice constants of LSAT and (110) $DyScO_3$ substrates are indicated by the positions of the corresponding arrows. The cross shows the observed T_c shift of a 500-A˚-thick $SrTiO_3$ film epitaxially grown on (110) $DyScO_3$. From *Haeni et al., 2004*

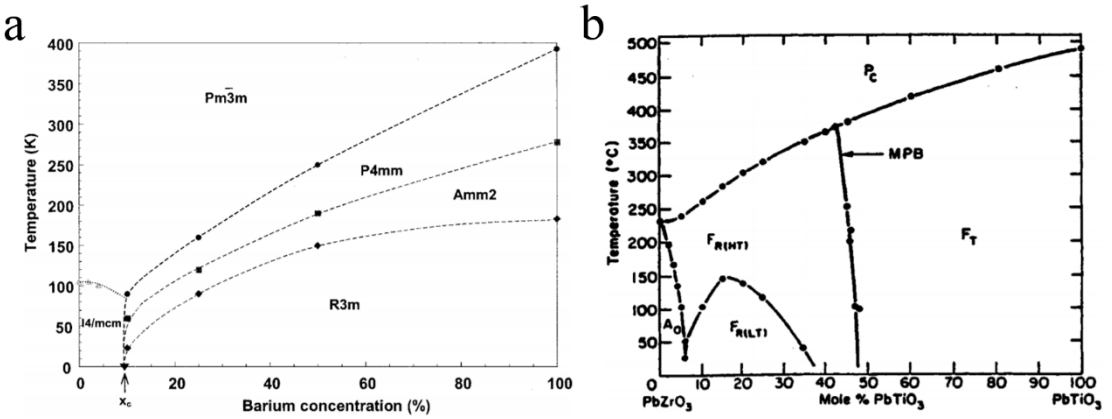

Figure 2.20: (a) Critical temperature vs concentration phase diagram of $Sr_{1-x}Ba_xTiO_3$, deduced from x-ray and neutron-diffraction studies (from *Menoret et al., 2002*). **(b)** PZT phase diagram. From *Noheda et al., 1999*, after *Jaffe et al., 1971*

particularly important to the study of ferroelectricity, as the formal valence counting yields insulating behaviour across the phase diagram, while the change in the cation can lead to shifts in transition temperatures as well as the appearance or disappearance of particular phases. For example, the substitution of Sr for Ba in $BaTiO_3$ lowers the transition temperatures in the phase sequence, with the transition being suppressed altogether as the $SrTiO_3$ endpoint is approached (*Menoret et al., 2002*), as shown in **Figure 2.20a**.

The most extensively studied and technologically important solid solution is $PbZr_{1-x}Ti_xO_3$ (PZT). The standard phase diagram is reproduced in **Figure 2.20b**. The endpoint compound $PbZrO_3$ is an antiferroelectric with 40 atoms per unit cell. However, the antiferroelectric structure is destabilized by even small amounts of Ti substitution to yield two rhombohedral ferroelectric phases (*Rabe et al., 2007*). The vertical phase boundary at about 50%, called the morphotropic phase boundary (MPB), is associated with the favourable piezoelectric properties of the system. At the MPB, an applied electric field can easily induce a transition between the rhombohedral and tetragonal phases, with a large associated strain response that is relatively insensitive to temperature. Recently, careful re-examination of the phase diagram showed the presence of a previously unknown monoclinic phase in a very narrow composition range in the vicinity of the MPB (*Noheda et al., 1999; 2006*). Structurally, this phase acts as a bridge between the tetragonal and the rhombohedral phase, as confirmed by first principles calculations (*Bellaiche et al., 2000*); this behaviour appears to be common to other lead-based perovskites as well (*Cox et al., 2001*).

The main characteristics of $BaTiO_3$, $Ba_xSr_{1-x}TiO_3$ and $PbZr_{1-x}Ti_xO_3$ bulk materials including lattice parameters, Curie temperature, density, permittivity, saturation and remanent polarization, coercivity, and piezoelectric coefficients are summarized and compared to in **Table 2.4.**

2.9 Conclusions

Multiferroic nanostructured composites have attracted a lot of attention due to the control of the extrinsic coupling between polarization and magnetization via strain or exchange bias (*Eerenstein et al., 2006; Nan et al., 2008; Fiebig, 2005; Wang et al., 2010*). This leads to a large number of potential applications including memory devices (e.g. random-access memory, reading and writing heads, hard drives), microwave magnetic devices (e.g. phase shifters, resonators, filters), sensors (magnetometer, electric current, voltage, transducers, gyrators), actuators, spintronic and energy harvesting devices (*Nan et al., 2008; Fiebig, 2005; Bibes & Barthélémy, 2008; Scott, 2007; Palneedi et al., 2016; Dong et al., 2003; Zhai et al., 2006; Fetisov & Srinivasan, 2006; Ustinov et al., 2007; Pettiford et al., 2007; Zhuang et al., 2017*). Intensive research in the field of multiferroic nanocomposites has opened new routes such as the fabrication of vertically aligned nanostructures, i.e. nanopillars embedded in a matrix, the so called (1-3) connectivity nanocomposite. These types of nanostructures offer the advantage to reduce the substrate imposed clamping effect, as compared to multilayered (2-2) types of multiferroic nanocomposites, and to enhance the interfacial area between the two phases, so that large magnetoelectric (ME) coupling can be expected (*Nan et al., 2008; Bichurin et al., 2003*). Up to now, large number of (1-3) thin-film nanocomposites from spinel and perovskite systems, including $BaTiO_3$-$CoFe_2O_4$ (BTO-CFO) (*Zheng et al., 2004*), $BiFeO_3$-$CoFe_2O_4$ (BFO-CFO) (*Zavaliche et al., 2005*), $PbTiO_3$-$CoFe_2O_4$ (PTO-CFO) (*Levin et al., 2006*), $PbZr_{0.52}Ti_{0.48}O_3$-$CoFe_2O_4$ (PZT-CFO) (*Wan et al., 2007*), $Bi_5Ti_3FeO_{15}$-$CoFe_2O_4$ (*Imai et al., 2013*), $PbMg_{1-x}Nb_xO_3$-$PbTiO_3$-$CoFe_2O_4$ (*Wang et al., 2014a*), $BiFeO_3$-$NiFe_2O_4$ (BFO-NFO) (*Benatmane et al., 2010*), and $BiFeO_3$-$Co_xNi_{1-x}Fe_2O_4$ (*Ojha et al., 2016*) were fabricated using pulsed laser deposition (PLD) technique. In order to control the long-range ordered vertical interface, anodic aluminium oxide (AAO) membranes were used as a hard mask to grow columnar multiferroic nanocomposites (*Gao et al., 2010*). Thick AAO membranes were also used as templates to fabricate multiferroic core-shell nanowire arrays using a combination of different synthesis processes, such as sol-gel processing, electrodeposition, and thermal annealing (*Liu et al., 2007; Sallagoity et al., 2016*).

However, to our best knowledge, there is no report on the fabrication of vertically aligned multiferroic nanocomposites based on a direct sputtering deposition of the ferroelectric film onto the top surface of the vertically aligned free-standing metallic nanopillar array structure, grown by electrodeposition into AAO masks supported on silicon (Si) substrates. Also, the sol-gel dip-coating deposition of ferroelectric layers onto the vertically aligned free-standing metal oxide nanopillar array structures, formed by thermal oxidation of metallic nanopillars, was not reported in literature yet. Moreover, the dip-coating sol-gel deposition of relatively thick PZT layers onto the

metallic 3D interconnected nanowire networks developed recently, is a unique and original technique for the synthesis of vertically aligned multiferroic nanocomposites.

In this work, we demonstrate a simple approach to synthesize vertically aligned $Ba_{0.7}Sr_{0.3}TiO_3$-$CoFe_2O_4$ (BSTO-CFO), BTO-CFO and PZT-CFO nanocomposites with three different types of architecture, where each of them features increased interfacial area between the ferroelectric and ferrimagnetic components, decreased substrate imposed clamping, and number of potential technology applications. Considering the number of steps for each process (see **Tables 3.13** in **Section 3.5**, p. 118), it is not explicitly simple. However, this can be understood in terms of low cost and large-scale fabrication of nanostructured composites with controlled geometry.

For example, the PZT-CFO core-shell nanocable arrays and PZT-CFO nanocomposites based on 3D interconnected nanowire networks show large aspect ratio of nanowires (ratio between nanowire's length and diameter ~500) and large interfacial area between two constituents, which can be used for the applications that require giant ME coefficients such as microwave magnetic devices, field sensors, actuators, and energy harvesting. Meanwhile the vertically aligned BSTO/BTO/PZT-CFO multiferroic nanocomposites based on relatively small CFO nanopillar arrays (aspect ratio < 6) are more suitable for the devices that require miniaturization of nanostructures, good ordering, and large packing density of nanopillars, as well large ME coupling, e.g. magnetoelectric random-access memories, reading heads, hard drives, and other spintronic devices.

Chapter 3

Sample Preparation and Experimental Techniques

Three different architectures of vertically aligned magnetoelectric systems were developed in this work. Chapter 3 consists of three main sections, wherein each section is dedicated to the fabrication of one particular ME system (see **Figure 3.1**). These systems include multiferroic core-shell nanocable arrays, (1-3) type multiferroic nanostructures, and nanocomposites based on 3D interconnected nanowire (NW) networks. The core-shell nanocable system was elaborated using commercial porous anodic aluminium oxide (AAO) templates (Synkera, Co) with a thickness of ~50 µm,

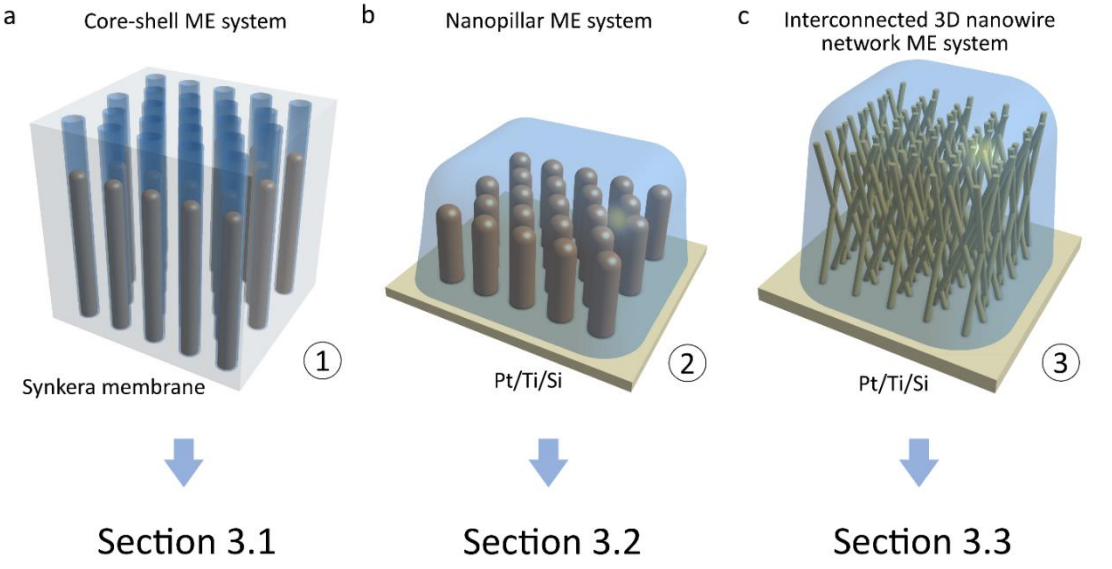

Figure 3.1: General illustration of the three geometrical designs for the vertically aligned magnetoelectric nanocomposites. **(a)** $PbZr_{0.52}Ti_{0.48}O_3$-$CoFe_2O_4$ core-shell nanocable array embedded into the commercial AAO membrane (Synkera Co.) **(b)** $Ba_{0.7}Sr_{0.3}TiO_3$-$CoFe_2O_4$, $BaTiO_3$-$CoFe_2O_4$ and $PbZr_{0.52}Ti_{0.48}O_3$-$CoFe_2O_4$ (1-3) nanocomposites, based on the ferromagnetic nanopillar array, fabricated on the metallized Si sub **(c)** $PbZr_{0.52}Ti_{0.48}O_3$-$CoFe_2O_4$ (3-3) nanocomposite, based on 3D interconnected ferromagnetic nanowire network, fabricated on the metallized Si wafer

and the height of FM $CoFe_2$ nanowire arrays grown inside AAO template pores, coated with FE nanotubes, was ~10 μm. The (1-3) type nanocomposites were fabricated using as-prepared AAO/Pt/Si templates with AAO thickness of ~1.3 μm implying radio-frequency magnetron sputter deposition of Al layer, formation of porous AAO nanostructures via anodization and chemical widening processes, and pulsed electrochemical deposition of $CoFe_2$ nanopillar arrays having a height in the range ~150-500 nm. Finally, the 3D interconnected NW network system was prepared using commercial track-etched polymer templates (it4ip, Co) with thickness of ~25 μm implying pulsed electrodeposition of $CoFe_2$ NW networks with heights of ~3.5 and 5 μm.

Section 3.1 presents the fabrication process of the first ME system the core-shell nanocable arrays (see **Figure 3.1a**), wherein FM nanowires are surrounded by FE nanotubes. The vertical alignment in the core-shell system is provided by the porous AAO membrane hosting the core-shell nanocable array. **Section 3.2** presents the fabrication of the second ME system namely the (1-3) type composite nanostructures (see **Figure 3.1b**), wherein vertical FM nanopillar arrays are embedded in a thin FE matrix. The vertical alignment of the FM nanopillars is ensured by the Pt/Si substrate on which the FM nanostructures were prepared. **Section 3.3** reveals the last ME system - 3D interconnected NW network based nanocomposites (see **Figure 3.1c**), where the 3D interconnected FM nanowire network, a robust self-supported free-standing system of vertically aligned $CoFe_2$ nanowires crossing each other, is embedded into a thick FE matrix. The vertical alignment of the 3D interconnected NW network based nanocomposites is ensured by Pt/Si substrate.

In the beginning of each section a complete fabrication process of the ME systems is demonstrated with all steps arranged in the same sequence as they take place during the fabrication process followed by the detailed explanation of each step. Some of the preparation steps are identical for different ME systems, thus these steps are discussed in detail only once to refrain from repetition. In the experimental chapter, a theoretical background was included for the clearness. Additional detailed information could be read in the cited references, listed at the end of this thesis. The last section of Chapter 3 presents characterization techniques, used in the present work, and their general working principles.

3.1 Preparation of $PbZr_{0.52}Ti_{0.48}O_3$-$CoFe_2O_4$ Core-Shell Magnetoelectric System

Vertically aligned core-shell nanocable arrays were prepared inside porous AAO membranes. A general fabrication process of the PZT-CFO core-shell nanocables, consisting of four steps, is illustrated in **Figure 3.2**.

In the first step, commercial AAO membranes with defined geometric parameters were purchased from Synkera Technology Inc., USA and were used as hosting

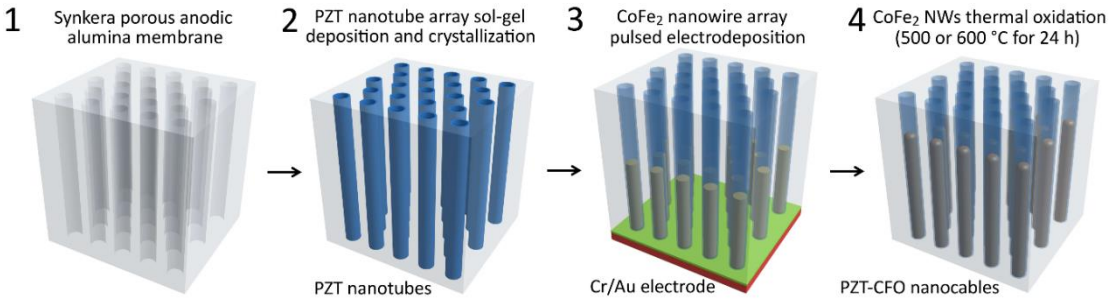

Figure 3.2: Three-step schematic fabrication of the $PbZr_{0.52}Ti_{0.48}O_3$-$CoFe_2O_4$ core-shell nanocable array using porous membrane. **(1)** Commercial anodic aluminium oxide (AAO) membrane (Synkera Co.) **(2)** Sol-gel deposition of the $PbZr_{0.52}Ti_{0.48}O_3$ nanotube array **(3)** $CoFe_2$ nanowire array pulsed electrodeposition into the $PbZr_{0.52}Ti_{0.48}O_3$-coated AAO membrane using Cr/Au pre-deposited working electrode **(4)** Thermal oxidation of the $PbZr_{0.52}Ti_{0.48}O_3$-$CoFe_2$ nanocable array to fabricate $PbZr_{0.52}Ti_{0.48}O_3$-$CoFe_2O_4$ phase

templates. In the second step of process, vertically aligned $PbZr_{0.52}Ti_{0.48}O_3$ nanotube (PZT NT) arrays were deposited into the pores of AAO membranes through sol-gel deposition and thermal crystallization. In the third step of process, one side of the PZT-coated AAO membrane was covered by a thin Cr/Au bilayer to close the pores and act as the working electrode for a following pulsed electrodeposition of the $CoFe_2$ nanowire (NW) arrays inside the PZT NTs. In the last step of process, after chemical etching of the Cr/Au electrode, the $CoFe_2$ NW arrays surrounded by the PZT NTs were thermally oxidized into $CoFe_2O_4$ phase forming $PbZr_{0.52}Ti_{0.48}O_3$- $CoFe_2O_4$ core-shell nanocable (PZT-CFO NC) arrays inside the AAO membranes. The above-mentioned steps are further discussed in detail.

3.1.1 First Step of Process: Commercial Self-Supported Anodic Aluminium Oxide Membranes

Commercial AAO membranes were used as the nanoporous host for the process development. The alumina templates with through pores such as Synkera and Wattman come with all sort of geometric parameters, i.e. pore diameter D_{pore} is in the range from few tens to few hundreds of nm, porosity P_{AAO} ~10 – 40%, and pores density ρ_{pore} ~10^9 – 10^{11} pores per cm^2.

The porosity and the pores density of the ordered AAO templates with hexagonal arrangement are defined as

$$P_{\text{AAO}} = \frac{\pi}{2\sqrt{3}}\left(\frac{D_{\text{pore}}}{D_{\text{cell}}}\right)^2 \times 100\%, \tag{3.1}$$

$$\rho_{\text{pore}} = \frac{2}{\sqrt{3}D_{\text{cell}}^2} \times 10^{14}\ \text{cm}^{-2}, \tag{3.2}$$

where D_{cell} is the cell size or inter-pore distance (center-to-center) (*Nielsch et al., 2002*; *Jessensky et al., 1998*; *Li et al., 1998a*). The AAO membranes prepared in different

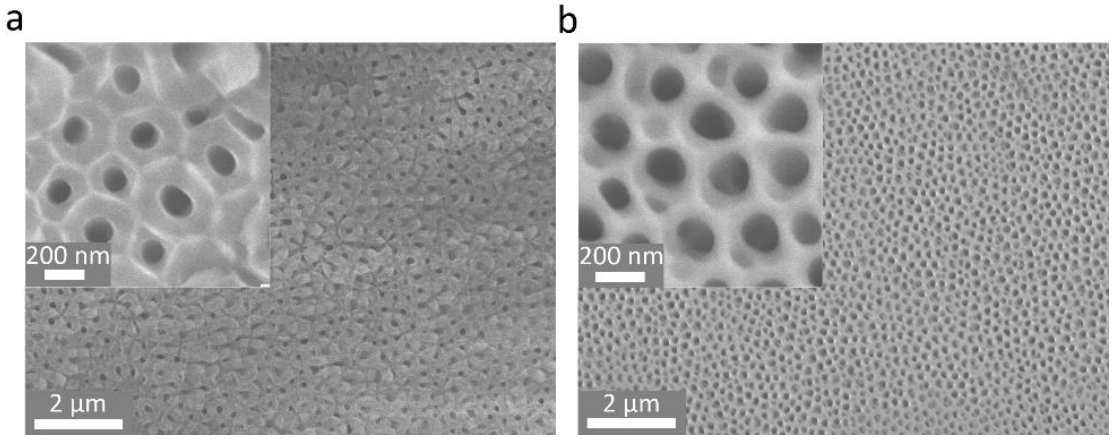

Figure 3.3: Top view SEM images of the two commercial aluminium oxide templates Synkera-1 **(a)** and Synkera-2 **(b)** used for the synthesis of core-shell nanocable arrays

electrolytes using two-step anodization technique show the best pore ordering when the volume expansion after the Al foil anodization is ~1.2-1.4 times and the porosity, P_{AAO}, is ~10-20% (*Jessensky et al., 1998*; *Li et al., 1998a*).

Figures 3.3a,b show the top view SEM images of two commercial alumina membranes Synkera-1 and Synkera-2, respectively. The AAO membranes used in this work featured the thickness of 50 µm and D_{pore}, D_{cell}, ρ_{pore}, and P_{AAO} as presented in **Table 3.1**.

Table 3.1: Geometric parameters of the commercial AAO membranes

Membrane	Thickness t_{AAO}, µm	Pore diameter D_{pore}, nm	Interpore distance D_{cell}, nm	Pore density ρ_{pore}, pores cm^{-2}	Porosity P_{AAO}, %
Synkera-1	49±1	100±10	240±20	2×10^9	15
Synkera-2	48±1	150±10	240±20	2×10^9	35

3.1.2 Second Step of Process: Sol-Gel Deposition of $PbZr_{0.52}Ti_{0.48}O_3$ Tubular Layers

The chemical solution deposition (CSD) of the PZT NT arrays into porous AAO membranes is described in this section. To fabricate the PZT NT arrays, a facile dip-impregnation sol-gel deposition was used. It is a flexible, low-cost and scale-up preparation technique that is normally used to synthesize ceramic thin-films and nanotubes. The random crystalline orientation is due to the chemical incompatibility of the interface of PZT nanotubes and AAO membrane, or PZT thin-films and Pt/Si substrate. The key point in using the AAO membranes instead of polymer membranes is their mechanical stability and resistance to high temperatures required for the PZT NTs crystallization (~500-700 °C).

Principles of Chemical Solution Deposition

In the 1980s, the development of metallo-organic decomposition and sol-gel synthesis gave possibility to fabricate ceramic PZT thin-films by chemical solution deposition (CSD) with properties similar to the ones of their bulk counterparts (*Fukushima et al., 1984*; *Budd et al., 1985*; *Dey et al., 1988*).

A general flow chart of the CSD procedure, the main body of which is subdivided into parts according to the different processing steps shown in **Figure 3.4** (*Schneller et al., 2013*). Typically, the CSD deposition begins with the solution preparation (**Figure 3.4a**). The precursors used for the solution could be salts, carboxylates, or metallo-

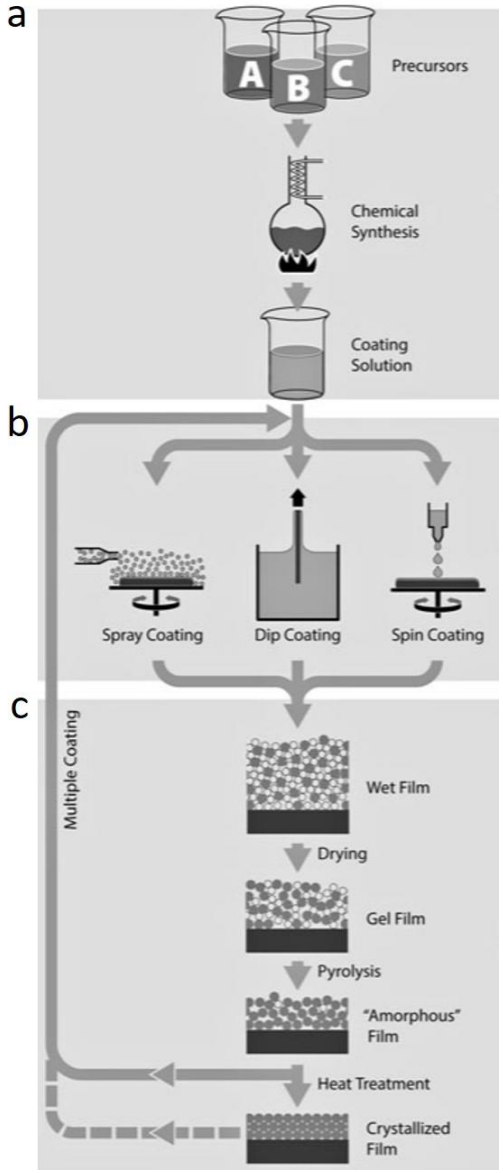

Figure 3.4: Flow chart of a typical chemical solution deposition process. It shows schematically the different processing steps starting with solution synthesis **(a)**, followed by deposition **(b)**, and crystallization **(c)** (from *Schneller et al., 2013*)

organic compounds such as metal alkoxides and metal β-diketonates, that are typically purchased commercially. The precursors are dissolved in suitable solvents. The stochiometric ratio of the mixed precursors correlates with the stoichiometry of a crystallized gels, but sometimes the composition correction is required due to the volatility of components such as Pb under critical temperatures. Chemical stabilizers can be added into the solution during its preparation process to adjust the properties of the coating solution such as surface tension, viscosity, and boiling point.

Next, the coating solution can be deposited using various techniques (**Figure 3.4b**). The most common among them are the spin-coating and dip-coating. Spray-coating and ink-jet printing are more complicated techniques that consume less material and allow to fabricate more conformal nanostructured coatings. Finally, the as-deposited layer is dried (80-200 °C), pyrolyzed to remove organic species (300-450 °C), crystallized (at 600-1000 °C) and in some cases post-annealed to densify the layer and adjust the microstructure (**Figure 3.4c**). Controlled thermal treatment of the deposited wet layers in the temperature range 200-800 °C results in its crystallization. The crystallization temperature depends on the nucleation and growth behaviours, so the temperature should be adjusted individually for each material. The thermal treatment of the deposited layers is typically carried out using a hot plate, oven and conventional furnace (maximum heating rate ~10 °C/min) or a rapid thermal annealing (RTA) oven which enables fast heating up to few hundred degrees per min. The deposited layer thickness can be easily adjusted by controlling the solution molar concentration and viscosity (*Tu et al., 1996*; *Yi et al., 1988*) or by repeating the coating and pyrolysis operations to build up thicker multi-layers prior to final crystallization.

In order to prepare FE layers with good quality using sol-gel deposition, a number of conditions for the precursor solutions, substrates, and processing should be fulfilled: (a) Good solubility of all precursors in the solvent forming a single coating solution stable for a relatively long period of time (few months); (b) Selected precursors shouldn't leave any elements apart from the metal ions and oxygen, while all other atoms from counter ions or ligands should be decomposed during thermal treatment; (c) Solution rheology should be adjusted for a particular synthesis technique to avoid problems such as poor thickness uniformity (striations); (d) Suitable wettability of the substrate; (e) Phase purity of the solution without phase separation during drying and pyrolysis; (f) Cracks formation and compositional non-uniformity must be avoided; (g) Interfacial diffusion between the deposited FE layers and substrate or between the FE nanotubes and hosting template; (h) Substrate and hosting membrane degradation during thermal treatment should be avoided.

Principles of Sol-gel Synthesis

Commonly the chemical solution deposition of perovskite layers is performed using metalloorganic compounds dissolved in a solvent. The reagents used to form a solution are typically metal alkoxides $[M(OR)_z]_n$, metal carboxylates $M(OOCR)_z$, and metal β-

diketonates $MO_x(CH_3\text{-}COCHCOCH_3)_x$, where *M* is a metal with the valence, *z*, *R* is a general organic residue (simple alkyl or alkenyl groups), and *n* represents the degree of molecular association. The solution synthesis techniques can be classified into three: (a) Sol-gel deposition using 2-methoxyethanol as a solvent (*Dey et al., 1988*; *Schwartz et al., 1997*); (b) Chelate processing using modified ligands such as acetic acid (*Yi et al., 1988*; *Takahashi et al., 1990*); (c) Metalloorganic decomposition using metal carboxylate compounds (*Vest & Xu, 1988*). The chemical reactions between starting reagents occurring during solution preparation will depend on the reactivity of compounds and preparation conditions such as reflux temperature.

In the first technique, the sol-gel synthesis of perovskite layers is commonly carried out using a 2-methoxyethanol ($CH_3OCH_2CH_2OH$) as solvent. The formation of a three-dimensional macromolecular oxide network (e.g., oligomers, polymers) is achieved by the hydrolysis and the condensation of alkoxide reagents and metal-oxygen-metal (*M*-O-*M*) bonds (*Livage et al., 1988*; *Sanchez et al., 1988*):

$$M(OR)_z + H_2O \rightarrow M(OR)_{z-1}(OH) + ROH. \qquad \text{(hydrolysis)}$$

During the hydrolysis, the alkoxy groups are replaced by the hydroxoligands (-OH) or the oxo-ligands (=O). Water acting as a Lewis base attacks the metal atom of alkoxide (Lewis acid), then a proton transfers from an entering water molecule to the leaving group in a transition state, and an alcohol molecule is released. The sensitivity towards hydrolysis and condensation depends mainly on the positive partial charge of the metal atom $\delta(M)$ (*Livage et al., 1988*) [for the $Ti(O^iPr)_4$ $\delta(M) = +0.60$ and for the $Zr(O^iPr)_4$ is $\delta(M) = +0.64$] and the ability to increase its coordination number, *N*, of coordinatively unsaturated metal atoms to their preferred value, e.g. Ti with $z = +4$ and $N = 4$ tends to achieve an octahedral coordination $N=6$, while Zr with $z = +3$ or $+4$ tends to achieve $N = 7$ or 8. A large positive partial charge is associated with rapid reaction rate. Thus, the $Zr(O^iPr)_4$ with larger number of coordinative unsaturation has higher sensitivity toward hydrolysis compared to the $Ti(O^iPr)_4$. In addition to the positive partial charge and ability to achieve higher coordination numbers, differences in the molecular structure of metal alkoxide with the same central metal will also lead to a different behaviour in hydrolysis and subsequent condensation reactions (*Livage et al., 1990*).

During the alkoxides condensation through oxolation, the metal-oxygen-metal bonds form due to the removal of water and alcohol, thus either the proton is transferred to the hydroxy ligand (oxolation) or to the alkoxy ligand (alkoxolation), respectively.

$$2M(OR)_{z-1}(OH) \rightarrow M_2O(OR)_{2z-3}(OH) + ROH.$$
(condensation by (alkox)olation and alcohol removal)

Similar to the hydrolysis, a nucleophilic attack of the oxygen lone pair in metal hydroxide species to the partially positive charged metal atom, *M*, occurs, leading to the proton's transfer and release of the water or alcohol molecule.

$$2M(\mathrm{O}R)_{z-1}(\mathrm{OH}) \rightarrow M_2\mathrm{O}(\mathrm{O}R)_{2z-2} + \mathrm{H_2O}.$$

(condensation and water removal)

Another reaction that occurs is an alcohol-exchange which causes the decrease of the hydrolysis sensitivity of starting reagents such as zirconium *n*-propoxide and titanium isopropoxide, used to deposit PZT layers:

$$M(\mathrm{O}R)z + zR'\mathrm{OH} \rightarrow M(\mathrm{O}R')z + zR\mathrm{OH}, \qquad \text{(alcohol exchange)}$$

where $\mathrm{O}R$ is a reactive alkoxy group and $\mathrm{O}R'$ is another less reactive alkoxy group such as 2-methoxyethoxy group. During preparation of PZT solutions, the 2-methoxyethanol is often used to dissolve carboxylate precursors such as lead acetate and to decrease the hydrolysis sensitivity of starting alkoxide reagents such as zirconium *n*-propoxide and titanium *i*-propoxide (*Dey et al., 1988*). Generally by refluxing the lead acetate in the 2-methoxyethanol, an acetate group is replaced, leading to the formation of soluble lead precursor $Pb(OOCCH_3)(OCH_2CH_2OCH_3)\cdot 0.5H_2O$. The lead acetate and the alkoxide compounds are typically refluxed in the 2-methoxethanol separately, followed by the mixing, refluxing, distillation, and dilution of solutions. Before the layer's deposition, the resulting solution is hydrolysed to enable oligomerization.

The second class of the solution synthesis is a chelate route ("hybrid route") or an inverse-mixing-order route, which utilizes alkoxide compounds (metal salts of alcohols) as starting reagents for B-site species and metal carboxylates as starting reagents for A-site species (*Schwartz, 2004*). Main difference between the chelate route and the first methoxyethanol based route is that the alkoxide compounds undergo a molecular modification through a reaction with chelating ligands such as acetic acid, acetylacetone, or amine compounds. The key point of alkoxide precursors is the ability to form polymeric species composed of *M*-O-*M* bonds when reacted with water (*Livage et al., 1988*). However, the principal of solution preparation in terms of formation of small oligomers species is similar. The chelate route is conducted using acetic acid as a solvent and chelating agent. The main two reactions that occur to from a 3-D network with branched -O-*M*-O-*M*- bonds are also the hydrolysis and condensation, i.e. the chelation of metal alkoxide (e.g. acetic acid):

$$M(\mathrm{O}R)_z + x\mathrm{CH_3COOH} \rightarrow M(\mathrm{O}R)_{z-x}(\mathrm{OOCCH_3})_x + xR\mathrm{OH}.$$

The hydrolysis occurs when a water molecule partially hydrolyses the alkoxide molecule to from $M^{z+}(\mathrm{O}R)_{z-1}(\mathrm{OH})$. The condensation occurs when a partially hydrolysed molecule reacts with another alkoxide molecule. The purpose of using the chelating agents is to reduce the hydrolysis sensitivity of alkoxide compounds. Since the alkoxide compounds are molecularly modified by the chelation, the structure and properties of the resulting species and pyrolysis behaviour are different. The chelation

route is a simpler technique compared to the 2-metoxyethanol route, because the distillation and refluxing steps are unnecessary. Normally, the chelation agents are added to alkoxide compounds during the first stage of solution preparation under inert atmosphere conditions (*Yi et al., 1988*).

For the fabrication of PZT layers, either lead acetate is first dissolved in acetic acid, and subsequently titanium and zirconium alkoxides are added (*Yi et al., 1988*; *Assink & Schwartz, 1993*), or the acetic acid can be added first to chelate the alkoxides, followed by the addition of lead acetate resulting in a more homogeneous distribution of the B-site cations compared to the solution prepared by the conventional 2-methoxyethaml route. The drawback of chelate route is that the continuous reactivity of precursor solution results in the change of precursor characteristics with time (normally after few weeks), which is due to the smaller compliance of acetate groups to hydrolysis than alkoxy groups, which can be attached by water leading to the change in molecular structure, the esterification of solution, the oligomerization and realkoxylation of species, and finally to the precipitation (*Boyle et al., 1997*).

The third chemical synthesis route of PZT solution is a metalloorganic decomposition (MOD), where large carboxylate compounds such as lead 2-ethylhexanote, zirconium neodecanoate and titanium dimethoxy dineodecanoate are used (*Vest & Xu, 1988*). Generally, the metalloorganic compounds are dissolved separately in a common solvent such as xylene, followed by the solutions mixing. An oligomerization process does not occur, because the starting compounds are water-resistant and the precursor species in the solution are similar to the starting molecules. The MOD route has been successfully used for the sol-gel synthesis of the PZT films (*Klee et al., 1992*). The main drawback of this route is that large organic ligands imply large shrinkage and weight loss leading to layer's cracking. In addition, low reactivity of the starting compounds limits the process flexibility in terms of the change of precursor species characteristics and layer's properties due to the chelation, hydrolysis, and condensation adjustment.

A common problem for all three types of syntheses techniques is the PbO volatilization during heat treatment of gels and crystallization of oxide layers. It is caused by the low oxygen partial pressure produced by the volatized hydrocarbon gas that occurs during pyrolysis (*Polli et al., 2000*). Typically, to compensate the loss of Pb, an excess of lead precursor (10-20 mole %) is added into solutions (*Saito et al., 1994*). The viscosity of the solution increases with the molecular weight of the related species. To obtain thinner PZT layers, to adjust viscosity and surface tension, and to improve the wettability of substrates, solution can be diluted with some combination of distilled water and propanol (*Yi et al., 1988*). Reducing the molar concentration of precursors in the solution can also decrease the layer thickness. However, the change of solution concentration affects morphology, structure, and properties of the layer as well, therefore must be conducted carefully (*Hoffmann et al., 1997*). Ethylene glycol can be added to solution to adjust its boiling point.

The cross-linked polymeric species at some point forms a gel consisted of a 3-D metal oxide network (*Livage et al., 1988*) within alcohol, with a significant portion of non-reacted -*M*-OH and -*M*-O*R* groups concealed within the tangled, molecular gel. The molecular gel could be transformed to an oxide when heated. Alkoxide solutions form brittle gels that are often subjected to cracking, which is a critical point for layer structure and physical properties. The main objective of using coating solution precursors is to enable the mixing of different precursor molecules, containing various metal elements, at the molecular scale so that long-range diffusion is not needed to synthesis a multielement compound. Mixing on the molecular scale leads to multielement layer synthesis at low temperatures, following pyrolysis.

Experimental Details of Solution Preparation for PZT Nanotubes Synthesis

Figure 3.5 illustrates a flow chart for the synthesis of a stock solution containing Pb, Zr and Ti precursors with 0.4 M concentration using inverse-mixing-order chelate route described earlier (*Assink & Schwartz, 1993*). This PZT solution was used for the sol-gel deposition of PZT NT arrays. The reagents and the solvents were selected in accordance with next requirements: (a) High metal content; (b) High solubility of compounds in solvents; (b) Thermal decomposition without evaporation; (c) Chemical compatibility between compounds; (d) Suitable boiling point, surface tension, viscosity of solvent; (e) High concentration of components in solution.

Lead(II) acetate trihydrate, $Pb(CH_3COO)_2 \cdot 3H_2O$, zirconium(IV) propoxide, $Zr(C_3H_7O)_4$ (70% in 1-propanol), and titanium(IV) isopropoxide, $Ti[(CH_3)_2CHO]_4$ (97%), were used as metal precursors. The acetic acid (99.85%) and 2-propanol (anhydrous, 99.5%) were used as solvents. The lead acetate was dissolved in acetic acid with 10% mole excess to compensate the PbO loss during heat treatment. All used chemical products were purchased from Sigma-Aldrich, MO, USA. The mass of lead acetate precursor with 0.4 M concentration was estimated as:

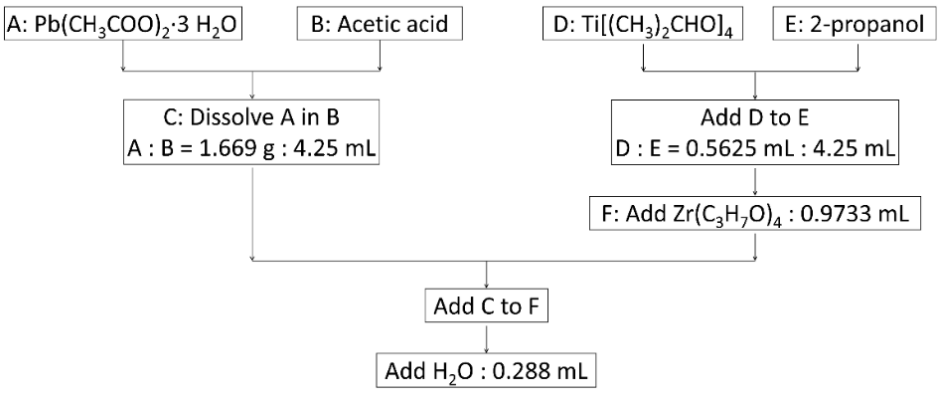

Figure 3.5: Flow chart diagram for the inverted mixing order synthesis of the PbZrTi solution used for the deposition of $PbZr_{0.52}Ti_{0.48}O_3$ nanotube arrays

$$m_{\mathrm{Pb}}\ [\mathrm{g}] = (n + n \times 10\%)\ [\mathrm{mol/L}] \times V\ [\mathrm{L}] \times M\ [\mathrm{g/mol}],$$

where n is a volume concentration, V is a volume, and M is a formula molar weight, thus

$$m_{\mathrm{Pb(CH_3COO)_2}} = (0.4 + 0.4 \times 10\%) \times 0.01 \times 379.33 = 1.669\ [\mathrm{g}].$$

The volumetric compositional ratio of Zr and Ti precursors added into 2-propanol was adjusted to 52:48 to ensure the formation of a PZT layer with the same Zr:Ti elemental composition 52:48. First, the $Ti[(CH_3)_2CHO]_4$ was added dropwise into the 2-propanol solution and stirred during 20 minutes, following by the addition of $Zr(C_3H_7O)_4$ compound into the same solution already containing Ti. The volumes of $Ti(O^iPr)_4$ (97% *wt* in isopropanol) and $Zr(O^nPr)_4$ (70% *wt* in 1-propanol) were estimated as:

$$V_{\mathrm{Ti}}\ [\mathrm{mL}] = \frac{\omega_{\mathrm{Ti}}}{97\%} = 48\% \times n\ \left[\frac{\mathrm{mol}}{\mathrm{L}}\right] \times V\ [\mathrm{L}] \times \frac{M}{97\%}\left[\frac{\mathrm{g}}{\mathrm{mol}}\right],$$

$$V_{\mathrm{Ti[(CH_3)_2CHO]_4}} = 48\% \times 0.4 \times 0.01 \times \frac{284.22}{97\%} = 0.5625\ [\mathrm{mL}],$$

$$V_{\mathrm{Zr}}\ [\mathrm{mL}] = \frac{\omega_{\mathrm{Zr}}}{70\%} = 52\% \times n\ \left[\frac{\mathrm{mol}}{\mathrm{L}}\right] \times V\ [\mathrm{L}] \times \frac{M}{70\%}\left[\frac{\mathrm{g}}{\mathrm{mol}}\right],$$

$$V_{\mathrm{Zr(C_3H_7O)_4}} = 52\% \times 0.4 \times 0.01 \times \frac{327.57}{97\%} = 0.9733\ [\mathrm{mL}].$$

After 20 minutes of stirring, the $Pb(CH_3COO)_2 \cdot 3H_2O$ was fully dissolved in the acetic acid, and the lead precursor solution was added dropwise into the solution containing titanium and zirconium alkoxides, the resulting solution was stirred for ~20 min at room temperature. A deionized water (VWR Chemicals, France) was added to initiate

Table 3.2. Reagents and solvents used for the preparation of the stock solution for PZT nanotubes arrays

Chemicals		Quantities
PZT nanotube arrays:		
Lead acetate	$Pb(CH_3CO_2)_2 \cdot 3H_2O$	1.669 g
Acetic acid	CH_3COOH	4.25 mL
Zirconium *n*-propoxide	$Zr(C_3H_7O)_4$	0.9733 mL
Titanium isopropoxide	$Ti[(CH_3)_2CHO]_4$	0.5625 mL
2-Propanol	$CH_3CH_2CH_2OH$	4.25 mL
Distilled water	H_2O	0.288 mL

hydrolysis and condensation reactions, followed by the final stirring during ~20 min. All chemical products used for the synthesis of PZT stock solution with Pb:Zr:Ti composition around 110:52:48 are shown in **Table 3.2**. The final solution was stored in a refrigerator for one month.

Principles of Sol-gel Deposition

Preparation of perovskite layers using chemical solution deposition routes implies a conversion of the oligomeric solution of precursor species into crystallized phase. In this process, structural rearrangements on several dimensions should occur to allow the crystallization to take place including the breaking of *M*-O-C and *M*-O-H bonds and formation of *M*-O-*M* bonds. In case of oxygen atoms, the coordination changes from nonbridging (O-H and O-C) or 2-fold (*M*-O-*M*) to 3-fold. Rearrangement takes place on larger scales as well, i.e. as-deposited bulk gels consist of the aggregation of oligomer species and clusters of few nanometres in size. During pyrolysis, these species rearrange into an inorganic amorphous layer by means of thermal treatment, then the amorphous layer is crystallized at higher temperature in the process of nucleation and growth.

Once a coating solution is prepared, PZT layer could be deposited using either spin-coating or dip-coating techniques, followed by the layer's transformation into a PZT crystallized phase using thermal treatment (see **Figures 3.4b,c**). The spin-coating deposition is normally conducted by putting a few drops of solution onto substrate. Then the coating solution is uniformly distributed via spinning at the rate ranging 1000-8000 rpm during a few tens of seconds. In case of the dip-coating, normally substrates or porous membranes are dipped into a solution to wet the top surface or inner walls of the substrates or porous membranes, respectively, followed by a pulling up from the precursor solution at the speed in the range of 0.01-10 mm/second. The factors impacting the thickness of the dip-coated film include gravitational force, solution viscosity, surface tension and the speed of the dipping (*Ji & Lin, 2016*). The thickness of the spin-coated films on the other hand can be controlled by rotation speed (rpm) of the spin coater, spinning time, and the solution viscosity. However, it is necessary the precursor solution should be with a proper viscosity for both spin-coating and dip-coating techniques. For ultrathin films synthesis, when viscosity is too low to meet the requirements of these two kinds of techniques, spray-coating can be used to conduct the film deposition. In the spray-coating, the precursor solution is transformed to aerosol by nebulizer or pressure. So, the solution viscosity should be very low for nebulizing or the formation of droplets. Then the droplets are transferred by a carrier gas. Finally, the coating on the substrate is deposited by spraying of the nebulized droplets. Herein, the gas pressure and the spraying time are the key factors for the optimization.

The minimal thickness of the spin-coated BTO-CFO nanocomposite and PZT film with good-homogeneity, obtained using optimal rotation or dipping speeds, viscosity, and surface tension, is typically limited to ~30 and 40 nm, respectively (*Liu et al., 2010*; *Maki et al., 2000*). Cycling operations of spin-coating, drying, and heating offer to reach the required thickness of the films while also reducing shrinkage stresses and cracking. The maximum thickness achieved without cracking via single-step deposition using alkoxide solutions containing polyvinylpyrrolidone (PVP) is ~2 μm for $BaTiO_3$

and PZT films (*Kozuka, 2016*). The PVP allowed to increase the uncracking critical by the C=O groups acting as the capping agent for the OH groups of the metalloxane polymers, suppressing the condensation reaction and promoting the structural relaxation.

Principles of Pyrolysis

After coating the substrate with the precursor solution, solvent evaporation causes the precursor molecules to consolidate and form a layer that is sufficiently elastic to support stresses (*Schneller et al., 2013*). At this moment, the layer's volume reduction occurs due to the further evaporation of O*R* and OH groups from the *M*-O-*M* backbone causing shrinkage. Since the as-deposited layer is bound to the substrate, the decreased volume is biaxially constrained, generating biaxial tensile stresses. The ability of layers to support large stresses depends on what precursors, solvents and modifying ligands (chelating ligands) are used. Alkoxide precursors form brittle gels that efficiently support tensile stresses. Although large chain carboxylates form weak inelastic layers that do not support large stress, they go through a large volume change during pyrolysis step to an elastic, inorganic layers which are able to support biaxial tensile stresses. The biaxial tensile stresses result in the formation of crack networks when the layer thickness is larger than a critical value, which for brittle gels is ~100 nm (*Schneller et al., 2013*).

To explain the reason for a critical thickness, **Figure 3.6** schematically shows a layer of thickness, *t*, containing a small crack of length, *c*, that spreads from the surface to the substrate. The layer has an elastic modulus, Y_f, and a Poisson's ratio, ν_f, and is exposed to a biaxial tensile strain, σ, due to the constrained shrinkage. The compressive stresses within the substrate will be very small when the as-deposited layer is much thinner compared to the substrate. Thus, only the tensile stresses in the layer should be considered. The strain energy accumulated in the layer, per unit volume, is:

$$\frac{\sigma^2(1-\upsilon)}{2Y_f} = \frac{\sigma^2}{2{Y_f}^*}, \tag{3.3}$$

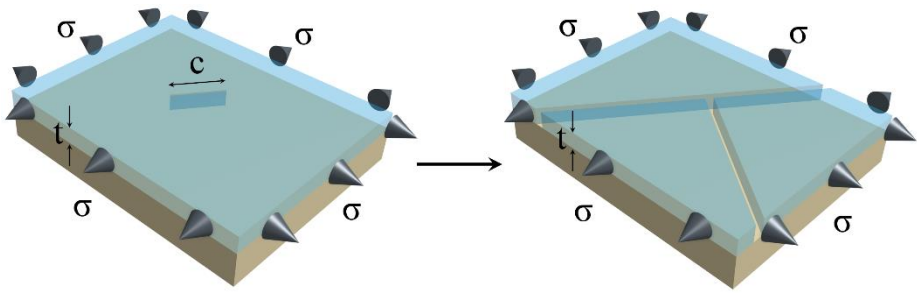

Figure 3.6: Portion of a thin layer of thickness, *t*, bonded to a thicker substrate and containing a crack of length, *c*, which extends along the length of the layer to form a crack pattern with the extension of other cracks (from *Schneller et al., 2013*)

while the strain energy in the layer of area, *S*, containing the small crack of length, *c*, is:

$$\frac{\sigma^2}{2{Y_f}^*}S \times t - \frac{\sigma^2}{2{Y_f}^*}Z \times c \times t^2, \tag{3.4}$$

where $Z \times c \times t^2$ is the volume of material near the crack where strain energy is relaxed as shown in the second term. The energy required to form the crack's surface is $c \times t \times G_c$, where G_c is the energy required to from two crack surfaces per unit area, and $c \times t$ is the area of the crack. So then, the total energy corresponding to the layer cracking is

$$U_t = \frac{\sigma^2}{2{Y_f}^*}S \times t - \frac{\sigma^2}{2{Y_f}^*}Z \times c \times t^2 + c \times t \times G_c. \tag{3.5}$$

According to the concept introduced by A. A. Griffith, a crack can only spread if this process reduces the free energy of the system when $\frac{\partial U_t}{\partial c \partial t} \leq 0$. Supposing that the stress, elastic properties, and strain energy relaxing rate (G_c) are constant of the layer, the only variables are the thickness and crack length. Differentiating the free energy function (Equation 3.5) with respect to the crack length and layer thickness, the coordination for crack spreading does not depend on the crack's length, rather depend on the layer thickness as shown by

$$\frac{\partial U_t}{\partial c \partial t} \leq G_c - Z\frac{\sigma^2}{2{Y_f}^*} \times t. \tag{3.6}$$

Appointing Equation 3.6 equal to zero, we can see the reason for a crack not being able to spread until the layer thickness exceeds a critical value (*Schneller et al., 2013*):

$$t \geq t_c = \frac{G_c {Y_f}^*}{Z\sigma^2}, \tag{3.7}$$

where Z changes with the crack geometry (*Hutchinson & Suo, 1991*). So, crack spreading can be avoided when the film thickness does not exceed a critical value.

For a specific stress (or shrinkage strain), Equation 3.7 reveals that the critical thickness can be increased by increasing the crack resistance of the precursor layer, i.e. by increasing G_c. According to that, brittle precursor gels form their crack pattern during drying when G_c is the smallest. Previously, it was shown that when 10 wt% of an elastomeric polymer was mixed with a precursor solution synthesized using a hybrid alkoxide, the critical thickness could be increased by an order of magnitude in the range of 0.1-1 μm, which is expected due to an increase of G_c by the elastomer (*Roeder & Slamovich, 1999*). However, for a thin film geometry, the most common technique to

increase the layer's thickness is still by building up the thickness with repeating solution coating and pyrolysis steps, avoiding cracking during each deposition.

Principles of Crystallization

Crystallization process implies the formation of a critical nucleus that grow when it spontaneously reduces its free energy (nucleation & growth process) (*Schneller et al., 2013*). The size of the nucleus is defined using the same principle as for crack spreading discussed above. Wherein, the free energy per unit volume ΔG_c, inducing the crystallization, is negative below the melting point, while the growing nucleus add a new interface, and so growth increases the free energy, as the nucleus becomes larger. Consequently, the strain energy arises both within and around the growing nucleus, which increases the free energy. The free energy can be expressed as (*Schneller et al., 2013*):

$$\Delta G = (U_{se} - |\Delta G_c|)\frac{4\pi}{3}r^3 + 4\pi r^2\gamma, \tag{3.8}$$

where U_{se} is the strain energy per unit volume, r is the radius of the nucleus, γ is the surface energy per unite area, and $|\Delta G_c|$ is the absolute value of ΔG_c, which is negative below the melting point. The maximal value ΔG in Equation 3.8 can be determined by its differential with respect to r

$$\frac{\delta \Delta G}{\delta r} = (U_{se} - |\Delta G_c|)4\pi r^2 + 8\pi r\gamma \tag{3.9}$$

By setting Equation 3.9 to zero, the critical nucleus allowing free energy of the system to decrease as it grows is determined as

$$r_c = \frac{2\gamma}{(|\Delta G_c| - U_{se})}. \tag{3.10}$$

Since the difference between the temperature of pyrolysis (200-400 °C) and the melting temperature of the inorganic is very large, $|\Delta G_c|$ will be large as well, and thus, r_c will be very small. Therefore, the crystallization of a connective network of nano-crystallite (< 2 nm) is often observed.

In the mixed compounds such as PZT, the layer can be crystallized in metastable phases, which will form the pyrochlore structure, rather than the stable perovskite structure. At lower temperature range with limited diffusion, the pyrochlore structure is kinetically favourable. As an example, in the study of the PbO-TiO_2 binary system (*Polli et al., 2000*), wherein TiO_2 rich PTO composition was prepared, a large number of metastable phases were formed. When heated to higher temperatures, the metastable pyrochlore phase transformed to the perovskite phase, however retaining its metastable Ti-rich composition. At higher temperatures, the two stable phases, TiO_2 (rutile) and $PbTiO_3$ (perovskite) are formed accompanied with a decrease of free energy during each of the kinetically limited steps.

A polycrystalline layer will undergo grain growth during heating process until the grain size is equivalent to the layer thickness. Once the horizontal grain size overcomes

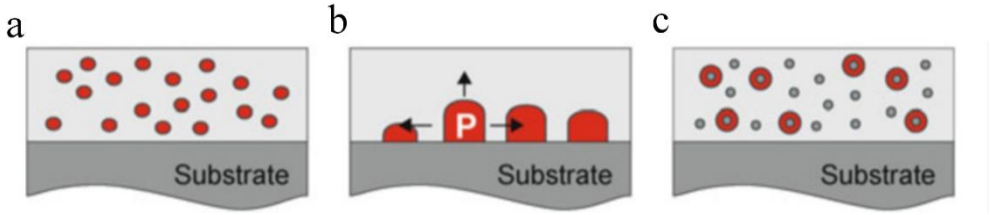

Figure 3.7: Schematic illustration of the different nucleation events which can take place during crystallization of amorphous CSD thin layers. **(a)** Homogeneous nucleation, **(b)** heterogeneous nucleation events at the interface, and **(c)** heterogeneous nucleation events at seeds. From *Schneller et al., 2013*

the layer's thickness, grains with specific orientation will undergo special grain growth due to their lower surface or interfacial energy (*Srolovitz & Safran, 1986*). In other words, these grains will have a lower free energy relative to other grains, and so consume neighbouring grains by grain boundary motion resulting in polycrystalline films with columnar microstructure, which in turn will facilitate the development of at least one preferred orientation.

Crystallization is characterized by a competition between homogeneous nucleation events within the volume of amorphous layer and heterogenous nucleation events at the interfaces (e.g. substrate/layer or layer-atmosphere) or at seeds (foreign particles or intermediate phases) inside the amorphous matrix (*Schneller et al., 2013*). The initial phases of growth starting from an amorphous matrix are shown in **Figures 3.7a-c**. Each of these events has its definitive nucleation and growth rate, and one of them may prevail over the others (*Schwartz et al., 1997; Gust et al., 1994; Sporn et al., 1995*), for more details see Chapter 6. Out-of-plane columnar growth in amorphous layers can be obtained only if the possibility for heterogeneous nucleation at the interface (i.e. substrate/layer) is favoured over other possible nucleation events. In addition, during the crystallization of a starting amorphous matrix a competition between the nucleation of different phases may take place as well, which might affect the crystallization of the targeted phase. The formation of a metastable intermediate phase could take place, which could be advantageous for the subsequent crystallization of the phase with a certain texture at higher temperatures (e.g. crystallization of PZT via the fluorite phase [*Seifert et al., 1995*]). The competition between the nucleation of different phases can be caused by small inhomogeneities of the cation and anion stoichiometry at the nanoscale. Rapid thermal annealing is typically used to avoid the formation of undesirable additional phases before the crystallization of the perovskite phase. This allows to kinetically limit the nucleation of the second phases and limit compositional heterogeneity.

Another critical parameter for the required phase formation as was already mentioned above is the control of the partial pressure of volatile species (such as PbO) during crystallization. This could be a major issue for the fabrication of ferroelectric thin layers since most of the time the thin layers crystallization is carried out not in a sealed environment but rather is a continuous gas stream. Thus, different techniques have been introduced to compensate evaporation of volatile compounds to avoid the

formation of undesired phases during crystallization. For example, an excess of the volatile precursor can be added into solution, or an enriched capping layer can be grown on the as-deposited layer.

Beside the volatility of used compound, the compositional homogeneity, control of grain size and texture (crystal orientation) are very important parameters affection ferroelectric and dielectric properties of the perovskite layers. For instance, the grain size in these layers can be modified by the control of the nucleation events leading to layers morphologies with nanocrystalline or columnar shaped grains. As for the texture control, one of the approaches in controlling the crystallinity is the adjustment of underlying substrate material (lattice mismatch) for the initialization of textured growth.

Therefore, among critical parameters defining the microstructure and crystalline orientation are: (1) Precursor chemistry; (2) Atmosphere; (3) Processing temperature; (4) Heating ramp; (5) Seed layer; (6) Compositional inhomogeneity; and (7) The underlaying substrate lattice misfit.

Experimental Details of PZT Nanotube Arrays Synthesis

Fabrication of the PZT NT arrays using sol-gel deposition inside porous AAO and silica membranes was previously reported by several groups (*Luo et al., 2003*; *Kim et al., 2008*; *Bharadwaja et al., 2006*; *Scott et al., 2008*; *Nonnenmann et al., 2009*; *Bernal et al., 2012*; *Xu et al., 2009*; *Zhigalina et al., 2006*). Typically, after the preparation of a PbZrTi coating solution, wet nanotubes are deposited by a dip impregnation of the solution inside the pores, followed by a formation of crystallized nanotubes using thermal treatment.

The PZT NT arrays preparation using sol-gel deposition is schematically illustrated in **Figure 3.8**. Two commercial AAO membranes, Synkera-1 and Synkera-2, with different porosities P_{AAO} and pore diameters D_{pore} (**Table 3.1**) were used as a porous hosting material for the process development. They feature a thickness of 50 μm, mean D_{pore} of 100 and 150 nm, and an inter-pore distance D_{cell} around 250–300 nm, generating the P_{AAO} ~15 and 35%, respectively. The top view SEM images of the AAO membranes are shown in **Figure 3.3**. Following the preparation of the stochiometric PZT precursor solution (see **Figure 3.5**) using inverse-mixing-order chelate processing (*Li et al., 1998*), the AAO membranes were immersed into the solution for one minute to impregnate the solution into the pores (**Figure 3.8a**). Due to the electrostatic interaction between the positively charged micelles of the initial sol and the membrane of a different charge, the sol particles adsorb to the pore walls (*Mishina et al., 2002*). Then the PZT-coated membrane was drawn up and the excess sol on the faces of the membrane was carefully blotted off with an absorbent paper to remove the wet PZT layer. Next the sol PZT was dried in an oven at 100 °C for 30 minutes to transform it into a gel PZT (**Figure 3.8b**). Finally, the PZT gel was pyrolyzed and crystallized into

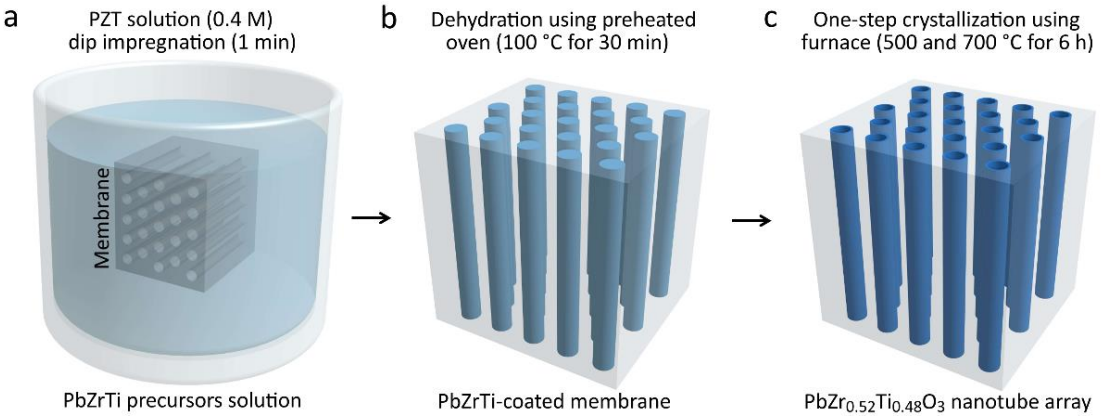

Figure 3.8: Schematic fabrication of the vertically aligned PZT nanotube array: **(a)** PZT solution (0.4 M) dip impregnation into porous AAO membranes **(b)** PZT-coated membrane dehydration (H_2O evaporation) in a preheated oven at 100 °C **(c)** Single-step processing of the PZT^{500} and PZT^{700} nanotube arrays, where the PZT gel layer is heated directly to the crystallization temperature of 500 and 700 °C for 6 hours, respectively, leading to initial evaporation of organics (pyrolysis) at lower temperature (300-400 °C), followed by crystallization at higher temperature (500-700 °C)

the PZT tubular geometry using the one-step crystallization process (**Figure 3.8c**), where the temperature of the PZT crystallization was 500 °C or 700 °C (henceforth referred to as the PZT^{500} and PZT^{700} nanotubes in the
following), the heating time was 6 h and the heating rate was 1.5 °C/min to ensure complete crystallization of the PZT while preventing phase transformation of the amorphous AAO into α-Al_2O_3 (*Sallagoity et al., 2016*). Thermal analysis was conducted to optimize the crystallization process of the PZT phase including the determination of the temperature corresponding to the evaporation of organic residuals (*Sallagoity et al., 2015b*). The PZT NT sidewall thickness was increased by using a multiple dip impregnation, i.e. the sol-gel deposition was repeated three times, while the overall aspect ratio of the nanostructure was kept constant. After each sol-gel deposition, the obtained sol PZT layer was dried at 100 °C for about 30 min and pre-crystallized at 500 °C for 3 hours at 1.5 °C/min heating rate. Finally, after the last PZT layer was deposited the sample was annealed in a furnace at 500 °C or 700 °C for 6 hours at 1.5 °C/min in order to crystallize the gel PZT nanotubes and obtain the perovskite PZT structure. Sol-gel multiple dip impregnation process was previously reported for the PZT nanotubes synthesis. The PZT sidewall thickness ranging from 5 to 25 nm after a few impregnations (*Bernal et al., 2012*; *Han et al., 2012*) could be increased up to 300 nm after 17 dip impregnations (*Bharadwaja et al., 2006*). PZT nanotubes sidewall thickness can also be controlled through other approaches by tuning their experimental parameters: spin-coating technique by changing the spinning rate (*Kim et al., 2008*), electrophoretic deposition duration (*Nourmohammadi et al., 2009*), and sol-gel deposition time at a fixed temperature (*Yourdkhani et al., 2017*).

3.1.3 Third Step of Process: Electrochemical Deposition of $CoFe_2$ Nanowire Arrays

Deposition of $CoFe_2$ nanowire (NW) arrays into the PZT-coated AAO membrane is described in this section. To fabricate the PZT-$CoFe_2$ core-shell nanocable (NC) arrays, a pulsed electrochemical deposition technique was used. It is a flexible, low-cost and scale-up technique which allows to grow polycrystalline FM nanowire arrays with large aspect ratio (a ratio between nanowire's diameter and length) into a porous membrane. The key point in using the AAO membranes instead of polymer membranes is the resistance to high temperatures required for the nanowires oxidation (~600 °C) and the hexagonal ordering of the membrane's pores with a fixed inter-pore distance, which defines the interwire distance and associated dipolar coupling between nanowires.

Understanding Template Approach for Electrodeposition of Metal Nanowire Arrays

A principle of magnetic nanowires electrodeposition is a confinement of metal ions inside the porous AAO membrane during their chemical reduction. The electrodeposition technique implies a conductive path through pores between the electrolyte contacting metal ions and the working electrode at the pore bottoms. The metal ions diluted in the electrolyte are reduced inside the nanopores through the conductive path by injecting an electrical current or a voltage. This low-cost technique has been used for more than 40 years to electrodeposit magnetic nanowires inside porous templates (*Kawai and Ueda, 1975*). The fabrication technique using the electrodeposition of NWs allows to grow the high-density arrays (around 10^8-10^{11} NWs per cm^2). The geometric parameters of the grown nanowires (e.g. diameter, height and inter-wire distance) are identical to the morphological features of the hosting AAO membrane. The templating method can be implemented using three main hosting materials, which are the block copolymer membrane, the polymer membrane, and the aluminium or silicon oxide membrane. For the thermal oxidation of magnetic nanowires, conducted in the present work, the porous AAO membrane is the most suitable among them due to the thermal resistance and the well-ordered hexagonal distribution of the cylindrical pores. The alloy nanowires elemental composition is tuned by varying the electrolyte composition of metal precursors. Typically, a physical vapour deposition is used to deposit conducting layers on one side of the AAO membrane to cover the pores and to serve as a working electrode (cathode) for the electrodeposition of nanowires.

In general, there are two modes of electrodeposition, namely potentiostatic and galvanostatic, which in the first case is conducted by injecting a constant voltage, and in the second case by injecting a constant current. For the homogeneous growth of the nanowires with a narrow distribution of the nanowires height, an electrodeposition in

the pulsed potential mode was used. Typically, the pulsed mode includes two stages: (1) the ions diluted inside the pores are reduced at one voltage pulse during time-on, and (2) a voltage pulse with smaller value during time-off allows the diffusion layer to "recover" from the deposition during the time-on.

Iron deposition occurs always in parallel with hydrogen evolution; the occluded or absorbed hydrogen, giving rise to embrittlement of the deposit, can be partly removed by subsequent annealing processes, though a small fraction of hydrogen tends to remain in the crystal lattice until nearly the melting point (*Gamburg & Zangari, 2011*).

One of the main problems in Fe deposition, especially for magnetic device applications, is the possibility of oxidation of Fe^{2+} to Fe^{3+}, due to oxidation at the anode and/or to reaction with oxygen dissolved in the electrolyte. In combination with the local increase in pH at the cathode due to hydrogen evolution, the presence of Fe^{3+} may lead to the precipitation of Fe(III) hydroxide, which is incorporated in the growing Fe films. The presence of Fe hydroxide results in embrittlement of the coating, decreases the saturation magnetization of the Fe thin layers and affects their magnetic properties by generating defects that hinder domain wall motion (*Gamburg & Zangari, 2011*).

The solutions used for the deposition of Fe-Co, Ni-Fe, and Fe-Co-Ni alloys are slightly acidic (pH ~2–3), and may contain either or both sulfates or chlorides of the various metals. Metal ion concentration is determined in part by the alloy composition sought for, and also by the fact that the Fe group metals exhibit the so-called anomalous codeposition, i.e. the less noble metal in the alloy is deposited preferentially. In order to deposit Permalloy for example the concentration of Ni salt (0.5 M) is kept 50 times larger than the Fe ion concentration (0.01 M). Buffering is needed in order to limit the pH increase at the interface resulting from the hydrogen evolution reaction; this is most often achieved by the use of boric acid (0.4 M) (*Gamburg & Zangari, 2011*).

Additives are used to better control the magnetic properties and to decrease the internal stresses; while many of these additives are proprietary, the most commonly used are saccharin (0.1–1 g/l), sodium lauryl sulfate or sodium dodecyl sulfate or sulfonate (SDS, 0.01–0.5 g/l).

Since Fe, Co and Ni present a similar dissociation behaviour in aqueous solutions, electrolyte preparation follows the same steps described for the preparation of Ni solutions.

Typical electrolyte formulations and process conditions to obtain soft magnetic alloy films with high magnetic moments are given in **Table 3.3**. The choice between metal sulfates or chlorides represents a compromise between deposition rate and stresses; the use of sulfates results in lower stresses but lower deposition rates. SDS and/or saccharin should be added in the concentrations suggested above.

Table 3.3: Summary of electrochemical solution parameters for electrodeposition of metal alloy magnetic thin films (*Gamburg & Zangari, 2011*)

Ni–Fe Permalloy		*Fe–Co–Ni*		*Fe–Co*	
$FeSO_4$ or $FeCl_2$	0.01 mol/l	$FeSO_4$ or $FeCl_2$	0.01–0.02 mol/l	$FeSO_4$ or $FeCl_2$	0.2–0.25 mol/l
$NiSO_4$ or $NiCl_2$	0.50 mol/l	$NiSO_4$ or $NiCl_2$	0.12–0.15 mol/l	$CoSO_4$ or $CoCl_2$	0.1–0.15 mol/l
H_3BO_3	0.4 mol/l	$CoSO_4$ or $CoCl_2$	0.1–0.15 mol/l	H_3BO_3	0.4 mol/l
-	-	H_3BO_3	0.4 mol/l	-	-
-	-	NH_4SO_4 or NH_4Cl	0.3–0.45 mol/l	-	-
pH 2.5–3	-	pH 2.5–3	-	pH 2–2.5	-
CD 4–6 mA/cm^2	-	CD 3–4 mA/cm^2	-	CD 3–5 mA/cm^2	-

CD is a current density

Principles of Electrodeposition of Co_xFe_{1-x} Nanowire Arrays

In his work, the $CoFe_2$ NW arrays were grown using a conventional three-electrode plating using pulsed voltage (AC) configuration, where the ions, dissolved in the electrolyte were reduced on the cathode at the pore base. The $CoFe_2$ NW arrays grew from the bottom working electrode (cathode) in a bottom-up process. Previously several groups reported the fabrication of the Co_xFe_{1-x} NW arrays inside the pores of AAO membranes using pulsed electrochemical deposition. Short summary of the preparation conditions for the reported Co_xFe_{1-x} NW arrays is shown in **Table 3.4**.

Interestingly it was shown that the "selectivity ratio" (SR), which is defined as an atomic ratio of Fe/Co in the deposit compared to the molar ratio of Fe^{2+}/Co^{2+} in the stirred electrolyte solution, obtained in $CoFe_x$ nanowires increased at the more negative potential, but when the $CoFe_x$ nanowire electrodeposition was conducted in the quiescent solution using reverse pulse electrodeposition, the SR value decreased at more negative potential (*Ghemes et al., 2017*).

Table 3.4: A summary of the synthesis studies of vertically aligned Co_xFe_{1-x} nanowire arrays prepared using pulsed electrodeposition technique

x in Co_xFe_{1-x}	Electrolyte composition	pH	Electrodeposition pulse voltage *E* (or current *I*) and pulse time *t*	D_{NW} nm	h_{NW} µm	D_{cell} nm	Ref.
40	$CoSO_4 \cdot 7H_2O$ (52.971 g/l) $FeSO_4 \cdot 7H_2O$ (32.551 g/l) H_3BO_3 (40 g/l) $C_6H_8O_6$ (1 g/l)	3	E_1 = 18/18 V; E_2 = 0 V; t_{off} = 10 - 400 ms	30	2	100	*Ramazani et al., 2014*

A: 40 B: 33	A: $CoSO_4 \cdot 7H_2O$ (17.9 g/l) $FeSO_4 \cdot 7H_2O$ (30 g/l) B: $CoSO_4 \cdot 7H_2O$ (14.32 g/l) $FeSO_4 \cdot 7H_2O$ (30 g/l) H_3BO_3 (10 g/l) $C_6H_8O_6$ (1 g/l)	-	E_1 = -50 V (50 Hz); t_{on} = 1 ms; E_2 = 0 V; t_{off} = 19 ms	A: 40 B: 50	A: 4 B: 8	A: 60 B: 100	*Ji et al., 2014*
27	$CoSO_4 \cdot 7H_2O$ (10 g/l) $FeSO_4 \cdot 7H_2O$ (15.18 g/l) H_3BO_3 (10 g/l) $C_6H_8O_6$ (1 g/l)	-	I_1 = 30 mA; t_{on} = 1 ms; I_2 = 0 mA; t_{off} = 20 ms	A: 27 B: 37	A: 1.2 B: 3.7	-	*Londoño-Calderón et al., 2017*
35	$CoSO_4 \cdot 7H_2O$ (0.1 M) $FeSO_4 \cdot 7H_2O$ (0.2 M) H_3BO_3 (0.3 M) $C_3H_4O_4$ (1 mM) Na-LS (0.3 mM)	3	E_1 = -1.15 V; t_{on} = 2.5 s; E_2 = -0.7 V; t_{off} = 1 s	A: 35 B: 200	20	A: 110 B: 250	*Ghemes et.al., 2017*
31	$CoSO_4 \cdot 7H_2O$ (0.045 M) $FeSO_4 \cdot 7H_2O$ (0.182 M) H_3BO_3 (0.54 M) $C_6H_8O_6$ (0.006 M) NaOH	4	I = 25.5 mA/cm^2; t_{on1} = 8 ms; E = 4.5 V; t_{off} = 1 ms	35	2-8	105	*Elbaile et al., 2012*
50	$CoSO_4 \cdot 7H_2O$ (0.3 M) $FeSO_4 \cdot 7H_2O$ (0.3 M) H_3BO_3 (45 g/l) $C_6H_8O_6$ (1 g/l)	5	E_1 = 18 V; t_{on} = 10 ms; E_2 = 0 V; t_{off} = 20 ms	60, 120	-	250	*Esmaeily et al., 2013*

It was shown that the atomic ratio of Fe/Co in nanowires was a little lower than the one in solution when the electrodeposition was performed at potential E = -50 V during t_{on} = 1 ms and t_{off} = 19 ms (*Ji et al., 2014*). Since Co^{2+} is less electronegative than Fe^{2+}, the deposition rate for Co^{2+} ions is slightly higher compared to Fe^{2+} ions. However, another study showed that in spite of identical concentration of Fe and Co in electrolyte and higher effective thermodynamic concentration or activity of Co^{2+} (-0.28 V) than

Fe^{2+} (-0.44 V) ions, more Fe atoms were obtained using electrodeposition with AC-pulse of 18/18 V reduction/oxidation voltage and various off-time between pulses (10-400 ms) (*Ramazani et al., 2014*), which was explained by a formation of the iron hydroxide ions on the cathode surface preventing deposition of Co atoms.

Description of Thermostatic Electrochemical Cell

All electrochemical procedures conducted in this work, such as anodization and pulsed electrodeposition, were performed using specially designed and fabricated for this purposes setup called "electrochemical cell". The operation principles are similar to the larger counterparts called "electrolytic baths (*Mátefi-Tempfli, 2008*). **Figure 3.9a** shows the schematic design of the electrochemical cell used herein (BSMA-IMCN, UCLouvain manufactured).

As different solutions and temperatures are applied during electrochemical processes, the material that the cell is built of is a Teflon. The setup is equipped with a temperature control system operating in the temperature range of -30–90 °C, consisting of three parts. The bottom part, which is responsible for cooling the hot part of the Peltier element, placed above it, and for stabilizing the temperature equilibrium, is operating using tubes with water circulation. The cold part of the Peltier is facing up to cool the sample placed above. The last part of the thermal system is an electrical resistive heating part, which is connected to a temperature controller and a temperature probe. Large heating rates of the temperature controller are compensated using the Peltier, which further stabilizes the temperature with high precision. The heat load is transferred to the sample, placed above, using a flat copper part, though a thin electrically separating glass.

The main body of the cell is then tightly fixed above the bottom part of the cell using rubbers in order to eliminate the leakage of the electrolyte introduced inside the cell and to isolate the sample's region, which is to be treated. The schematic of the

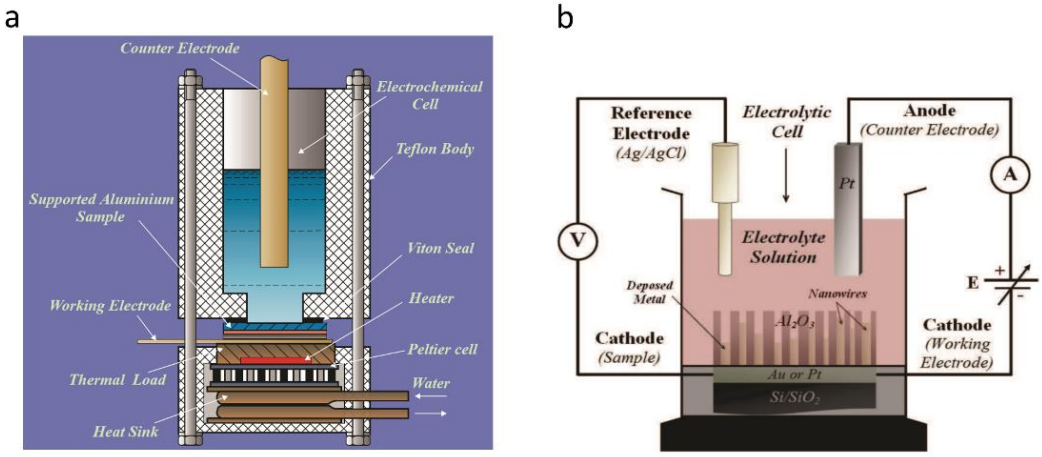

Figure 3.9: (a) The construction diagram of a typical electrolytic cell with temperature controlling features (from *Mátefi-Tempfli, 2008*) **(b)** Schematic of the "3-electrodes" potentiostatic electrochemical deposition setup (from *Antohe, 2012*)

electrodeposition setup (*Antohe, 2012*) is shown in **Figure 3.9b**, which is based on the same electrochemical cell in **Figure 3.9a**. The electrodeposition cell is equipped with two electrodes, one is working electrode, which is a sample contacted through an aluminium foil, and the second one is a counter electrode, which is normally Al or Pt bar immersed inside the solution. Additional reference electrode, used for the electrodeposition, is immersed into the solution as well.

To reduce the cations from the electrolyte onto the working electrode at the pore's bottom, the constant potential (specific value for each material) is applied between the cathode also called working electrode (sample) and the anode also called counter electrode (a Pt foil). To make sure that this potential is constant, and the cations are constantly separated, a PAR 263A Potentiostat/Galvanostat was used in a three-electrode potentiostatic configuration having the additional reference electrode (Ag/AgCl), which controls the potential difference between the anode and cathode (*Darques et al., 2004*). The potential between the reference electrode and the cathode allows to measure the potential changes for the anode-cathode, and subsequently the Potentiostat adjusts the voltage level, through an integrated comparator (*De La Torre Medina, 2009*).

Principles of Electrodeposition of $CoFe_2$ Nanowire Arrays

In the present work, arrays of $CoFe_2$ nanowires were deposited inside PZT-coated self-supported commercial AAO membranes by pulsed potential electrodeposition using a three-electrode potentiostatic setup with a Pt foil acting as counter electrode (see **Figure 3.9a**). The growing process of NW arrays can be easily observed by monitoring time dependence of the cathodic current. **Figure 3.10a** shows the typical effect of cathode potential on the time dependence of cathodic current in the solution containing Co^{2+} and Fe^{2+} ions. At the beginning of electrolysis within several seconds, a sharp increase of cathodic current up to around 1 mA is observed due to the changes in ions concentration in the solution and cathodic reduction for the nucleation of nanowires. The concentration of metal ions in the pores decreases with increasing electrodeposition time, while the ions are moving from the bulk electrolyte into the nanopores, resulting in the rapid decrease of cathodic current up to around 0.85 mA. Then the gradient of ions concentration is equilibrated, thus the current stays relatively stable, and the metallic NWs are growing vertically with constant speed, and when the desired volume of metal was deposited, the deposition was stopped.

The height the nanowires was controlled by changing the deposition time or charge density. The electrochemical reaction taking place when a potential is applied in the electrolyte can be expressed as $A^{z+} + ze^- \rightarrow A$, where A are the metallic ions with charge z, and e^- is the electronic charge. Simultaneously during the metallic ions reduce to the cathode (the sample) inside the pores, an oxidation takes place on the anode $H_2O \rightarrow ½O_2 + 2H^+ + 2e^-$, which provides electrons for the metal reduction process in the

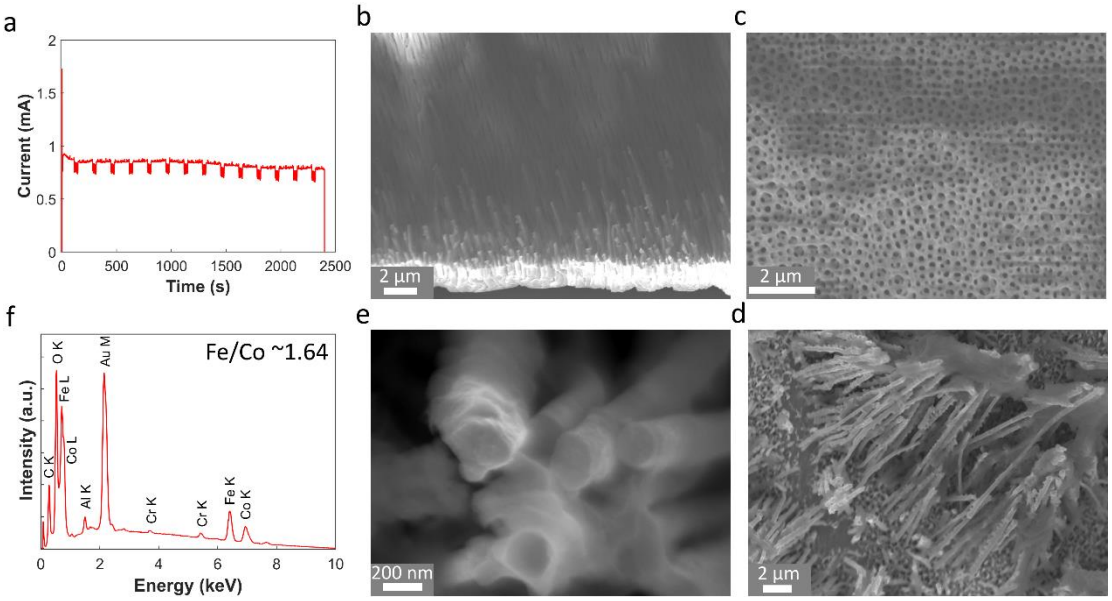

Figure 3.10: (a) Typical cathodic current plot for the electrodeposition of the $CoFe_2$ nanowire arrays shown in **(b,d,e)**; Tilted section **(b)** and top **(c)** views SEM images of the Synkera membranes after electrochemical deposition of the $CoFe_2$ nanowire arrays; **(d,e)** Top view SEM images of the $CoFe_2$ nanowire arrays after alumina membrane's chemical dissolution; **(f)** EDX spectrum for the as-deposited $CoFe_2$ nanowire arrays

pores. The volume of the deposited material or the nanowires height in our case can be monitored by measuring the accumulated charge (Q) during the electrodeposition as

$$Q = z \times F \times N_p \times \frac{V_p}{V_M}, \tag{3.11}$$

where $z = 2$ for the divalent Co^{2+} and Fe^{2+} ions, F is the Faraday constant, V_M is molar volume of Co and Fe, V_p is the volume of the deposited nanowires, and N_p is the number of pores. The nanowire's volume and the pores number are estimated as

$$V_{NW} = L \times D_{NW}^2 \times \frac{\pi}{4}, \tag{3.12}$$

where L is the length of the wires, d_c is effective wire diameter, and

$$N_{NW} = \rho_{pore} \times D_{rub}^2 \times \frac{\pi}{4}, \tag{3.13}$$

where ρ_{pore} is a pores density, and D_{rub} is a diameter of the rubber seal used in the electrochemcial cell, here D_{rub} = 5 mm (*Schonenberger et al., 1997*). Otherwise the nanowire's height can be estimated by measuring the deposition time as

$$Q = \int I dt, \tag{3.14}$$

where I is a deposition current. In other words, by monitoring the deposition time and accumulated charge (the surface area below the current curve), the nanowires height can be measured (*De La Torre Medina, 2009*). **Figure 3.10a** shows the typical plating current as a function of time for the pulsed electrodeposition of the vertically aligned $CoFe_2$ nanowire arrays. **Figure 3.10b** shows the titled section view of the $CoFe_2$ nanowiress inside the Synkera-1 membrane (**Figure 3.10c**) after the electrodeposition.

The electrodeposition duration was ~2400 sec, and the accumulated during the deposition charge Q ~3.5 C. Finally, the AAO membrane was dissolved to obtain the free-standing $CoFe_2$ NW arrays (see **Figures 3.10d,e**). An average elemental composition was provided by the EDX analysis showing a value of the Fe/Co ratio close to 1.64 (see **Figure 3.10f**). In further experiments regarding the PZT-$CoFe_2$ nanocable arrays, the Fe/Co ratio was increased to ~2 by increasing the molar concentration of the Fe concentration in the electrolyte from 0.1 M to 0.14 while maintaining the concentration of the Co precursors at 0.1 M.

Experimental Details of Membrane's Chemical Dissolution

The AAO membrane was dissolved using chemical dissolution process illustrated in **Figure 3.11**. First the alumina membrane containing the $CoFe_2$ NW arrays was glued to the Si substrates using a double-sided conductive carbon tape (**Figure 3.11a**), which was used for a two-fold purpose: (1) to serve as a hydrophobic surface for the chemical etching of the AAO membrane and (2) to keep the $CoFe_2$ nanowires glued to the tape after the hosting membrane chemical dissolution for the SEM and EDX analysis. Then a drop of 1 M NaOH solution was placed on the top surface of the AAO membrane at room temperature and kept during 10 minutes (**Figure 3.11b**), where the hydrophobic carbon tape placed below restricted the drop's casting over the whole service and kept it on top of the membrane. Next the drop of sodium hydroxide was resorbed and water drops were used to wash away the dissolved membrane (**Figure 3.11c**). Finally, the specimen was dried in an oven heated to ~45 °C for 30 min (**Figure 3.11d**). The above procedure was repeated several times. The top view SEM images on the $CoFe_2$ nanowires glued to the carbon tape after the AAO membrane dissolution is shown in **Figure 3.10d**.

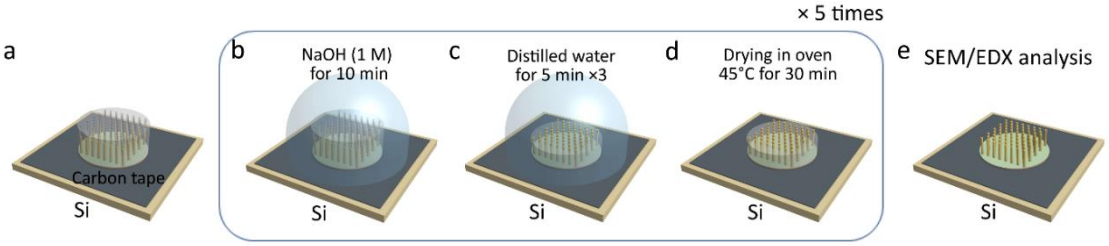

Figure 3.11: Illustration of the alumina membrane chemical dissolution procedure. **(a)** Alumina membrane containing electrodeposited $CoFe_2$ nanowires arrays was glued to conductive carbon tape pasted on Si substrates; **(b)** A drop of 1 M NaOH solution was placed on top of the AAO membrane for 10 min, and then resorbed with pipette; **(c)** Three drops of H_2O were placed on top of the membrane to for 5 min to wash the sample; **(d)** The alumina membrane was placed in a pre-heated oven at 45 °C for 30 min to dry water; **(e)** The whole procedure was repeated several times, and then the $CoFe_2$ nanopillars were analysed by SEM and EDX

Experimental Details of Electrodeposition of $CoFe_2$ Nanowire Arrays into PZT-Coated AAO Membranes

The $CoFe_2$ NW arrays were grown into the PZT-coated commercial AAO membranes using the pulsed potentiostatic electrodeposition method. The geometric parameters of the commercial Synkera AAO membranes were summarized in **Table 3.1**.
One surface of the PZT-coated AAO membrane was metallized using e-beam thermal evaporation to cover the pores and form a continuous cathode (*Bhushan, 2004*). Typically, the metal to be deposited is placed in a crucible and heated up using an electronic beam to a temperature at which evaporation takes place. The deposition rate is usually high, although step coverage is relatively poor but sufficient. The process starts by an e-beam evaporation of a thick Au layer (~2 µm) on one side the membrane with deposition rate around 0.5 nm/sec. The chamber pressure is typically set to around 10^{-7} mbar. A thin adhesive Cr layer (~50 nm) was deposited between the membrane and Au layer to serve as an adhesive layer. Then, the $CoFe_2$ nanowires were electrodeposited at ambient temperature from a single deionized water (VWR Chemicals, France) based electrolyte containing 0.1 M cobalt(II) sulfate heptahydrate $CoSO_4 \cdot 7H_2O$ (98%, Alfa Aesar, Karlsruhe, Germany), 0.14 M iron(II) sulfate heptahydrate $FeSO_4 \cdot 7H_2O$ (Merck, Darmstadt, Germany) and 0.16 M boric acid H_3BO_3 (99.5%, Sigma-Aldrich, St. Louis, MO) in a standard three-electrode potentiostatic configuration using a PAR 263A Potentiostat/Galvanostat and a Pt foil as a counter electrode. The electrodeposition process parameters are summarized in **Table 3. 5**.

Table 3.5. Pulsed electrodeposition process parameters and geometric parameters of the as-deposited $CoFe_2$ nanowire arrays within thick AAO commercial templates with thickness of ~50 µm

Sample	Electrolyte composition	pH	Electrodeposition pulse voltage E (or current I) and pulse time t	D_{NW} (nm)	h_{NW} (µm)	D_{cell} (nm)
$CoFe_2$	$CoSO_4 \cdot 7H_2O$ (0.1 M) $FeSO_4 \cdot 7H_2O$ (0.14 M) H_3BO_3 (0.16 M)	3	E_1 = -1.5 V; t_{on} = 20 ms E_2 = -0.5 V; t_{off} = 80 ms	A: 100 B: 150	10	240

D_{NW} is a nanowire diameter
h_{NW} is a nanowire arrays height
D_{cell} is a cell size of AAO membrane or inter-wire distance

The operated potential stepped from - 1.5 V during 20 milliseconds and -0.5 V during 80 milliseconds versus an Ag/AgCl reference electrode (KCl saturated). The plating current was recorded as a function of time and the electrodeposition process was stopped before filling the pores of AAO membrane to preserve the one-dimensional $CoFe_2$ nanowires taking into account the volume expansion along the pore axis during

the metal oxidation step, which follows after the electrodeposition. The height of the electrodeposited $CoFe_2$ nanowires h_{NW} was limited to ~10 μm.

3.1.4 Forth Step of Process: Thermal Oxidation of $CoFe_2$ Nanowires Arrays inside PZT Nanotube Arrays

In this section, the oxidation process of the metal $CoFe_2$ NW arrays inside PZT nanotubes, grown using the pulsed electrodeposition within the nanopores of AAO membranes is discussed.

Difficulties of $CoFe_2$ Nanowires Thermal Oxidation

The major advantage of the templated electrodeposition technique is that the relatively robust metallic 1D nanostructures can be transformed into spinel metal oxide using thermal annealing at temperatures up to 1000 °C (*Mallet et al., 2005*). Previously it was shown that the minimal temperature sufficient for the transformation of the $CoFe_2$ film into the spinel $CoFe_2O_4$ film is around 650 °C (*Engin & Fitzgerald, 1973*).

The critical issue for the thermal oxidation of the $CoFe_2$ phase into the $CoFe_2O_4$ phase is the stability of alumina templates at relatively high temperatures (above 600 °C). An alumina masks showed good stability when the synthesis of the $CoFe_2O_4$ nanodot and PZT nanotube arrays was conducted using pulsed laser deposition through those alumina masks at T ~550 – 650 °C (*Gao et al., 2009*; *Lee et al., 2008*). However, when the deposited materials were oxidized inside the alumina templates using thermal annealing the process was not so stable. For instance, the annealing of the Fe NW arrays, encased in the alumina matrix, at T_{ann} ≥600 °C resulted in some fading of the black colour of alumina, and these changes intensified with further increase of T_{ann}. A typical Mössbauer spectrum of the NW arrays with nanowires diameter 30 nm after annealing at 600 °C revealed the complete transformation of the FM Fe into two components, i.e. $FeAl_2O_4$ and $(Fe_xAl_{1-x})_2O_3$ (*Jagminas et al., 2009*).

Interdiffusion effects during thermal treatment inside commercial AAO membranes were also pointed out for AAO/PZT nanotube arrays (*Sallagoity et al., 2016*), wherein the partially crystallized Al-rich interphase was formed under crystallization conditions at 700 °C for 6 h, which was identified by the tubular double-shell mixture of Al-rich interphase at the outer surface and pure PZT inside. Whereas, the PZT structures crystallized at lower temperature of 500 °C showed thinner walls and presented flatter and more uniform surface after the AAO wet etching, and EDX analysis showed that the residual AAO was entirely removed and the formation of Al-rich interphase was prevented. In addition, it was demonstrated that the $CoFe_2$ nanowire arrays can be effectively transferred into CFO phase via their thermal treatment at 500 °C inside PZT nanotubes forming PZT-CFO core-shell multiferroic nanostructures with both

improved morphology and structural characteristics as compared to PZT-$CoFe_2$ nanostructures oxidized at 600 °C.

Other reports are in agreement with these results, where it was also demonstrated that during heat treatment of the PZT nanotubes inside AAO membranes the Pb and Ti mobility and their incorporation into AAO took place leading to the formation of a lead aluminate/aluminum titanate phase (*Han et al., 2012*). The percentage of the lead aluminate/aluminium titanate increased greatly by ~30% when annealing temperature was raised from 700 to 750 °C, while the percentage of the perovskite PZT decreased as a result of a higher percentage of lead aluminate/aluminium titanate in the PZT nanotubes, consistent with observed increase in the wt. % of Al.

Experimental Details of $CoFe_2$ Nanowires Thermal Oxidation

The Au(2-μm)/Cr(50-nm) bilayer electrode used for the electrodeposition was chemically etched following the procedure shown in **Figure 3.12**. The AAO membrane containing PZT-$CoFe_2$ nanocables was placed on the flat Teflon part with the Au/Cr electrode looking upwards (**Figure 3.12**). Then a drop of aqueous KI/I_2 solution (KI: 100 g/l and I_2: 25 g/l in H_2O) was put on the top of the membrane covering the entire surface of Au electrode for 10 minutes (**Figure 3.12a**). The sample was washed three times with distilled water and dried in an oven at T ~45 °C for 30 minutes (**Figure 3.12b,c**). After the procedure was repeated 5 times, a drop of Cr etchant (Sigma Aldrich Co.) was put on the exposed Cr layer for 30 min (**Figure 3.12d**). The sample was washed with distilled water again and finally the membrane was dried in air (**Figure 3.12e,f**). **Figures 3.12g,h** show the top view SEM image of the alumina membrane after the partial **(g)** and full **(h)** electrode etching procedures. Two regions on the membrane's surface can be distinguished in **Figure 3.12g**, one region with an unetched Au layer on the left side of the image, and the second region with fully etched electrode and exposed AAO membrane on the right side.

In situ thermal oxidation of the PZT-$CoFe_2$ NC arrays was performed using a procedure schematically shown in **Figure 3.13**. The PZT-$CoFe_2$ NC arrays were exposed to a thermal heating process at 500 or 600 °C for 24 hours at 2 °C/min heating rate (henceforth referred to as the PZT-CFO^{500} and PZT-CFO^{600} nanocables in the following) to transform the metal $CoFe_2$ nanowires into the insulating metal oxide CFO phase (**Figure 3.13c**). Next, to perform SEM and EDX analyses of the PZT-CFO nanocables the AAO membranes was dissolved using chemical dissolution process shown in **Figure 3.11**.

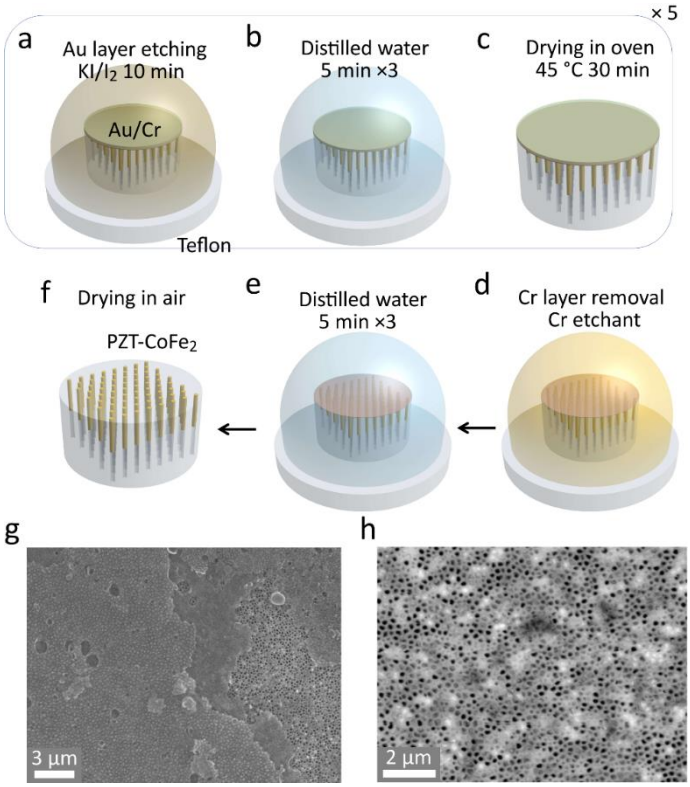

Figure 3.12: Flow chart of the alumina membrane working electrode chemical etching process. **(a)** Alumina membranes hosting PZT-$CoFe_2$ nanocable arrays was placed on clean, flat Teflon part in a way that the bilayer Au/Cr is facing upwards; and a drop of KI/I_2 solution was placed on top of the electrode covering the whole layer surface for 10 min to etch Au layer, and subsequently resorbed via a pipette; **(b)** Drop of distilled water was placed on the electrode for 5 min three times to clean the surface; **(c)** the membranes were dried in a pre-heated at 45 °C oven for 30 min; **(d,e)** Similar procedure as **(a-c)** was reproduced but replacing the KI/I_2 solution with commercial chromium etchant to remove Cr adhesive layer; **(g,h)** Top view SEM images of the alumina membrane's surface after electrode etching procedure with two distinctive regions of partially **(g)** and fully etched regions **(h)**.

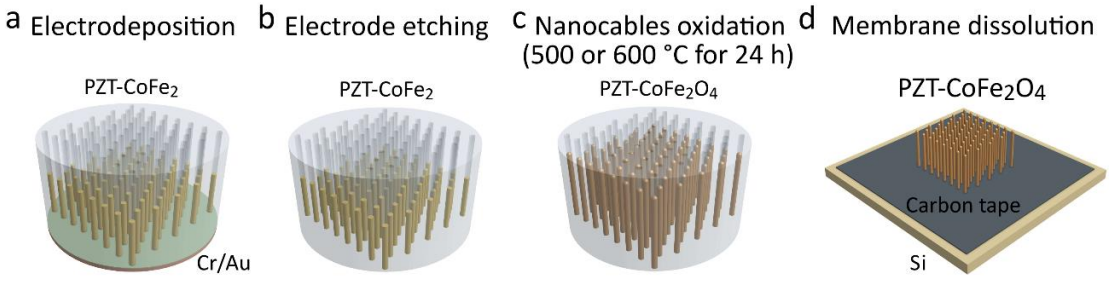

Figure 3.13 Vertically aligned PZT-CFO nanocable arrays fabrication using thermal oxidation of PZT-$CoFe_2$ nanocables. **(a)** Pulsed electrodeposition of PZT-$CoFe_2$ nanocable arrays inside porous alumina membrane, **(b)** Bilayer Cr/Au (10nm/2µm) electrode chemical etching process (see **Figure 3.12**), **(c)** PZT-CFO^{500} and PZT-CFO^{600} nanocable arrays formation using in-situ thermal annealing of the electrodeposited PZT-$CoFe_2$ nanocable arrays inside alumina membrane at 500 or 600 °C for 24 hours, respectively **(d)** Alumina membranes attaching on the SiO_2/Si wafer using conductive carbon tape, followed by the membrane's dissolution process (see **Figure 3.11**)

3.2 Preparation of (1-3) Vertically Aligned Magnetoelectric System

Vertically aligned (1-3) magnetoelectric system is based on the free-standing FM nanopillar arrays. The (1-3) type nanocomposites were fabricated using as-prepared AAO/Pt/Si templates with AAO thickness of ~1.3 μm implying magnetron sputter deposition of Al layer, formation of porous AAO nanostructures via anodization and chemical widening processes. The close-packed array of the vertically aligned $CoFe_2$ FM nanopillars was produced by an electrochemical deposition within nanopores of the supported AAO template, following a slightly modified protocol as previously reported (*Mátéfi-Tempfli et al., 2009a*; *Mátéfi-Tempfli et al., 2009b*). The $CoFe_2O_4$ FM nanopillar arrays were obtained using thermal oxidation of the deposited $CoFe_2$ nanopillars after the removal of the AAO template. The $Ba_{0.7}Sr_{0.3}TiO_3$ and $BaTiO_3$ FE layers were deposited on the metal $CoFe_2$ nanopillar arrays using a rf magnetron sputter deposition and the $PbZr_{0.52}Ti_{048}O_3$ FE layer was deposited on the insulator metal oxide CFO nanopillar arrays using a sol-gel dip coating deposition.

A general fabrication process of the (1-3) magnetoelectric nanopillar system in 5 or 6 steps is illustrated in **Figure 3.14**. In the 1st processing step, commercial bulk Si wafers were used as substrates. A conductive Pt layer was deposited on the entire Si substrate to serve as an electrode with high conductivity for the electrodeposition of FM nanopillars and for the physical measurements of the nanopillar based magnetoelectric systems. It does not oxidize in air or under electrochemical conditions, and it prevents nanopillars contamination via diffusion during the subsequent thermal

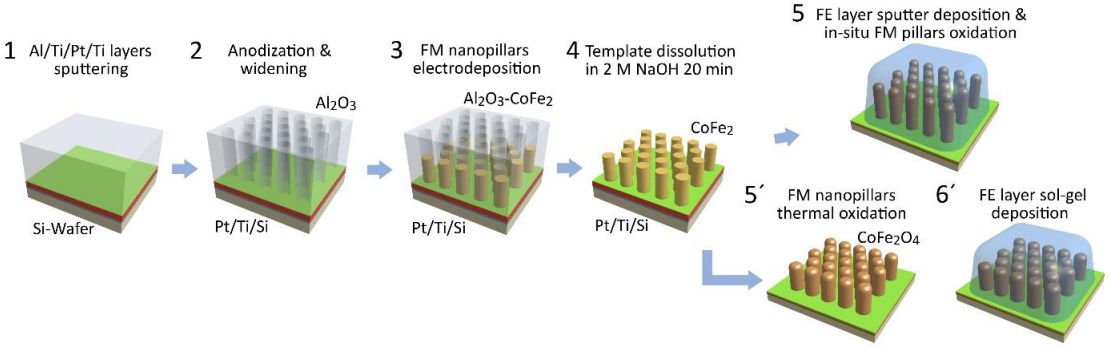

Figure 3.14: Schematic fabrication of the vertically aligned magnetoelectric nanocomposites based of ferromagnetic $CoFe_2O_4$ nanopillars. **(1)** Sputter deposition of the Al/Ti/Pt/Ti multilayer (~1 μm/5nm/50nm/5nm) on the SiO_2/Si wafer; **(2)** Top Al/Ti bilayer anodization & widening process to form porous AAO template on the Pt/Ti/SiO_2/Si substrate; **(3)** Pulsed electrodeposition growth of $CoFe_2$ nanopillar array; **(4)** Chemical dissolution of the hosting AAO template; **(5)** RF magnetron sputtering of the $Ba_{0.7}Sr_{0.3}TiO_3$ or the $BaTiO_3$ matrix layer on the $CoFe_2$ nanopillar arrays, which are simultaneously in-situ oxidized into $CoFe_2O_4$ phase; **(5')** Thermal oxidation of the free-standing $CoFe_2$ nanopillar array in a furnace; **(6')** Sol-gel dip coating deposition of the $PbZr_{0.52}Ti_{0.48}O_3$ matrix layer on the $CoFe_2O_4$ nanopillar array

treatment. A thick Al layer was sputtered on top of the Pt electrode using an adhesive Ti inter-layer. In the 2nd step, the Al layer was oxidized into the AAO template using an electrochemical anodization technique leading to the self-organization of the pores. In the 3rd step, the porous AAO template was filled with the metal $CoFe_2$ nanopillars using a pulsed electrodeposition technique. In the 4th step, the hosting AAO template was removed using a chemical dissolution leading to the free-standing $CoFe_2$ nanopillar array. In the 5th step, the BSTO and BTO FE layers were sputtered onto the $CoFe_2$ nanopillar arrays. In the 5' step, the $CoFe_2$ nanopillar arrays were transformed into the insulating CFO nanopillars using thermal annealing. Finally, in the 6' step the PZT FE layer was deposited on the CFO nanopillar arrays using a sol-gel deposition technique.

3.2.1 First Step of Process: Substrate Preparation

One of the most widely used material in the semiconductor industry is Si. It can be used for different nanostructured devices such as transistor due to its electronic properties, tunable resistivity, and good availability in different sizes and shapes on the market. It is suitable for fabrication of devices, as it is smooth, flat, low-cost, and compatible with most of the microfabrication machines. After cutting Si into wafers, the surface is aligned in one of crystal orientations, which makes easier cutting it into smaller individual chips ("dies") by slightly incising them along cleavage planes. Therefore, for future device production, reproducibility and integration into other devices, the fabrication of the (1-3) vertically aligned magnetoelectric systems was done using Si wafer as a substrate.

Commercial Si wafers p-doped with boron had a round shape with the diameter of 100 mm, thickness of 525 μm, and crystal orientation <100> (Siegert Wafer GmbH, Germany). It had a relatively low resistivity of <0.005 Ohm/cm, necessary for the following electrochemical experiments conducted on the Al/Ti/Pt/Ti multilayers grown on the Si wafers.

Principles of Metal Films Deposition

The first step of the process is a deposition of a conductive Al/Ti/Pt/Ti multilayer on Si wafers. The metallization of smooth and flat surfaces with thin metallic layers is typically conducted using a physical (PVD) or a chemical (CVD) vapor deposition techniques as they allow to grow high quality films with good thickness control. The PVD techniques including sputtering, evaporation, and molecular beam epitaxy (MBE) are conducted using argon plasma or electron beam to sputter the required material from the metal or oxide target to the wafer. Since no other chemical is used in PVD, the contamination from carbon, hydrogen and chlorine is much lower compared to CVD techniques or atomic layer deposition (ALD).

The 4-inch Si wafer was directly put into a deposition chamber to avoid any contamination with dust or chemicals, then the wafer was metallized using magnetron sputter deposition (Plassys MP500S) to obtain lower deposition rate and better adherence between the layers. The magnetron sputtering is a deposition of particles whose origin is from the target's surface being sputtered using ions of a gaseous material accelerated in an electric field or radio frequency (RF) magnetic field, that is direct current (*dc*) and RF magnetron sputtering (*Mattox, 1998*). Herein the targets are bombarded using argon ions (Ar^+) produced in a DC or RF fields. Another advantage of sputtering is a possibility of depositing different materials from different target simultaneously or sequentially to fabricate alloys or multi-layers.

The Pt conducting layer was used for a three-fold purpose: (1) to serve as an anodization barrier during the oxidation of Al layer; (2) to serve as a bottom working electrode for anodization, electrodeposition of nanopillars, and physical measurements; (3) to prevent nanopillar contamination via diffusion during the subsequent thermal treatment. Ti layers were used for a two-fold purpose: (1) to improve the adherence between the Si substrate and the Pt and Al layers thus preventing alumina template detaching during the anodization process; (2) to serve as an oxidation barrier during the anodization.

Experimental Details of Al/Ti/Pt/Ti Multilayer Sputter Deposition

The deposition process of the Al/Ti/Pt/Ti multi-layer is summarized in **Table 3.6**. Firstly, the Si wafer was cleaned using RF magnetron sputtering at 80 W during one minute, followed by a surface ionization and activation process using soft plasma etching at 60 W for 30 seconds to provide a better attachment to the substrate of the 1st layer of Ti atoms. Next, the 5-nm-thick Ti adhesive layer was sputtered using a *dc* of 0.1 A during 2 minutes at the Ar gas pressure of 10 mT (~50 sccm). Then, the 50-nm-thick Pt layer was sputtered at a *dc* of 0.5 A for 5 minutes at the same Ar gas pressure. The 2nd Ti adhesive layer was sputtered. Finally, the ultra-compact 1-μm-thick Al layer was

Table 3.6: Al/Ti/Pt/Ti multilayer sputter deposition parameters

Steps	Thickness (nm)	Power (RF) & current (*dc*)	Duration, seconds	Ar pressure, mT	*T*, °C
Wafer cleaning	-	RF: 80 W	60	5	15
Surface activation	-	RF: 60 W	30	5	15
Ti layer	5	DC: 1A/0.1A	30/120	10	15
Pt layer	50	DC: 0.5A/0.1A	30/300	10	15
Ti layer	5	DC: 1A/0.1A	30/120	10	15
Al layer	1000	DC: 2 A/1.5A	30/600	10	3

deposited at *dc* of 1.5 A during 10 minutes at the same Ar gas pressure but at lower temperature of 3 °C. To obtain the compact Al layer without hillocks and pits, the substrate temperature and deposition rate have to be carefully adjusted (*Mattsson et al., 1991*). The resulting Al layer was compact up to the thickness of around 1 μm when sputtering was carried at lower substrate temperatures ~3 °C with the deposition rate ~100 nm/min (*Vlad, 2009*).

3.2.2 Second Step of Process: Preparation of Porous Anodic Aluminium Oxide Templates

Principles of Anodization Process

Generally, the anodization of the supported Al layer was carried out using similar protocol as used for anodization of Al foils in sulfuric, oxalic and phosphoric acids. The anodization setup was based on the electrochemical cell shown in **Figure 3.9a**, which was used for the pulsed electrodeposition of $CoFe_2$ NW arrays. The Al bar served as a cathode (counter electrode), the supported Al layer served as an anode (working electrode) and the electrolyte was a solution of oxalic acid (**Figure 3.15a**).

The application of the anodic potential between two electrodes to the aluminium layer (anodization) immersed in the acidic electrolyte (pH < 6) results in the growth of the porous aluminium oxide (AAO) with either ordered or disordered cellular structure (*O'Sullivan & Wood, 1970*) and the reaction taking place during the anodization $2Al+3H_2O \rightarrow Al_2O_3+3H_2$. The formation process consists of several stages, which can be easily identified by measuring the dependence of the voltage (or current) on time (see **Figure 3.15b**).

Five stages of the development of porous structure and the schematic diagram of the kinetics of porous oxide growth on the suported Al layer in potentiostatic regime are shown in **Figures 3.15c,d**. In the first stage, immediately after switching on the voltage a barrier oxide layer starts to grow producing a fast and sharp decrease of the current, very high current in the beginning identifies short-circuting of the anode (sample) with the cathode through electrolyte. Then in the second stage, relatively fine featured pathways are revealed in the outer regions of the barrier oxide prior to any true pore formation, this process featured by an irregular barrier-layer thickening and the distribution of current during pore initiation in the pore-forming electrolytes. Next, in the third stage, further anodizing results in the propagation of individual paths through the barrier oxide with their heads becoming enlarged due to the oxide dissolutin of paths and the formation of a new barrier oxide leading to the gradually increasing current. In the forth stage, a competitive equilibrium between the two chemical reactions takes place, and a steady state pore structure is formed by closely packed cylindrical cells, where each cell contains a pore at the center, and it is separated from

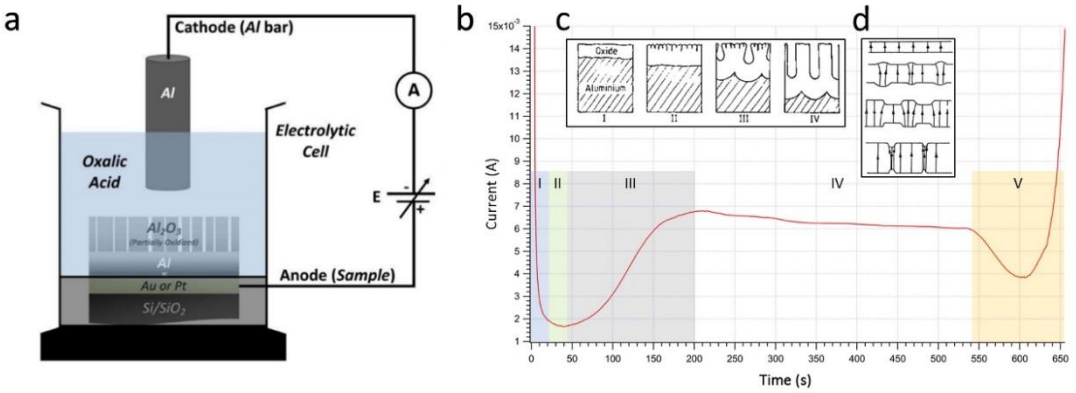

Figure 3.15: (a) Anodization setup integrated into the electrolytic cell shown in **Figure 3.7a** (from *Antohe, 2012*), **(b)** Typical anodization current curve for a complete oxidation in oxalic acid of an Al(1µm)/Ti(5nm) bilayer at 60 V. **(c,d)** Five current stages can be noticed during the anodization process, leading to an alumina thickness around 1.3 µm (from *Parkhutik & Shershulsky, 1992*; *O'Sullivan & Wood, 1970*)

the conductive Pt layer by a layer of scalloped hemispherical barrier oxide. Finally, in the fifth stage, the process reaches the Ti inter-layer, where the same 4-stage anodization process takes place but at lower oxidation rate compared to the anodization of Al layer, which ensures a nice distribution of the AAO pores reaching the conductive Pt layer, featured by gradual increase of the current.

The mechanism of the pore nucleation, growth and self-organization was reported previously (*O'Sullivan and Wood, 1970*) (**Figure 3.15c**). In this paragraph this process will be reviewed only briefly. Once the anodic potential is applied to the Al film, the non-uniform thickening of the barrier layer takes place at constant current density. The "nuclei" or spots of thicker oxide (a few tens of nm in diameter) increase in number and size until they finally merge, leaving thin areas of oxide between them. **Figure 3.15d** shows the non-uniform current distribution during this process, with initial concentration at the thickening regions but eventual concentrations at the thin areas which are the precursors of the future steady-state pores. With anodic potential increasing, the pore and cell diameters increase, and a smaller number of major pores grow. The local thickening could be due to easier ions penetration into the Al film at the defects.

The pore dissolution process happening at the pore tips in the oxide/electrolyte interface under applied voltage as explained in **Figure 3.16** (*O'Sullivan and Wood, 1970*). The dissolution of the ionic Al_2O_3 requires the breaking of Al-O bonds, which can be facilitated by two processes, hydrogen bonding of the outer regions of the barrier layer weakening inter-ionic bonding and the electric field across the oxide-electrolyte interface at the pore base. **Figure 3.16a** shows the oxide before the voltage is applied as a simple NaCl structure. The voltage effectively polarizes the oxide bonds (**Figure 3.16b**) and at the barrier layer surface the Al-O bonds increase in length, as the field is pulling the O^{2-} ions into the oxide and pushing the Al^{3+} ions into the electrolyte solution.

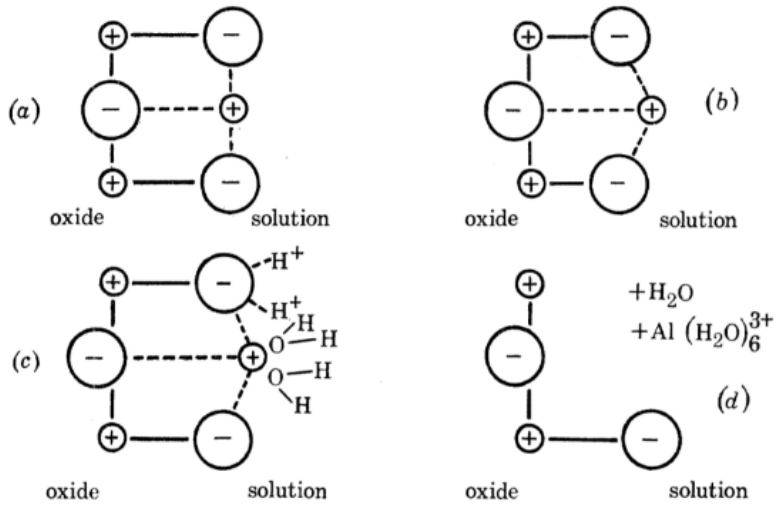

Figure 3.16: Schematic representation of the field-assisted dissolution of Al_2O_3 **(a)** before polarization, **(b)** after polarization, **(c)** removal of Al^{3+} and O^{2-} ions, and **(d)** the remaining oxide (from *O'Sullivan and Wood, 1970*)

Solvation of Al^{3+} ions by water molecules via the activated complex, and the removal of O^{2-} ions by H_3O^+ ions, giving water, are facilitated (see **Figures 3.16c,d**).

In the beginning of the anodization, the nanopores are relatively disordered, however for longer anodization the nanopores tend to merge and form the defect-free domains with hexagonal distribution of cells (*Masuda and Fukuda, 1995*; *Li et al., 1998b*). To increase the size of those domains, a two-step anodization technique is typically used (*Jessensky et al., 1998*). In the first anodization step the Al foil is partially anodized to ensure the "bad" irregular pores merge and self-organize into hexagonal arrangement. The disordered AAO layer is removed by electropolishing or chemical etching leaving the regular hexagonal domain pattern of the shallow pitches on the Al surface, then the second step of anodization is conducted until the entire Al foil is oxidized. High degree of pores ordering, and regularity was achieved using two-step anodization process, although generally only for the thicker Al layer such as foils (*Mátéfi-Tempfli et al., 2009*; *Jessensky et al., 1998*; *Li et al., 1998b*), and just recently even for supported Al thin layers with thickness < 2 μm, a four-step anodization technique was used to improve the nanopores arrangement at a low anodization rate ensured by using a low voltage of 40 V (*Son et al., 2013*).

To explain the self-organization process using only a model (*O'Sullivan and Wood, 1970*) based on the field distribution, used to explain the pore propagation and barrier layer formation, is not enough. The hexagonal arrangement of the neighbouring pores was explained by the repulsive interaction between the pores (*Jessensky et al., 1998*). To explain the pores self-organization process happening during the stage IV in **Figure 3.15c**, a steady-state pores growth was considered (see **Figure 3.17**). As was explained previously (**Figures 3.15c,d)** the pores penetrate inside the Al layer with balanced oxide dissolution at the oxide/electrolyte interface and oxide growth at the metal/oxide interface (*Parkhutik et al., 1992*; *O'Sullivan and Wood, 1970*). The oxidation is caused

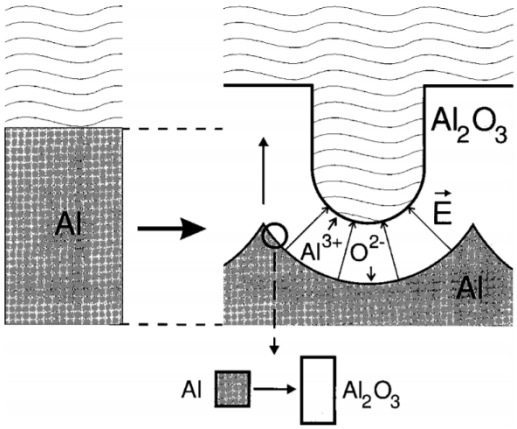

Figure 3.17: Expansion of the alumina during anodic oxidation. On the left the level of the unoxidized metal surface is depicted, reproduced (from *Jessensky et al., 1998*)

by the migration of oxygen containing ions (O^{2-}/OH^-) from the electrolyte through the oxide layer at the pore base, and the Al^{3+} ions are moving in the opposite direction through the oxide layer into the electrolyte at the oxide/electrolyte interface. The injection of Al^{3+} ions into the solution is a prerequisite for the porous oxide formation, thus the atomic density of aluminium in oxide layer is two times lower than in the prior to anodization Al layer. Therefore, the expansion during the oxidation process at the metal/oxide interface could result in the mechanical stress, which leads to forces between neighbouring pores. Since the oxidation occurs at the entire pore bottom simultaneously, the material can only expand in one direction, thus the pore walls are pushed upwards. Normally the anodized layer expands less than two times compared to the original Al volume, which is explained by the mobility of Al^{3+} ions in the oxide under applied voltage, thus partly the oxidized Al does not contribute to the oxide formation. No oxide formation takes place at the oxide/electrolyte interface during porous oxide growth but all cations reaching the interface are ejected into the electrolyte, this observation can be explained by a variation of the relative transport numbers of Al^{3+} and (O^{2-}/OH^-) ions with voltage and electrolyte composition. For the 0.3 M oxalic acid electrolyte the anodization was performed at 30, 40 and 60 V. Moderate voltages of 30 and 40 V showed a higher degree of the hexagonal ordering of cylindrical pores, which authors associated with a moderate expansion of the aluminium during oxidation. With volume contraction or strong expansion during oxide formation, no ordered structures can be achieved. While in the case of contraction no repulsive forces between the pores are expected, large volume expansion may result in structural defects in the alumina and irregular pore's growth. A large volume expansion is also associated with high anodizing voltages and growth rates and therefore with reduced interaction between the neighbouring pores. The AAO templates prepared in different electrolytes using two-step anodization technique shows the best pore ordering when the volume expansion is ~1.2-1.4 times and has porosity around ~10-20% (*Jessensky et al., 1998*; *Li et al., 1998b*).

Beside the two-step anodization technique there are other techniques used to pattern the Al top surface before anodization such as imprint lithography (*Masuda et al., 1997a*; *Choi et al., 2003*), focused ion-beam lithography (*Peng et al., 2005*; *Robinson et al., 2007*; *Liu et al., 2003*), photoresist patterning, interference/holographic lithography (*Sun et al., 2002*; *Krishnan et al., 2007*), pattern transfer using nano-sphere lithography (*Fournier-Bidoz et al., 2004*; *Kim et al., 2007*), and pattern transfer via Al deposition on the nano-structured substrates (*Nishio et al., 2008*). Small pitches on the surface of Al serve as nanopores nucleation spots in the following anodization.

After the anodization process is complete, the pores diameter D_{pore} can be radially enlarged, pore walls smoothed, and barrier oxide layer dissolved (alumina layer between pore base and bottom electrode) using a chemical widening process. Previously, the pores widening by chemical dissolution was found to depend quadratically or linearly on the time that the AAO membrane is immersed in the bath (*AlMawlawi et al., 1991*; *Takahashi & Nagayama, 1978*). The pores widening process via chemical etching with controlled widening time is a very powerful technique that enables the simultaneous barrier layer dissolution, smoothing of pore walls and tuning of pore diameters.

Control of Geometric Parameters of AAO Template

The thickness of the anodized layer increases linearly with increasing anodization time and temperature, and the alumina growth rate is proportional to the anodization voltage (*Sun et al., 2010*; *Ohgai et al., 2004*; *Lee et al., 2007*). The anodization time also controls the pores depth. The dependence of the barrier-layer thickness on voltage shows linear increase with a slop of ~1.04 nm/V when Al is immersed in a 0.4 M phosphoric acid and anodized for 1 h at 25 °C (*O'Sullivan and Wood, 1970*) but it can vary slightly by changing the anodization conditions and electrolyte. The cell size D_{cell} or inter-pore distance, which is a diameter of the escribed circle of the hexagonal cell increases with increasing anodization voltage at the rate of ~2.5 nm V^{-1}. The cell-wall thickness is ~0.71 times of the barrier layer thickness for the voltage range of 80-120 V. The pore diameter $D_{pore} = D_{cell} - 2\times0.71t_{barrier}$, where $t_{barrier}$ is a thickness of the barrier layer. The D_{pore} is also proportional to the forming voltage, but this relationship varies with anodization conditions. Therefore, Al films anodized at different voltages and under the same conditions should have similar porosity P_{AAO}. It can be explained by fact that the cross-sectional area of the pore $\pi D_{pore}^2/4$ is proportional to V^2, and the number of pores is inversely proportional to V^2.

The temperature of electrolyte does not affect the template parameters much besides a slight variation of the anodization rate and barrier-layer thickness, and normally is maintained in the range of 0-20 °C. The barrier layer nm/V ratio $\zeta_{barrier}$ decreased from 1.14 to 1.04 nm/V at constant voltage when temperature was increased from 20 to 30 °C. Increasing the molarity of the electrolyte from 0.4 to 2.5 M decreases the barrier layer from 87 to 67 nm and decreases $\zeta_{barrier}$ from 1.09 to 0.82 nm/V at

constant voltage (*O'Sullivan and Wood, 1970*). A decrease of $t_{barrier}$ with the increasing electrolyte concentration under applied voltage is caused by the increasing dissolution rate at barrier layer/electrolyte interface. Pore diameters and cell size should not be affected much by the acid concentration and dissolution rates, but depend mainly on the applied voltage, where both D_{pore} and D_{cell} are proportional to the applied voltage (*Myung et al., 2004*; *Li et al., 1998a*; *Sun et al., 2010*; *Lee et al., 2006*; *Masuda & Fukuda, 1995*; *Masuda et al., 1997b*; *Nielsch et al., 2002*; *Chu et al., 2005*)**.** In order to maintain the nanopores self-ordering when increasing voltage, it is necessary to decrease the pore's base dissolution rate and $\zeta_{barrier}$ by increasing the pH level of the electrolyte. The acid aggressiveness decreases in the order sulphuric > oxalic > phosphoric. Typically, three main voltage regimes are used to obtain the desired D_{pore} and D_{cell}. For the voltage range of ~20-30 V a sulfuric acid (H_2SO_4) with lower pH is used to provide faster pore dissolution rate, and for other two regimes of 40-100 V and 120-200 V an oxalic ($C_2H_2O_4$) and phosphoric ($C_2H_2O_4$) acids are used to lower the dissolution rate. The change of the D_{cell} with applied voltage is defined by the cell size nm/V ratio ζ_{cell} ~2.5 nm/V (*O'Sullivan and Wood, 1970*; *Masuda et al., 1997a*; *Myung et al., 2004*; *Lee et al., 2007*) but it can be affected by the purity of films and number of defects.

Since both D_{pore} and D_{cell} increases with increasing voltage, it is a big challenge to control P_{AAO} of the AAO template by only changing one of the template parameters (e.g. D_{pore}, D_{cell} or ρ_{pore}). For instance, decreasing the voltage from 195 to 160 V using phosphoric acid increases P_{AAO} to ~40% (*Nielsch et al., 2002*; *Lee et al., 2006*) and increasing voltage from 40 to 150 V using oxalic acid decreases P_{AAO} to ~3 %. With increasing electrolyte concentration, the D_{pore} can be tuned maintaining the same D_{cell}, for example P_{AAO} was decreased from 31% to 15% with increasing sulfuric acid concentration from 1.8 to 4.7 M at fixed current density 100 mA/cm^2 (*Myung et al., 2004*; *Ebihara et al., 1982*; *Parkhutik & Shershulsky, 1992*).

Experimental Details of Supported AAO Templates Preparation

A schematic fabrication process of supported AAO templates on a smooth conductive Ti/Pt/Ti multilayer, deposited on top of a solid Si wafers is shown in **Figures 3.18a-c**. High quality analytical grade (99.99%, unless otherwise specified) chemicals were used in this work as provided, without further purification. The aqueous solutions were prepared with ultra-pure deionized water (VWR Chemicals, France). The as-prepared Al/Ti/Pt/Ti/Si substrate (**Figure 3.18a**) was exposed to a single step anodization process in 0.3 M oxalic acid ($H_2C_2O_4$), by applying an anodic potential of 60 V from a Keithley 2400 sourcemeter during ~1000 sec. The anodization process was stopped by the program automatically after the current gradually increased and reached the set limit of 20 mA, which identifies the end of the anodization process and indicates that

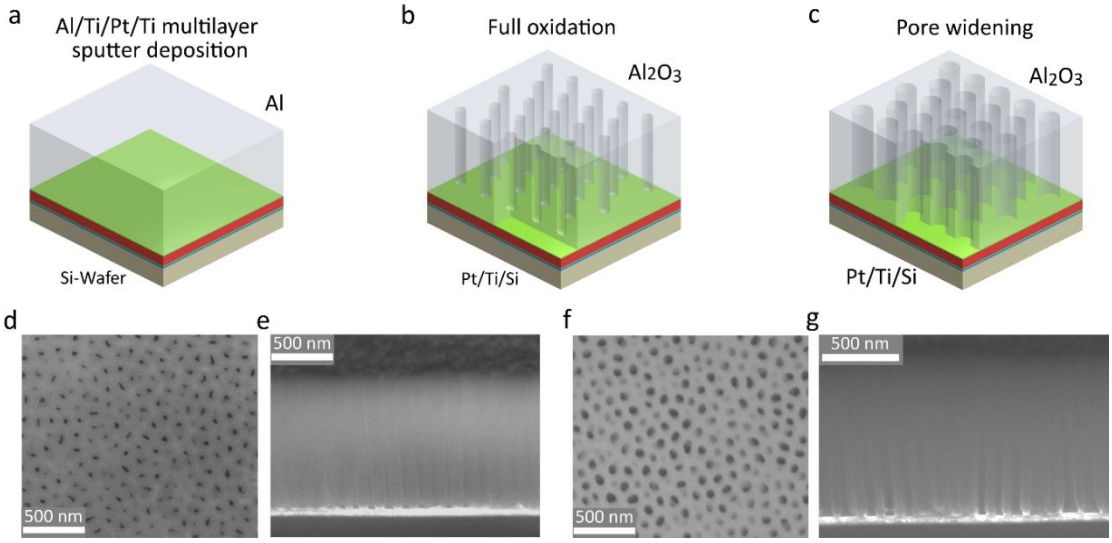

Figure 3.18: Schematic illustration of the formation of porous alumina template. **(a)** Sputtering deposition of the Al/Ti/Pt/Ti multilayer on the SiO_2/Si wafer, **(b)** Anodization of the Al/Ti bilayer, **(c)** Chemical dissolution of the barrier layer at the pore base and the pores chemical widening. **(d,e)** Top and section view SEM images of the anodized Al film, **(f,g)** Top and section view SEM images of the alumina pores after the chemical widening process

the template's pores reached the conductive Pt layer (**Figure 3.18b**). To slow down the oxidation process during anodization and to improve the quality of AAO template, the temperature was kept around 2±0.2 °C. The anodization process was followed by a chemical widening of the nanopores and barrier layer dissolution in a 0.5 M sulphuric acid (H_2SO_4) solution (Merch, Germany) at 40 °C for 60 and 70 min (**Figure 3.18c**). The resulting AAO film had a thickness t_{AAO} ~1.3-1.4 µm with a nanopores interspacing D_{cell} ~130-150 nm (the distance from centre to centre of nanopores) and an average D_{pore} ~70-90 nm, generating a porosity factor P_{AAO} ~25-35 % (*Nielsch et al., 2002*) and a pores density ρ_{pore} ~7×10^9 pores/cm^2. The data observed by SEM for the geometric parameters of the anodized Al layer before and after widening during 60 and 80 min is summarized in **Table 3.7**.

Top and cross section view SEM images of the alumina templates after the anodization procedure are shown in **Figures 3.18d,e**. The values for the inter-pore distance D_{cell} ~125 nm, pore diameter D_{pore} ~20 nm, and barrier layer thickness $t_{barrier}$ ~70 nm are similar to the previously reported values for the anodization of Al foils carried out at 60 V potential (*Li et al., 1998a*; *O'Sullivan and Wood, 1970*; *Chu et al., 2005*). The data obtained by SEM (**Figures 3.18d-g**) showed that the enlargement time of 60 min results in D_{pore}~70 nm and D_{cell} ~130 nm, while after 80 min of the pores widening D_{pore} and D_{cell} increase to ~90 and 150 nm, respectively.

Table 3.7. Geometric parameters of the as-prepared alumina templates

Sample	t_{AAO} µm	D_{pore} nm	D_{cell} nm	$t_{barrier}$ nm	ρ_{pore} pores/ cm^2	P_{AAO} %	Voltage V	Widen. time min
Al/Ti/Pt	1.3±0.1	20±5	125±10	70±10	7×10^9	10	60	-
Al/Ti/Pt	1.3±0.1	70±10	130±10	30±10	7×10^9	25	60	60
Al/Ti/Pt	1.3±0.1	90±10	150±10	-	6×10^9	35	60	70

t_{AAO} is a thickness of AAO template
D_{pore} is a pore diameter
D_{cell} is a pore interspacing
$t_{barrier}$ is a thickness of barrier layer
ρ_{pore} is a pores density
P_{AAO} is a porosity of AAO template

For the multistep anodization of the thin Al layers (e.g. two-, three- or four-step) it is necessary to know the anodization rate, so that the anodization can be stopped and the oxide layer can be chemically ethced leaving a highly-ordered pattern of pits on the top surface of the non-anodized Al layer. By knowing the concentration of the acid (e.g. 0.3 M oxalic acid), anodization voltage, and anodization surface (here 0.2 cm^2, calculated from the rubber seal parameters used in the electrochemcial cell see **Figure 3.9a**), the thickness of the anodized Al layer can be estimated by calculating the area below the graph of the current-time dependence (**Figure 3.15b**). **Figures 3.18d,e** show the top view and tilted section view of the anodized supported Al layer. The interpore distance D_{cell} ~125 nm, pore diameter D_{pore} ~20 nm, and barrier layer thickness t_b ~70 nm, which are similar to the previously reported alumina parameter for the anodization carried out at 60 V potential (*Li et al., 1998a*; *O'Sullivan & Wood, 1970*; *Chu et al., 2005*).

3.2.3 Third Step of Process: Electrochemical Deposition of Vertically Aligned Nanopillar Arrays into Supported Anodic Alumina Templates

The pulsed electrodeposition of $CoFe_2$ nanowire arrays was discussed in detail in ***Section 3.1.3*** *(page 53).*

In this paragraph, the fabrication process via an electrodeposition of the metal $CoFe_2$ nanopillars arrays using supported nanoporous alumina is discussed.

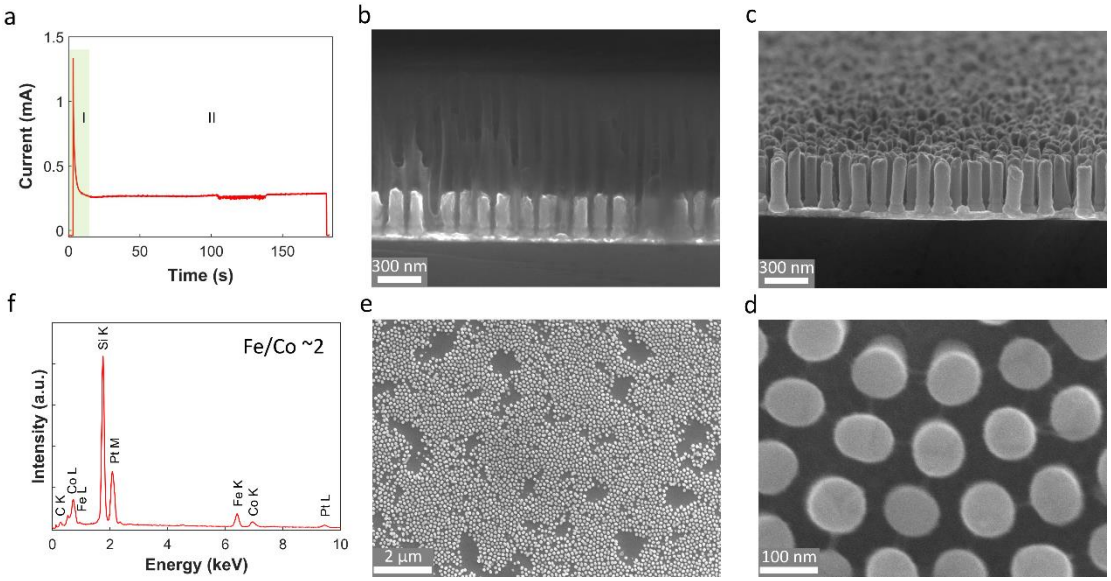

Figure 3.19: (a) The $CoFe_2$ electrodeposition current-time curve, **(b)** A cross section view SEM image of the nanoporous alumina host, partially field with electrodeposited $CoFe_2$ nanopillars, **(c-e)** Tilted section view and top view SEM images of the $CoFe_2$ nanopillar array after the template removal, **(f)** EDX spectrum obtained from the free-standing $CoFe_2$ nanopillars

Experimental Details of $CoFe_2$ Nanopillar Arrays Pulsed Electrodeposition

The pulsed electrodeposition technique was previously described in detail for the deposition of the $CoFe_2$ nanowire arrays in **Section 3.1** (p. 58). Briefly, to fabricate the vertically aligned $CoFe_2$ nanopillar arrays on top of the conductive Pt layer with the optimized aspect ratio, nanopillars diameter D_{pillar} and inter-spacing between nanopillars D_{pillar}, a standard three-electrode potentiostatic configuration using a PAR 263A Potentiostat/Galvanostat and a Pt foil as a counter electrode was used (see **Figure 3.9b**). The three-electrode setup includes: (1) the Pt-coated Si substrate at the bottom of the pores serving as a working electrode: (2) Pt foil as counter electrode: (3) Ag/AgCl reference electrode. The height of the $CoFe_2$ nanopillars h_{pillar} was easily controlled in the range of ~200–500 nm by varying the charge-controlled electrodeposition duration. The growing process of the $CoFe_2$ nanopillar array was investigated by monitoring a time dependence of the cathodic current (**Figure 3.19a**). Two stages of the electrodeposition were observed: (1) a sharp increase of the cathodic current to ~1 mA due to a change of the ion concentration in the solution; (2) a decrease to the current of ~0.25 mA due to a moving of the ions from the solution into the pores. The electrodeposition duration of 180 sec leads to the $CoFe_2$ nanopillar arrays with h_{pillar} ~350 nm (**Figures 3.19 b,c**). **Figure 3.19c** shows a tilted section view SEM image of the free-standing $CoFe_2$ nanopillar array after the AAO template removal. Both ordering and uniformity in D_{pillar} ~90 nm of the $CoFe_2$ nanopillars are shown on the

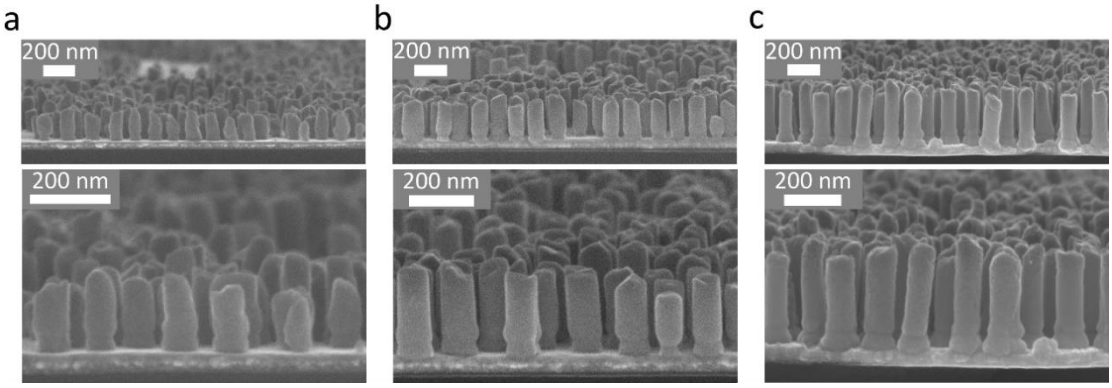

Figure 3.20: Tilted view SEM images of the $CoFe_2$ nanopillar arrays developed on the Pt/Ti/SiO_2/Si substrate using electrodeposition process into the anodic alumina template. The fine adjustment of the nanopillars height can be noticed. **(a-c)** SEM images of the $CoFe_2$ nanopillar arrays with pillar heights of ~200, 250 and 350 nm, respectively

top-view SEM images (**Figures 3.19d,e**). An average chemical analysis was provided by EDX analyser confirming a value of the Fe/Co ratio close to 2 (**Figure 3.19f**).

The pulsed electrodeposition conditions for the $CoFe_2$ nanopillar growth and the geometric parameters of the nanopillars are summarized in **Table 3.8**.

Table 3.8: Pulsed electrodeposition processing and geometric parameters of the prepared $CoFe_2$ nanopillar arrays within as-prepared AAO/Pt/Si templates with AAO thickness ~1.3 µm

Sample	Electrolyte composition	pH	Electrodeposition pulse voltage E (or current I) and pulse time t	D_{pillar} (nm)	h_{pillar} (nm)	D_{cell} (nm)
$CoFe_2$	$CoSO_4 \cdot 7H_2O$ (0.1 M) $FeSO_4 \cdot 7H_2O$ (0.14 M) H_3BO_3 (0.16 M)	3	E_1 = -1.5 V; t_{on} = 20 ms E_2 = -0.5 V; t_{off} = 80 ms	90	200-500	150

Figures 3.20a-c show the experimental variation of the height of $CoFe_2$ nanopillar arrays with the duration of electrodeposition. The tilted section view SEM images of the $CoFe_2$ nanopillars shows that with increasing the electrodeposition time and accumulated charge from ~120 s and 60 mC to ~300 s and 157 mC, the h_{pillar} increases from around ~200 nm to 500 nm.

3.2.4 Forth Step of Process: AAO Template Removal using Chemical Dissolution

The AAO template dissolution process is shown in **Figure 3.21**. Once the electrodeposition was complete, the alumina template was dissolved in a 2 M of sodium hydroxide solution NaOH (Merch, Germany) at room temperature during 20 minutes (**Figures 3.21a-e**) and washed using distilled and ultra-pure deionized water (**Figures 3.21f,g**), thus leading to a free-standing and vertically aligned $CoFe_2$ nanopillar arrays

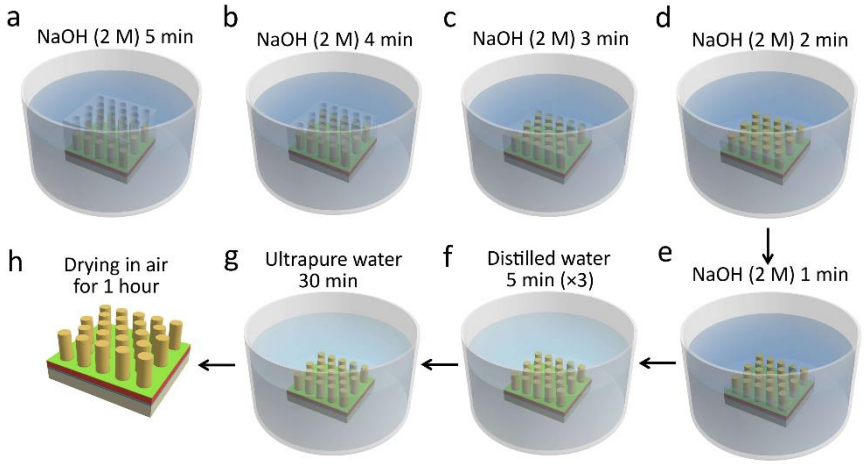

Figure 3.21: Flow chart of the chemical dissolution procedure for the anodic alumina templates. **(a-e)** Dissolution of the templates hosting $CoFe_2$ nanopillar arrays using 2 M NaOH solutions for 5 min **(a)**, 4 min **(b)**, 3 min **(c)**, 2 min **(d)** and 1 min **(e)**, **(f)** Washing of the free-standing $CoFe_2$ nanopillar arrays using the distilled water three times for 5 min in each bath and **(g)** using the deionized water for 30 min. **(h)** Drying of the $CoFe_2$ nanopillar arrays in air

on the Pt/Ti/Si substrate. The experiments showed that the critical height of nanopillars is ~600 nm, and the nanopillar arrays with height larger than ~600 nm tend to come down after the dissolution of AAO templates.

3.2.5 Fifth Step of Process: RF Magnetron Sputter Deposition of $BaTiO_3$ and $Ba_{0.7}Sr_{0.3}TiO_3$ FE Thin Layers and in situ FM Nanopillars Oxidation

The top-down PVD preparation of the BSTO and the BTO FE layers on the $CoFe_2$ nanopillar arrays is described in this section. To fabricate the BSTO and the BTO layers, a facile radio-frequency (RF) magnetron sputter deposition (sputtering) was used. It is a synthesis technique which allows to fabricate high-quality thin films with the good crystal structure and interface matching. Using the RF magnetron sputtering it is possible to grow films with thickness in the range from 50 nm to 1 μm and at the deposition rates of 40-200 nm/hour. The key point in using the RF magnetron sputtering for the deposition of FE layers on FM metal nanopillar arrays is the possibility of a simultaneous oxidation (*in situ*) of metal $CoFe_2$ nanopillars into insulator metal oxide CFO nanopillars. In the following paragraphs, the detailed explanation of the BSTO and BTO layers deposition and the general description of sputter deposition technique is presented.

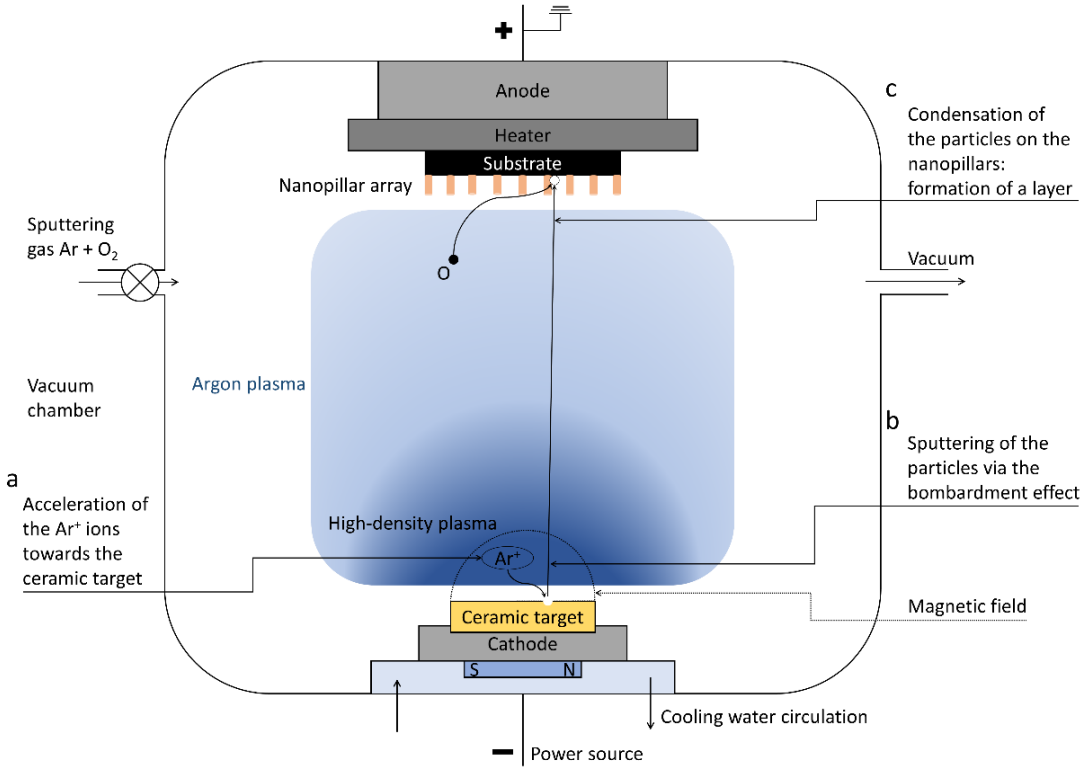

Figure 3.22: Sketch of sputter deposition processing. **(a)** Gaseous Ar^+ ions are accelerated towards the ceramic target. **(b)** Particles are generated from the target's surface being sputtered via the Ar^+ ions bombardment. **(c)** Particles are transferred towards the substrate and are condensed on the nanopillar array and on the bottom Pt electrode forming a ceramic perovskite matrix layer

Principles of RF Magnetron Sputtering Deposition of Perovskite Layers

The RF magnetron sputtering is one of the most commonly used PVD techniques for the growth of perovskite thin films. The schematic illustration of the sputter deposition processing is shown in **Figure 3.22**. Briefly, the working principle of the magnetron sputtering can be described as a physical vaporization of the surface atoms via transfer originated in the bombardment by energetic particles. The energetic particles are represented by gaseous Ar^+ ions (**Figure 3.22a**), which are accelerated in the electric field or radio frequency (RF) magnetic field, so-called *dc* and RF magnetron sputtering (*Mattox, 1998*). The sputtering of surface particles from the target, facilitated by the bombardment effect (**Figure 3.22a)**, is followed by the particles condensation on the pre-heated sample forming perovskite layers.

For the RF magnetron sputtering, conducted at frequencies above 50 kHz, the ions are not mobile enough to form a *dc* diode-type discharge and the applied potential is felt through the space between the electrodes. The ionizing collisions in the space between the electrodes is generated by the electrons with sufficient energy, and the plasma is generated throughout the space between the electrodes. The alternating positive-negative potential occurs on the surface, when the RF potential with a large

peak-to-peak voltage is capacitively coupled to the electrode. The ions are accelerated to the surface with sufficient energy for sputtering during part of each half-cycle, and during alternative half-cycle, the electrons move towards the surface to prevent any charge build-up. RF frequency is typically in the range of 0.5-30 MHz. RF sputtering is conducted at low gas pressures ($<10^{-3}$ mBar). Since the target is capacitively coupled to the gaseous plasma, the sputtering can be performed from the surface of both conductive and insulating targets with a condition that the insulator target covers the whole surface of the metal electrode to avoid a shorting out the capacitance formed by the metal-insulator-sheath-plasma. A major drawback of the RF sputtering of ceramic targets is a poor thermal conductivity, large thermal expansion coefficients, and high brittleness of insulating materials, which can generate large thermal gradients and targets fracturing when high power is applied.

Experimental Details of $BaTiO_3$ Target Preparation

The $BaTiO_3$ (BTO) targets were prepared using solid-state chemistry processing illustrated in **Figure 3.23**. First, the $BaCO_3$ 67.7 g and the TiO_2 23.7 g powders (Sigma-Aldrich, St. Louis, MO) were mixed and milled in a centrifuge using agate balls at 200 rpm for 30 minutes. After washing the powders with ethanol, they were pressed into a pellet at the pressure of 100 bar in a hydraulic press, followed by a calcination at 1150 °C for 3 hours at 3 °C /min heating rate. Then the calcinated pellet was milled

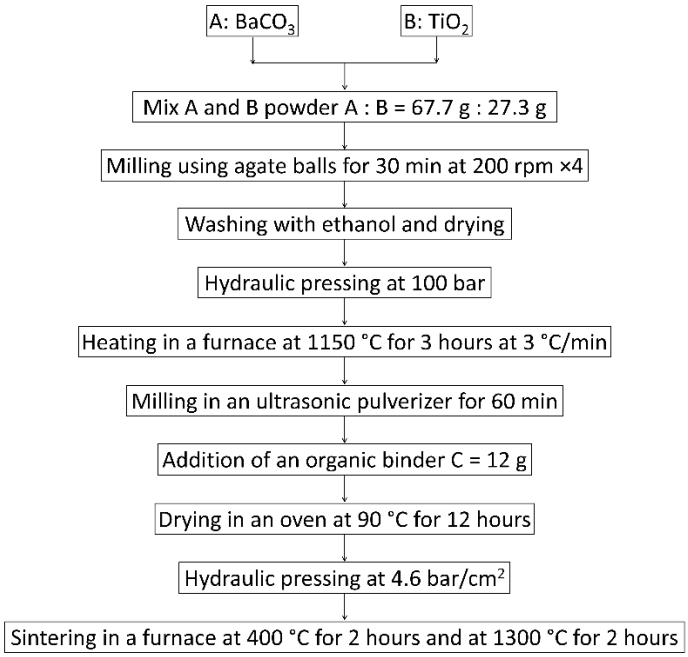

Figure 3.23: Flow diagram for the solid-state chemistry route used to elaborate the ceramic perovskite BTO targets used for the rf magnetron sputtering deposition of the BTO matrix layers on the vertically aligned magnetic nanopillar arrays

using an ultrasonic pulveriser (Fritsch analysette 3 SPARTAN) for 1 hour, and subsequently pressed into the BTO target in hydraulic press at 4.6 bar/cm^2. Next, the targets were heated at intermediate temperature of 400 °C for 2 hours to make sure that the organic binder (Optapix) is evaporated before sintering process, and then sintered at 1300 °C for 2 hours. The as-prepared BTO targets had rectangular shape with dimensions ~70×50 mm (top surface ~35 cm^2). Finally, two home-made BTO targets were fixed in facing target configuration (90° off-axis geometry) inside the PVD vacuum chamber for the RF magnetron sputtering of the BTO FE layers.

The home-made $BaSr_{0.7}Ti_{0.3}O_3$ targets we used were prepared by Dr. S. Payan and Dr. Q. Simon (ICMCB-CNRS, Université de Bordeaux, France).

Experimental Details of $BaTiO_3$ and $BaSr_{0.7}Ti_{0.3}O_3$ Thin Layers Preparation

The BSTO and BTO thin layers preparation using the RF magnetron sputtering deposition is schematically illustrated in **Figure 3.24**. The $CoFe_2$ nanopillar arrays having the average height of ~150-500 nm were considered (**Figure 3.24a**). The BSTO and the BTO thin layers were deposited by the RF magnetron sputtering (Plassys MP700) in facing target configuration (90° off-axis geometry) using two home-made targets (RF power density ~2.1 W/cm^2) and reactive Ar/O_2 plasma (5 Pa and 1% O_2) (**Figure 3.24b**). Upon deposition, the substrates were kept at 650 °C with a substrate-to-plasma distance close to 40 mm. The deposition time was adjusted to fill the internal space of the pillar arrays as well as to obtain the desired BSTO and BTO thin layers with thicknesses ~200 and 600 nm at the top of the nanopillar structure (**Figure 3.24c**). The $CoFe_2$ nanopillar arrays were transformed into an insulator $CoFe_2O_4$ phase *in situ* during the deposition of BSTO and BTO FE thin layers, thus preserving the nanopillars morphology, reducing the surface roughness and avoiding free spaces and pin-holes.

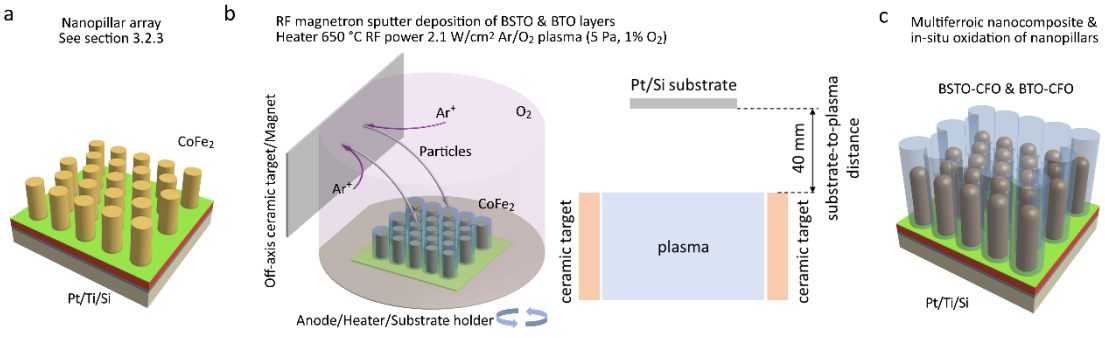

Figure 3.24: Schematic illustration of the vertically aligned $Ba_{0.7}Sr_{0.3}TiO_3$-$CoFe_2O_4$ and $BaTiO_3$-$CoFe_2O_4$ nanocomposites preparation using RF magnetron sputter deposition of ferroelectric matrix layer on the vertically aligned $CoFe_2$ nanopillar array **(a)**, **(b)** Vacuum chamber with two $Ba_{0.7}Sr_{0.3}TiO_3$ or $BaTiO_3$ targets in facing target configuration (90° off-axis geometry) at 40 mm distance from the substrate, **(c)** Formed $Ba_{0.7}Sr_{0.3}TiO_3$-$CoFe_2O_4$ and $BaTiO_3$-$CoFe_2O_4$ multiferroic nanostructures with in-situ oxidation of the $CoFe_2$ nanopillar array

We must note that the initial surface oxidation of the $CoFe_2$ nanopillar can occur during the pre-sputtering step before the actual FE layer deposition. However, since this step is very short 20 min, only ultrathin surface layer can be oxidized, while the bulk of $CoFe_2$ nanopillars is expected to be transformed into CFO mainly during FE film sputtering process that lasts 6-12 hours.

3.2.6 Fifth' Step of Process: Thermal Oxidation of $CoFe_2$ Nanopillar Arrays

Thermal annealing of $CoFe_2$ nanowire arrays was discussed in detail in ***Section 3.1.4*** *(p. 84)*

Experimental Details of Thermal Oxidation of $CoFe_2$ Nanopillar Arrays

After the dissolution of AAO templates using the procedure shown in **Figure 3.21**, the $CoFe_2$ nanopillar arrays, free-standing on the Pt/Ti/Si substrate (**Figure 3.25a**), were transformed into the CFO phase using thermal annealing (**Figure 3.25b**). The $CoFe_2$ nanopillar arrays were placed in a tubular furnace (Carbolite, England) and heated in air at T_{anneal} ~600 °C for 24 hours at the heating rate of 2 °C/min. **Figures 3.25c,d** show the top view SEM images of the $CoFe_2$ and CFO nanopillar arrays, respectively. The diameter of nanopillars D_{pillar} increased after the thermal annealing from ~90 to 120 nm. The tilted view SEM images of the nanopillars arrays before and after annealing revealed a significant change of the surface roughness morphology of the pillars (see **Figures 3.25e,f**). This a key point for the preparation of the BSTO-CFO and BTO-CFO (1-3) ME nanostructures, because the surface roughness, change of morphology, and increase of nanopillars diameter will directly affect the microstructure of FE thin layers deposited on the FM nanopillars using RF magnetron sputtering. The tilted section view SEM images showed that h_{pillar} increased from around 200 to 350 nm after thermal oxidation (**Figures 3.25g,h**). The EDX spectroscopy showed the Fe/Co ratio was maintained at ~2 after thermal treatment (**Figures 3.25i**). The significant increase of the oxygen K line in the EDX spectrum is assigned the nanopillar arrays oxidation.

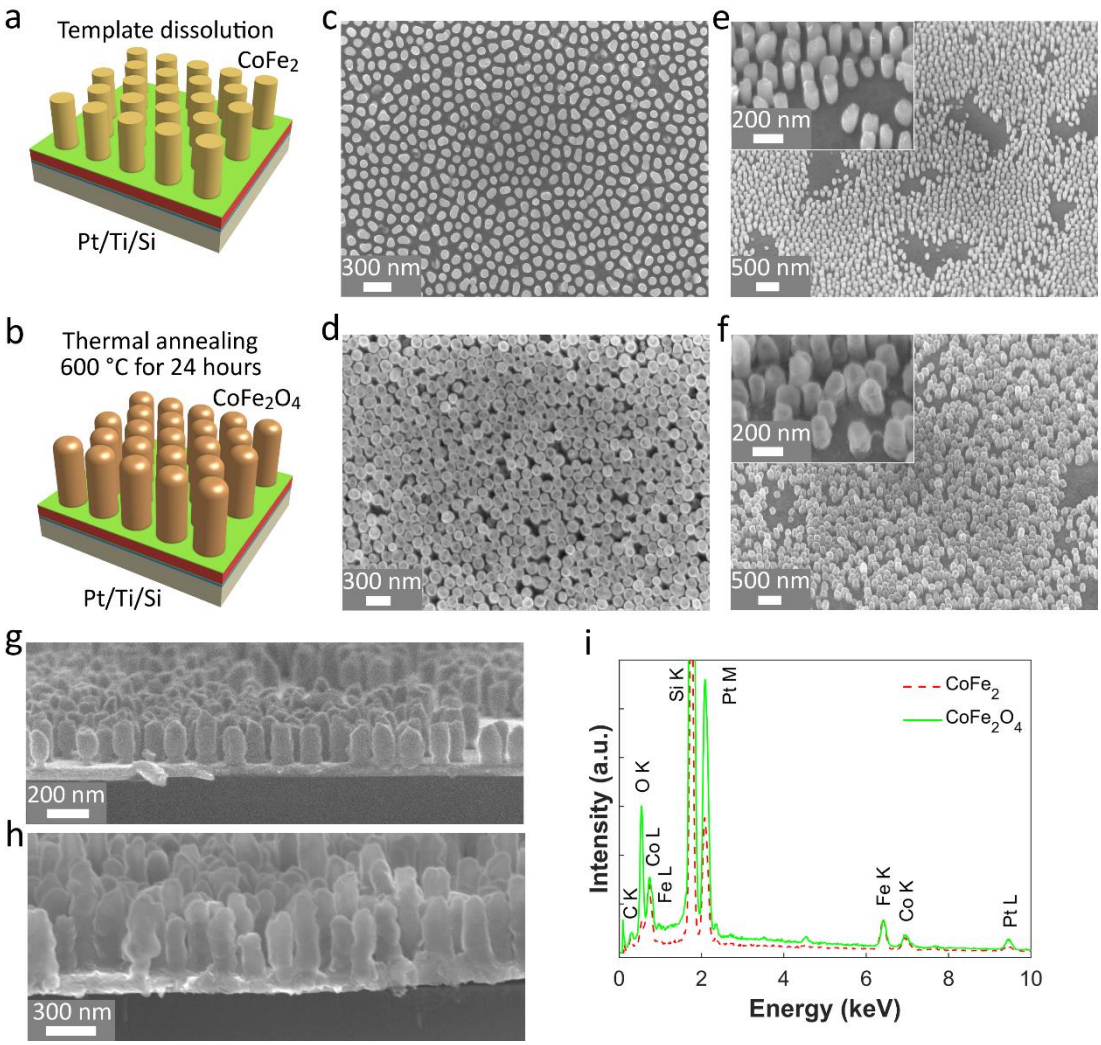

Figure 3.25: (a-b) Schematic fabrication of the $CoFe_2O_4$ nanopillar arrays using *ex situ* thermal oxidation of $CoFe_2$ nanopillar arrays. **(a)** Dissolution of the anodic alumina template, hosting nanopillar arrays in 2 M NaOH, **(b)** Annealing of the free-standing $CoFe_2$ nanopillar arrays in air at 600 °C for 24 hours. Top view **(c, d)**, tilted top view **(e,f)** and tilted section view **(g,h)** of the as-deposited $CoFe_2$ nanopillar arrays **(c,e,g)** and the annealed nanopillar arrays **(d,f,h)**, respectively. **(i)** EDX spectra of the corresponding $CoFe_2$ and CFO nanopillar arrays

When we consider nanostructures, their properties can differ from the bulk.. Although EDX analyses of the nanopillars indicates that the initial stoichiometry Fe/Co~2 is preserved, the local non-stoichiometry is possible. As was previously shown for $CoFe_2/CoFe_2O_4$ multilayers, prepared using sputtering of $CoFe_2$ layers and its oxidation into CFO using RF Ar/O_2 plasma activation, it is important to investigate local stoichiometry of CFO (*Jurca et al., 2003a; 2003b*). There is a possibility of presence of lacunar spinel type structures such as γ-Fe_2O_3 whose structure and cell parameter are close to a lacunar spinel of formula $(Co_{0.33}Fe_{0.66})_2O_3$, wherein a larger oxygen to metal ratio can be observed for γ-Fe_2O_3. Therefore, TEM observation is needed to control local stoichiometry and affinity of nanopillars after thermal oxidation.

Experimental Details of Thermal Oxidation of $CoFe_2$ Nanopillar inside AAO Template

Another strategy for the thermal oxidation of $CoFe_2$ nanopillar arrays was also tested, where the thermal oxidation was conducted directly after the pulsed electrodeposition of the $CoFe_2$ nanopillars confined inside the AAO template (**Figure 3.26a**). However, due to several important drawbacks, discussed below, this strategy was not further pursued in the preparation of vertically aligned multiferroic nanocomposites. The $CoFe_2$ nanopillar arrays were annealed in the furnace at T_{anneal} ~600 °C for 24 hours at the heating rate of 2 °C/min (**Figure 3.26a**), followed by the chemical dissolution of the AAO template (**Figure 3.26c**). The tilted view SEM images of the free-standing

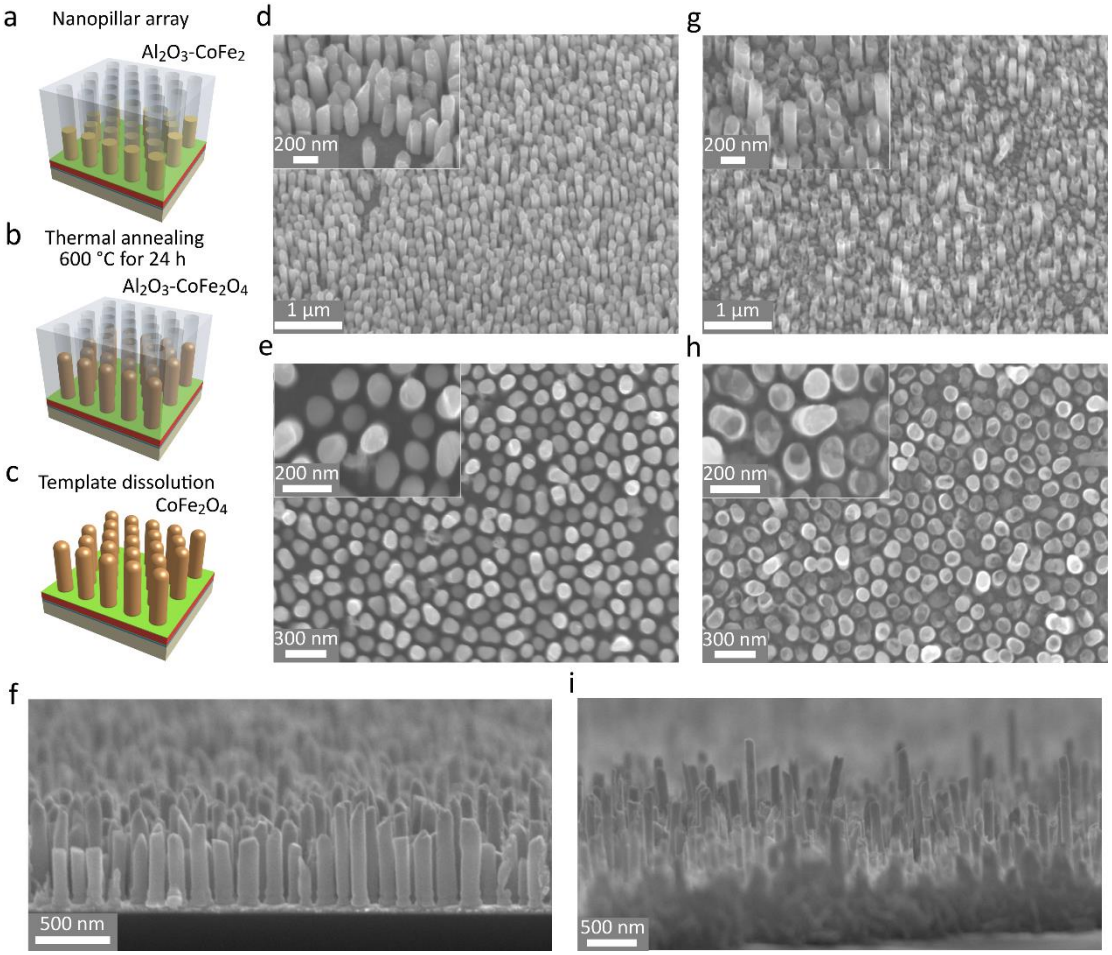

Figure 3.26: (a-c) Flow chart of the in-situ thermal oxidation $CoFe_2$ nanopillar arrays: **(a)** Pulsed electrodeposition of the $CoFe_2$ nanopillar array into the anodic alumina template, **(b)** Thermal annealing of the $CoFe_2$ nanopillar array inside the templates at 600 °C for 24 hours, **(c)** Template dissolution in 2 M NaOH; Tilted **(d),** top **(e),** and **(f)** section view SEM images of the as-prepared $CoFe_2$ nanopillars; Tilted **(g),** top **(h),** and **(i)** section view SEM images of the thermally oxidized nanopillar arrays.

$CoFe_2$ nanopillar arrays before and after the thermal oxidation are shown in **Figure 3.26d,g**. Some parts of the nanopillars were broken and washed away during the AAO template's dissolution. Since during annealing the $CoFe_2$ nanopillars were confined inside the AAO template, the nanopillars diameter was not affected by the oxidation process (see **Figures 3.26e,h**), whereas their height increased by nearly 2 times from ~600 to 1200 nm after the thermal procedure (**Figure 3.26f,i**).

3.2.7 Sixth' Step of Process: Sol-Gel Deposition of Ferroelectric $PbZr_{0.52}Ti_{0.48}O_3$ Thin Layers

*Sol-gel deposition of FE layers was discussed in detail in **Section 3.1.2** (p. 60)*

The bottom-up chemical solution deposition of the PZT FE thin layers on the CFO nanopillar arrays is described in this section. To deposit the PZT thin layers on the nanopillars, a facile, scale-up, and low-cost sol-gel deposition was used. It is a solution based technique which allows to fabricate polycrystalline thin and thick films with high density and large range of thicknesses ranging from 100 nm to 2 μm. The key point in using the sol-gel deposition for the growth of the FE layers on the FM nanopillar arrays is the possibility for the solution to effectively penetrate the highly-packed CFO nanopillar arrays and thus a way to improve the interface quality between the FE layer and the FM pillars. In the following paragraphs, the PZT layers deposition is presented.

Experimental Details of PZT Precursor Solution Preparation

The PZT precursors solution used for the deposition of the PZT thin layers was prepared using an inverse-mixing-order route (chelate route) similarly to the preparation of the PZT solution (**Figure 3.5,** p. 66) used for the deposition of the PZT nanotube arrays described in **Section 3.1** (p. 58). A new solution was slightly adjusted for the synthesis of FE layers with a thin film geometry. The second solution preparation is schematically shown in **Figure 3.27**. The volume of the solvents (i.e. acetic acid and 2-propanol) was reduced from 4.25 mL to 3 mL. In addition to the procedures shown in **Figure 3.5** (p. 66), an ethylene glycol 2.5 mL was added into the solution of precursors in the final step. All chemical products used for the synthesis of

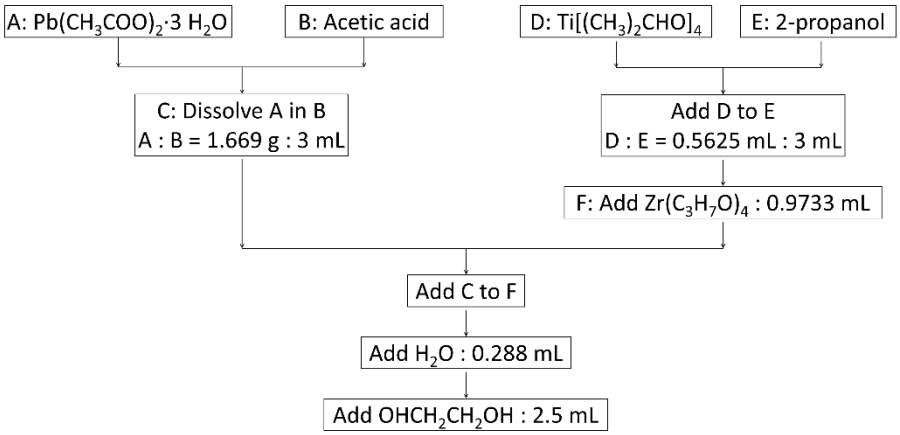

Figure 3.27: Flow chart diagram for the inverse-mixing-order route synthesis of the PZT solution used for the deposition of the PZT matrix layers

the PZT stock solution with Pb:Zr:Ti composition around 100:52:48 are shown in **Table 3.9**. The as-prepared solution was stored in a refrigerator for one month.

Table 3.9: Reagents and solvents used for the preparation of stock solution for the PZT matrix layers

Chemicals		Quantities
PZT matrix layer:		
Lead acetate	$Pb(CH_3CO_2)_2 \cdot 3H_2O$	1.669 g
Acetic acid	CH_3COOH	3 mL
Zirconium propoxide	$Zr(C_3H_7O)_4$	0.9733 mL
Titanium isopropoxide	$Ti[(CH_3)_2CHO]_4$	0.5625 mL
2-Propanol	$CH_3CH_2CH_2OH$	3 mL
Ethylene glycol	$OHCH_2CH_2OH$	2.5 mL
Distilled water	H_2O	0.288 mL

Table 3.10: Comparison of solvents used in the present sol-gel processing (*Lide, 2006*)

Solvent	Surface tension 25 °C mN/m	Viscosity 25 °C mPa s	Boiling point °C	Vapor pressure 100 °C mmHg
Acetic acid (CH_3COOH)	27.10	1.056	117.9	400
2-propanol ($CH_3CH_2CH_2OH$)	20.93	2.038	82.3	1500
Water (H_2O)	71.99	0.890	100	760
Ethylene glycol ($OHCH_2CH_2OH$)	47.99	16.1	197.3	50

The initial reaction has to be complete before the ethylene glycol is added because the residual zirconium and titanium alkoxides can alcolyze with ethylene glycol and form a condensed solid material. The ethylene glycol was used for several purposes: (1) a well-suited solvent for both carboxylate and alkoxides; (2) to increase the boiling point of the coating solution and slow down the evaporation of water and organics; (3) to increase the viscosity of the solution thus stabilizing suspended particles better. The

comparison between the solvents parameters used in the synthesis of PZT solutions is given in **Table 3.10** (*Lide, 2006*).

Principles of Thermal Treatment and Crystallization of PZT Gel Layers

The one-step technique to crystallize the as-deposited PZT gel layer into the perovskite PZT tubular layers described in **Section 3.1** (p. 58) was modified by including an additional thermal treatment called pyrolysis, which is a commonly used for the synthesis of FE thin films (see **Figure 3.4c**, p. 61). Firstly, before the crystallization the as-deposited PZT gel layer is exposed to the pyrolysis by placing it on a hot-plate, which was pre-heated at 200-400 °C for several minutes to evaporate the organic species and form a PZT amorphous layer. Interestingly no cracking of the films appears during this rapid heating process, because the hot-plate pyrolysis allows the evaporation of organic species to happen before the amorphous network collapses. It was reported that the sol-gel derived PZT layers were amorphous with a short-range order, but after the heat treatment was carried out the development of the medium-range order and chemical heterogeneity at nanoscale were observed. Then, with increasing temperature the heterogeneity decreased, and above the pyrolysis temperature of 500 °C, the layers crystallized into an intermediate phase, which finally was transformed into the perovskite phase above 600 °C (*Lakeman, 1995*). To crystallize the pyrolyzed amorphous layers into the homogeneous perovskite ceramic counterparts and to simultaneously remove all organic species left in the structure after the pyrolysis, the layers are heated to higher temperatures (500-700 °C) at heating rate ranging from 5-6000 °C/min. In this work, the crystallization of the PbZrTi gel layers into the PZT perovskite layers on the CFO nanopillar arrays was conducted using a combination of the pyrolysis on a hot-plate and thermal crystallization in a conventional furnace.

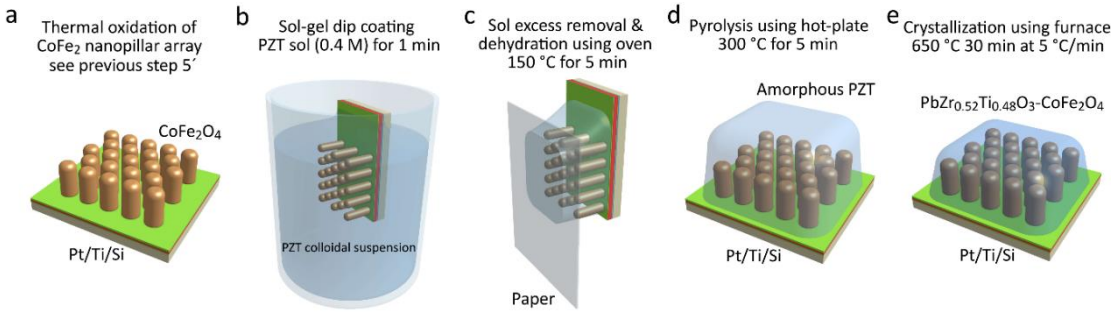

Figure 3.28: Schematic representation of the vertically aligned PZT-CFO nanocomposites preparation using a sol-gel dip coating technique. **(a)** Vertically aligned CFO nanopillar array prepared via pulsed electrodeposition and thermal oxidation technique (see 5'processign step), **(b)** Dip coating of the PZT sol layer on the CFO nanopillar array in 0.4 M PZT sol for 1 min, **(c)** Excess PZT sol blotting with the absorbent paper and gelation in the pre-heated oven at 150 °C for 5 min, **(d,e)** Two-step PZT gel crystallization approach with hot-plate pyrolysis at 300 °C for 5 min and thermal crystallization in furnace at 650 °C for 30 min

Experimental Details of PZT Thin Layers Preparation

The (1-3) PZT-CFO ME nanocomposites were prepared using sol-gel dip coating deposition. The schematic preparation flow chart is shown in **Figure 3.28**. The second most common technique for the deposition of the PZT gel layers, a dip coating technique (**Figure 3.4**, p. 61), was used to deposit PZT gel layers on the vertically aligned CFO nanopillar arrays. Following the PZT gel layers deposition, a two-step crystallization approach is typically used to crystallize the PZT gel into the perovskite ceramic matrix layer using the hot-plate pyrolysis and furnace crystallization (*Yi et al., 1988*; *Kingon & Srinivasan, 2005*). $CoFe_2$ nanopillar arrays having an average height of 400 and 500 nm were considered. The transformation of the $CoFe_2$ nanopillars into the vertically aligned CFO nanopillars was conducted using thermal treatment in air at 600 °C for 24 hours at 2 °C/min heating rate (**Figure 3.28a**), after which the nanopillar height is expected to increase by around 1.5-2 times.

In the first step, a PZT solution was deposited on the CFO nanopillar arrays, followed by the gelation (dehydration) at 150 °C for 5 min using the pre-heated oven (**Figures 3.28b,c**). After the gelation of the PZT sol, a two-step thermal process was used to crystallize the PZT gel into the perovskite PZT thin layer through a hot-plate pyrolysis and a thermal crystallization in the furnace (*Yi et al., 1988*; *Kingon & Srinivasan, 2005*). The pyrolysis was conducted at 300 °C for 5 minutes by placing the sample on the pre-heated hot-plate inside a hood (**Figure 3.28d**). The exact pyrolysis conditions such as
temperature and duration are very important parameters, that affect the film quality (e.g. cracking, crystal orientation) and the resulting phase purity (e.g. presence of pyrochlore) (*He et al., 2008*). The PZT layers were then crystallized and densified using a thermal annealing at 650 °C for 30 min at 5 °C/min heating rate in air (**Figure 3.28e**). The resulting the PZT-CFO (1-3) type ME nanocomposites had thickness of 600-1300 nm.

3.3 Preparation of $PbZr_{0.52}Ti_{0.48}O_3$-$CoFe_2O_4$ Nanocomposites Based on 3D Interconnected Nanowire Networks

Vertically aligned (1-3) interconnected ME system is based on the three-dimensional (3D) interconnected FM nanowire networks. The 3D interconnected $CoFe_2$ nanowire networks were produced by a pulsed electrochemical deposition within porous polymer membranes, following the same ECD protocol as previously described in **Table 3.5** (p. 83). The $PbZr_{0.52}Ti_{048}O_3$ FE layers were deposited on the $CoFe_2$ 3D NW networks using a sol-gel dip coating deposition previously explained in detail in **Section 3.2** (p. 87). The metal $CoFe_2$ 3D NW networks were transformed into the metal oxide CFO phase

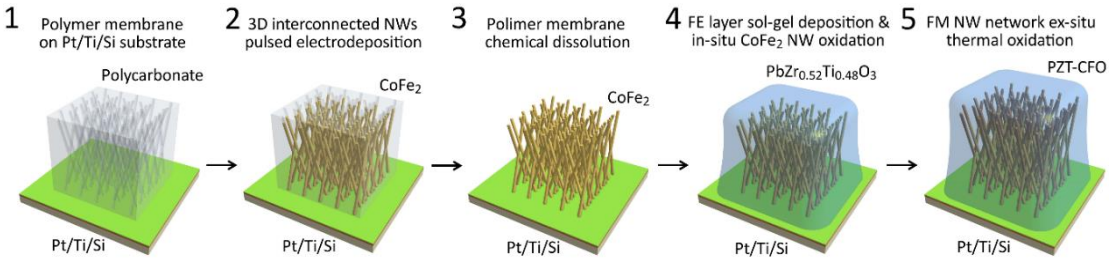

Figure 3.29: Fabrication of the 3D $PbZr_{0.52}Ti_{0.48}O_3$-$CoFe_2O_4$ multiferroic nanocomposite. **(a)** Manual transfer of the commercial polymer membrane onto the Pt/Ti/Si substrate, **(b)** Pulsed electrochemical deposition of the 3D interconnected $CoFe_2$ nanowire network inside a polymer membrane, **(c)** Chemical dissolution of the polymer membranes in a dichloromethane solution, **(d)** Sol-gel dip coating deposition of the $PbZr_{0.52}Ti_{0.48}O_3$ matrix layer on the $CoFe_2O_4$ interconnected nanowire network

using an *in situ* thermal oxidation technique, which is a simultaneous oxidation of the $CoFe_2$ phase and crystallization of the PZT amorphous thick layer. An additional *ex situ* oxidation technique was used to complete the oxidation process of the $CoFe_2$ 3D NW networks.

A general fabrication process of the (1-3) magnetoelectric nanowire network system in 5 steps is illustrated in **Figure 3.29**. In the 1st processing step, a porous polymer membrane was attached to the Pt/Ti/Si substrate. In the 2nd step, the polymer template was filled with the metal $CoFe_2$ 3D NW network using the pulsed electrodeposition. In the 3rd step, the hosting polymer template was removed using a chemical dissolution technique leading to the $CoFe_2$ free-standing 3D NW network. In the 4th step, the PZT FE layer was deposited on the $CoFe_2$ 3D NW network using the sol-gel dip coating deposition and thermal crystallization, which simultaneously leads to the *in situ* oxidation of the $CoFe_2$ phase. Finally, in the 5th step the oxidation of the $CoFe_2$ 3D NW network was completed using a post-annealing *ex situ* technique.

3.3.1 First Step of Process: Preparation of Polymer Template on Pt/Ti/Si Substrate

Track-etching technology is based on the beaming of polymer films such as polycarbonate with energetic particles or heavy ions generated by nuclear fusion leading to the formation of radiation damage trails, which show up as linear damaged tracks across the irradiated polymer film. These tracks are then chemically etched into the nanopores (*Fleisher et al., 1975*; *Ferain and Legras, 2003*). The combination of the processing of tracks and their subsequent etching is called track-etching. The randomly arranged nanopores of the track-etched polymer membranes have uniform pore size and shape. The pore size D_{pore} can be varied in the range of 10 nm – 30 µm by changing the conditions of the pores etching (e.g. duration, temperature, solution concentration). The pores density ρ_{pore} (number of tracks per square centimetre) is well defined between

10^3–10^{10} pores/cm^2 by the intensity of an ion beam and rewinding speed of the polymer film. The porosity $P_{polymer}$ can be as small as 2-5 %.

Although the commercial polymer track-etched membranes with vertically aligned nanopores (Nucleopore, Poretics, Millipore) are widely used to fabricate the vertically aligned nanowire arrays, the commercial track-etched polymer membranes with 3D interconnected nanopores are still rare (it4ip, Belgium).

Figure 3.30a illustrates the schematic fabrication of polymer membrane using track-etching process. The 25-µm-thick interconnected nanopores network was fabricated via an irradiation of polycarbonate films with the energetic heavy ions at fixed angles of ±25° (PC-2) or angles ranging between -45→+45° (PC-1) with respect to the normal of the film's plane. Then, the 2nd ion irradiation at the same fixed angles of ±25° (PC-2) or ranging angles between -45→+45° (PC-1) but after 90° in-plane rotation of the polymer film (**Figures 3.30b,c**). Next, a chemical etching in 0.5 M NaOH at 70°C was done to adjust the nanopore diameters to ~40 and ~230 nm, and to adjust the membrane volumetric porosity $P_{polymer}$ around 20% (see **Figure 3.30d**).

The polycarbonate (PC) polymer membranes, supplied by it4ip (Belgium) were used as the porous host templates for the process development. They featured a thickness $t_{polymer}$ of 25 µm with a pore diameter D_{pore}, a pores density ρ_{pore}, a porosity $P_{polymer}$ and a tilt angle of the irradiation summarized in **Table 3.11**. On one face of the track-etched polymer membrane a multilayer of Cr/Cu/Au was deposited using electron-beam evaporation technique.

Table 3.11: Geometric parameters of commercial track-etched polycarbonate membranes

Polymer membrane	Thickness $t_{polymer}$ µm	Pore diameter D_{pore} nm	Pore density ρ_{pore} pores cm^{-2}	Porosity $P_{polymer}$ %	Tracks tilt angle α_{tilt} to film's normal
PC-1	25	40±5	10^8	20±5	range between -45°→+45°
PC-2	25	230±10	10^7	20±5	fixed to 25°

3.3.2 Second Step of Process: Electrochemical Deposition of $CoFe_2$ 3D Nanowire Networks into Supported Polymer Template

*Electrodeposition process was already discussed in detail in **Section 3.1.3** (p. 75)*

Experimental Details of $CoFe_2$ 3D Nanowire Networks Pulsed Electrodeposition

The 3D interconnected cylindrical nanochannels of a polymer membrane can be filled with a 3D network of the metal crossed nanowires using electrochemical deposition. Recently, the fabrication of the 3D interconnected NW networks was reported for the

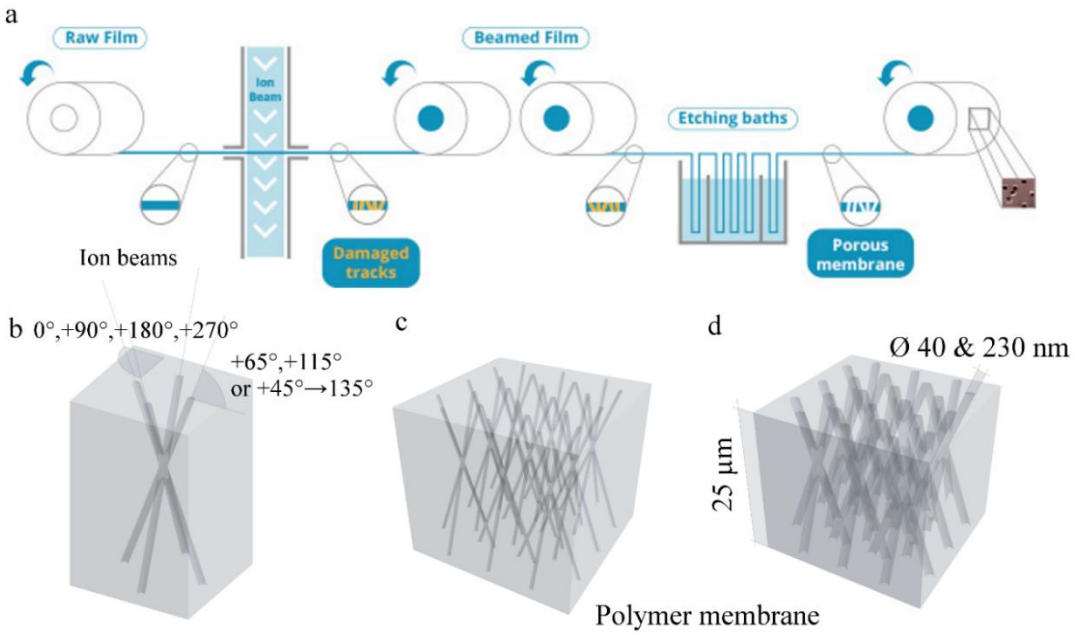

Figure 3.30: (a) Schematic fabrication of the trach-etched polycarbonate membranes (from *it4ip*, Belgium). **(b)** Heavy ions irradiation direction with respect to the film's plane, **(c)** Polycarbonate membrane with 3D nanochannel tracks network after heavy ion beam irradiation, **(d)** The membranes with D_{pore}~40 and 230 nm after chemical etching of the tracks

simple Ni, Co and Cu, for the alloys of $NiCo_x$ and $NiFe_x$, and for the Ni-Cu core-shell and the Co-Cu multilayers networks (*Araujo et al., 2015*; *Vlad et al., 2016*; *da Câmara Santa Clara Gomes et al., 2016a*, *2016b*; *da Câmara Santa Clara Gomes et al. 2017*; *Muench et al., 2017*). In the present work, the fabrication process via a pulsed electrodeposition of the metallic $CoFe_2$ 3D NW networks using supported porous polymer templates is developed.

The pulsed electrodeposition technique was previously described in detail for the deposition of the $CoFe_2$ nanowire and nanopillar arrays (see **Section 3.1.3**, p. 75 and **Section 3.2.3,** p. 97). The pulsed electrodeposition conditions for the growth of the $CoFe_2$ 3D NW network and the geometric parameters such as D_{NW} and h_{NW} are summarized in **Table 3.12**.

Table 3.12: Pulsed electrodeposition processing and geometric parameters of the fabricated $CoFe_2$ 3D nanowire networks within track-etched commercial polymer membranes with thickness of ~25 µm

Sample	Polymer membrane	Electrolyte composition	pH	Electrodeposition pulse voltage E (or current I) and pulse time t	D_{NW} nm	h_{NW} µm
$CoFe_2$	PC-1	$CoSO_4 \cdot 7H_2O$ (0.1 M) $FeSO_4 \cdot 7H_2O$ (0.14 M) H_3BO_3 (0.16 M)	3	E_1 = -1.5 V; t_{on} = 20 ms E_2 = -0.5 V; t_{off} = 80 ms	40	5
	PC-2				230	3.5

D_{NW} is a diameter of nanowires

H_{NW} is a height of $CoFe_2$ 3D nanowire network

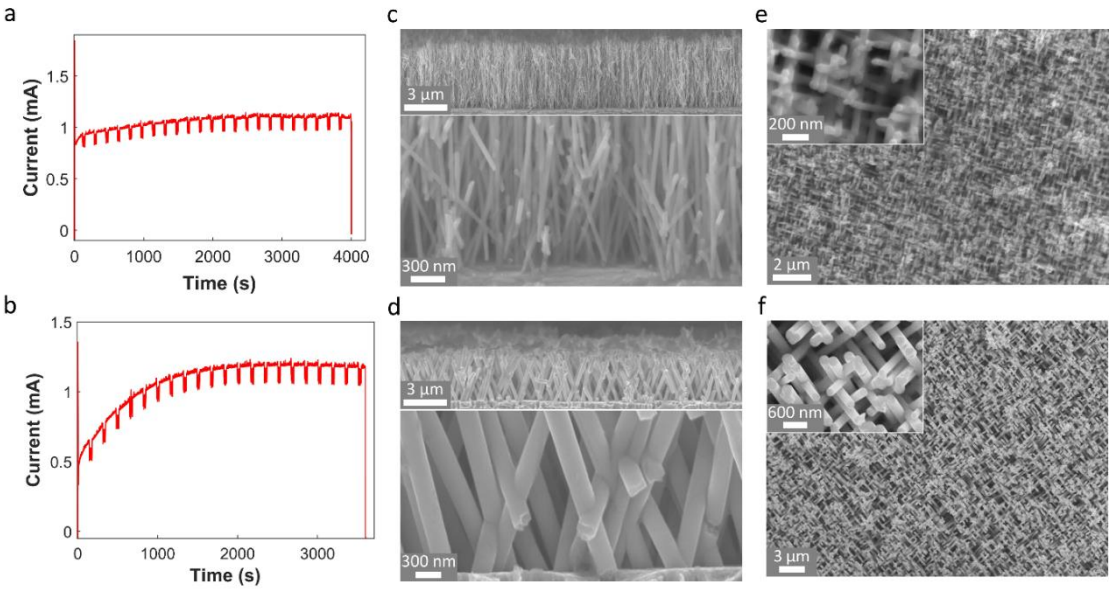

Figure 3.31: (a,b) Cathodic current plots for the electrodeposition of the $CoFe_2$ 3D nanowire networks with nanowire diameters of ~40 and 230 nm, respectively. Tilted cross section view **(c,d)** and top view **(e,f)** on the as-deposited 40 nm and 230 nm diameter $CoFe_2$ 3D NW networks, respectively

Generally, the 3D NW network is a robust nanostructure, which is self-supported and does not require template or substrate to maintain its geometry and architecture. Therefore, only the thickness of the polymer membrane ~25 µm limits the height of CoFe2 NW networks. The growing process of the $CoFe_2$ 3D NW networks with D_{NW} of 40 and 230 nm was investigated by monitoring the time dependence of the cathodic current shown in **Figures 3.31a,b**, respectively. The pulsed electrodeposition duration of 4000 sec leads to the $CoFe_2$ NW networks with h_{NW} ~5 µm. **Figure 3.31c** shows the tilted cross section view SEM image of the 5-µm-thick $CoFe_2$ 3D NW network with D_{NW} ~40 nm. The pulsed electrodeposition duration of 3500 sec leads to the $CoFe_2$ 3D

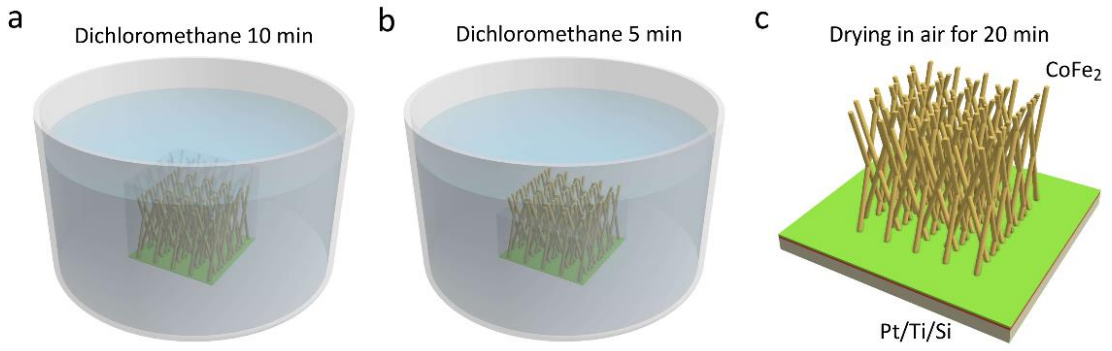

Figure 3.32: Flow chart of the polymer membrane chemical dissolution process. (a) Immersing of the polymer membrane hosting $CoFe_2$ 3D interconnected nanowire network into a vessel containing dichloromethane solution for 10 min, **(b)** Immersing in the 2nd dichloromethane solution for 5 min, **(c)** Drying of the $CoFe_2$ interconnected nanowire network in air for 20 min

NW networks with h_{NW} ~3.5 µm. **Figure 3.31d** shows the tilted cross section view SEM image of the 3.5-µm-thick $CoFe_2$ NW network with D_{NW} ~230 nm. The estimated deposition rate ~1.2 nm/sec is lower compared to the deposition rate of ~1.6 nm/sec observed for the $CoFe_2$ vertically aligned nanopillar arrays, which can be due to various factors such as the difference between the deposition areas, in the template porosities P_{AAO} and $P_{polymer}$, and the architecture of the cylindrical nanochannels. The top view SEM images of the $CoFe_2$ 3D NW networks (**Figures 3.31e,f**) confirm the values of the NWs diameters ~40 and ~230 nm, respectively, as expected from the morphological features of the track-etched polymer membranes (see **Table 3.11**).

3.3.3 Third Step of Process: Polymer Template Removal using Chemical Dissolution

After the $CoFe_2$ 3D NW networks pulsed electrodeposition, the hosting polymer template was dissolved using two identical dichloromethane CH_2Cl_2 (Merck, Darmstadt, Germany) chemical bath (see **Figure 3.32**). The sample was kept in the first bath for 10 minutes (**Figure 3.32a**), then in the second bath 5 minutes (**Figure 3.32b**), next the sample was dried in air leading to the free-standing $CoFe_2$ 3D NW network on Pt/Ti/Si substrate (**Figure 3.32c)**

3.3.4 Fourth and fifth steps of process: Ferroelectric $Pb_{0.52}Zr_{0.48}TiO_3$ layer deposition on $CoFe_2$ 3D nanowire network and $CoFe_2$ thermal oxidation

*Sol-gel deposition of FE layers was discussed in detail in **Section 3.1.2** (p. 60) and **Section 3.2.7** (p. 107)*

The preparation of the stoichiometric PZT solution with 0.4 M concentration using the inverse-mixing-order route was described in detail in **Figure 3.5** (p. 66) with additional modification for the PZT thin layer geometry explained in **Section 3.2.7** (p. 107).

Experimental Details of PZT Thik Layers Deposition

The PZT-CFO 3D interconnected ME nanocomposites were prepared using a similar sol-gel dip coating technique as for the preparation of the PZT-CFO nanopillar ME system (see **Section 3.2: the 6' processing step**). A schematic preparation of the PZT-CFO 3D interconnected ME system is shown in **Figure 3.33**.

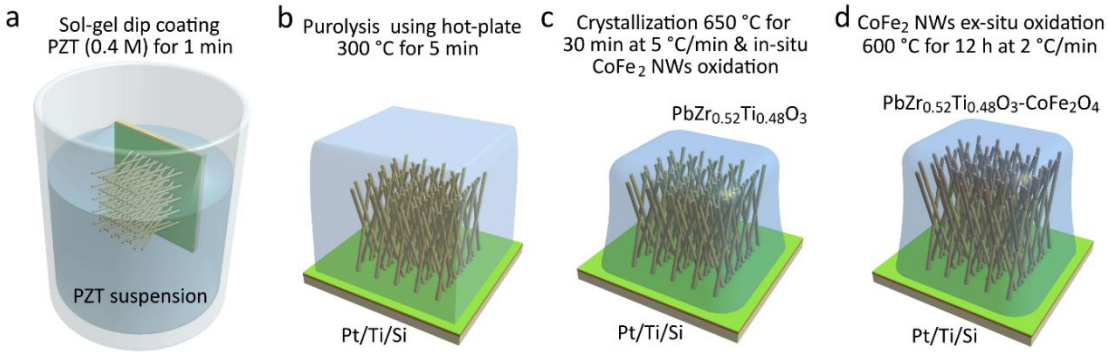

Figure 3.33: Schematic illustration of the preparation of the $PbZr_{0.52}Ti_{0.48}O_3$-$CoFe_2O_4$ 3D interconnected ME nanocomposite using a sol-gel dip coating technique. **(a)** Dip coating of the PZT solution layer on the $CoFe_2$ 3D nanowire network in 0.4 M PZT sol for 1 min and dehydration in the pre-heated oven at 150 °C for 5 min, **(b,c)** Two-step PZT thick layer crystallization with a hot-plate pyrolysis at 300 °C for 5 min **(b)** and a thermal crystallization in furnace at 650 °C for 30 min **(c)**. **(e)** *Ex situ* oxidation of the $CoFe_2$ 3D nanowire network embedded into the PZT layer using post-annealing at 600 °C for 12 h at 2 °C/min

The $CoFe_2$ 3D NW networks having an average height of 3.5-10 µm were considered. In the first step, after the chemical dissolution of the polymer template, a PZT sol layer was deposited on the $CoFe_2$ 3D NWs using a sol-gel dip coating, followed by the gelation (dehydration) at 150 °C for 5 min using the pre-heated oven (**Figure 3.33a**). After the gelation of the PZT sol layer, a common two-step crystallization approach was used to crystallize the PZT gel layer into the perovskite PZT thick layer through a hot-plate pyrolysis and a thermal crystallization in the furnace (*Yi et al., 1988*; *Kingon & Srinivasan, 2005*). The pyrolysis process was undertaken at 300 °C for 5 minutes by placing the sample on the pre-heated hot-plate inside a hood (**Figure 3.33b**). Typically, the pyrolysis parameters such as temperature and time affect the quality, the microstructure, the cracking, and the phase purity of the pyrolyzed layer. Next, the PZT layer was crystallized and densified by thermal annealing in a conventional furnace at 650 °C for 30 min at 5 °C/min heating rate (**Figure 3.33c**), and simultaneously the metal $CoFe_2$ 3D NW network was oxidized into the metal oxide CFO phase. To fully oxidize the $CoFe_2$ 3D NW network, the network was exposed to another step of *ex situ* thermal treatment at 600 °C for 12 h (**Figure 3.33d**). The resulting thickness of the vertically aligned PZT-CFO 3D interconnected ME nanocomposites was ~7 µm for PC-2 3D NW network and 12 µm for PC-1 3D NW network.

3.3.5 Summary of Methods and Synthesis Steps for Nanocomposites Preparation

Table 3.13: Summary of methods and preparation steps for multiferroic PZT-CFO core-shell nanocables, BTO/BSTO/PZT-CFO nanocomposites based on CFO nanopillar arrays, and PZT-CFO nanocomposites based on CFO 3D nanowire networks

Step №	Nanostructured composites				
	PZT-CFO core-shell nanocables		BTO/BSTO-CFO based on free-standing $CoFe_2$ nanopillars		
	Method	Description	Method	Description
1st	Inverse-mixing-order chelate route & Sol-gel dip-impregnation	PZT solution synthesis & Impregnation of PZT solution into 50-μm thick AAO template	Magnetron sputter deposition	Al/Ti/Pt/Ti multilayer deposition
2nd	Oven heating	Dehydration of PZT solution	Electrochemical anodization	Oxidation of 1-μm-thick Al layer
3rd	Furnace annealing	Crystallization of PZT nanotubes	Chemical dissolution	Pores widening & barrier dissolution
4th	E-beam deposition	Deposition of Au and Cu electrodes	Pulsed electrodeposition	Deposition of $CoFe_2$ nanopillar arrays
5th	Pulsed electrodeposition	Preparation of CoFe electrolyte & Deposition of $CoFe_2$ nanowires inside PZT nanotubes	Chemical dissolution	Removal of AAO template
6th	Chemical etching	Removal of Au and Cu cathode	RF magnetron sputter deposition	Deposition of BTO/BSTO layers on top of $CoFe_2$ nanopillars & $CoFe_2$ *in situ* oxidation into CFO
7th	Furnace thermal annealing	Thermal oxidation of $CoFe_2$ into $CoFe_2O_4$ phase		

Step №	Nanostructured composites			
	PZT-CFO based on free-standing $CoFe_2$ nanopillars		PZT-CFO based on free-standing 3D $CoFe_2$ nanowire networks	
	Method	Description	Method	Description
1st	Magnetron sputter deposition	Al/Ti/Pt/Ti multilayer deposition	E-beam deposition	Deposition of Au and Cu electrodes
2nd	Electrochemical anodization	Oxidation of 1-µm-thick Al layer	Pulsed electrodeposition	Preparation of CoFe electrolyte & Deposition of $CoFe_2$ 3D NW networks
3rd	Chemical dissolution	Pores widening & barrier dissolution	Chemical dissolution	Removal of polymer template
4th	Pulsed electrodeposition	Preparation of CoFe electrolyte & Deposition of $CoFe_2$ nanopillar arrays	Inverse-mixing-order chelate route & Sol-gel dip-coating	PZT solution synthesis & Deposition of PZT solution on CFO 3D NW networks
5th	Chemical dissolution	Removal of AAO template	Oven heating & Hot-plate heating & Furnace annealing	Dehydration of PZT solution & Pyrolysis of PZT layer & Crystallization of PZT nanotubes
6th	Furnace annealing	$CoFe_2$ nanopillars *ex situ* oxidation into CFO		
7th	Inverse-mixing-order chelate route & Sol-gel dip-coating	PZT solution synthesis & Deposition of PZT solution on CFO nanopillars		
8th	Oven heating & Hot-plate heating & Furnace annealing	Dehydration of PZT solution & Pyrolysis of PZT layer & Crystallization of PZT nanotubes		

3.4 Measurement and Characterization Techniques

The ME nanocomposites were characterized using various techniques for their structural and physical properties. Surface morphology was investigated using a High-resolution Scanning Electron Microscopy (HR-SEM) equipped with an Energy Dispersive X-ray Spectrometer (EDX) to perform elemental analysis. Structural characterization was performed using Transmission Electron Microscopy (STEM-BF). Crystal structure was characterized using an X-ray diffraction in Grazing Incidence X-ray configuration (GI-XRD), an *in situ* X-ray diffraction (*in situ* XRD), and a standard powder X-ray diffraction (XRD). Room temperature magnetic properties were investigated using an Alternating Gradient Magnetometer (AGM). Dielectric properties (capacitance and loss tangent) were measured using an impedance analyser. Ferroelectric properties were locally characterized using a Piezo-Response Force Microscopy (PFM). Magnetoelectric voltage coefficient (i.e. magnetoelectric voltage response) was measured using an adjusted Quantum Design Physical Property Measurement System (PPMS). In the next paragraphs, the working principals of the measurement systems are described.

3.4.1 Scanning Electron Microscopy Technique

The Scanning Electron Microscope (SEM) is a device for observation of specimen surfaces. Generally, when the specimen is irradiated with a fine electron beam, secondary electrons are emitted from the specimen surface. Topography of the surface can be observed by scanning of the electron beam over the surface and acquisition of the image detecting secondary electrons. The SEM requires an electron optical system to produce an electron probe, a specimen stage to place the specimen, a secondary-electron detector to collect secondary electrons, an image display unit, and an operation system. **Figure 3.34a** shows a basic construction of the SEM, where the electron optical system consists of an electron gun, a condenser lens and an objective lens to produce an electron beam, a scanning coil to scan the electron probe, and other components.

The electron optical system (inside the microscope column) and a space surrounding the specimen are kept at vacuum.

Three types of electron gun are generally used, the most common is a thermionic emission gum, and other electron guns are the field-emission electron and the Schottky-emission electron gun. In this work, a JEOL 7600F SEM was used, where to deliver

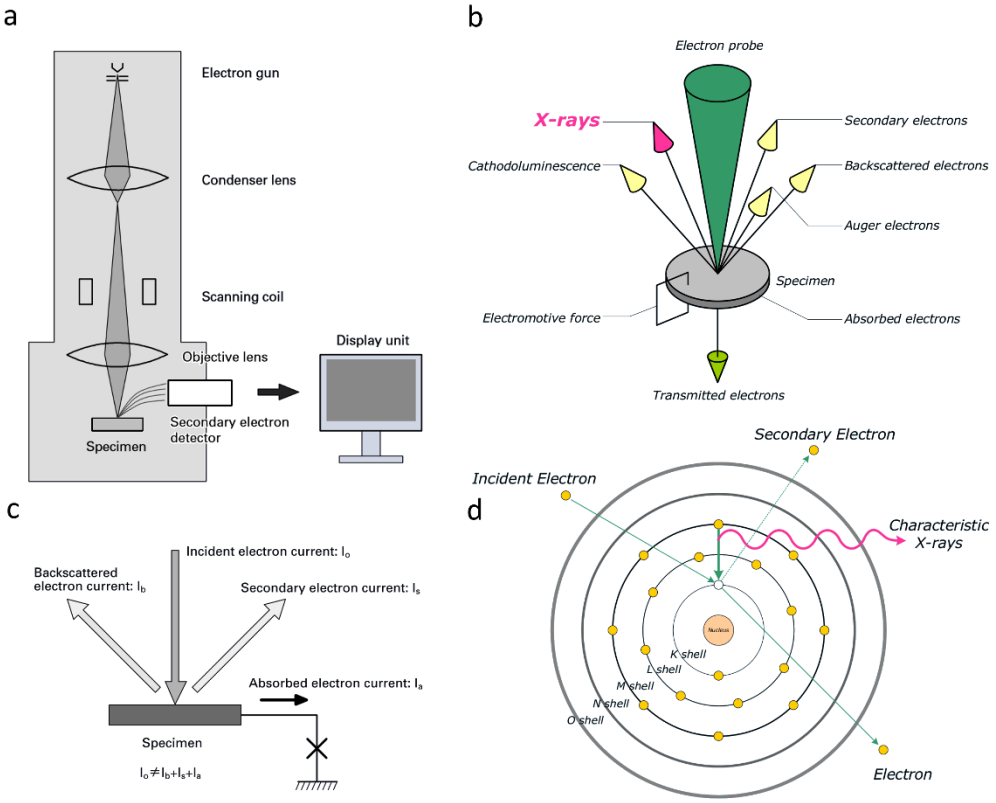

Figure 3.34: (a) Basic construction of a SEM, **(b)** emission of various electron and electromagnetic waves from the specimen, **(c)** electric flow in a nonconductive specimen, **(d)** principle of the generation of characteristic X-rays.

ultrahigh resolution combined wide range of electron probe (electron beam) currents (1pA to more than 200nA) Schottky field emission gun was used.

The secondary electron (SE) gun utilizes the Schottky-emission effect that takes place when a high electric field is applied to a heated metal surface. An advantage of the SE gun is that the electron- beam current is highly stable because the emitter, which is placed in an ultrahigh vacuum of about 10^{-7} Pa, is kept at a high temperature and no-gas absorption occurs.

The SEM generally uses a magnetic lens. When you pass a direct electron current through a coil-wound electric wire, a magnetic field is formed, and a lens action is produced on an electron beam. The main feature of the magnetic lens is that when you change the current passing through the coil, the strength of the lens is also changed. Placing a lens below the electron gun allows you to adjust the diameter of the electron beam. The electron beam from the electron gun is focused by the two-stage lenses, which combines the condenser and objective lenses, and a small electron beam is produced.

The secondary electron detector is used for detecting the secondary electrons emitted from the specimen. The detector is incorporated either in the specimen chamber, or if the SEM is equipped with a strongly excited objective lens for higher resolution,

a secondary electron detector is placed above the objective lens and the secondary electrons are detected by utilizing the lens magnetic fields.

Figure 3.34b shows a schematic diagram illustrating various signals emitted from the specimen when the incident electron beam enters the specimen. The SEM uses these signals to observe the specimen surface (or just beneath the surface). When the incident electron beam enters the specimen, secondary electrons are produced from the emission of the valence electrons of the constituent atoms in the specimen. Since the energy of secondary electrons is very small, only those generated at the top surface of the specimen are emitted outside of the specimen. Backscattering electrons are those scattered backwards and emitted out of the specimen, when the incident electrons are scattered in the specimen. Since backscattered electrons have higher energy than secondary electrons, a relatively deep region can be analysed by the backscattering electrons.

The electrons that entered the specimen lose their energy and they are absorbed in the specimen. If a specimen is conductive, the electrons from through the specimen stage, but if a specimen is insulating, the electrons stop in the specimen and the charging occurs. **Figure 3.34c** shows the schematic illustration of the charging. If some reason causes the number of the electrons exiting from the specimen to be larger than that flowing to the specimen, the specimen is positively charged. The most typical method to prevent the charging is conductive coating of an insulating specimen with a highly-conductive thin metal layers with a thickness ranging from a few to 10 nm (e.g., Au, Pt, Au-Pd, Pt-Pd).

To examine the cross section of the (1-3) ME nanopillar based nanocomposite, the thin layers were first frozen inside liquid nitrogen for 2 minutes, then the layers surfaces were scratched using diamond tip and by pressing on one side of scratch, the samples were broken. Finally, the thin layer samples were fixed on the specimen holder using double sided carbon tape in a way, that the electron beam is irradiated normal to the cross section of thin layers.

To observe the surface of nanotubes or core-shell ME nanocables, AAO porous membranes hosting nanotube and nanocable arrays were chemically dissolved on the double-sided carbon tape (see **Figure 3.11**, p. 82).

3.4.2 Energy Dispersive X-ray Spectrometer Characterization

When the incident electrons enter a specimen, various electrons and electromagnetic waves are emitted from the specimen surface (**Figure 3.34b**). **Figure 3.34d** shows the schematic diagram of the generation of characteristic X-rays. When electrons in the inner shells are emitted from the constituent atoms in the specimen due to the irradiation of the incident electrons, the vacant orbits are filled with outer-shell electrons, and the substance emits X-rays whose energies correspond to the energy

difference between the outer-shell electrons and the inner-shell electrons. These X-rays are used for elemental analysis. The X-rays that are emitted by the excitation of atoms and emission of the electrons in K shells are called “K lines”, whereas those emitted by the L and M shells are called “L lines” and “M lines”, respectively. As the constituent element is heavier, the X-rays energy is higher, therefore high-energy incident electrons are required to excite X-ray from heavy elements.

The EDX is used to analyse X-ray spectra by measuring the energies of the X-rays. The advantage of the EDX is that the X-rays from a wide range of elements are analysed simultaneously. X-ray spectra enable us to perform quantitative analysis that identifies what elements are present in a specimen area irradiated by an electron beam. Three analysis modes are available: Point analysis to obtain a spectrum from a point irradiated with an electron beam, Line analysis to display one-dimensional distribution of elements on a specified line, and Mapping to display two-dimensional distributions of elements in a specified area. Since the intensity of X-rays is proportional to the concentration of the corresponding element, quantitative analysis can be performed. If you try to analyse an insulating specimen without highly-conductive coating, this specimen is analysed with a low accelerating voltage caused by the charging effect, thus, X-rays with high excitation energies cannot be detected, and the accuracy of quantitative analysis is degraded.

3.4.3 Transmission Electron Microscopy Technique

In a conventional TEM (**Figure 3.35**), a thin specimen is irradiated with an electron beam, and the working principle of the TEM is similarly to the SEM. The TEM requires higher voltage of standard instruments compared to the SEM, typically around 100-200 kV (*Reimer & Kohl, 2008*). Electron beams are irradiated in the electron gun by Thermal Electron, Cold Field- or Schottky- emission. A three-, four-step condenser lenses system enables the range of the luminescence aperture and the area of the specimen irradiated. The electron intensity distribution after the sample is displayed with a lens system formed of several lenses, onto a fluorescence screen. The image is recorded through direct illumination of a photoemulsion of a signal plate inside the vacuum, or through a fluorescent screen connected by a fiber-optic plate to a Charge-Coupled camera.

The microscope is also affiliated with a selected-area electron-diffraction (SAED), which gives information about crystal structure and orientation. In terms of the crystal lattice and its defects in crystalline material analysis, integration of electron diffraction and the different imaging modes is a very important characteristic of TEM. With SAED analysis, through changing the excitation of the diffraction or intermediate lens, it is possible to switch modes and to choose the diffraction image from areas 0.1-1 μm in diameter. A STEM operating at an accelerating voltage of 200 kV was used for

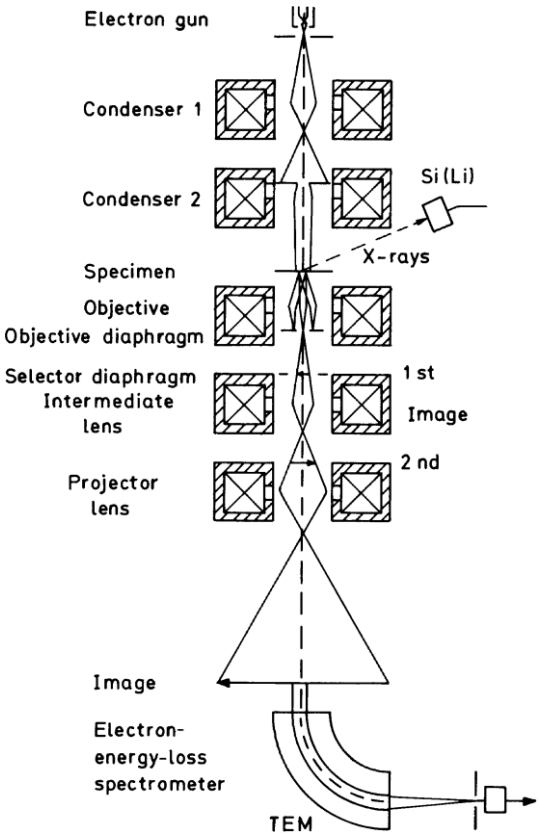

Figure 3.35: Schematic electron beam path for a TEM

observation. The STEM detector with bright-field (BF) imaging mode coupled with EDX was used to analyse elemental spectra mapping.

To examine the nanotube and nanocable specimens with TEM, hosting AAO membrane was removed by repeating a few times the dissolution process: (1) chemical dissolution in 5 NaOH solution for 1 min; (2) mixing and agitated during 5 minutes at room temperature with a vortex shaker; (3) the precipitates were centrifuged for 5 minutes and the NaOH solution was poured out; (4) the precipitates were washed with ethanol and distilled water. The above-mentioned steps were repeated until the colloid had a homogeneous grey colour. Finally, the specimens were dispersed in ethanol using an ultrasonic bath and 1-2 drops of these solutions were mounted on a TEM mesh grid.

3.4.4 X-ray Diffractometer Crystal Structure Analysis

X-ray diffraction (XRD) is a technique used to measure the atomic arrangement of specimens (*Cullity, 1978; Jenkins & Snyder, 1996*). When a monochromatic X-ray beam hits a specimen, in addition to absorption and other phenomena, we observe X-ray scattering with the same wavelength as the incident beam, called coherent X-ray scattering. The coherent scattering of X-rays from a specimen is not evenly distributed

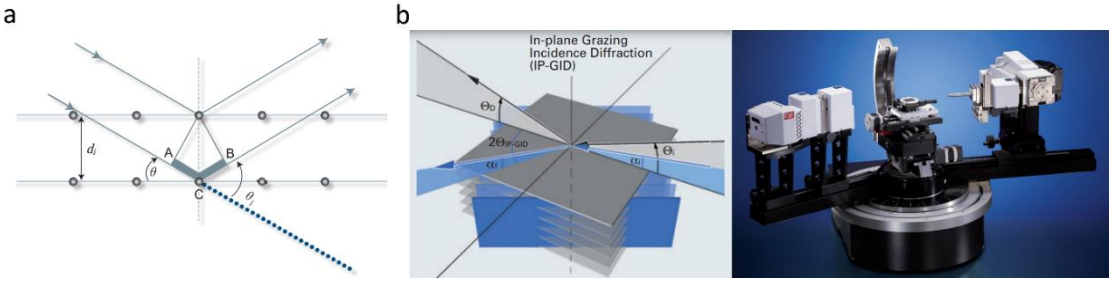

Figure 3.36 (a) The incident X-rays and reflected X-rays make an angle of Θ_i symmetric to the normal of the crystal plane. **(b)** the principle of the Grazing Incidence X-ray diffraction and the GI-XRD illustration

in space but is a function of the electron distribution in the specimen. The atomic arrangement in specimens can be ordered like a single crystal or disordered like glass or liquid. As such, the intensity and spatial distributions of the scattered X-rays form a specific diffraction pattern which is the "fingerprint" of the specimen.

There are many theories and equations about the relationship between the diffraction pattern and the material structure. Bragg's law is a simple way to describe the diffraction of X-rays by a crystal. In **Figure 3.36a**, the incident X-rays hit the crystal planes in an angle Θ, and the reflection angle is also Θ. The diffraction pattern is a delta function when the Bragg condition is satisfied:

$$n\lambda = 2d_i \times sin\Theta_i, \tag{3.15}$$

where the wavelength λ is defined by the X-ray tube used, peak positions $2\Theta_i$ are defined by the lattice spacing d_i, and peak intensities are defined by the geometrical and elemental structure of the lattice.

For real specimens, the diffraction patterns are different from the theoretical delta functions with discrete relationships between points to continuous distributions with spherical symmetry. The diffraction beams from a single crystal point to discrete directions each corresponding to a family of diffraction planes. The diffraction pattern from a polycrystalline specimen forms a series of diffraction cones if a large number of crystals oriented randomly in the space are covered by the incident X-ray beam. Each diffraction cone corresponds to the diffraction from the same family of crystalline planes in all constituent grains. Polycrystalline materials consist of many crystalline domains, numbering from two to more than a million in the incident beam. In single-phase polycrystalline materials, all of these domains have the same crystal structure with multiple orientations. Polycrystalline materials could also be multiphase materials with more than one kind of crystal blended together. Polycrystalline materials can also be bonded to different materials such as thin films on single crystal substrates. The crystalline domains could be embedded in an amorphous matrix or stressed from a forming operation. Usually, the sample undergoing X-ray analysis has a combination of these effects. Polycrystalline diffraction deals with this range of scattering to determine the constituent phases in a material or the effect of processing conditions on

the crystallite structure and distribution. In this work, a standard powder diffractometer PANalytical X'Pert Pro with Cu radiation was used.

Nonambient temperature measurements of the ME core-shell nanocables were conducted by the *in situ* X-ray diffraction using a powder diffractometer PANalytical X'Pert Pro Anton Paar HTK1200 (1200 °C) with Co anticatode.

Grazing Incidence X-ray Diffraction Technique

Modern thin-film technology deals with increasingly thinner and more complex layered structures. The analysis of such challenging samples pushes classic diffraction methods to their limits. The Bruker D8 Discover has a winning combination of powerful X-ray sources, dedicated optics, the most sensitive 1- and 2-dimensional detectors, and a tilt stage to assure that no reflections are lost (**Figure 3.36b**). It directly evaluates the in-plane lattice parameters (perpendicular to the sample surface), determines the in-plane crystallite size and measures the in-plane texture and the domain structure. As an added feature, these parameters can be determined as a function of depth.

The crystal structure of the vertically aligned nanopillar arrays and (1-3) ME nanopillar based nanocomposites was characterized using the Bruker D8 Discover diffractometer in grazing incidence X-Ray diffraction configuration (GI-XRD), operating with CuKα radiation ($CuK\alpha_1$ = 1.5406 Å, $CuK\alpha_2$ = 1.5443 Å) and with an incident beam angle of 2°.

3.4.5 Alternating Gradient Magnetometer Measurement of Magnetic Properties

The alternating gradient (field) magnetometer (AGM) is a modification of the well-known Faraday balance that determines the magnetic moment of a sample by measuring the force exerted on a magnetic dipole by a magnetic field gradient. The principle of the instrument is schematically illustrated in **Figure 3.37** (*Czichos et al., 2011*). The force is measured by mounting the sample on a piezoelectric bimorph, which creates a voltage proportional to the elastic deformation and, hence, to the force acting on the sample. By driving an alternating current through the gradient coils, with lock-in detection of the piezo voltage and by tuning the frequency of the field gradient to the mechanical resonance of the sample mounted on the piezoelectric element by a glass capillary a very high sensitivity can be achieved that approaches that of a SQUID magnetometer under favourable conditions. The main advantage of the AGM is its relative immunity to external magnetic noise and the resulting high signal-to-noise ratio and short measuring time. A major disadvantage is the difficulty in obtaining an absolute calibration of the magnetic moment because the signal is not only proportional to the sample magnetic moment but also to the Q-factor of the sample-capillary-piezo

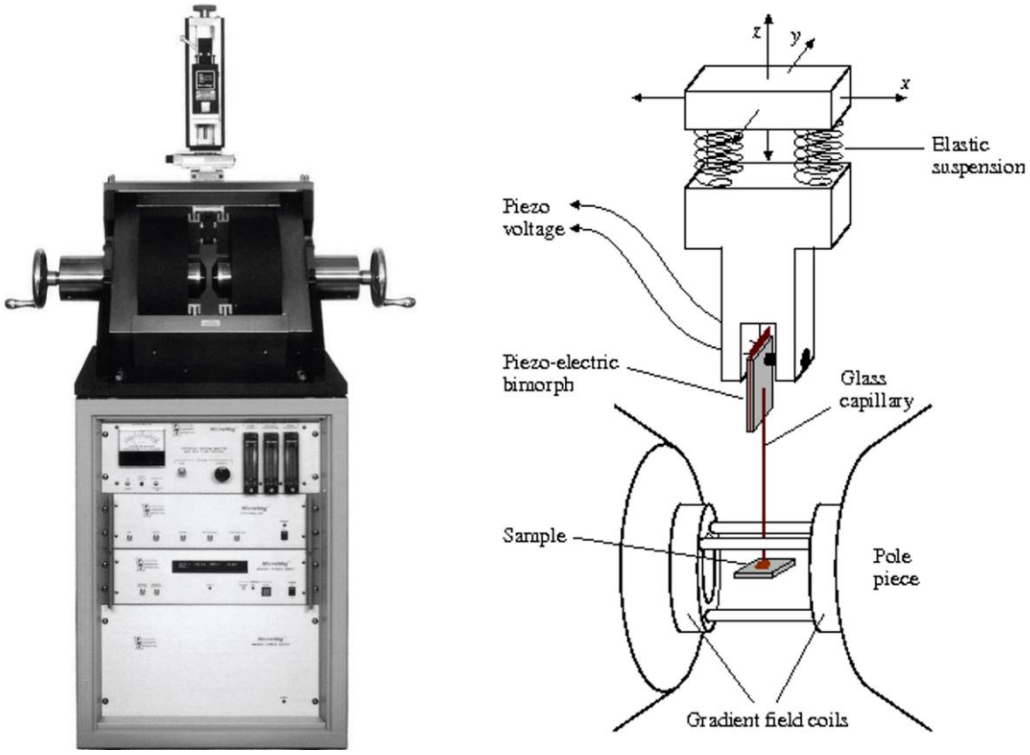

Figure 3.37: Alternating (field) gradient magnetometer MicroMag 2900 and principles of the AGM; the gradient field coils are fed with an alternating current with a frequency tuned to the mechanical resonance of the specimen-capillary-piezo system. The specimen and gradient coils are mounted between the pole pieces of an electromagnet

system, which varies with sample mass and temperature. This problem can be overcome by inserting a small calibration coil close to the sample position. Also, difficulty in obtaining an exact angular orientation of the sample relative to the external magnetic field is a drawback of this instrument. Room temperature magnetic properties of the magnetic and ME specimens were investigated using an alternating gradient magnetometer (PMC MicroMag AGM) with a maximum magnetic field of ±14 kOe.

3.4.6 Impedance Analyser Characterization of Dielectric Properties

The dielectric properties are governed by reorientational motions of molecular dipoles (dipolar relaxation) and motions of electrical charge carriers (electrical conduction), which leads to continuous dielectric dispersion and absorption that is observed in the frequency range of 10^{-6} –10^{12} Hz.

Permittivity describes the interaction of a material with an electric field. The principal equations are shown in **Figure 3.39a**. Dielectric constant (κ) is equivalent to the complex relative permittivity (ε_r*) or the complex permittivity (ε*) relative to the

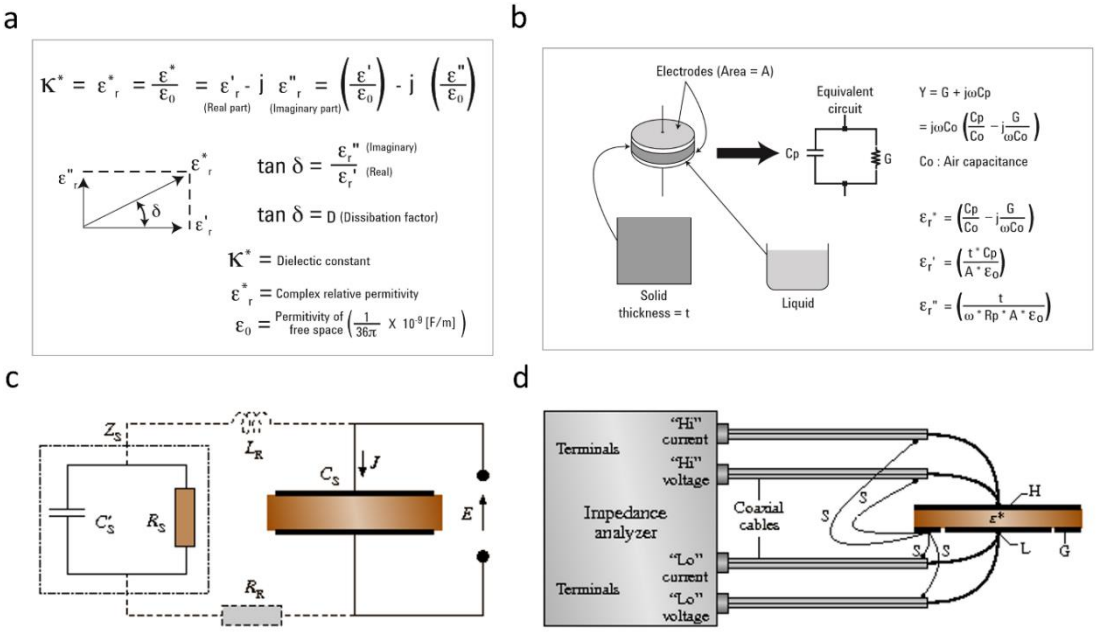

Figure 3.39: (a) Definition of relative complex permittivity (ε_r*), **(b)** parallel plate method, (c) equivalent electrical circuit of a dielectric material, **(d)** a 3T cell to an 4T impedance analyser. H and L are the high and low potential electrodes respectively; G is the guard electrode; S are the return current loops of coaxial shield connection (from *Czichos et al., 2011*)

permittivity of free space (ε_0). The real part of complex relative permittivity (ε_r') is a measure of how much energy from an external field is stored in a material; $\varepsilon_r' > 1$ for most solids and liquids. The imaginary part of complex relative permittivity (ε_r'') is called the loss factor and is a measure of how dissipative or lossy a material is to an external field. The loss factor includes the effects of both dielectric loss and conductivity.

When complex permittivity is drawn as a simple vector diagram as shown in **Figure 3.39a**, the real and imaginary components are 90° out of phase. The vector sum forms an angle δ with the real axis (ε_r'). The tangent of this angle, tanδ or loss tangent, is usually used to express the relative "lossiness" of a material. The term "dielectric constant" is often called "permittivity" in technical literature. In this application note, the term permittivity will be used to refer to dielectric constant and complex relative permittivity.

When using an impedance-measuring instrument to measure permittivity, the parallel plate method is usually employed. An overview of the parallel plate method is shown in **Figure 3.39b**. The parallel plate method, also called the three-terminal method in ASTM D150-98, involves sandwiching a thin sheet of material or liquid between two electrodes to form a capacitor. The measured capacitance is then used to calculate permittivity. In an actual test setup, two electrodes are configured with a test fixture sandwiching dielectric material. The impedance-measuring instrument would measure vector components of capacitance (*C)* and dissipation (*D*).

In the frequency range below 1 GHz, the dielectric specimen maybe treated as a circuit of lumped parameter components (*Czichos et al., 2011*). Because the mathematical manipulations are relatively simple, the lumped parameter circuit approximate equations can always be used when they yield the required accuracy over sufficiently broad frequency range. The equivalent complex impedance Z_s of the relaxation circuit shown in **Figure 3.39c** can be measured to determine the complex capacitance C_s and then the material's relative complex permittivity ε_r^*. In the following discussion complex impedance $Z_s=Z_s'-iZ_s''$ is considered to be a constant proportionality of sinusoidal voltage and current. Parameters shown in bold face indicate complex (vector) quantities. When a capacitor is filled with a dielectric material the resulting capacitance is C_s and the permittivity is defined by

$$\varepsilon_r^*(\omega) = \varepsilon_r'(\omega) - i\varepsilon_r''(\omega) = \frac{C_s(\omega)}{C_0}, \tag{3.16}$$

where C_0 is the capacitance of the empty cell and ω is the angular frequency ($\omega=2\pi f$).

If the sinusoidal electric field $E(\omega)=E_0 \exp(i\omega t)$ is applied to C_s, then the permittivity can be determined by measuring the complex impedance Z_s of the circuit.

$$\frac{1}{Z_s(\omega)} = i\omega C_s, \tag{3.17}$$

$$\varepsilon_r^*(\omega) = \frac{1}{i\omega Z_s C_0}. \tag{3.18}$$

Consistent with the electrical equivalent circuit of the real capacitance C_s' in parallel with a resistance R_s the impedance is given by

$$\frac{1}{Z_s(\omega)} = \frac{1}{R_s} + i\omega C_s', \tag{3.19}$$

and the direct expressions for ε_r' and ε_r'' are

$$\varepsilon_r' = \frac{C_s'}{C_0}, \tag{3.20}$$

$$\varepsilon_r'' = \frac{1}{\omega R_s C_0}. \tag{3.21}$$

The capacitance of the empty cell C_0 (cell constant) is typically determined from the specimen geometry or measurements of standard materials with known permittivity.

In the frequency range of up to about 10^8 Hz, a four terminal (4T) impedance analyser can be employed to measure complex impedance of the capacitance C_s and then the permittivity can be calculated. The 4T methodology refers to the direct phase sensitive measurement of the specimen's current and voltage. The recently developed

dielectric instrumentation incorporates into one device a digital synthesizer-generator, sine wave correlators and phase sensitive detectors, capable of automatic impedance measurements from 10^{-2} to 10^{13} Ω. The broad impedance range also allows a wide capacitance measurement range with resolution approaching 10^{-15} F. The instrumentation should be calibrated against appropriate impedance standards. The dielectric samples typically utilize a parallel plate or cylindrical capacitor geometry (**Figure 3.39b**) having capacitances of about 10 pF to several hundred pF. The standard measurement procedures recommend a three-terminal (3T) cell configuration with a guard electrode (G), which minimizes the effect of the fringing and stray electric fields on the measurements. The optimal method for connecting a 3T circular cell to a 4T impedance analyser is shown in **Figure 3.39d**.

The high current and voltage terminals should be connected via coaxial cables directly to the unguarded electrode H, while the low current and voltage should be connected to the electrode that is surrounded by the guard electrode. Note that the return current loop of coaxial shields connections S should be short and connected to G at a single common point. The return current loop S is absolutely necessary for accurate impedance measurements, especially above 1 MHz. In a two-terminal configuration (2T) without the guard electrode, the connections S should be simply grounded together.

The permittivity, dielectric loss and the relaxation frequency are temperature dependent. Therefore, it is essential to measure the specimen temperature and to keep it constant (isothermal conditions) during the measurements.

Capacitance-Voltage $C(V)$ curves are important in characterization of the switching properties of ferroelectric thin layers (*Scott 1993*). Some textbooks suggest that $C(V)$ data are the voltage derivative of the Polarization-Voltage $P(V)$ hysteresis data. In fact, $C(V)$ data and hysteresis data are in general redundant. The reason is that they are carried out at different frequencies. Hysteresis curves are almost always run at 50 Hz (Europe), 60 Hz (USA), or 1 kHz, whereas the $C(V)$ data are run with a very slow linear voltage ramp (whose Fourier transform is of order 0.1 Hz) with a small high frequency "ripple" (few kHz) superimposed. Since the overall characteristic frequency of the $C(V)$ probe is slow, there is time for space charge at interface to respond to it. A subtle comparison of the two values would allow quantitative evaluation of the polarization due to the lattice switching and the polarization due to switched interfacial space charge.

Details of Dielectric Properties Measurement on Multiferroic Nanocomposite

Pt top electrodes having approximate diameters of 300 μm and 600 μm were deposited on the surface of the nanocomposites by rf magnetron sputtering through a shadow mask for the dielectric and magnetoelectric characterizations, followed by the gluing of silver Ag wires with the wire thickness of 50 μm using a commercial Ag paste (see **Figure 3.40**). The dielectric properties (capacitance and loss tangent) were measured

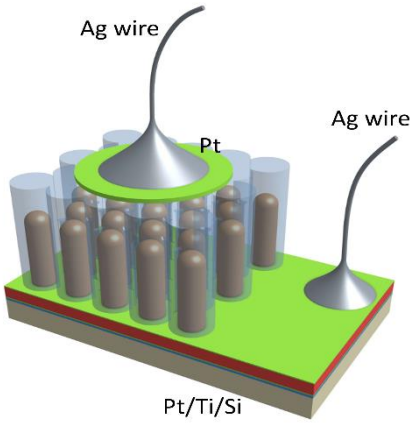

Figure 3.40 Sputtering of the top Pt contacts and pasting of the Ag wires for the dielectric characterization

as a function of temperature (from 80 K to 400 K), frequency (from 100 Hz to 1 MHz), and bias voltage (with a maximum electric field ±5 V) using a HP 4194A impedance analyser. The effective permittivity and loss tangent of the deposits were calculated as $\varepsilon = C \times t/(\varepsilon_0 \times S)$ and $\tan\delta = D$, using the measured capacitance value C [F], $\varepsilon_0 \approx 8.854\times10^{-12}$ [F/m], the top Pt electrode's surface area S [m^2], the total average thickness of the deposit t [m] and the dissipation factor (measured value) D, assuming that the nanocomposite can be considered as a continuous material.

3.4.7 Scanning Probe Microscope Technique

Scanning probe microscope (SPM) was developed to detect small interactions between a scanning probe tip and the specimen's surface under investigation (*Li et al., 2015b*). **Figures 3.41a,b** show schematic illustration of an atomic force microscope (AFM) system consisting of four main components: (1) a cantilever that serves as a force sensor; (2) a laser photodiode that measures cantilever deflection; (3) a scanner that moves the sample relative to the cantilever in three dimensions; (4) a data acquisition and control unit. When the cantilever is brought close to the specimen's surface by an actuator in z direction, the interaction between the probe tip and the specimen's surface will attract or repel the cantilever, resulting in a deflection s that is measured by photodiode. If the spring constant k_{spring} of the cantilever is known or calibrated, then the interaction force is given by

$$F_{tip\ sample} = k_{spring} \times s. \tag{3.22}$$

Meanwhile the displacement Z of the entire cantilever along the z axis is independently controlled, and the tip-sample distance D_{tip} is given by

$$D_{tip} = Zs, \tag{3.23}$$

when an appropriate sign convention is adopted, allowing us to measure the tip-sample interaction force $F_{tip\text{-}sample}$ as a function of their distance D_{tip}.

Piezoresponse Force Microscopy (PFM) is a technique based on contact mode that maps out the inverse piezoelectric effect on a sample. The sample is electrically stimulated, and the topographic response of the sample is monitored using lock-in techniques. Amplitude and phase information reveal information about the strength and direction of the polarization on the sample.

The imaging mechanism of piezoresponse force microscopy (PFM) is based on the detection of dynamic strain or displacement of the specimen. An *ac* voltage is applied to the specimen through the conductive probe in contact with the sample, which often serves as the top electrode, with the bottom electrode grounded underneath the specimen (see **Figure 3.41c**). Since the probe tip is in contact with the specimen's surface, the cantilever is bent upward, and the set point (force exerted by the cantilever to the specimen's surface) is usually fixed by feedback control. Therefore, the

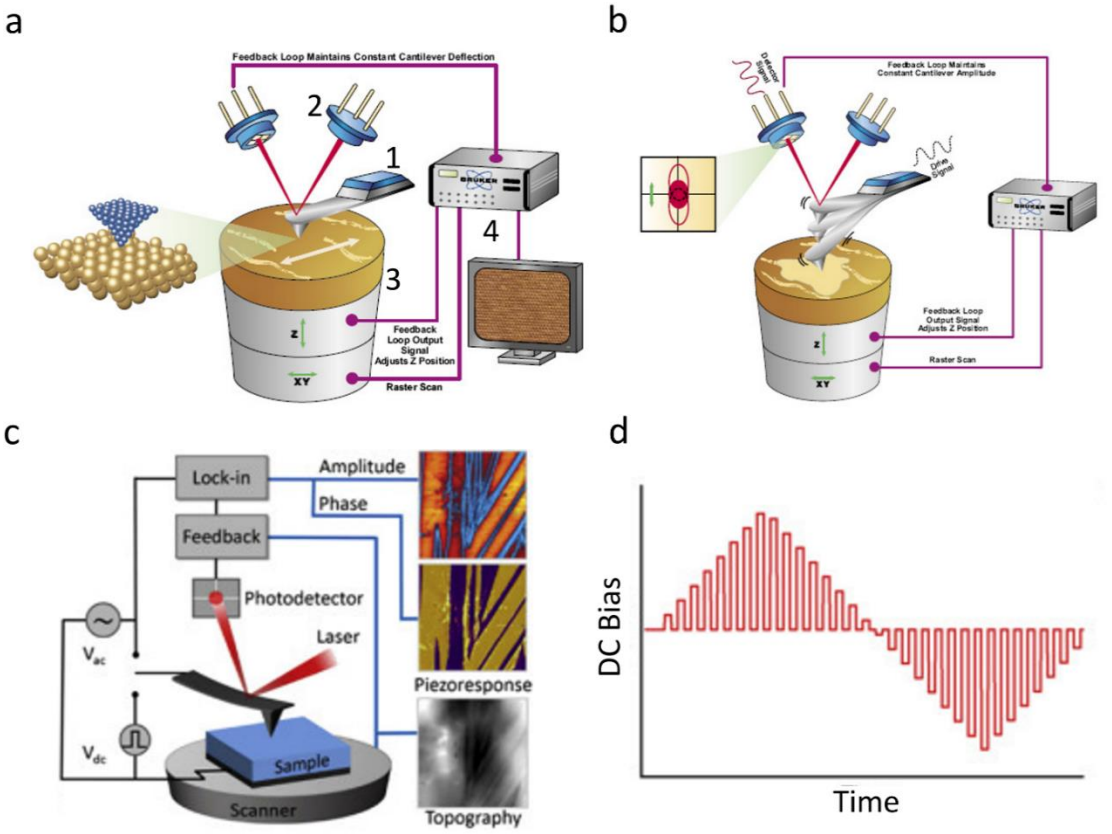

Figure 3.41: Configurations of a typical SPM systems. **(a)** Contact Mode AFM. The probe is a microfabricated cantilever with a sharp tip. Tip and sample are in perpetual contact during the raster-scan. Detector signal is a measure of cantilever deflection in z. In feedback mode, output signal usually adjusts the z position of the scanner to maintain a deflection setpoint. **(b)** Tapping Mode AFM. The probe is a microfabricated cantilever with a sharp tip. A drive signal, applied to the "tapping piezo," mechanically oscillates the probe at or near its resonance frequency (usually the fundamental resonance). Detector signal is cantilever oscillation amplitude, or phase (relative to drive signal). In feedback mode, output signal usually adjusts the z position of the scanner to maintain an (rms) amplitude setpoint. **(c)** Configuration of a typical PFM setup. **(d)** Voltage profile for *dc* manipulation, triangular wave (from *Li et al., 2015b*)

topography of the specimen's surface can be mapped simultaneously with the surface displacement. The applied electric field will trigger a localized surface vibration of the specimen due to its electromechanical coupling, which in turn induces vibration of the cantilever that can be measured by the photodiode.

The surface displacement induced in PFM are relatively small, in the range of picometers (pm), thus it is necessary to amplify the signal to enhance the sensitivity. This is often achieved by exciting the surface vibration at the cantilever-sample resonance and measuring the resulting displacement using a lock-in amplifier at the driving frequency (**Figure 3.41c**). The lock-in enables to measure the displacement at the frequency of interest with the noise at the other frequencies filtered, thus enhancing the signal to noise ratio. The relationship between driving and measuring frequencies can be adjusted. When the driving frequency is at the cantilever-sample resonance, the magnitude of the displacement is amplified by orders of magnitude allowing to detect displacement in the pm range.

In order to maintain high sensitivity, it is thus necessary to drive the *ac* voltage at cantilever-sample resonant frequency. However, during scanning, the resonant frequency often shifts due to changes in contact stiffness, which may be caused by material heterogeneity or topography variation. Thus, the resonant frequency should be tracked during scanning.

In addition to exciting surface vibration of specimens using *ac* voltage, *dc* voltage can be applied as well to switch the dipoles of the specimen (*Li et al., 2015b*). This is often conducted using a sequence of *dc* voltages in triangular waveform, on top of which *ac* voltage is simultaneously exerted to excite surface vibration (see **Figure 3.41d**). For ferroelectric materials, the sequence of *dc* voltages would switch the dipoles of the specimen when the coercive field is exceeded, and this is referred to as a switching spectroscopy PFM (SS-PFM) (*Jesse et al., 2006*). Between each *dc* bias step, the so-called ON state, the voltage is stepped back to OFF state with zero voltage, and the response is usually measured during the OFF state to minimize the electrostatic interactions between the probe and specimen.

DC voltage can also be applied on the desired area of the specimen's surface. While scanning a desired region on the surface, positive and negative voltages can be applied, which changes the specimen's polarization direction, resulting in a change of structure in the specimen. For FE materials, this corresponds to positively and negatively polarized regions, which can be observed on both PFM amplitude and phase mapping.

Details of AFM Measurements

The surface morphology of the nanotubes and core-shell nanocables was characterized using a Dimension Icon Bruker atomic force microscope in the tapping mode. Silicon

probes (Nanoscope, PPP-FMR 20, spring constant 0.9365 N m^{-1}) were used for the measurements. The working frequency ω_{AC} = 66 kHz was selected.

3.4.8 Piezoelectric Force Microscope Characterization of Microscopic Ferroelectric Properties

Piezoresponse Force Microscopy measurements were performed by the group of Prof. Bernard Nysten at Bio and Soft Matter division of Institute of Condensed Matter and Nanosciences (MICA platform), Université catholique de Louvain, Belgium.

Details of PFM Measurements on PZT Nanotubes and Core-Shell Nanocables

The ferroelectric properties of the PZT nanotubes and core-shell nanocables were investigated by PFM using a Dimension Icon Bruker AFM in contact mode. Pt/Ir-coated conductive probes (Bruker, SCM-PIT, nominal spring constant 2.8 N m^{-1}, nominal tip radius 20 nm) were used for the measurements. A nonmagnetic tip holder was used, the PFM was measured by applying to the bottom Pt layer electrode a small oscillating voltage of amplitude V_{AC} and frequency f_{AC}, and to the PFM tip a static voltage V_{DC}. The working frequency f_{AC} = 300 kHz was selected, and the corresponding V_{AC} = 2 V. The switching spectroscopy-PFM (SS-PFM) curves in which the PFM amplitude and phase of a single PZT nanotube and core-shell PZT-CFO nanocable were measured by ramping DC bias in a triangular waveform from -10 V to 10 V, then back to -10 V.

3.4.9 Magnetoelectric Voltage Response Measurement of Magnetoelectric Properties

To measure direct ME effect in terms of magnetically induced voltage ($\alpha_E = \partial E/\partial H$) or charge ($\alpha_P = \partial P/\partial H$), it is common to record the dynamic change in voltage or charge induced by the application of a magnetic field (*Wang et al., 2010*). Generally, there are two characteristic modes for the direct ME effect measurement (*Wang et al., 2008*). The first is an active mode ("static measurement method"), such as magnetoresistive (MR) and magnetodielectric (MD) effect, wherein it requires a constant *dc* test current *I* passing through the specimen to obtain a change of voltage amplitude induced by a magnetic field or a *dc* pulse test voltage on the sample to obtain a change of polarization signal induced by a magnetic field in the *P(E)* loop measurement. Thus, when making ME measurement on multiferroic samples in the

active mode, i.e., direct measurement of the *P(E)* loop or permittivity change under magnetic field, the contribution from magnetoresistance and interfacial capacitive effects such as Maxwell-Wagner interfacial polarization effects must be taken into account. On the other hand, the ME effect can be measured using so-called passive mode, where no *dc* and *ac* test currents (or *dc* test voltage) is applied through the sample. Instead, the ME voltage response induced by a magnetic field applied perpendicular to the thin layer's plane is read directly, normally via lock-in amplifier. Therefore, the magnetoresistive and interfacial capacitive effects appearing in the active mode would not contribute to the ME output signals measured in passive mode.

When measuring the dynamically induced voltage ("dynamic measurement method") in thin layers, which can be considered as capacitors, by applying a small *ac* magnetic field H_{ac} superimposed on a *dc* magnetic bias field H_{dc} and monitoring the voltage (in the open-circuit condition) or the electric charge through a charge amplifier (in the short-circuit condition) across the capacitor with an oscillography or lock-in amplifier , much care has to be taken to distinguish the real ME signal from Faraday effect. This can be done by analysing the difference between the ME effect and electromagnetic induction. The ME voltage has the same or opposite phase as H_{ac}, while the phase of electromotive force is behind or ahead of 90 degrees. If the phase difference between the measured signal and H_{ac} is neither 0° (180°) nor ±90°, it means the measured signal is a mixture of ME voltage and faradaic effect (*Ma et al., 2011*).

Typically, for dynamic measurements, the ME voltage response V_{ac}, is measured with a phase-sensitive technique using a lock-in amplifier (*Buschow, 2011*). A *dc* magnetic bias field H_{dc} is applied with an electromagnet together with a small constant-amplitude H_{ac}, in the range of 1 to 10 Oe, sinusoidal magnetic field using a pair of Helmholtz coils. As the H_{dc} from the electromagnet is changing, the curve of ME coefficient as a function of this *dc* field is obtained. This small H_{ac} allows to measure the ME coefficient for different valued of H_{dc}. **Figure 3.42a** shows a schematic

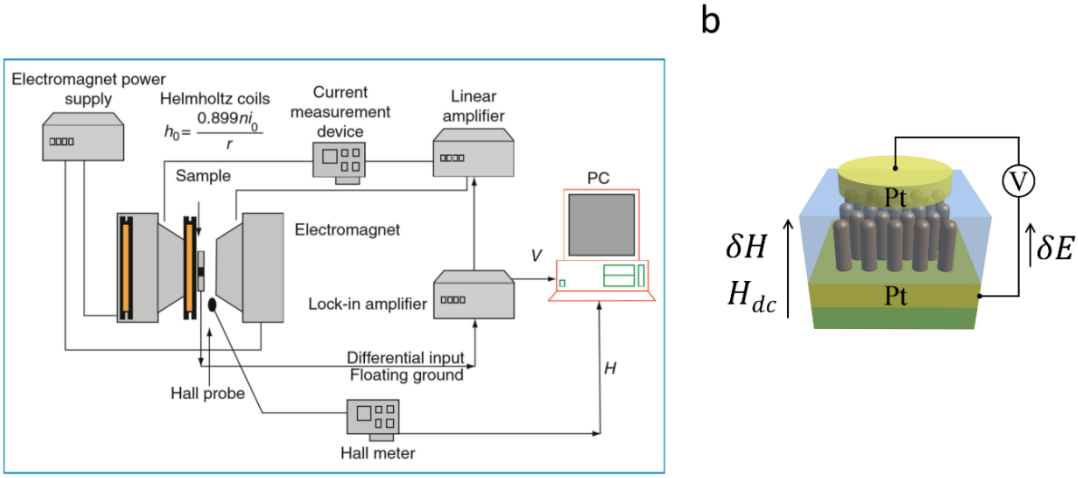

Figure 3.42: (a) Schematic experimental set-up for the measurement of the cross-sectional magnetoelectric coefficient with the dynamic method (from *Buschow, 2011*). **(b)** Schematic illustration of ME measurement used in this work

illustration of the set-up for the measurement of the cross-sectional ME coefficient with the dynamic method.

The ME voltage in the multiferroic nanocomposites containing a magnetostrictive constituent part is associated with the bias magnetic field H_{dc}. The induced ME voltage, δV, as a function of *dc* magnetic field, H_{dc}, follows the line shape of piezomagnetic coefficient $q = \delta\lambda/\delta H_{dc}$ (*Ma et al., 2011*). Thus, the V_{ac} increases with the increase of H_{dc} until q reaches saturation. The frequency dependence of the induced ME voltage shows a flat response before reaching the resonance frequency, where the ME response shows a sharp increase.

Details of ME Voltage Response Measurements on Multiferroic Nanocomposites

Dynamic magnetoelectric measurements of the magnetoelectric voltage response were performed by the group of Prof. Kristiaan Temst and Dr. Vera Lazenka at Instituut voor Kern- en Stralingsfysica, KU Leuven, Belgium. The ME voltage coefficient was measured using an adjusted Quantum Design physical property measurement system (PPMS). The principles of ME voltage measurement were previously described in detail (*Lazenka et al., 2012*; *Dong et al., 2004*; *Deng et al., 2008*). Briefly, the *ac* magnetic field (δH = 10 Oe) was generated at a fixed frequency of 1 kHz by sending an *ac* current (Keithley 6221) through a coil (1290 turns of AWG 36 phosphor bronze wire, with a diameter of 18 mm), which was assembled on the standard sample puck for PPMS electrical transport measurements. The *ac* voltage induced across the BSTO–CFO capacitor structure (δE) in response to a small *ac* magnetic field was measured with a lock-in amplifier (Stanford Research Systems, SR 830). Additionally, an *ac* magnetic field δH was superimposed onto the *dc* magnetic field H_{dc} (up to 4 Tesla) produced by the PPMS-internal superconducting magnet. Both the *ac* and *dc* magnetic fields were applied in out-of-plane direction (perpendicular to the nanostructure plane) and in the same direction as the measured ME voltage response δE as shown in **Figure 3.42b**. The ME coefficient was calculated using the relation

$$\alpha_E = \frac{\delta E}{\delta H} = \frac{\delta V}{t \times \delta H} = \frac{V_{ac}}{t \times H_{ac}}, \tag{3.27}$$

where V_{ac} is the magnetically induced *ac* electric voltage across the sample, and t is the sample thickness.

Chapter 4

Vertically Aligned PZT-CFO Core-Shell Nanocables

We propose to build vertically oriented arrays of PZT-CFO nanocables (NC). In **Figure 4.1** we remind the main steps for the fabrication of core-shell PZT-CFO NC arrays. The full fabrication process was schematically illustrated in **Figure 3.2**, p. 59. Compared to core-shell BTO-Ni NC arrays (*Sallagoity et al., 2015a*), the synthesis of PZT-CFO nanocables implies an additional critical step consisting of an *in situ* thermal oxidation process to reach the final spinel CFO phase. Taking into account the above-mentioned temperature-related limitations, the optimal thermal energy required for material crystallization should be thus carefully considered.

In the present work, we studied the fabrication of PZT-CFO core–shell NC arrays within commercial AAO membranes with thickness ~50 µm, focusing on the annealing temperature effects. We demonstrated the role of the PZT nanotubes as a diffusion barrier and the benefit of the direct *in situ* oxidation of the metal $CoFe_2$ nanowires into the metal oxide CFO nanowires during the crystallization of PZT nanotubes with regards to interface control. We took advantage of the flexibility of the combined

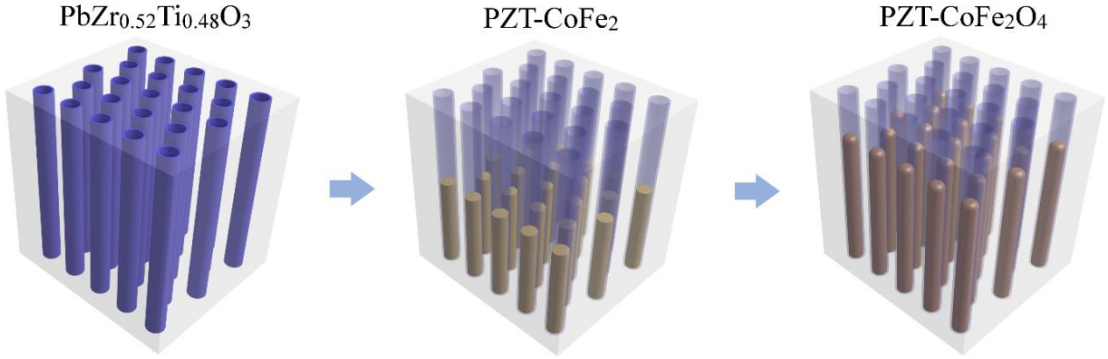

Figure 4.1: Schematic illustration of fabrication process of the core-shell $PbZr_{0.52}Ti_{0.48}O_3$-$CoFe_2O_4$ nanocable arrays by sol-gel dip-impregnation of PZT nanotubes into a commercial AAO membrane, pulsed electrodeposition of $CoFe_2$ nanowires arrays into PZT nanotubes, and their thermal oxidation into $CoFe_2O_4$ phase nanowires

impregnation–electrodeposition approach to lower the process temperature and to design nanocables with improved microstructure while ensuring a significant improvement in their microstructure and chemical integrity of the two-phase materials, an important concern when seeking enhanced multiferroic properties. Magnetic and Piezoresponse Force Microscopy (PFM) characterizations were conducted to study the magnetic and microscopic ferroelectric properties of the prepared core-shell PZT-CFO nanocable arrays.

4.1 PZT Nanotube Arrays Crystallization

HR-SEM investigations were carried out to check PZT^{700} and PZT^{500} morphology and nanostructuration (**Figure 4.2**) after the subsequent removal of the AAO template in a 1 M NaOH (aq.) solution using the dissolution process described in **Figure 3.11**, p. 82. In both cases, bundle of PZT tubular high aspect-ratio nanostructures were observed, driven by strong interactions between their hydrophilic surfaces. The amount of residual AAO (τ_{Al}) remained on their surfaces after the template removal was estimated from Energy Dispersive X-ray Spectroscopy (EDX) analysis, according to the following equation:

$$\tau_{\mathrm{Al}} = \frac{\mathrm{at\%_{Al}}}{\mathrm{at\%_{(Pb+Zr+Ti)}}}. \tag{4.1}$$

The measured for the PZT^{700} specimen mean value of $\tau_{\mathrm{Al}} \sim 3$ indicates that after the AAO template complete dissolution process the Al is still present in the specimen annealed at 700 °C. This is supported by the fact that the PZT^{700} tubular structures were rough and granular as shown in **Figure 4.2a,b**.

Compared to BTO, PZT is a complex ternary system, and metastable binary oxides such as PbO, PbO_2, ZrO_2, TiO_2, can be formed during the pyrolysis reaction occurring in the temperature range of 300–400 °C. The volatility of PbO is also a recurring issue. In contrast, it was shown that annealing temperatures up to 700 °C carry enough energy to induce Pb diffusion into AAO through oxygen vacancies (*Han et al., 2012*). This phenomenon may thus promote crystallized interphases formation of $Pb_2Al_2O_5$, $PbAl_{12}O_{19}$ or Al_2TiO_5 (**Figure 4.3a**).

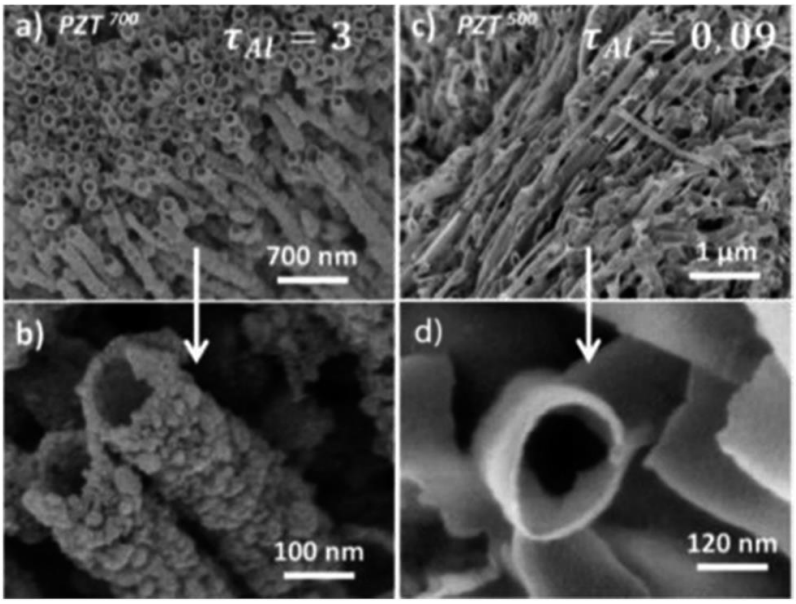

Figure 4.2: HR-SEM micrographs showing bundles of PZT^{700} **(a)** and PZT^{500} **(c)** tubular structures (D_{NT} ~150 nm, P_{AAO} ~35%) after the AAO template removal. **(b)** and **(d)** Corresponding higher magnification images. The pronounced granular aspect of the PZT^{700} structures can be observed in panel **(b)**

Considering the small amount of PZT nanotubes and complex diffusion process, thermogravimetric and XRD analyses did not allow a reliable identification and discrimination of interphases. However, the presence of residual amorphous Al and Al-rich crystallized phases were unambiguously detected by HR-SEM. From the microstructural analysis, we can thus deduce that (1) partially crystallized Al-rich interphase is formed under crystallization conditions at 700 °C for 6 h, and (2) the AAO interphase cannot be fully removed using 1 M NaOH (aq.) wet etching conditions. Consequently, the PZT^{700} nanostructures revealed in these soft conditions consist in a

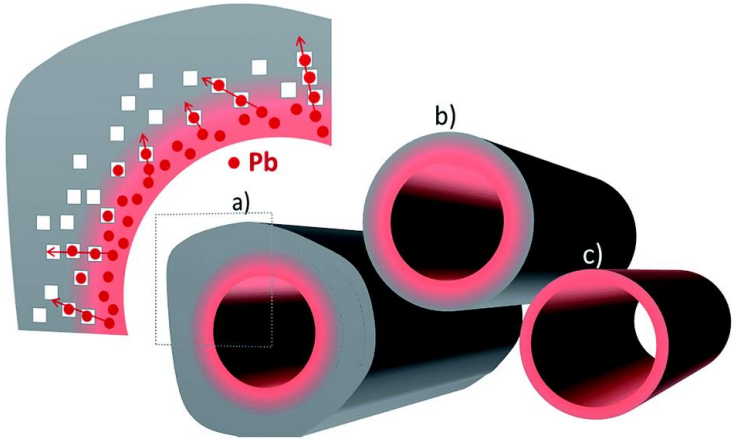

Figure 4.3: (a) Schematic illustrations of the Pb–Al interphase formation during PZT crystallization at 700 °C for 6 h inside the AAO template. The inset shows a magnified view at the interface between the two constituents, highlighting the diffusion process of Pb into the amorphous AAO. **(b)** A single PZT^{700} tubular structure obtained after the chemical dissolution of the AAO template, consisting in a tubular core-shell PZT-AAO system. **(c)** A single AAO-free PZT^{700} tubular structure after a 5 M NaOH µ-wave etching step

tubular double-shell mixture of Al-rich interphases at the outer surface and pure PZT inside (as illustrated in **Figure 4.3b**). Their high surface roughness (see **Figure 4.2b**) can be thus explained by the formation of a granular shell made of Al-rich phase. Note that by surface roughness we imply an average estimation based on the SEM image. Dissolution process was then performed in extreme conditions (5 M NaOH under μ-wave at 160 °C, followed by an ultrasonic dispersion in ethanol) in order to unambiguously evaluate PZT^{700} inner nanostructure (see **Figure 4.3c**). In comparison, PZT^{500} structures (prepared using three dip-impregnations) and crystallized at lower temperature (500 °C) have thinner walls and present smooth and uniform surface after the AAO wet etching step (see **Figure 4.2c,d**). The thickness of the PZT^{500} nanotubes, consisted of three tubular layers formed after three subsequent dip-impregnations, was estimated close to 15 nm by STEM-EDX analysis. The mean τ_{Al} value calculated close to 0.1 indicates that the residual AAO was entirely removed and the formation of Al-rich interphase was prevented. As a result, pure PZT^{500} tubular structures with smooth outer surfaces were observed (see **Figure 4.2d**).

4.2 Multiple Dip-Impregnation of PZT Nanotubes

Dimensions of FE nanostructures including nanoparticles, nanotubes, nanowires, nanofibers, and nanorods, play a major role on their FE properties (*Buessem et al., 1966*). Curie temperature, T_C, above which FE turns into paraelectric, electric polarization, P, coercive field, E_c, switching rate of polarization, and fatigue show thickness dependence (*Shaw et al., 2000*). Typically, remanent polarization drops, coercive field increases, Curie temperature decreases, and FE properties vanish when the FE film thickness reaches a specific size called critical thickness below which a spontaneous electric polarization cannot be sustained in a material due to the intrinsic size or depolarizing field effects (*Fong et al., 2004; Shaw et al., 2000; Kretschmer & Binder, 1979; Batra & Silverman, 1972; Mehta et al., 1973*). This change in properties, usually called size effect, can be ascribed to a surface layer associated with the nature of the film-electrode interface for the FE films (*Tagantsev & Stolichnov, 1999*), or to the intrinsic limits on the stability of the FE phase in FE nanotubes, where the overall energy of the system cannot be further reduced by creation of non-180° domain walls, that are no longer favourable (*Bernal et al., 2012*). The processing and quality of electrode interface determine the critical film thickness value. Thus, the limit of finite-size thickness at which size effects are observed can be reduced by improving the surface and interfacial boundary conditions. For instance, for FE thin films this can be accomplished by heteroepitaxial strain, surface chemical environment and tuning of ferroelectric-electrode interface. In practical thin films and devices, the absence of

critical thickness is possible due to the structural imperfection at the interface and surface.

Theoretical density functional theory (DFT) calculations on the structural, ferroelectric, and electronic properties of ultrathin $PbTiO_3$ nanotubes showed that ferroelectricity can be retained in the nanotube with sidewalls thinner than the critical limit of the thin-film geometry at which the thin-film loses ferroelectricity; this indicated the absence of an intrinsic critical size for ferroelectricity in nanotubes (*Shimada et al., 2012*). They modelled the PTO nanotubes by rolling up a (100) ultrathin film about the [001] axis with two possible configurations of the outside-inside tube-wall stacking sequence, the PbO/TiO_2 (PbO-outside) and the TiO_2/PbO (TiO_2-inside) layers. The nanotube radius R was determined by the number of perovskite unit cells N arranged in the circumferential direction, while the tube curvature was $1/R$, where the radius R is the average of the outside and inside radii, $R = (R_{out} + R_{in})/2$. The highest cohesive energy of $E_c = 39.25$ eV/cell was located at $\frac{1}{R} = 0.089$ Å^{-1} ($N = 18$) for the PbO-outside nanotubes in which the outside-PbO and inside-TiO_2 radii are $R_{out} = 11.89$ Å and $R_{in} = 10.17$ Å, indicating the stability of the nanotubular structure, while the TiO_2-outside case was energetically unfavourable.

The authors explained it by the fact that the antiferrodistortive (AFD) oxygen rotation due to compression in the structure induced by the nanotubular shape involves ferroelectric distortions. Since there is a curvature with respect to the flat thin film geometry, bending deformation is homogeneously applied to the tube sidewall, thus the inside TiO_2 layer is subject to relatively high compression. This results in the emergence periodic clockwise and counterclockwise tilting of oxygen atoms in the circumferential direction, namely, of the AFD rotations, whereas the AFD rotations were not found in the TiO_2-outside nanotubes, in which the TiO_2 layer is subject to tension. The emergence of the AFD displacement plays a central role in stabilizing both the nanotubular structure and FE distortions due to direct AFD-FE coupling; hence, the nanotubes have no intrinsic critical size. It was observed that the FE axial polarization, P_z, and AFD oxygen rotation are directly coupled, therefore the polarization increases smoothly as the AFD rotation is enhanced by increasing the curvature (compressing the inner TiO_2 layer) for the PbO-outside nanotubes. Further the authors systematically investigated the effect of axial tensile and compressive strains on ferroelectricity in the nanotube. During tension, FE distortions appear purely in the axial directions, and P_z increases smoothly due to the increase of tetragonal distortion of the perovskite lattice as well as the enhanced AFD oxygen rotation, while the AFD rotation and FE are directly coupled. On the other hand, under axial compression, the system reverts the FE phase at $u_{zz} = -0.05$, and a polarization vortex forms due to the spontaneous polarization being aligned in the circumferential direction. In another study the ferroelectric properties of the single-wall PTO nanotubes folded from (110) nanosheets

with a specific chirality were reported (*Wang et al., 2014b*). Similar to the (100) nanotubes, the lowest energy for the (110) nanotubes corresponds to $N = 18$ located at $\frac{1}{R} = -0.097$ Å^{-1}. Interestingly, the curvature of the O-outside (110) nanotube with the lowest energy is the same as that of the PbO-outside (100) $PbTiO_3$ nanotube. However, the minimum total energy (-0.343 eV/cell) for the (110) nanotube is much lower than that (-0.082 eV/cell) for the (100) nanotube, indicating that the $PbTiO_3$ nanotube rolled from (110) nanosheets is more stable that that from (100). It was reported that the spontaneous polarization of the (110) nanotube existed only in nanotubes with a rolling direction of (m_{NT},0), and it was one order of higher than that in the (100) $PbTiO_3$ nanotubes. The FE-AFD coupling was claimed to be responsible for the stability of the FE distortion in the nanotubes as well, which gives rise to the axial polarization existed for the O-out nanotubes even though the sidewall was much thinner than the critical thickness for ferroelectricity of the flat thin film.

First-principle ab initio calculations showed that $BaTiO_3$ thin films between two metallic $SrRuO_3$ electrodes lose their FE properties below a critical thickness of about 6-unit cells (~24 Å) (*Junquera & Ghosez, 2003*). A depolarizing electrostatic field, caused by dipoles at the ferroelectric-metal interfaces, is the reason for the disappearance of the ferroelectric instability. Experimentally observed critical thicknesses for epitaxial ferroelectric films usually are a few unit cells. In the $BaTiO_3$ films, the critical thickness was reported in the range between 4-unit cells (*Tenne et al., 2009*) and 7-unit cells (*Wen et al., 2013*). For $BiFeO_3$, the ferroelectricity was shown in 4 and 5-unit cells thick films (*Chu et al., 2007; Maksymovych et al., 2012*). The ferroelectricity in $PbTiO_3$ was observed in 3-unit cells (~12 Å) using synchrotron X-ray diffraction to record the structure of $PbTiO_3$ thin films as a function of temperature for the range of different film thicknesses (*Fong et al., 2004*). Their method allowed them to distinguish between the centrosymmetric structure, in which there is no net polarization, and the off-centred ferroelectric phase. The critical thickness reported for the PZT thin films grown on STO substrate using scanning probe was 10-unit cells (~40 Å) (*Tybell et al., 1999*; *Nagarajan et al., 2004*). Recently, the critical thickness of 1.5-unit cells was reported in PZT ultrathin films grown on bare STO substrate (*Gao et al., 2017*). The stable polarization through-out the film was reported to be significantly suppressed to ~16 and 22 μC cm^{-2} for the 1.5 and 2.5-unit cells thick films, respectively, dominated by the thickness-dependent depolarization field. The atomic structure showed that the robust covalent Pb-O bonds mainly account for the residual polarization below 3-unit cells in the PZT films. Although the ferroelectricity does not disappear in the ultrathin PTO, BTO and PZT films, the magnitude of polarization is normally progressively decreasing as the critical thickness is approached (*Lichtensteiger et al., 2005*; *Kim et al., 2005*; *Nagarajan et al., 2004*). Some of these values are in good agreement with the theoretical calculations, where the critical thickness was reported to be 3-unit cells for PTO (*Ghosez & Rabe, 2000*) and 6-unit cells for BTO (*Junquera & Ghosez, 2003*).

In this work, in the one-layered PZT nanotubes with sidewalls in the range ~50-100 Å, the nanotubes curvatures (i.e. $\frac{1}{R} = \frac{1}{(R_{out}+R_{in})/2}$) are around 0.0007 Å^{-1} and 0.001 Å^{-1} for the outer radii ($R_{out} = D_{pore}/2$) ~750 and 500 Å, respectively. According to the previously reported DFT calculations (*Shimada et al., 2012*), the value of the nanotube curvature is relatively low (<0.05 Å^{-1}), thus the AFD oxygen rotation is too small and the inner TiO_2 layer is not compressed enough for either the FE axial polarization or the FE circumferential polarization vortex to occur. Therefore, the intrinsic size effects existed in ferroelectric thin films such as a critical volume, required to align the electric dipoles (*Shaw et al., 2000*), or increasing depolarization field with the decrease of thickness, caused by the incomplete compensation of polarization bound charges at interfaces and leading to the instability of ferroelectricity in ultrathin films and fine particles (*Shaw et al., 2000; Batra & Silverman, 1972; Mehta et al., 1973*), as well as the vapour environments through ionic absorbate at the free surface (*Fong et al., 2006*) are possible for the as-prepared PZT nanotubes.

In order to avoid critical size effects and to preserve the ferroelectricity in PZT nanotubes, sidewalls were thickened by repeating the sol-gel dip-impregnations three times. **Figure 4.4** shows the top view SEM images of the PZT^{500} NT arrays consisted of one (**Figures 4.4a,b**), and three (**Figures 4.4e,f**) PZT tubular layers fabricated using multiple dip-impregnations of coating solution into AAO membranes (D_{pore} ~150 nm, P_{AAO} ~35 %) with pores length around 50 µm. SEM observation revealed an average wall thickness of the single-layer and three-layer PZT^{500} nanotubes ~5 and 15 nm,

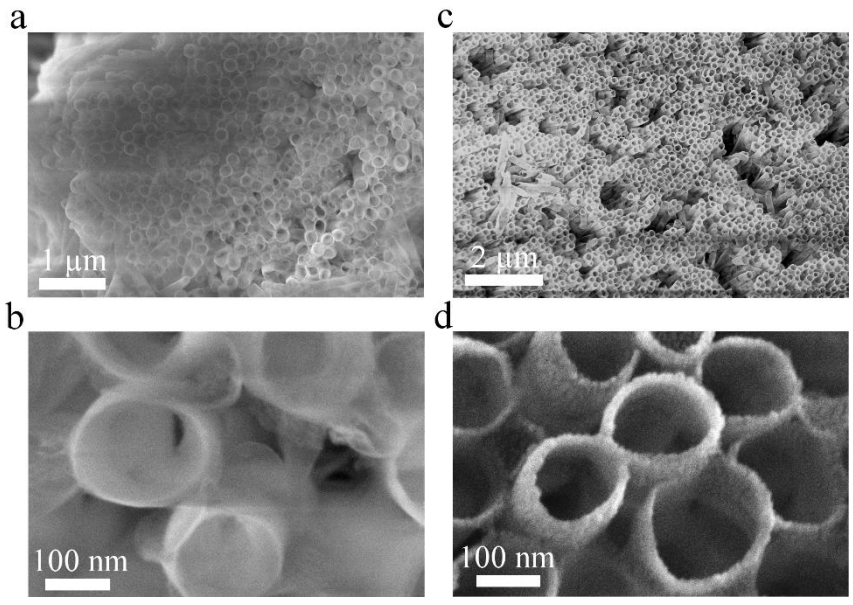

Figure 4.4: HRSEM images of free-standing PZT^{500} nanotubular structures (D_{pore} ~150 nm, P_{AAO} ~35 %) prepared using **(a,b)** one and **(c,d)** three consequent sol-gel dip-impregnations in AAO membranes. The PZT nanotubes were collected on the carbon tape after the hosting AAO membrane was dissolved in the concentrated NaOH solution using the AAO dissolution procedure shown in **Figure 3.11**, p. 82

respectively. Note that, this SEM observation of the PZT nanotubes wall thickness is just a qualitative estimation, because large non-uniformity in the wall thickness of PZT nanotubes was observed. The wall thickness in the single-layer and three-layer PZT nanotubes is in the range of 5-10 and 10-20 nm, respectively. Therefore, in order to precisely control nanotubes wall thickness, the sol-gel multiple dip-impregnation technique has to be improved. The SEM micrographs from **Figures 4.4a,c** are of a poor quality due to the charging effect , which is often observed in non-conductive specimens (for more detail see **Figure 3.34c**, p. 121).

4.3 $CoFe_2$ Nanowire Arrays Electrodeposition within PZT Nanotubes Coated on Pores of AAO Membranes

The metallic $CoFe_2$ NW arrays were grown inside both PZT^{700} and PZT^{500}-coated AAO membranes using a pulsed electrodeposition process forming a PZT-$CoFe_2$ core-shell nanocable structure, the deposition procedure was described in **Section 3.1.3** (p. 75). However, the properties of electrodeposited PZT-$CoFe_2$ nanocables are discussed in Section 4.4 only for PZT^{500} specimen, since the PZT^{500} nanotubes have smoother inner and outer surfaces, more uniform wall thickness, and near-zero diffusion with AAO.

Figure 4.5a shows the tilted top view SEM image of the PZT^{500}-$CoFe_2$ nanocables after the partial dissolution of the AAO membrane showing an average height of the PZT^{500}-$CoFe_2$ nanocables ~10 µm. The filling of the PZT^{500} was homogeneous and the $CoFe_2$ growth was stopped after 3000 seconds when the deposited nanowires height, h_{NW}, was about 10 µm. After the AAO membrane was fully dissolved, as expected two distinct phases are thus clearly evidenced (see **Figure 4.5b**) the PZT nanotubes region (light grey) and the electrochemically-grown metallic $CoFe_2$ solid cores (white). The observed nanocable with branches on it's right side in the middle of SEM image reveals

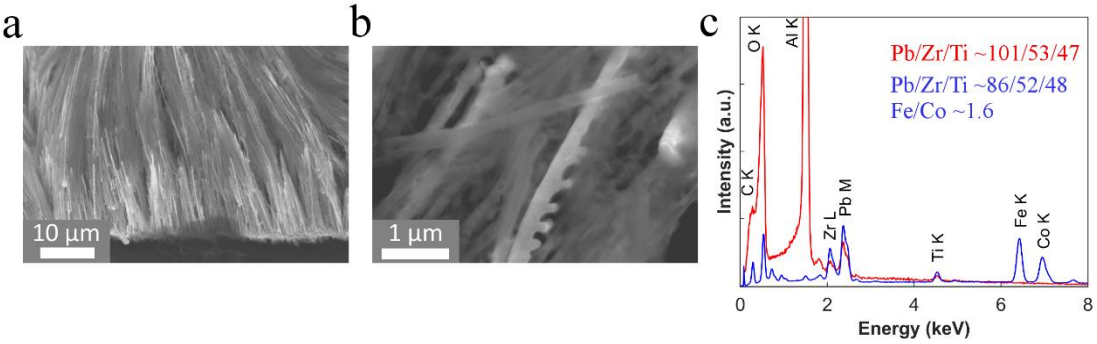

Figure 4.5: (a) Tilted top view SEM image of the PZT_{500}-$CoFe_2$ nanocables after partial dissolution of the alumina (D_{pore} ~150 nm, P_{AAO} ~35%). **(b)** Top view SEM images of the $PZT^{500°C}$-$CoFe_2$ C arrays after full AAO dissolution, top segment of the PZT^{500} nanotubes (unfilled with $CoFe_2$) can be distinguished by their transparent look and the PZT^{500}-$CoFe_2$ nanocables can be found by their bright colour. **(c)** EDX spectra of the crystallized PZT^{500} NTs inside AAO (red) and PZT-$CoFe_2$ nanocables after AAO dissolution (blue)

the defective shape of some pores of AAO membrane, note that this type of defects was observed only for the samples prepared using the commercial membranes with 15 % porosity. An average elemental analysis was provided by EDX (**Figure 4.5c**) confirming the composition of $PbZr_{1-x}Ti_xO_3$: x = 0.47 for the PZT^{500} nanotubes, which is close to the PZT morphotropic phase boundary region with x=0.48. The Fe/Co composition ratio close to 2 was observed in the PZT^{500}-$CoFe_2$ nanocables collected on the carbon tape after the AAO membrane dissolution. The Zr/Ti composition ratio in the PZT^{500}-$CoFe_2$ remained the same 52/48, but the atomic ratio of Pb has reduced by about 15%, which can be a result of the diffusion process in the PZT/AAO interface. The ordered arrays of AAO-embedded PZT^{500}-$CoFe_2$ nanocables were magnetically characterized to determine the impact of the nanocable architecture on the magnetic properties.

For the arrays of metallic $CoFe_2$ nanowires, the magnetocrystalline anisotropy can be neglected and the effective field, H_{eff}, in the saturated state is only determined by magnetostatic contributions, i.e. shape anisotropy and dipolar interaction. It can be thus expressed as (*Encinas-Oropesa et al., 2001*):

$$H_{\text{eff}} = 2\pi M_{\text{s}} - 6\pi M_{\text{s}} P_{\text{NW}}, \tag{4.2}$$

where $2\pi M_s$ is the shape anisotropy, $6\pi M_s P_{NW}$ is the dipolar interaction field in the saturated state, with P_{NW} is the nanowires packing factor (corresponding to the template porosity, i.e. 15% and 35%, in case the whole cross section of the nanochannel array of the pristine AAO template is completely filled by $CoFe_2$) and M_s ~1900 emu cm^{-3} is the saturation magnetization for $CoFe_2$ (*Cullity & Graham, 2009*). For comparison, an array of $CoFe_2$ nanowires was prepared using the same electrochemical conditions and porous AAO template. **Figure 4.6** shows the normalized magnetic hysteresis loops measured at room temperature using alternating gradient magnetometer (AGM) with the field applied along the in-plane (perpendicular to NW axis) and out-of-plane (parallel to the revolution axis of nanowires) for the AAO-embedded $CoFe_2$ NW arrays (**Figure 4.6a,c**) and three PZT^{500}-$CoFe_2$ core-shell NC arrays (**Figures 4.6b,d,e**).

For the $CoFe_2$ NW arrays (D_{pore} ~100 nm, P_{AAO} ~15%), **Figure 4.6a** reveals the easy axis of magnetization along out-of-plane direction, which means that uniaxial shape anisotropy along the out-of-plane direction of individual nanowires overcomes the shape anisotropy associated with the infinite NW array behaving as a film, since packing density is low and aspect ratio of the NWs is relatively large (*Dmitriiev et al., 2013*). As expected, the PZT^{500}–$CoFe_2$ nanocables (membrane: D_{pore}~100 nm, P_{AAO}~15%) (**Figure 4.6b**) sample is more easily magnetized than the $CoFe_2$ NWs (membrane: D_{pore}~100 nm, P_{AAO}~15%) sample counterpart (**Figure 4.6a**). This can be explained by the nanocable morphology, which leads to a packing factor, P_{NW}, of the PZT^{500}-$CoFe_2$ system smaller than that of the purely metallic $CoFe_2$ NW arrays. As a result, the interaction field is smaller leading to a higher effective field and stronger uniaxial anisotropy in the core-shell nanocables (**Eq. 4.2**). By knowing the average wall

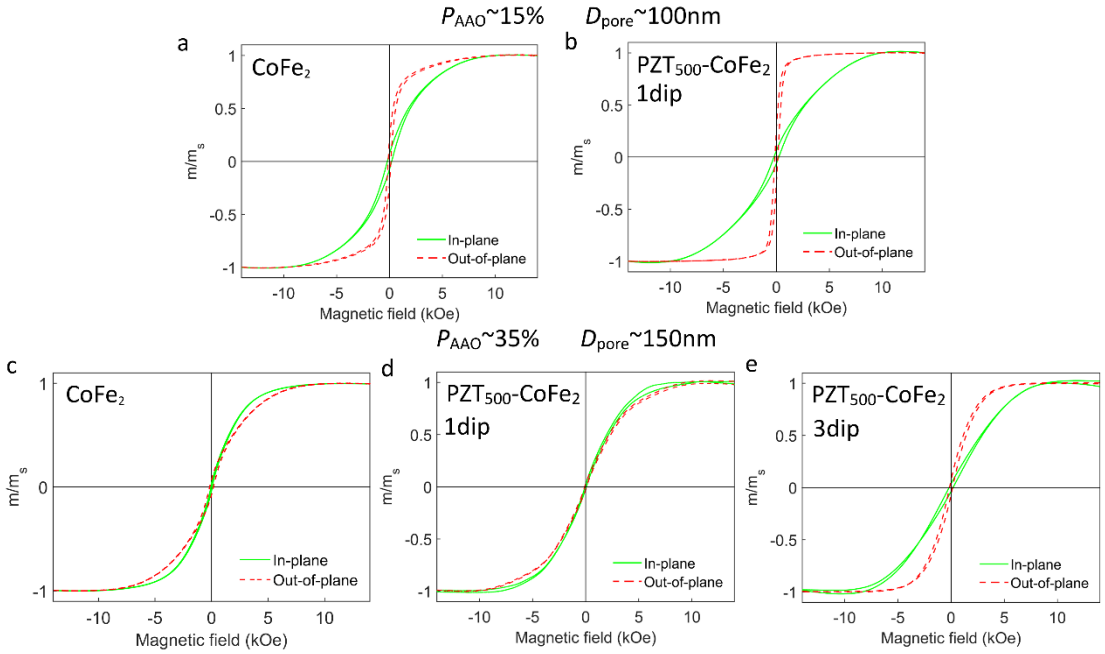

Figure 4.6: Room temperature hysteresis loops along in-plane (solid line) and out-of-plane (dashed line) directions for a vertically aligned $CoFe_2$ nanowire array **(a,c)** and the PZT^{500}-$CoFe_2$ multiferroic nanocable arrays consisted of one-layer **(b,d)** and three-layer PZT nanotubes **(d)**.

thickness of the single-layer PZT shells ~5-10 nm and the diameter of $CoFe_2$ cores D_{NW} ~80-90 nm, the average packing factor of the $CoFe_2$ cores can be estimated using Eq. 3.1 as

$$P_{\mathrm{PZT-CF15\%}} \sim \frac{\pi}{2\sqrt{3}} \times \left(\frac{85 \pm 12.5}{240 \pm 20}\right)^2 = 0.11 \pm 0.05, \tag{4.3}$$

which is lower than the packing factor of pure $CoFe_2$ NW arrays

$$P_{\mathrm{CF15\%}} \sim \frac{\pi}{2\sqrt{3}} \times \left(\frac{100 \pm 10}{240 \pm 20}\right)^2 = 0.16 \pm 0.06. \tag{4.4}$$

In contrast, **Figure 4.6c** shows that the higher packing value of $CoFe_2$ NWs (membrane: D_{pore}~150 nm, P_{AAO}~35%) results in out-of-plane easy direction of magnetization for the $CoFe_2$ NW arrays

$$P_{\mathrm{CF35\%}} \sim \frac{\pi}{2\sqrt{3}} \times \left(\frac{150 \pm 10}{240 \pm 20}\right)^2 = 0.35 \pm 0.11, \tag{4.5}$$

which can be explained by stronger dipolar interactions which responsible for the shearing of the hysteresis loop (*Zighem et al., 2011*). **Figures 4.6d** shows almost isotropic magnetic behaviour of the PZT^{500}-$CoFe_2$ NC arrays (D_{pore} ~150 nm, P_{AAO} ~35%), consisted of single-layer PZT shells. Since the packing factor of $CoFe_2$ cores

$$P_{\mathrm{PZT-CF35\%}} \sim \frac{\pi}{2\sqrt{3}} \times \left(\frac{135 \pm 12.5}{240 \pm 20}\right)^2 = 0.29 \pm 0.10 \tag{4.6}$$

is close to ~0.3, the effective field, H_{eff}, tends to turn to zero (see **Eq. 4.2**). The magnetic moments saturate almost at the same field in the out-of-plane, OOP, (parallel to nanowire central axis) and in-plane, IP, (perpendicular to nanowire central axis) directions of the applied field. However, for the PZT^{500}-$CoFe_2$ NC arrays (membrane: D_{pore} ~150 nm, P_{AAO} ~35%) consisting of three-layer PZT shells (i.e. using 3 dip-impregnations), the easy axis of magnetization is switched back to the OOP direction of the nanowires due to the increase of PZT shells wall thickness to ~15±5 nm and thus the reduction in $CoFe_2$ cores diameter D_{NW} to ~120±20 (**Figure 4.7e**). So, the reduction

$$P_{\mathrm{PZT-CF35\%}} \sim \frac{\pi}{2\sqrt{3}} \times \left(\frac{120 \pm 20}{240 \pm 20}\right)^2 = 0.22 \pm 0.12 \qquad (4.7)$$

leads to a similar behaviour as the one observed in $CoFe_2$ NW arrays (membrane: D_{pore} ~100 nm, P_{AAO} ~15%) grown in the AAO membrane with lower porosity (**Figure 4.7a**). Therefore, by thickening the PZT nanotubes sidewall the dipolar interaction between $CoFe_2$ nanowires in the PZT-$CoFe_2$ NC arrays was reduced.

4.4 $CoFe_2$ Nanowires Thermal Oxidation into $CoFe_2O_4$ Phase within PZT Nanotubes

Recently it was reported that the reactivity of amorphous AAO in contact with metallic nanowires increases with increasing temperature, through the so called Kirkendall effect (*Qin et al., 2010*; *Wang et al., 2009*; *Prasad & Paul, 2007*). Our preliminary oxidation tests performed at 600 °C during 24 h in air, corresponding to the usual conditions reported in most papers from literature (*Hua et al., 2007*; *Jung et al., 2005*; *Chen et al., 2013*; *Pirouzfar & Ebrahimi, 2014*; *Pham-Huu et al., 2003*), within pure AAO templates showed strong interdiffusion effects between Co, Fe and Al, and formation of an Al-rich interphase between CFO^{600} oxidized nanowires and AAO membrane. However, when considering PZT^{700} within AAO membranes, the reactivity between AAO and $CoFe_2$ seems to be stabilized due to the PZT shell which acts as an efficient diffusion barrier layer. **Figures 4.7a,b** show HR-SEM images of oxidized PZT^{700}-CFO^{600} nanocables after chemical dissolution of the AAO template, revealing that the core/shell morphology has been maintained after the $CoFe_2$ oxidation process.

Mean τ_{Al} values for oxidized PZT^{700}-CFO^{600} nanocables were typically measured between 3.9 and 5.1. The oxidation step is thus followed by a significant increase of residual AAO in comparison with the PZT^{700} tubular structures (see **Figures 4.2a,b**). In other words, diffusion between the PZT shell and AAO template is enhanced during the second thermal treatment for converting the $CoFe_2$ into $CoFe_2O_4$ at 600 °C.

Bright field (BF) STEM experiments coupled with EDX compositional mapping were performed on the PZT^{700}-CFO^{600} nanocables following two different protocols

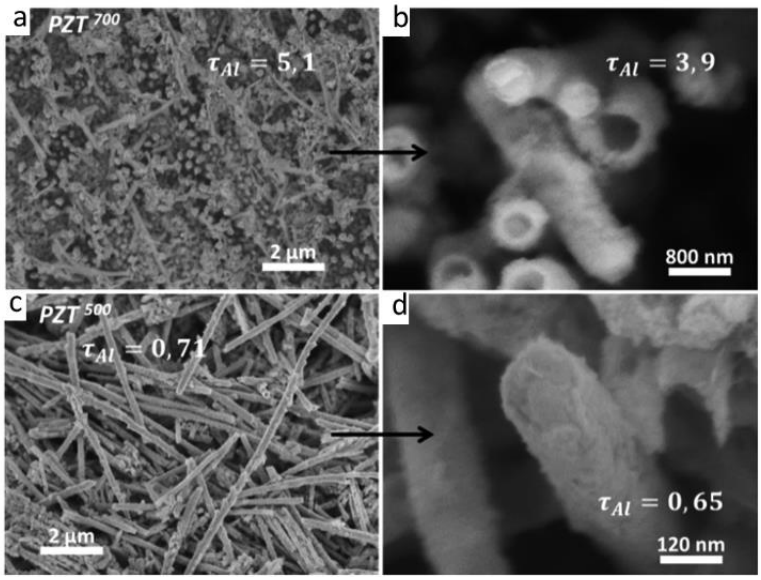

Figure 4.7: (a) and **(b)** HR-SEM micrographs at different magnifications, showing the dense arrays of PZT^{700}-CFO^{600} NCs (D_{pore} ~150 nm; P_{AAO} ~35%) after the AAO template etching in 1 M NaOH. **(c)** and **(d)** Micrographs at different magnifications acquired from the PZT^{500}-CFO^{500} nanocables prepared in similar conditions

for the sample preparation (**Figure 4.8**). The elementary analysis evidences atomic diffusion of Pb inside the AAO template (**Figure 4.8b**) and the presence of Al-rich crystallized interphase on the surface of single free nanocables obtained after NaOH etching (**Figures 4.8c,d**). As expected, the decrease of both PZT crystallization temperature from 700 to 500 °C and $CoFe_2$ to CFO oxidation temperature from 600 to 500 °C leads to a significant decrease of τ_{Al} values (approximatively divided by 5 with respect to PZT^{700}-CFO^{600} see **Figures 4.8c,d**). Similarly, the surface of free PZT^{500}-CFO^{500} nanocables observed by STEM-BF after AAO template etching in 1 M NaOH (aq.) and dispersion in ethanol is smooth and well defined (see **Figures 4.8e,f**).

Accordingly, no contribution of Al (expected to appear in blue colour on the chemical mapping image) occurs in such optimized annealing conditions. Therefore, from the electron microscopy investigations, it clearly appears that reduction of the crystallization temperature of the PZT shells and oxidation temperature of metallic cores, leads to a significant improvement of both morphological and structural characteristics of the CFO–PZT core-shell assembly.

To further support the latter statements, $CoFe_2$ to CFO oxidation inside pre-annealed PZT^{500} tubular structures consisting of three PZT layers was followed by *in situ* X-ray diffraction using a PANalytical X'Pert Pro Anton Paar diffractometer with cobalt anticathode (see **Figure 4.9**). Taking into account the very low quantity of matter inside the AAO template and the strong nanostructuration of the phases (either for PZT shells or for $CoFe_2$ cores), specific preparation techniques were developed in order to accurately and unambiguously determine the structural features of the PZT-CFO nanocables. A PZT multi-dip impregnation process (three successive impregnations with intermediate crystallization steps) was carried out to provide thick enough tubular

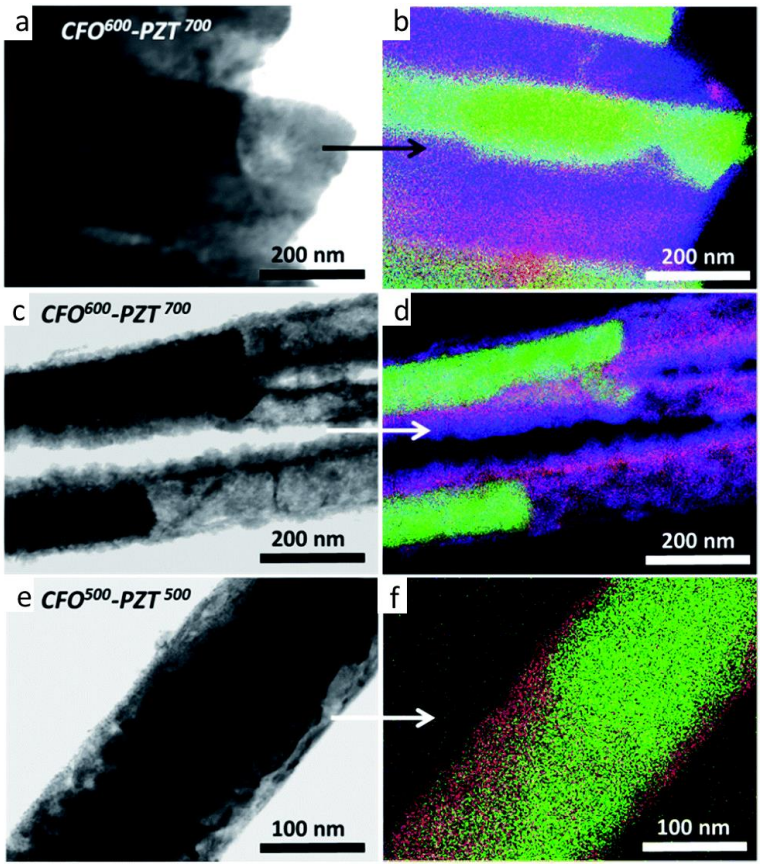

Figure 4.8: (a) STEM-BF micrograph of the PZT^{700}-CFO^{600} core-shell architecture (D_{pore} ~150 nm; P_{AAO} ~35%) within the AAO template after grinding and dispersion in ethanol. **(c)** The same sample after AAO etching in 1 M NaOH and dispersion in ethanol. **(e)** The PZT^{500}-CFO^{500} system after template etching and dispersion in ethanol. **(b, d and f)** Corresponding chemical mapping, with Pb, Fe and Al represented in red, green and blue, respectively

structures. Electrodeposition step was maintained longer to increase the $CoFe_2$ NWs height. The cubic $CoFe_2$ (110) most intensive peak 44.7° represented by the black dotted line is surrounded by two peaks very close, attributed to PZT and Au (contribution of the Cu/Au bilayer cathode used for electrodeposition). However, the contribution of each phase can be easily discriminated when increasing the temperature. Progressive disappearance of the $CoFe_2$ (110) peak is observed between 20 °C and 500 °C whereas CFO spinel phase starts to crystallize at 300 °C (green marked peaks (220), (311), (400), (511), and (440) at 30.1°, 35.4°, 43.1°, 56.9° and 62.6°, respectively).

This evolution indicates that the metallic $CoFe_2$ and the oxide CFO coexist over a temperature range going from 300 °C to 500 °C. The intensity of spinel CFO peaks increases with temperature while the mid-height width decreases, in good agreement with a gradual increase in the crystallite size within the oxidized cores. Moreover, relative intensities of (220) (30.1°) and (440) (62.6°) peaks are raised meaning a preferential orientation of the CFO phase along (*hk*0) planes, possibly attributed to the highly anisotropic confinement given by the porous structure of the AAO template. We

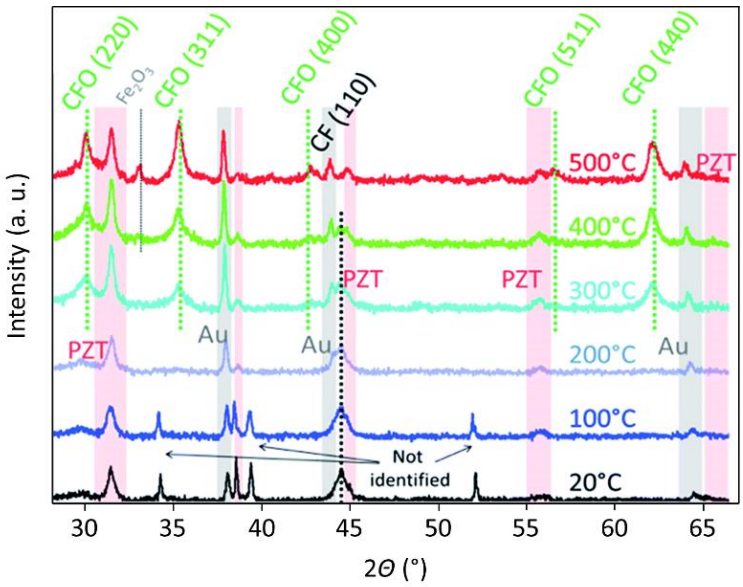

Figure 4.9: $CoFe_2$ to CFO NWs in-situ oxidation inside PZT NTs followed by in-situ X-ray diffraction at different temperatures with an increment of 100 °C. The starting room temperature $CoFe_2$ pattern is represented in black and the final CFO oxidized one is in red (D_{pore} ~150 nm; P_{AAO} ~35%)

can then assume that $CoFe_2$ to CFO oxidation should be effective at lower temperature than 600 °C. In addition, PZT^{500} crystalline signature is evidenced by the presence of five peaks (marked in red on **Figure 4.9**) that are attributed to a pseudo-cubic phase of PZT, as confirmed by profile matching using EVA software (Bruker Co.). HRTEM investigation conducted on PZT nanotubes consisted of three tubular layers (not shown), which were prepared using three dip-impregnations, confirmed the high crystallinity of PZT nanoparticles (mean diameter ranging between 5 and 10 nm). This size belongs to the critical range with regards to the alteration of ferroelectricity. However, it was clearly shown in literature that in confined 1-D geometry, the contribution of defects, surface tension, strain induced domain configuration, effective screening of the surfaces charges by chemisorbed hydroxyl groups could locally stabilize a polar state (*Kim et al., 2008*; *Spanier et al., 2006*; *Hua et al., 2008*). The value of mean PZT particle diameter obtained by XRD for the multilayer PZT nanotubes differs from the value obtain by STEM and SEM ~15 nm, which confirms the non-uniformity of PZT walls thickness obtained after three dip-impregnations of PZT coating PZT solution.

Figure 4.10 shows the normalized magnetic hysteresis loops measured at room temperature with the external field applied along OOP (**Figure 4.10a**) and IP (**Figure 4.10b**) directions for the PZT^{500}-CFO^{500} and PZT^{500}-CFO^{600} NC arrays. The magnetic moments of the PZT-CFO nanocables were normalized by the PZT-$CoFe_2$ maximum value of magnetic moment in the saturation state. For the $CoFe_2$ NW arrays, magnetocrystalline anisotropy can be neglected and the effective anisotropy is entirely magnetostatic, as pointed out previously. In contrast, large coercivity fields and squareness have been achieved in the PZT^{500}-CFO^{600} NC arrays (see **Table 4.1** for

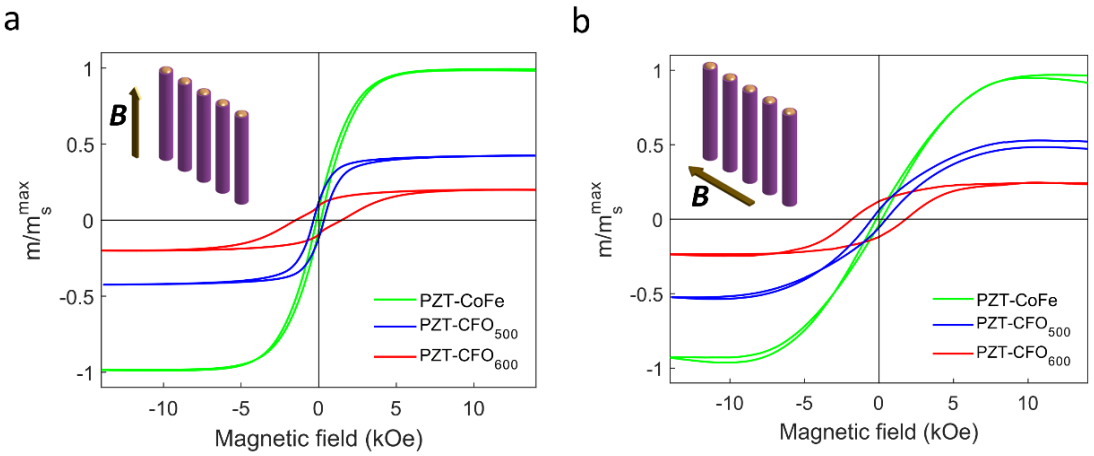

Figure 4.10: Room temperature hysteresis loops along out-of-plane (parallel to NWs axis) **(a)** and in-plane (perpendicular to NWs axis) **(b)** directions for the vertically aligned PZT^{500}-$CoFe_2$ nanocable arrays (green line), the PZT^{500}-CFO^{500} (blue line) and PZT^{500}-CFO^{600} (red line) nanocable arrays (D_{pore} ~150 nm; P_{AAO} ~35%). The magnetic moments are normalized to the maximal value in the saturation state for the same direction of applied field

details). Such high coercive fields ~1.8 kOe are associated with the magnetocrystalline anisotropy of CFO material (*Bozorth, 1955*). The results showed that oxidation performed at 600 °C during 24 h under air is followed by a significant decrease of the saturation magnetic moment by a factor of 4 for the magnetic field, *H*, applied in IP and by a factor of 5 for *H* applied in OOP. Given that the average volume expansion during oxidation (~1.5) of the nanowires, this reduction of the PZT-CFO nanocables magnetic moment roughly corresponds to a large reduction in the saturation magnetization by a factor ~7. This can be explained by the reduction

Table 4.1. Oxidation conditions (temperature and time) for the PZT^{500}-$CoFe_2$ nanocables and corresponding magnetic properties (normalized magnetic moment m/m_s^{max}, coercivity H_c, and squareness m_r/m_s in out-of-plane (OOP) and in-plane (IP) directions) for the PZT^{500}-$CoFe_2$, PZT^{500}-CFO^{500} and PZT^{500}-CFO^{600} nanocable arrays

Sample (**Fig. 4.10**)	*T* °C	Time h	m_s/m_s^{max} OOP μemu	m_s/m_s^{max} IP μemu	H_c OOP Oe	H_C IP Oe	m_r/m_s OOP	m_r/m_s IP
PZT^{500}-$CoFe_2$ (green line)	-	-	1	1	141	187	0.07	0.04
PZT^{500}-CFO (blue line)	500	24	0.42	0.53	337	480	0.28	0.11
PZT^{500}-CFO (red line)	600	24	0.20	0.25	1479	1804	0.47	0.50

in saturation magnetization, M_s, of CFO phase. The obtained results correspond to the expected ratio between the saturation magnetization of $CoFe_2$ (~1900 emu/cm^3) and CFO (~ 400 emu/cm^3) bulk materials at room temperature (*Cullity & Graham, 2009; Ojha et al., 2016*).

A large increase of the coercive field from 141 Oe to 1479 Oe for *H* applied in OOP, and from 187 Oe to 1804 Oe for *H* applied in IP was observed as well (see **Figure 4.10,** red line and **Table 4.1**). As shown in **Figure 4.10** (blue line), oxidation at a lower temperature (500 °C for 24 h) leads to a somewhat smaller reduction in the saturation magnetic moment ~1.9 for the *H* applied in IP and ~2 for *H* applied in OOP, and coercive field around 337 Oe for *H* in IP and 480 Oe for *H* in OOP.

We probe magnetic properties of the CFO NW arrays (D_{pore}~100 nm; P_{AAO}~15%) oxidized at 500 °C (hereinafter CFO^{500}) and 600 °C (hereinafter CFO^{600}) for 24 hours (**Figures 4.11a,b**), and PZT-CFO NC arrays (**Figures 4.11c-h**), wherein PZT^{500}-CFO^{500} and PZT^{500}-CFO^{600} with single-layer PZT nanotubes in **Figure 4.11c,d** correspond to D_{pore}~100 nm and P_{AAO}~15%, PZT^{500}-CFO^{500} and PZT^{500}-CFO^{600} with single-layer PZT nanotubes in **Figure 4.11e,f** correspond to D_{pore}~150 nm and P_{AAO}~35%, and PZT^{500}-CFO^{500} and PZT^{500}-CFO^{600} with three-layer PZT nanotubes in **Figures 4.11g,h** correspond to D_{pore}~150 nm and P_{AAO}~35%. All geometric parameters and magnetic properties of the nanowire and nanocable arrays (**Figure 4.11**) are summarized in **Table 4.2**.

Table 4.2: Effects of oxidation conditions on magnetic properties of the $CoFe_2$ nanowire arrays deposited into AAO membranes

Sample (**Figure 4.11**)	D_{pore} nm	P_{AAO} %	# PZT layers	T_{ox}, °C	Time, h	H_C OOP Oe	H_C IP Oe	m_r/m_s OOP	m_r/m_s IP
CFO^{500}	100	15	0	500	24	423	764	0.60	0.24
CFO^{600}	100	15		600	24	588	773	0.31	0.27
PZT^{500}-CFO^{500}	100	15	1	500	24	355	573	0.48	0.14
PZT^{500}-CFO^{600}	100	15		600	24	355	389	0.31	0.16
PZT^{500}-CFO^{500}	150	35	1	500	24	662	716	0.36	0.27
PZT^{500}-CFO^{600}	150	35		600	24	515	611	0.20	0.22
PZT^{500}-CFO^{500}	150	35	3	500	24	432	483	0.45	0.10
PZT^{500}-CFO^{600}	150	35		600	24	1722	1989	0.55	0.52

The easy axis of magnetization in OOP direction observed in the $CoFe_2$ NW arrays and PZT^{500}-$CoFe_2$ nanocable arrays (**Figure 4.5**) associated with the uniaxial shape anisotropy along the out-of-plane direction of the individual nanowires, low packing density and relatively large aspect ratio of the nanowires (*Dmitriiev et al., 2013*) was indicated after the thermal oxidation at 500 °C for 24 hours at 1.5 °C/min heating ramp (see **Figures 4.11a,c,e,g**). This OOP easy axis in the CFO^{500} NW and PZT^{500}-CFO^{500} NC arrays was attributed to the incomplete thermal oxidation of the metal $CoFe_2$ phase into the metal oxide CFO phase. This also caused relatively small values of coercivity, H_c, (~400-700 Oe) for both CFO^{500} nanowires and PZT^{500}-CFO^{500} nanocables (see **Table 4.2**). A clear difference in the values of m_r/m_s in OOP and IP directions for both CFO_{500} nanowires and PZT^{500}-CFO^{500} nanocables was observed. However, very close

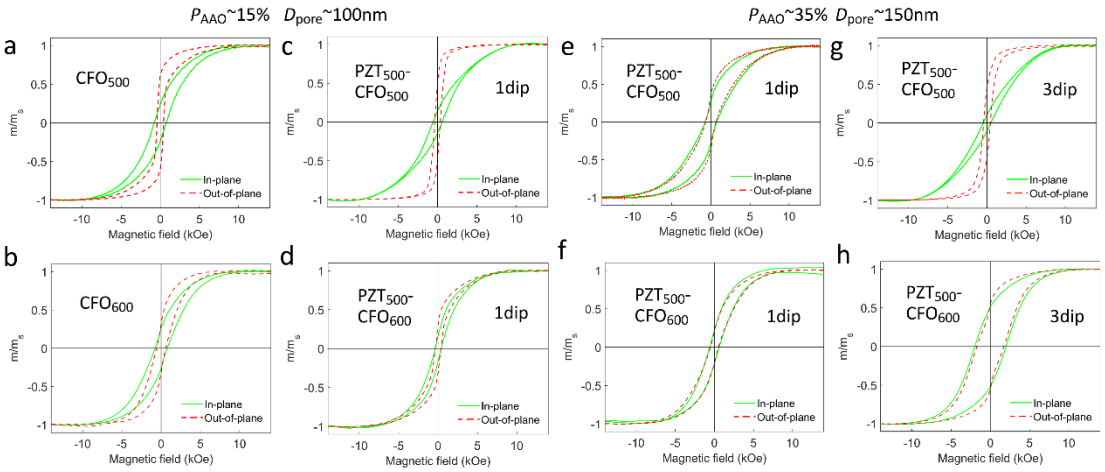

Figure 4.11: Room temperature hysteresis loops along in-plane (solid line) and out-of-plane (dashed line) directions for the vertically aligned CFO^{500} **(a)** and CFO^{600} **(b)** nanowire arrays (D_{pore}~100 nm; P_{AAO}~15%), consisted of single-layer PZT nanotubes PZT^{500}-CFO^{500} **(c)** and PZT^{500}-CFO^{600} **(d)** nanocable arrays (D_{pore}~100 nm; P_{AAO}~15%) and PZT^{500}-CFO^{500} **(e)** and PZT^{500}-CFO^{600} **(f)** nanocable arrays (D_{pore}~150 nm; P_{AAO}~35%), and consisted of three-layer PZT nanotubes PZT^{500}-CFO^{500} **(g)** and PZT^{500}-CFO^{600} **(h)** nanocable arrays (D_{pore}~150 nm; P_{AAO}~35%)

values of m_r/m_s in OOP and IP ~0.36 and 0.27, respectively were observed for the PZT^{500}-CFO^{500} NC arrays (D_{pore}~150 nm; P_{AAO}~35%) consisted of single-layer PZT nanotubes (**Figure 4.11e**). Such a small difference between two values is not due to the full oxidation of $CoFe_2$ NWs at 500 °C but rather associated with the nanowires packing factor, P_{NW}, ~30% resulting in H_{eff} going towards zero (see **Equation 4.2**).

Figures 4.11b,d,f,h show the magnetic hysteresis loops for the CFO^{600} nanowires (**Figure 4.11b**) and PZT^{500}-CFO^{600} nanocables (**Figures 4.11d,f,h**) oxidized at 600 °C during 24 hours. As compared to the above nanowires and nanocables oxidized at 500 °C the hysteresis loops became more isotropic (looking similar in both OOP and IP directions), and the difference in values of H_C and m_r/m_s for IP and OOP directions was reduced (**Table 4.2**), thus indicating a dilution of magnetic anisotropy due to the efficient oxidation of the metallic $CoFe_2$ phase into the metal oxide CFO phase after annealing at 600 °C for 24 hours. Since magnetocrystalline anisotropy constant of the CFO K_1~2.6-3.5×10^6 erg/cm^3 (*Tachiki, 1960*) is larger than for the $CoFe_2$ K_1~10^5 erg/cm^3 (*Bozorth, 1937*), the magneto-crystalline anisotropy energy dominates in the CFO^{600} nanowires and PZT^{500}-CFO^{600} nanocables, and there is no preferred crystallite orientation along the wire axes. Although large coercive field, H_c, ~1990 Oe and remanence, m_r/m_s, ~0.55 were achieved for the PZT^{500}-CFO^{600} nanocables samples (D_{pore}~150 nm; P_{AAO}~35%) consisting of three-layer PZT nanotubes with (**Figure 4.11h**) However, we must precise that only 10 % of PZT^{500}-CFO^{600} samples with three-layer PZT nanotubes showed such strong magnetic properties and other 90% of the PZT^{500}-CFO^{600} NC arrays, especially ones consisting in single-layer PZT tubes, showed relatively low coercivity, H_c, (~400-700 Oe) and remanence ratio, m_r/m_s (~0.2-0.3). Such small value of H_c for single-layer PZT nanotubes in PZT^{500}-CFO^{600}

nanocables could be explained by the interdiffusion between AAO, PZT, and CFO through thin single-layer PZT walls increasing the possibility of Al impurities in the CFO nanowires phase. However, higher reproducibility of the PZT^{500}-CFO^{600} nanocables with large coercivity and remanence were obtained when three-layer PZT nanotubes were used in nanocables.

Summary of magnetic properties of corresponding CFO nanowires and nanofibers prepared using three major techniques (templated electrodeposition, sol-gel infiltration and sol-gel electrospinning) is presented in **Table 4.3**. The values of coercive fields and remanence observed in our work are comparable to the room temperature values reported in the literature.

Table 4.3: Magnetic properties of CFO 1D nanowires and nanofibers prepared using various techniques

CFO 1D materials preparation	T_{ox}, °C	Time, h	D_{pore}, nm	H_c^{max}, Oe	M_r/M_s^{max}	Reference
Electrodeposition & oxidation inside AAO membrane	600	24	150	**1804**	**0.50**	*This work (PZT^{500}-CFO^{600} nanocables)*
	600	24	150	**1989**	**0.55**	
	500	12	200	630	-	*Carlier et al., 2006*
		24		845		
	620	30	100	**1900**	**0.48**	*Hua et al., 2007*
Sol-gel deposition & crystallization inside AAO membrane	600	2	60	1600	-	*Jung et al., 2005*
	600	10	80	1100	-	*Yuan et al., 2009*
	600	-	150	1050	-	*Pirouzfar et al., 2014*
	500	10	40	1405	-	*Ji et al., 2003*
	550	2	50	**1800**	-	*Pham-Huu et al., 2003*
	600			1400		
	600	5	20	1495	**0.49**	*Wu et al., 2011*
			30	1280	0.42	
Nanofibers electrospinning & crystallization	600	4	-	1123	0.33	*Cheng et al., 2011*
	700			1207	0.37	
	450	2	-	**1802**		*Jing et al., 2016*
	550			1523	-	
	650			1430		
	700	1	-	1162	-	*Lu et al., 2014*
	800			1098		
	500	3	-	1117	0.44	*Sangmanee & Maensiri, 2009*
	600			1185	**0.47**	
	400	0.5	-	1370	-	*Xiang et al., 2013*

4.5 Ferroelectric Characterization of PZT^{500} Nanotubes, Core-Shell PZT^{500}-$CoFe_2$ and PZT^{500}-CFO^{600} Nanocables

Macroscopic evidence of ferroelectricity in nano-objects remains challenging, since it is not possible to apply electrodes in the same way for electric characterization, as for thin films (*Morrison et al., 2003*). It is difficult to compare the values of piezoelectric coefficients to bulk material and thin films, since the measurement performed on a tube geometry has a relatively complicated field distribution and vibrational modes (*Scott, 2007b*). Although, some attempts were made to measure ferroelectric properties of the PZT nanotubes inside AAO membrane by polishing the membrane and depositing the top aluminium electrodes of ~1 μm thickness using thermal evaporation (*Hua et al., 2008*), but large leakage currents did not allow to observe a clear hysteresis loop, unless the measurement frequency is increased to 100 kHz, and the leakage current contribution are minimized, then distinct *P-E* hysteresis loops can be observed (*Kim et al., 2008*).

Switching of ferroelectric nanotubes is generally provided via an AFM tip (*Scott et al., 2005*). In order to evaluate quantitatively the combination of d_{ij} piezoelectric coefficients contributing to the AFM piezo-response, it is necessary to have a theory for piezoelectricity in tubes with arbitrary polarization. The polarization in fine-grained ceramic nanotubes can be along the tube length, *z*, along the tube wall radius, *r*, or along the azimuthal direction, Θ, around the tube. Polarization switching in a single nanotube of PZT collected on a metal substrate with a sputtered top contact, was previously reported (*Luo et al., 2003*). This gave a small circumference around which switching hysteresis could be observed in the piezo-AFM mode. Hence, they measured $P(\Theta)$, they correctly described this result as only a ''d_{ij} effective,'' since no theory exists as yet to relate the measurement to conventional d_{ij} coefficients for the geometry used.

Local probe measurements such as PFM were used in this work to confirm the polarization switching and microscopic ferroelectric properties of nanocables. Piezoresponse Force Microscopy measurements were performed by the group of Prof. Bernard Nysten at Bio and Soft Matter division of Institute of Condensed Matter and Nanosciences (MICA platform) of Université catholique de Louvain, Belgium.

The three-layer PZT nanotubes and PZT-$CoFe_2$ and PZT-CFO core-shell nanocables consisting of three-layer PZT shells were considered for the PFM characterization. To collect the nanotubes and nanocables on the platinized Si wafers the AAO membranes hosting the nanotubes and nanocables were chemically dissolved using the same procedure as for TEM observation described in **Section 3.4.3** (p. 123). **Figures 4.12a** show top-view SEM images of the horizontally positioned PZT^{500} nanotubes on the Pt/Ti/Si substrate. The nanotubes outer diameter is ~150 nm, as

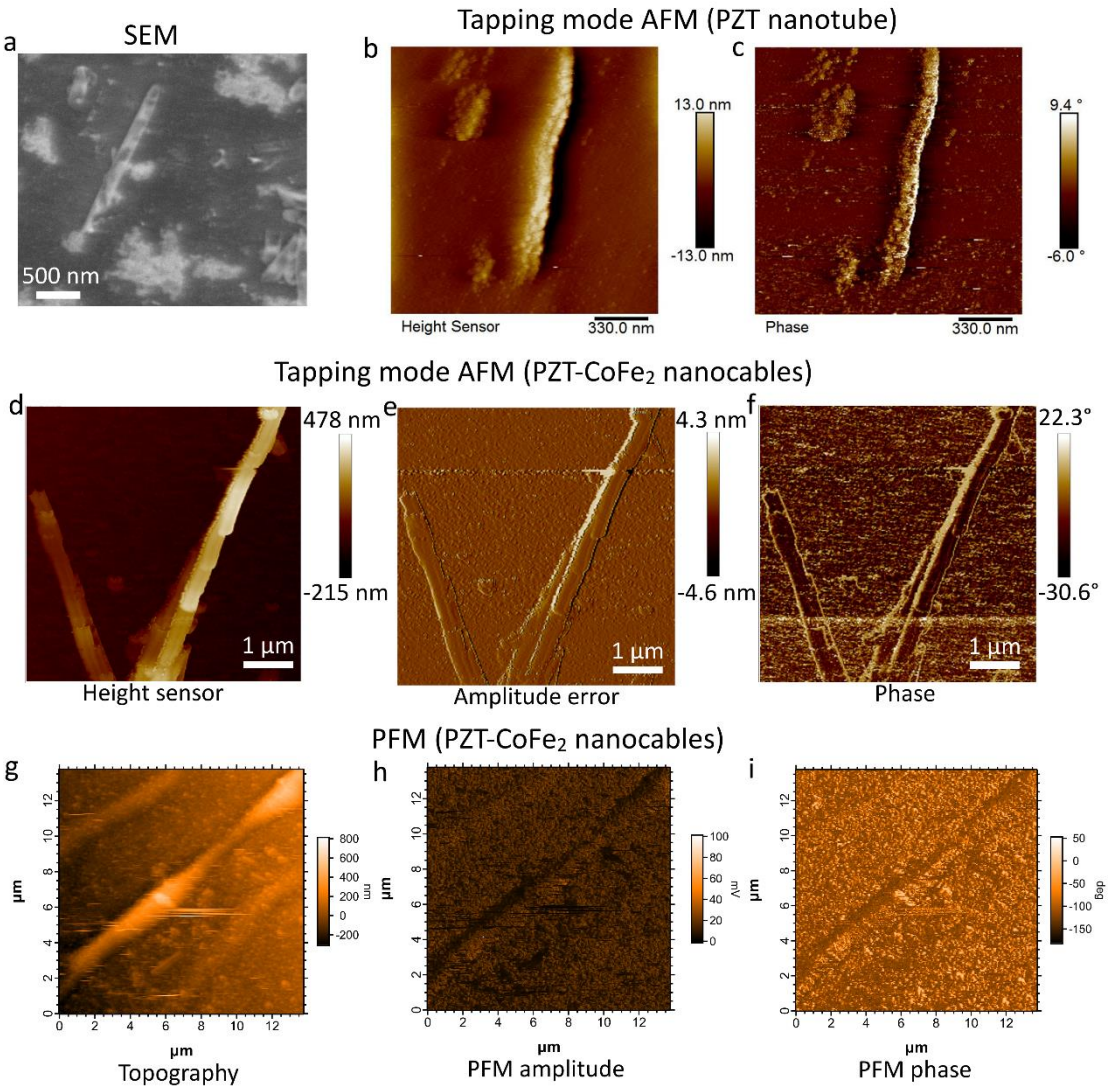

Figure 4.12: (a) HRSEM images of the three-layered PZT^{500} nanotube collected on the platinized Si substrate after AAO membrane dissolution. Tapping mode AFM topography **(b)** and phase **(c)** images corresponding to the PZT^{500} nanotube. Tapping mode AFM topography (d), amplitude error (e), and phase (f) of the PZT^{500}-$CoFe_2$ nanocables. PFM topography (g), amplitude (h), and phase (i) of the PZT^{500}-$CoFe_2$ nanocables.

expected from the morphological features of the porous Synkera-2 membrane (see **Table 3.1,** p. 60.

The ferroelectric properties of the PZT^{500}-$CoFe_2$ nanocables were studied by Piezoresponse Force Microscopy (PFM) in contact mode. **Figures 4.12c,d** show tapping mode AFM topography **(b)** and phase **(c)** scans for the PZT^{500} nanotube with outer diameter ~150 nm for an area of 2 × 2 µm^2.

Figures 4.12d,e,f show tapping mode AFM topography **(d)**, amplitude error **(e)**, and phase **(f)** images taken on the PZT^{500}-$CoFe_2$ nanocables with outer diameter ~150 nm for an area of 5.5 × 5.5 µm^2 (right) and 2.6 × 2.6 µm^2 (left). **Figures 4.12g,h,i** show PFM topography (g), amplitude (h), and phase (i) images of the corresponding PZT^{500}-$CoFe_2$ nanocables. The phase image (**Figure 4.12i**) implies that the ferroelectric

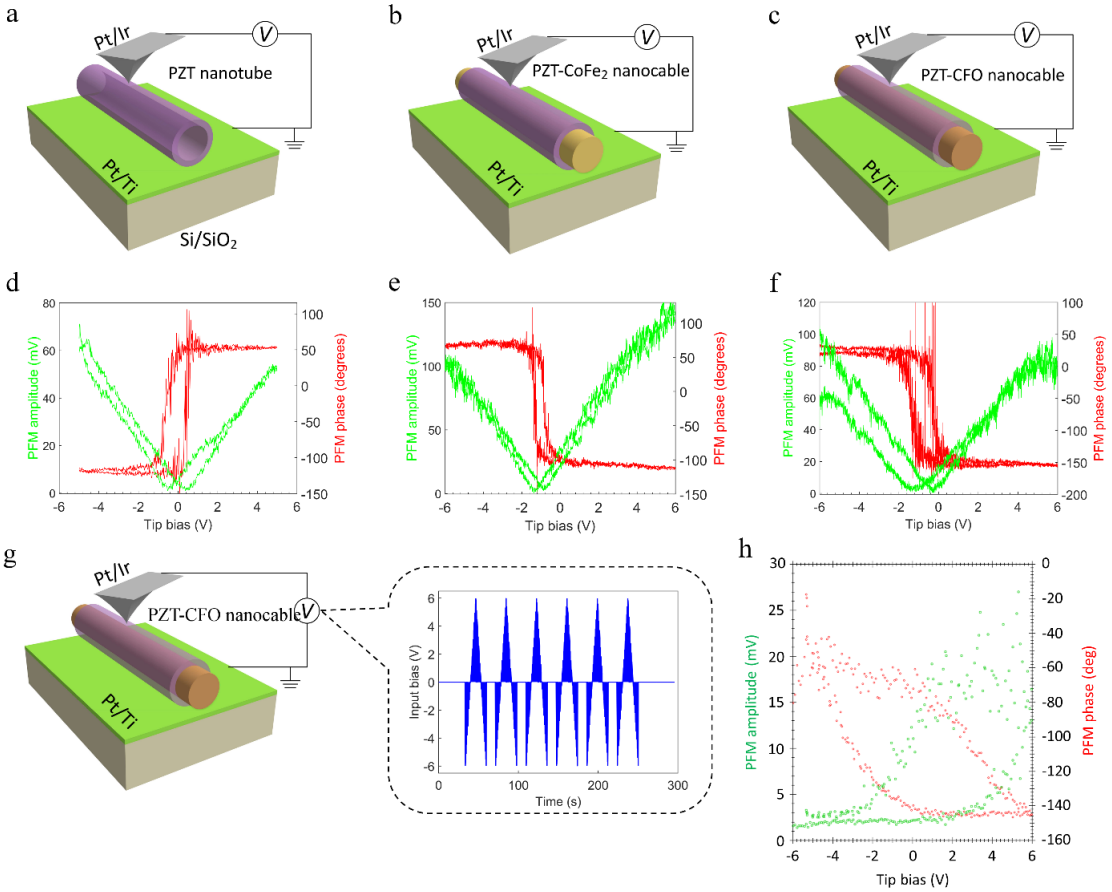

Figure 4.13: Schematic of localized ferroelectric characterization and domain switching shown by in-field phase (red line) and amplitude (green line) hysteresis loops for **(a,d)** the three-layered PZT^{500} nanotube; **(b,e)** the PZT^{500}-$CoFe_2$ nanocable; **(c,f)** the PZT^{500}-CFO^{600} nanocable. **(g)** Switching spectroscopy PFM (SS-PFM) mode with application of triangular-shaped voltage pulses; **(h)** SS-PFM measured amplitude (green dots) and phase (red dots) hysteresis loops for the PZT^{500}-CFO^{600} nanocable

domains located at the top margin of the PZT^{500}-$CoFe_2$ nanocables are mostly polarized downwards, indicated by the darker colour than that in the central area of nanocables.

To further investigate the ferroelectric nature of an individual PZT^{500} nanotube, or PZT^{500}-$CoFe_2$ and PZT^{500}-CFO^{600} nanocables, the electromechanical amplitude and phase hysteresis loops were measured using PFM, where a conductive tip served as a top electrode in capacitor geometry while the Pt/Ti/Si substrate acted as the bottom electrode as schematically shown in **Figures 4.13a-c**. Firstly a three-layer PZT nanotube or nanocables containing three layer PZT shell were identified by the AFM scan in tapping mode, and then the phase and amplitude piezoresponse signals in contact mode were measured in the central region of nanotube or nanocable by applying AC electric field and DC bias voltage with amplitude of 5 V and 6 V and at a frequency of 300 kHz through the conductive tip (*Gruverman et al., 1998*). **Figures 4.13d-f** show the out-of-plane phase (red line) and amplitude (green line) hysteresis loops measured in the central region of the PZT^{500} nanotube **(d)**, the PZT^{500}-$CoFe_2$ nanocable **(e)**, and the PZT^{500}-CFO^{600} nanocable **(f)**. The phase variation in the PZT^{500} nanotube was

around 170° after the bias voltage was increased from -5 to +5 V, and for the PZT^{500}-$CoFe_2$ and PZT^{500}-CFO^{600} nanocables with voltage changing from -6 to +6 V the phase change was around 180°. The domain switching voltages were (+0.4) – (+0.5) V, (-0.9) – (-1.3) V, and (-0.4) – (-1.3) V for the PZT^{500} nanotube, PZT^{500}-$CoFe_2$ and PZT^{500}-CFO^{600} nanocables, respectively. The maximal switching voltage shows values, which are in the same order of magnitude with some of the previously reported values measured by PFM for the ferroelectric PZT nanotubes (*Luo et al., 2003*; *Nonnenmann et al., 2009*; *Nonnenmann et al., 2010*) and PZT-CFO (*Tang et al., 2017*; *Xie et al., 2008a*), PZT-NFO (*Xie et al., 2008b*), and PZT -Co (*Johnson et al., 2011*) nanocables, but at the same time by an order of magnitude lower than in other reports corresponding to the PZT nanotubes (*Bernal et al., 2012*; *Scott et al., 2008*) and PZT-CFO core-shell nanocables (*Xie et al., 2011*).

The PFM amplitude hysteresis show typical butterfly loops for each sample. For the PZT^{500}-$CoFe_2$ and PZT^{500}-CFO^{600} nanocables (**Figure 4.13ef**), negative shifts of coercive fields in the phase and amplitude hysteresis loops were observed, which can be attributed to the presence of surface charges at the interface between $CoFe_2$ or CFO^{600} nanowires and PZT^{500} shells as was previously reported for the case of PZT-LSMO multilayers, PZT films, and PZT nanowires (*Wu et al., 2000*; *Hong et al., 2001*; *Zhang et al., 2004*).

To remove the artefact contributions of surface charge from the piezoresponse, local ferroelectric hysteresis measurement of the individual PZT^{500}-CFO^{600} nanocable was conducted using switching spectroscopy PFM (SS-PFM) (*Jesse et al., 2006*), in which electromechanical hysteresis loops were collected by measuring the PFM amplitude and phase after applying *dc* bias with maximal voltage of 6 V in a triangular waveform (see **Figure 4.13g**). The location of the measurement was the same as for the hysteresis loops measured in **Figure 4.13c**. The SS-PFM amplitude (green dots) and phase (red dots) hysteresis loops are shown in **Figure 4.13h**. The phase coercivity shift observed in **Figure 4.13f** was not identified in the SS-PFM phase hysteresis (**Figure 4.13h**). The most probable reason is that the applied bias is not large enough, the experiment must be repeated for wider voltage bias ~10-20 V. Another possibility is that we can have some artefacts contributing to the PFM signal, but most probable reason is not sufficiently large bias voltage.

In a recent review a question "why so many materials exhibit "ferroelectricity" on nanoscale?" was addressed (*Vasudevan et al., 2017*), where the authors present a list of possible mechanisms that can contribute to electromechanical response and sometimes hysteresis, as well as their typical experimental features (see **Figure 4.14**). For example, observation of a clockwise hysteresis loop is not a feature of a standard ferroelectric and is strongly suggestive of charge injection or other phenomena. Alternately, formation of electrochemical dipoles is associated with a continuum of states in the contact Kelvin PFM (cKPFM) response, a feature that is absent in standard ferroelectrics with two stable polarization states. Although the existence of non-

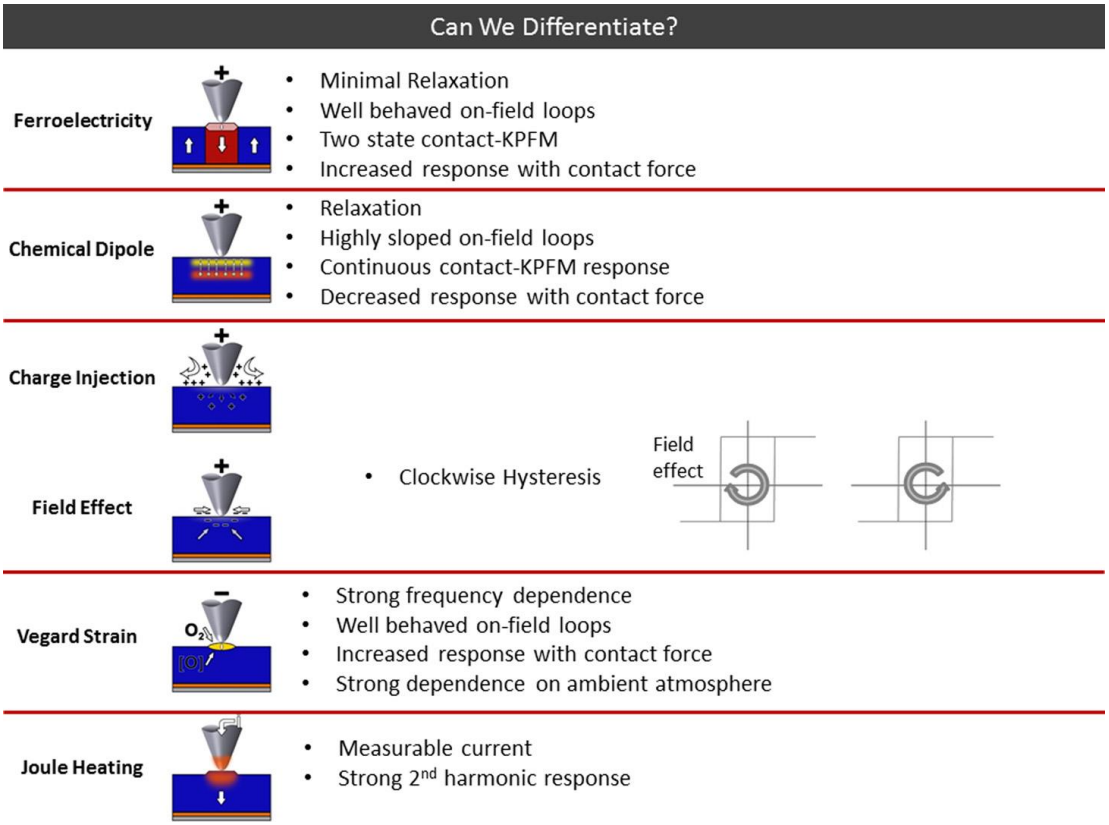

Figure 4.14: Differentiating the different mechanisms from tip bias-induced experiments. Presented in this figure are some characteristic features of the various physical and (electro)chemical processes that can occur in contact AFM when bias is applied, and how they may be separated. From *Vasudevan et al., 2017*

ferroelectric signal contribution in SPM-type experiments is widely acknowledged, clear guidelines on how to avoid or distinguish them from ferroelectric responses have been described in detail (*Vasudevan et al., 2017*).

The next step for the characterization of PZT-CFO and PZT-$CoFe_2$ core-shell nanocables would be an investigation of the strain-mediated magnetoelectric coupling by applying different static magnetic fields to the PZT-CFO nanostructures in the out-of-plane direction with respect to the substrate and recording the induced change of the PFM phase and amplitude, i.e. phase width, polarization switching voltage and coercivity. The main challenge in this regard is to ensure that the location of the nanocables doesn't change after the AFM identification as well as application of the static magnetic field, meaning that the bonding of the magnetic nanocables to the conductive substrates should be strong enough to resist the mechanical and electrostatic forces from the tip and applied magnetic field. Previously, attempts for the magnetoelectric characterization of the core-shell nanowires using static magnetic field induced change of PFM phase and amplitude (**Figure 4.15**) were reported for the PZT-CFO and PZT-Co core-shell nanocables (*Xie et al., 2011*; *Johnson et al., 2011*).

Figures 4.15a show the schematic of reported scanning probe microscope setup, where an in-plane magnetic field is applied to the PZT-CFO core-shell nanowire

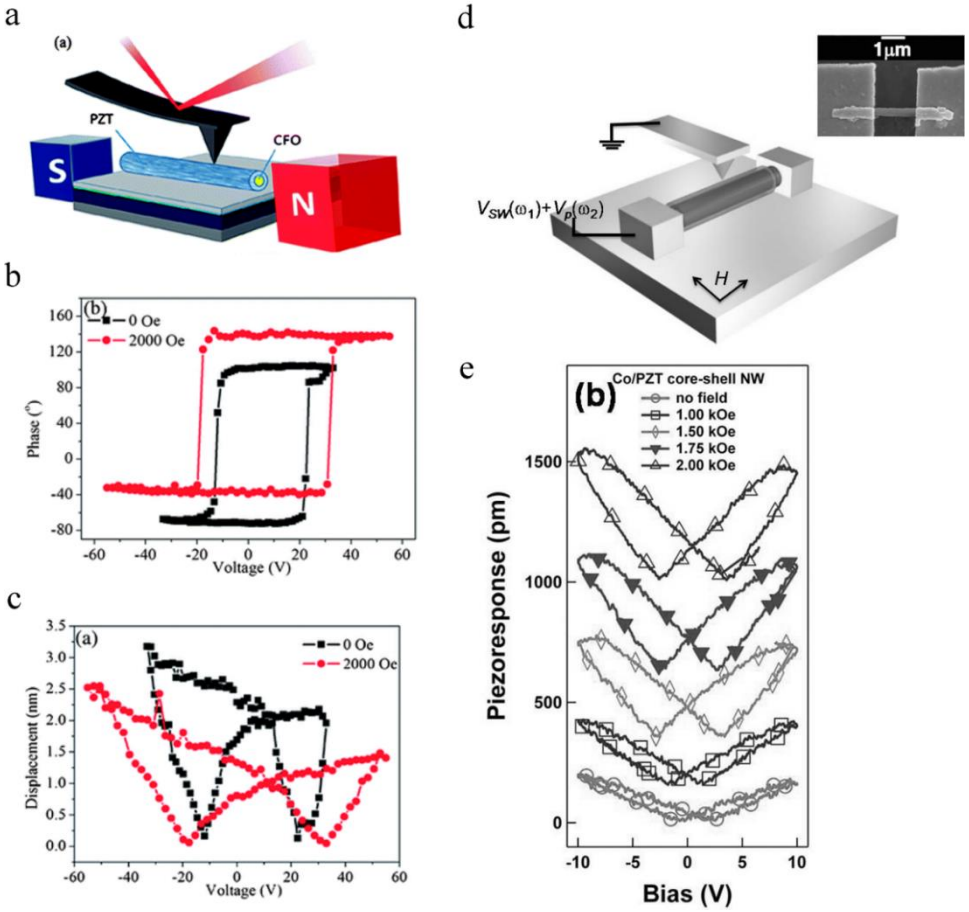

Figure 4.15: The magnetoelectric characterization of the core-shell nanowires: **(a)** The schematic scanning probe microscopy setup used for the ME measurements of the PZT-CFO nanofibers. The switching characteristics of piezoresponse in a PZT-CFO core-shell nanofibers before and after the application of external magnetic field by variable field module; **(b)** Phase-voltage hysteresis loop, **(c)** Amplitude-voltage butterfly loop (from *Xie et al., 2011*). **(d)** Schematic illustration of the magnetoelectric PZT-Co core-shell NW, electrode configuration, and probing geometry. Inset: scanning electron micrograph of an electrically contacted core-shell NW, **(e)** Piezoresponse amplitude, plotted as functions of voltage applied across the shell, at selected values of applied magnetic field, *H*, as denoted in the legend, for Co-core, $PbZr_{0.52}Ti_{0.48}O_3$ NW (from *Johnson et al., 2011*)

resulting in the induced variation in PFM phase and amplitude (**Figures 4.15b,c**). It was reported that after application of external magnetic field of 2000 Oe the maximum PFM amplitude decreased from 3.2 nm to 2.5 nm and the corresponding coercive voltage increased from 17 V to 22 V, confirming the ME coupling in PZT-CFO core-shell nanofiber. Another research group reported the ME coupling characterization of the PZT-Co core-shell nanocables using PFM setup schematically shown in **Figure 4.15d**. H_{dc} was applied along the axis of the nanowire, *z*, and alternately in plane of the substrate while a waveform comprising switching (V_{SW}) and probing (V_P) components were applied directly to the electrically contacted Co core, which is a different measurement principle as for the ME characterization shown in **Figure 4.15a**. **Figure 4.15e** shows that the application of an *H*-field perpendicular to the axis of the

PZT-Co nanocable during collection of the variation of piezoresponse amplitude with voltage results in approximate doubling in d_{33} over the range $0<H<2$ kOe, and the voltage difference between the two minima in the piezoresponse amplitude increase from ~0.4 to 1.1 V for $0<H<2$ kOe.

4.6 Conclusions

In summary, PZT-CFO core-shell nanocables have been successfully prepared combining the cost-effective dip-impregnation based on sol-gel chemical solution deposition and pulsed electrodeposition processes. The colloid containing Pb, Zr and Ti precursors was prepared using inverted mixing order chelate processing. The pyrolysis and crystallization of the dehydrated PZT tubular layers were carried out in a single heating step at 500 °C. One of the critical points for the preparation of PZT nanotubes to ensure good ferroelectric properties is the nanotube wall thickness. The wall thickness of PZT nanotubes was increased by increasing the number of sol-gel dip-impregnations to three. The thermal treatment required to transform metal $CoFe_2$ phase into the insulating $CoFe_2O_4$ spinel phase is a key step with respect to the interdiffusion phenomena between AAO membrane, PZT shells, and $CoFe_2$ nanowires. We demonstrated that PZT nanotubes act as an efficient diffusion barrier between the $CoFe_2$ nanowires and AAO template. We overcame the thermal constraints and demonstrated the benefit of a global lowering of the processing temperature to preserve both architecture and structural integrity of this complex system. Such control of interfaces opens a promising pathway towards low-cost processing of magnetoelectric nanocomposites.

Magnetic properties of the PZT-$CoFe_2$ core-shell nanocables, such as magnetic anisotropy, remanence and coercivity, are affected mainly by the dipolar interaction between the nanowires in highly packed arrays and shape anisotropy of individual nanowires at low packing densities. It was shown that the packing density and corresponding dipolar coupling of the $CoFe_2$ nanowire arrays can be reduced by increasing the surrounding PZT shell thickness. For the PZT^{500}-CFO^{600} core-shell nanowires ($CoFe_2$ oxidized at 600 °C) the magnetocrystalline anisotropy is dominant leading to the isotropic hysteresis behaviour regardless of the direction of applied magnetic field.

We investigated the local ferroelectric properties of nanotubes and core-shell nanocables by PFM polarization switching. The measured PFM phase change in the PZT nanotube was ~170° while the voltage was switched from -5 to +5 V, as for the PZT-CFO core-shell nanocables the phase variation was ~180° with the voltage changed from -6 to +6 V. To separate ferroelectric polarization from electrostatic interaction between the PFM conductive tip and PZT nanotube, as well as from surface charges trapped in the PZT/CFO interfacial area, switching spectroscopy PFM mode was used for the PZT-CFO core-shell nanocable. The SS-PFM hysteresis was not

observed due not large enough window bias voltage. Therefore, the experiment must be repeated using larger applied bias voltage.

In general, the limitations of the ME system based on PZT-CFO core-shell nanocable arrays include the inter-diffusion between PZT nanotubes and AAO membrane, non-uniform wall thickness of PZT nanotubes, incomplete oxidation of $CoFe_2$ nanowires at lower temperatures (used to prevent inter-diffusion), and poor reproducibility of the CFO nanowires with large coercivity. These limitations would make it difficult to obtain good quality ME specimens and challenging to use the PZT-nanotubes based core-shell nanostructures in real technology applications.

Chapter 5

Vertically Aligned CFO Nanopillars – Ferroelectric Matrix Nanocomposites

5.1 CFO Nanopillars within BSTO And BTO Thin Layers

(1-3) Vertically Aligned Nanostructures

In **Figure 5.1** we remind fabrication steps for the BSTO-CFO and BTO-CFO vertically aligned multiferroic nanocomposites. These processes are schematically shown in **Figure 3.14**, p. 87 and discussed in detail in **Section 3.2**. Ferromagnetic, ferroelectric and elastic properties of ceramic CFO, BSTO and BTO materials are summarized in **Tables 2.3** and **2.4**, p. 45. The $Ba_xSr_{1-x}TiO_3$ solid solution is chosen due to the tunability of both the Curie temperature (T_C) and the permittivity values by varying the Ba/Sr ratio, e.g. for the composition 70 atomic % Ba (x ~0.7) T_C is close to room temperature (*Parker et al., 2002*) and $\varepsilon_{33}/\varepsilon_0$ of ceramic BSTO ~20,000 (*Mitsui, 1970*). The $BaTiO_3$ FE material is chosen due to its large piezoelectric coefficient d_{ij} ($d_{15} = 270$ pC/N, $d_{31} = -79$ pC/N, $d_{33} = 191$ pC/N) and suitable dielectric properties ($\varepsilon_{33}/\varepsilon_0 \sim 1350$) at room temperature (*Mitsui, 1970*). The CFO FM material chosen due to the large magnetocrystalline anisotropy constant $K_1 \sim 2.6 - 3.8 \times 10^6$ erg/cm^3 and magnetostriction coefficient λ_{ijk} ($\lambda_{100} \sim -590 \times 10^{-6}$, $\lambda_{111} \sim 120 \times 10^{-6}$) (*Folen, 1970*).

Compared to the PZT-CFO core-shell NC arrays discussed in **Chapter 4**, the oxidation of the metal $CoFe_2$ nanopillars into the metal oxide CFO spinel phase requires an additional step of the AAO template dissolution to prevent the interdiffusion between nanopillars and AAO template favoured by the thermal oxidation. The original *in situ* synthesis of vertically aligned multiferroic nanostructures allows to improve the ordering of the magnetic nanopillars inside the matrix, and to preserve the nanopillar

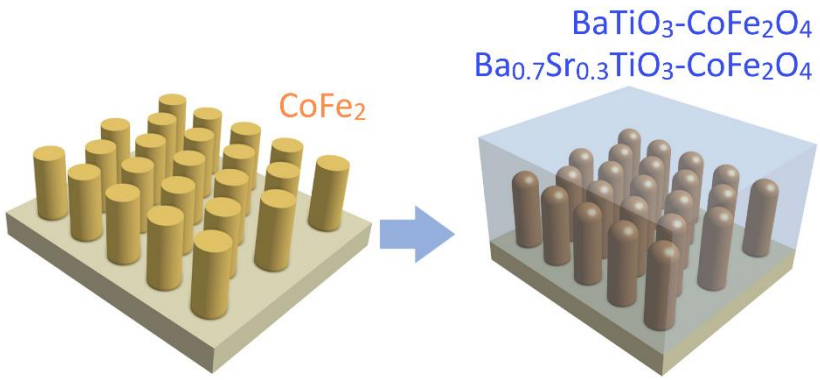

Figure 5.1 Sketch of the fabrication process of the vertically aligned $Ba_{0.7}Sr_{0.3}TiO_3$-$CoFe_2O_4$ and $BaTiO_3$-$CoFe_2O_4$ by RF magnetron sputtering of the FE layers on the metal $CoFe_2$ nanopillar arrays

morphology. Indeed, when the oxidation of the free-standing $CoFe_2$ nanopillars was conducted by thermal treatment prior to FE layer deposition, a significant change of the surface roughness morphology of pillars, and an increase of their diameter were found, which could prevent the penetration of FE layer through the ordered pillar arrays. We used different techniques to characterize the electrical and magnetic properties and to quantify the magnetoelectric coefficient of the resulting BSTO-CFO and BTO-CFO multiferroic nanostructures.

5.2. Characterization of Vertically Aligned CFO Nanopillar – BSTO Matrix Nanocomposites

A tilted-view cross-section SEM image of the vertically aligned and free-standing $CoFe_2$ nanopillar arrays on Pt/Ti/Si substrate, obtained after removal of the AAO template, is shown in **Figure 5.2a**. Both ordering and uniformity in diameter of the $CoFe_2$ nanopillars can be seen on the top-view and tilted-view SEM images (**Figure 5.2b,c**).The nanopillars height is ~200 nm and diameter is ~90 nm, as expected from the morphological features of the porous AAO template. A tilted-view SEM image (**Figure 5.2d**) of the BSTO-CFO nanostructure shows that the BSTO matrix penetrates the spacing between the pillars to form the two-phase columnar structure made of the CFO pillars coated by the BSTO shells (schematically represented in **Figure 5.2d**). In addition to the 200-nm-thick BSTO coverage of nanopillars, a continuous BSTO layer of thickness ~250 nm is also formed at the top of the CFO nanopillars (**Figure 5.2f**) with a rather high surface roughness (**Figures 5.2e**). Note that by surface roughness we imply an average estimation based on the SEM image. To improve the roughness analysis, AFM technique can be used for nanopillars horizontally positioned on substrate. The total thickness of the BSTO-CFO nanostructure is about 500 nm as schematically illustrated in **Figure 5.2f**, which is larger than the sum of the initial $CoFe_2$ nanopillars height ~200 nm and the BSTO top-layer thickness ~250 nm indicating the volume expansion of the nanopillars. Similar volume expansion was

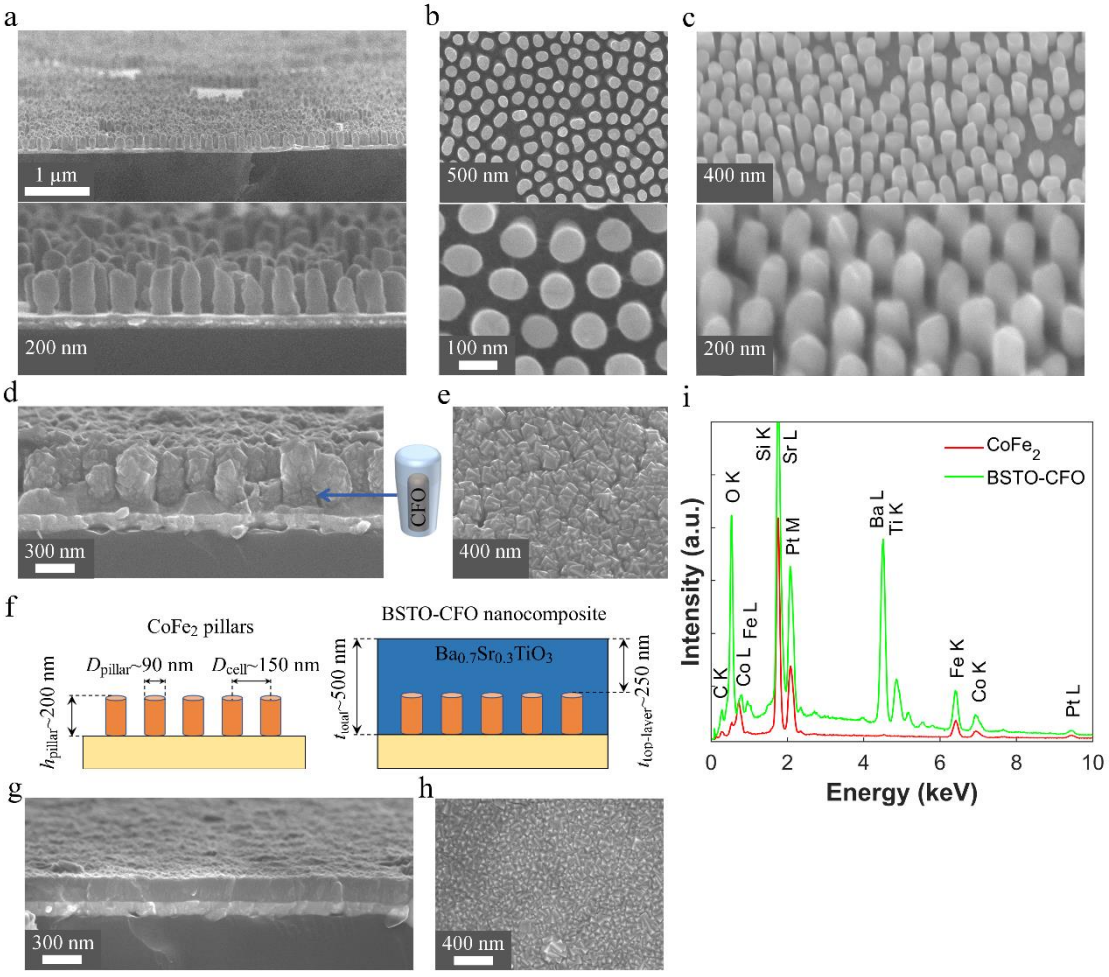

Figure 5.2: (a,b,c) Tilted-view and top-view SEM images of the vertically aligned $CoFe_2$ nanopillar array. **(d,e)** SEM images of the samples corresponding to a tilted-view and a top-view on the BSTO-CFO nanostructure **(f)** Schematic illustration of cross-section view of the $CoFe_2$ nanopillar array and BSTO-CFO nanocomposite with dimensions (nanopillars height, h_{pillar}, and diameter, D_{pillar}, inter-pillar distance, D_{cell}, total thickness of nanocomposite, t_{total}, and thickness of the BSTO top layer above CFO nanopillars, $t_{top\text{-}layer}$). **(g,h)** SEM images of the samples corresponding to a tilted-view and a top-view on the BSTO thin film. **(i)** EDX spectra of the vertically aligned $CoFe_2$ nanopillar arrays (red), and the BSTO-CFO nanostructure (green)

observed after the thermal treatment of the free-standing $CoFe_2$ nanopillar arrays (**Figures 3.25** and **3.26,** p. 105-6). The reference BSTO thin film had a thickness of ~250 nm as shown on a tilted-view SEM image (**Figure 5.2g**). The top-view SEM images showed a smaller surface roughness of the BSTO film compared to the BSTO-CFO nanocomposite (**Figure 5.2h**). An average chemical analysis was provided by EDX (**Figure 5.2i**) confirming a value of the Fe/Co ratio close to 2. An estimation of the elemental analysis in the BSTO constituent layer was not possible due to the close positions of Ba L (4.464 keV) and Ti K (4.508 keV) lines, as well as Sr L (1.806 keV) and Si K (1.739 keV) lines on the energy axis.

The critical step to achieve BSTO-CFO nanostructure is clearly the *in situ* oxidation of the $CoFe_2$ metallic pillars during BSTO deposition. Both structural and magnetic

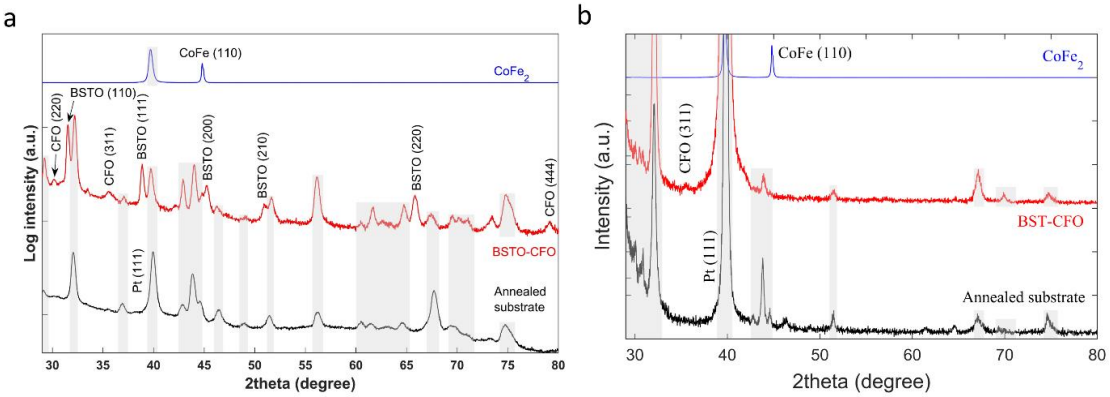

Figure 5.3: In-plane GI-XRD **(a)** and out-of-plane powder XRD **(b)** patterns of the vertically aligned $CoFe_2$ nanopillar arrays (blue), the BSTO-CFO nanostructure (red), and the Pt/Ti/Si substrate annealed at ~600 °C (black)

characterization have been conducted to probe the oxidation efficiency of the nanopillar arrays. **Figures 5.3a,b** shows in-plane GI-XRD and out-of-plane powder XRD patterns of the BSTO-CFO nanostructure, the $CoFe_2$ nanopillar arrays (JCPDS # 48-1816), and the Pt/Ti/Si substrate annealed at ~600 °C (temperature selected close to the one used for the sputtering process), respectively. The oxidation of the $CoFe_2$ nanopillar array into a polycrystalline CFO nanopillar array during the BSTO matrix deposition was confirmed by XRD through the appearance of the CFO peaks (220), (311), and (444) on the GIXRD spectrum and the (311) peak on powder XRD spectrum (JCPD # 22-1086). Note that the (222), (440) and (511) – peaks are not visible in **Figure 5.3a** because the phases corresponding to CFO and the annealed substrate can hardly be discriminated. The in- plane GIXRD diffraction pattern of the BSTO-CFO nanostructure confirms the crystallization of the BSTO matrix with all peaks corresponding to the perovskite structure. Pt peaks and additional peaks resulting from reactions and associated phase formation during annealing are observed in the XRD pattern of the Pt/Ti/Si substrate.

Figures 5.4a and **5.4b** show the normalized magnetic hysteresis loops measured at room temperature with the field applied along the in-plane (perpendicular to pillar axis) and out-of-plane (parallel to pillar axis) directions. The effective magnetic anisotropy in a nanopillar array in the saturated state is determined by different contributions, namely shape anisotropy, dipolar inter-pillar coupling and magnetocrystalline anisotropy (*Encinas-Oropesa et al., 2001*). For the $CoFe_2$ nanowire array, the magnetocrystalline anisotropy can be neglected and the effective anisotropy is entirely magnetostatic, as pointed out previously (*Hua et al., 2007*). **Figure 5.4a** reveals the easy axis of magnetization along the in-plane direction, as shape anisotropy, associated with the infinite array of the vertically aligned nanopillars behaving as a whole film, overcomes the uniaxial shape anisotropy along the out-of-plane direction of the individual nanopillars due to the high packing density and relatively small aspect ratio of the individual nanopillars (*Dmytriiev et al., 2013*). In addition, this causes the coercivity H_c ~ 190 Oe and the remanence-saturation ratio ~0.08 to become relatively

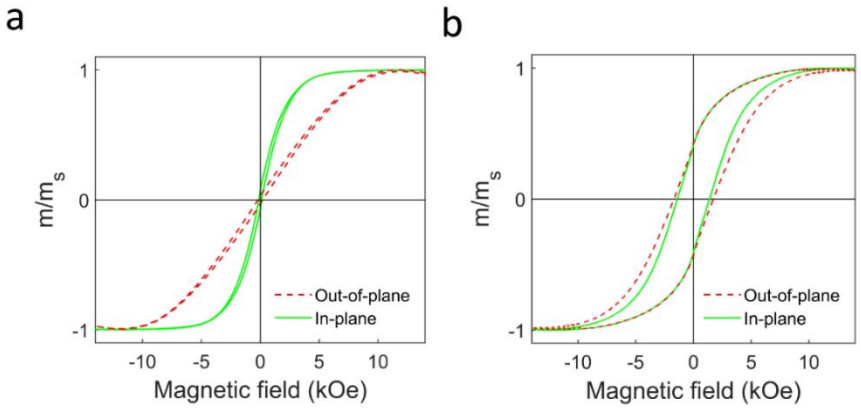

Figure 5.4: Room temperature hysteresis loops along in-plane (solid line) and out-of-plane (dashed line) directions for a vertically aligned $CoFe_2$ nanopillar array **(a)** and the BSTO-CFO multiferroic nanostructure **(b)**. The magnetic moment is normalized to its value in the saturation state

small, irrespective of the direction of the applied field. **Figure 5.4b** shows the magnetic hysteresis curve for the embedded $CoFe_2O_4$ nanowire array in the BSTO matrix. The shapes of the hysteresis loops are similar in the in-plane and out-of-plane directions as was previously observed for the case of the PZT-CFO core-shell NC arrays (see **Figure 4.11**, p. 153). This can be ascribed to the fact that the magneto-crystalline anisotropy energy dominates shape anisotropy in the CFO nanopillar arrays (*Zheng et al., 2004*), no magnetocrystalline anisotropy is expected between [001] and [100] directions of CFO, and there is no preferred crystallite orientation along the wire axes. Besides, large coercive field (H_c ~1.7 kOe) and remanence (m_r/m_s ~0.44) have been achieved in the BSTO-CFO multiferroic nanostructure. Such high coercive field is associated with the large magnetocrystalline anisotropy $K_1 \sim 2.6 - 3.8 \times 10^6$ erg/cm^3 (*Bozorth et al., 1955*). Previously the dependence of coercivity on grain size was reported for the CFO nanoparticles revealing that the maximum value of coercivity could be obtained for the grain size approaching the single-domain critical value (*Chinnasamy et al., 2003*). Thus, in future work HR-TEM analysis should be conducted to understand the dependence of coercivity on grain size in the CFO nanopillars inside BSTO matrix. The coercive fields for CFO nanowires are comparable to the room temperature values reported in the literature (see **Table 4.3**, p. 154), thus confirming the efficiency of the *in situ* oxidation of the $CoFe_2$ nanopillars during the deposition of the BSTO matrix (*Chinnasamy et al., 2003*). We also found that the experimentally measured magnetic moment of the metal nanopillar array decreased by a factor of 3.15 after the *in situ* oxidation. Taking into account the approximate oxidation-induced volume expansion (~1.5) of the nanowires, this reduction of the sample's magnetic moment roughly corresponds to a large reduction in the saturation magnetization by a factor 4.7. This result is in good agreement with the expected ratio between the saturation magnetization for the $CoFe_2$ (~1940 emu/cm^3) and CFO (~400 emu/cm3) bulk materials at room temperature (*Cuilty & Graham, 2009*; *Ojha et al., 2016*). The magnetic moments reduction by a factor of 4-5 after oxidation of the metal $CoFe_2$ NW

arrays was also demonstrated in Chapter 4 for the PZT-CFO core-shell NC arrays (see **Figure 4.10**, p. 151).

A macroscopic evidence of ferroelectricity is a prerequisite to expect magnetoelectric coupling in such BSTO-CFO nanostructured composites. However, this remains challenging considering the complexity of these vertically aligned heterostructures. Dielectric investigations were performed, taking the well-behaved BSTO thin film as a reference for the BSTO-CFO nanostructures. Since the geometry of both sets of samples is quite different, only the capacitance and dielectric losses will be compared in the following.

Figure 5.5 shows the thermal variations at three frequencies (10 kHz, 100 kHz, and 1 MHz) of capacitance and dielectric losses for both a pure BSTO thin film (**Figure 5.5a** and **5.5b**) and the BSTO-CFO nanostructure (**Figure 5.5c** and **5.5d**). The pure BSTO thin film on the Pt/Ti/Si substrate, obtained after the chemical dissolution of top AAO template, exhibits a broad $C(T)$ anomaly in a wide range of temperature, corresponding to a diffuse ferroelectric-to-paraelectric transition (**Figure 5.5a**). This diffuse behaviour is associated with a maximum of the capacitance occurring at lower temperature (250 K) compared to the ceramic counterpart (T_C ~310 K for the bulk $Ba_{0.7}Sr_{0.3}TiO_3$), as commonly observed for thin films (*Parker et al., 2002*; *Tagantsev et al., 2003*). These discrepancies can arise from the microstructure of ferroelectric thin films including small grain size, residual strain and interfacial contributions (*Tagantsev et al., 2003*; *Lobo et al., 1995*). Therefore, the ferroelectric properties of the BSTO thin film are still partially present at room temperature. Over the whole temperature range, the dielectric losses of the BSTO thin film remain below ~0.05 (**Figure 5.5b**). For the BSTO-CFO nanostructure, the capacitance slightly increases when the temperature is raised from 80 to 200 K, similar to the pure BSTO thin film (see **Figure 5.5c** and inset). However, the maximum in capacitance associated with the ferroelectric-to-paraelectric transition close to 250 K can only be observed at high frequency ~1 MHz. At lower frequency this maximum is hindered by a strong increase of the apparent capacitance above 200 K. Accordingly, the dielectric losses showed pronounced peaks (**Figure 5.5d**), whose maximum is shifted to higher temperature as the frequency increases. The relaxation follows an Arrhenius law with an activation energy E_a ~0.45 eV, estimated from a fit over 30 frequencies in the range 1 kHz – 200 kHz (**Figure 5.6**) using the following equation:

$$E_a = \frac{s \times k_B}{1.6 \times 10^{19}} = \frac{5199 \times 1.38 \times 10^{-23}}{1.6 \times 10^{-19}} = 0.45\ eV \qquad (5.1)$$

where s = -5199 is a slope of the $ln(\omega)$ against $1/T$ relation, ω is a frequency at which the loss tangent was measured, and k_B is Boltzmann constant. This thermally activated relaxation process is responsible for an artificial increase of both the capacitance and losses at high temperature. This effect can be ascribed to conduction mechanism of the polycrystalline CFO phase due to electron hopping between multivalent cations like Fe

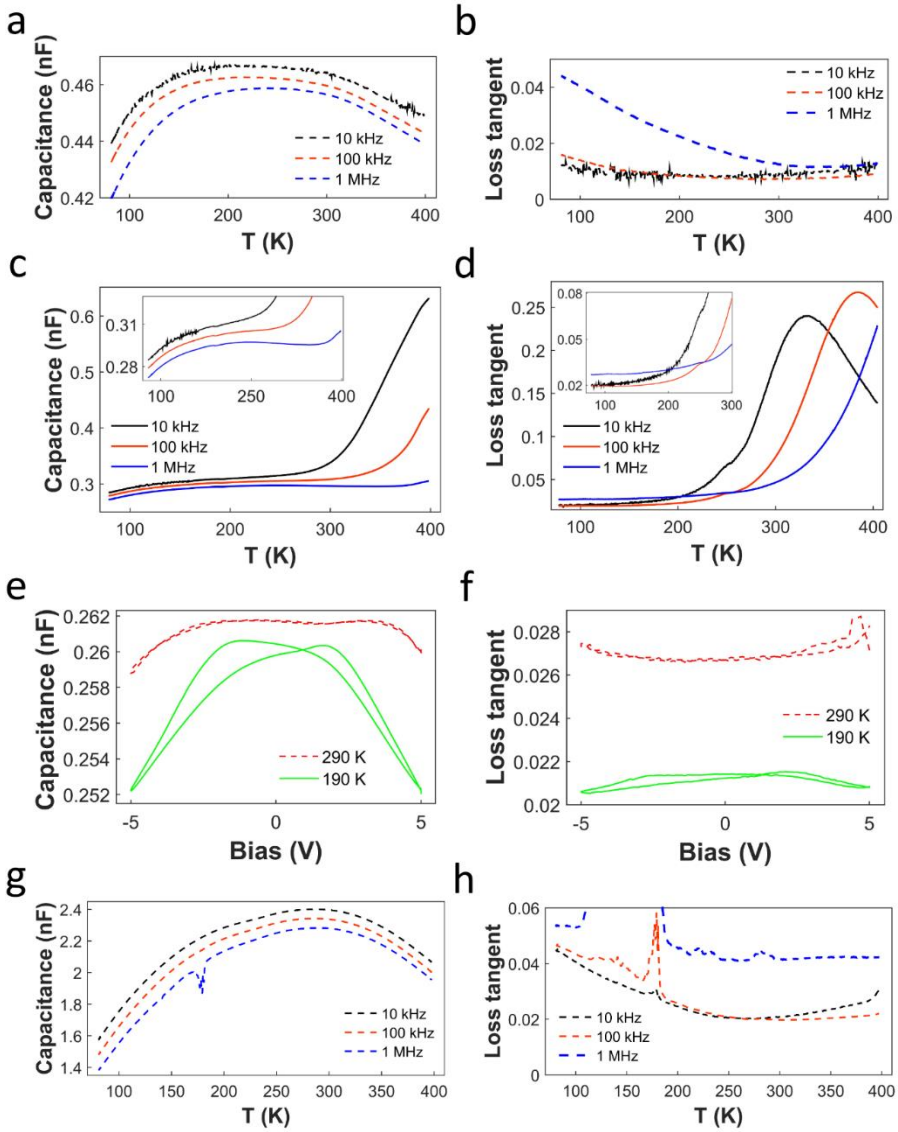

Figure 5.5: Capacitance and dielectric losses as a function of temperature for the BSTO thin film with thickness ~250 nm grown on the Pt/Ti/Si substrate, obtained after top Al layer anodization and its chemical dissoltuion **(a, b)**, and the BSTO-CFO nanostructure capacitor **(c, d)**, capacitance and dielectric losses **(e, f)** as a function of bias voltage for the BSTO-CFO nanostructure at two distinct temperatures, T = 190 K and T = 290 K. Capacitance and dielectric lossed as a function of temperature for the BSTO thin film deposited on the Si wafer platinized using magnetron sputtering **(g,h)**

and Co (*Jonker, 1959*; *George et al., 2007*), for which an activation energy ~0.4 eV is reported in the literature (*Jonker, 1959*). Another contribution can be related to charged defects inducing a Maxwell-Wagner type of interfacial polarization in agreement with Koop's two-layer model. Thus, the actual activation energy that we observed may result from several contributions including interactions among charged defects and interfacial accumulation of charges between BSTO and CFO due to the different types of charged defects in both phases. Without a deeper insight into the microscopic defects states based on local spectroscopies (such as EPR), we cannot discuss further the activation energy value and compare it to the literature.

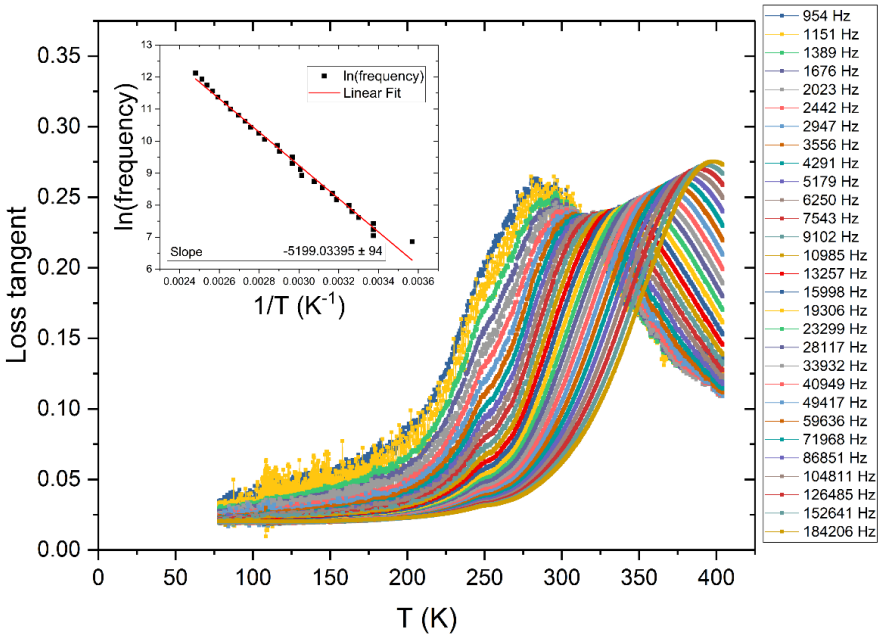

Figure 5.6: Temperature dependence of loss tangent for the BSTO-CFO nanostructure in the range 80 K – 400 K, the inset plot is the temperature dependent natural logarithm of frequency obtained from the peak points of loss tangent in the frequency range 1 kHz – 200 kHz

Figures 5.5g,h show the thermal variations at three frequencies (10 kHz, 100 kHz, and 1 MHz) of capacitance and dielectric losses for the reference BSTO thin film deposited on the pre-sputtered Pt layer. The reference BSTO thin film exhibits a similar broad $C(T)$ anomaly in a wide range of temperature, corresponding to a diffuse ferroelectric-to-paraelectric transition (**Figure 5.5g**) as was observed for the BSTO film deposited on the Pt/Ti/Si substrate obtained after top AAO dissolution (**Figure 5.5a**). However, the maximum of the capacitance occurs at higher temperature (300 K) close to the ceramic counterpart (T_C ~310 K for the bulk $Ba_{0.7}Sr_{0.3}TiO_3$) (*Tagantsev et al., 2003*). In the reference BSTO thin film, a typical behaviour of $Ba_{0.7}Sr_{0.3}TiO_3$ films was observed with maximum in capacitance at high temperature due to cubic-tetragonal transition and a shoulder at lower temperature due to tetragonal-orthorhombic and orthorhombic-rhombohedral transitions (*Tagantsev et al., 2003*). In addition, there is no intense peak at the transition temperature in the loss tangent curves at low frequencies (**Figure 5.5h**). The difference between $C(T)$ curves of the BSTO thin films on the pre-treated Pt/Ti/Si (after AAO dissolution) and reference Pt/Si substrates is imposed mainly by the stress relaxation (*Shaw et al., 1999*). Substrates can strongly affect thin films behaviour, especially stress can impact the structural phase diagram, thus shifting transition temperature. Previously it was reported that "incipient ferroelectric" $SrTiO_3$ (STO), which is generally behaving like a paraelectric material down to 0 K and never becoming a ferroelectric), can be obtained as a classic ferroelectric in highly epitaxially strained STO materials (*Haeni et al., 2004*). Strain-stress can both act to downshift or upshift the paraelectric-ferroelectric transition

temperature. Over the whole temperature range, the dielectric losses of the reference BSTO thin film remain below ~0.06 (**Figure 5.5h**).

The effective permittivity of the BSTO-CFO nanostructures and BSTO thin films was calculated as

$$\varepsilon = \frac{C \times t_{total}}{\varepsilon_0 \times S}, \tag{5.2}$$

using the capacitance value, C, [F] measured at 100 kHz frequency of $V_{ac} = 0.1$ V, $\varepsilon_0 = 8.854 \times 10^{-12}$ [F/m], the top Pt electrode's surface area, S [m^2], and the total average thickness of the deposit, t_{total} [m] (see **Figure 5.2f**), assuming that the nanocomposite can be considered as a continuous material. However, we must precise that this corresponds to an effective permittivity, since the considered experimental thickness, t_{total}, is not homogeneous and it was measured from the SEM images (±50 nm), therefore only a qualitative comparison with the error bar ~10% is proposed when dealing with ε.

In the low temperature range ($T < 200$ K), for which the conductivity contribution can be neglected, the effective permittivity of the BSTO-CFO nanostructure, corresponding to **Figure 5.5c,** where $t_{total} = 500 \pm 50$ nm (**Figure 5.2d**), top Pt contact diameter, $D = 600$ µm (or area, $S = \frac{\pi D^2}{4} = \frac{3.14 \times (0.6 \times 10^{-3})^2}{4} = 0.28 \times 10^{-6}$) is

$$\varepsilon_{\mathrm{BSTO-CFO}} = \frac{0.303 \times 10^{-9} \times (500 \pm 50) \times 10^{-9}}{8.854 \times 10^{-12} \times 0.28 \times 10^{-6}} \sim 60 \pm 6. \tag{5.3}$$

The effective permittivity of the BSTO thin film obtained after top AAO dissolution (T~200 K), corresponding to **Figure 5.5a**, where $t_{total} = 250 \pm 50$ nm (**Figure 5.2g**), top Pt contact diameter, $D = 300$ µm (or area, $S = \frac{3.14 \times (0.3 \times 10^{-3})^2}{4} = 0.07 \times 10^{-6}$) is

$$\varepsilon_{\mathrm{BSTO1}} = \frac{0.462 \times 10^{-9} \times (250 \pm 50) \times 10^{-9}}{8.854 \times 10^{-12} \times 0.07 \times 10^{-6}} \sim 180 \pm 37. \tag{5.4}$$

The effective permittivity of the reference BSTO thin film (T~200 K), corresponding to **Figure 5.5g,** with $t_{total} = 300 \pm 50$ nm, top Pt contact diameter, $D = 300$ µm (or area, $S = \frac{3.14 \times (0.3 \times 10^{-3})^2}{4} = 0.07 \times 10^{-6}$ m^2) is

$$\varepsilon_{\mathrm{BSTO2}} = \frac{2.213 \times 10^{-9} \times (300 \pm 50) \times 10^{-9}}{8.854 \times 10^{-12} \times 0.07 \times 10^{-6}} \sim 1060 \pm 177. \tag{5.5}$$

So, the effective permittivity of the BSTO-CFO nanostructure ($\varepsilon_{\mathrm{BSTO-CFO}}$~60) (**Figure 5.5c**) is lower than the one of the pure BSTO thin film ($\varepsilon_{\mathrm{BSTO1}}$~180) (**Figure 5.5a**), deposited on the pre-treated Pt/Ti/Si substrate, which is lower than the one of reference BSTO thin film ($\varepsilon_{\mathrm{BSTO2}}$~1070) (**Figure 5.5g**), deposited on the high-quality

Pt/Si substrate. This indicates the additional contribution of the low permittivity CFO phase and residual stress effects imposed by substrates.

In order to minimize the contribution at low frequency of space charge conductivity, ferroelectricity was probed by performing the capacitance-voltage $C(V)$ measurements at 1 MHz. The capacitance and dielectric losses measured at 190 K show two maxima with an opening of a hysteresis loop (**Figures 5.5e** and **5.5f**). In ferroelectric thin films, this is due to polarization reversal thus confirming the ferroelectric behaviour of our BSTO-CFO nanostructures. The same experiment performed at 290 K showed the progressive disappearance of the ferroelectric features and dominant paraelectric behaviour of the BSTO-CFO nanostructure in agreement with the diffuse ferroelectric-paraelectric transition around 250 K.

Direct measurement of the ME effect was performed to prove the magnetoelectric nature of the vertically aligned BSTO-CFO nanostructures and to provide a macroscopic estimation of the magnetoelectric coupling. Dynamic magnetoelectric measurements of the magnetoelectric voltage response were performed by the group of Prof. Kristiaan Temst and Dr. Vera Lazenka at Instituut voor Kern- en Stralingsfysica, KU Leuven, Belgium. We must note that since the considered experimental thickness, t_{total} , is not homogeneous and it was measured from the SEM images (±50 nm), the error bar can reach ~10%.

The temperature dependence of the ME voltage coefficient α_E in the range 10-300 K is shown in **Figure 5.7**. The maximal value of the ME coefficient ~340±29 mV cm^{-1} Oe^{-1} was observed around T~250 K. A decrease of the temperature between 250 K and 10 K leads to a reduction of the ME coefficient by ~17 %. The shape of the $\alpha_E(T)$ curve can be ascribed to the temperature dependence of the dielectric and magnetic properties of the multiferroic nanocomposite. Since the Curie temperature for bulk CFO (T_C ~790 K) is much higher than room temperature, the peak in the curve can be

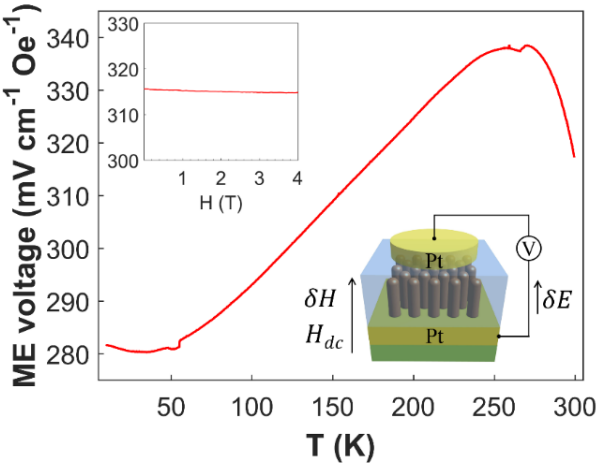

Figure 5.7: Temperature dependence of the ME voltage coefficient for the BSTO-CFO nanostructure. Schematic illustration of ME measurement and room-temperature variation with external dc magnetic field are shown in the bottom-right and top-left inset, respectively

associated with the ferroelectric-paraelectric transition of the $Ba_{0.7}Sr_{0.3}TiO_3$ phase around T_C ~250 K, as illustrated in **Figure 5.5c** and **5.5e**. In previous works performed on PZT-$La_{0.7}M_{0.3}MnO_3$ (M = Sr, Ca) multilayers and PZT-$La_{1.2}Sr_{1.8}Mn_2O_7$ thin films, the highest ME coefficient values were observed around the Curie temperature of the ferromagnetic phase (*Srinivasan et al., 2002; Wu et al., 2006*).

At room temperature, the ME voltage coefficient of the BSTO-CFO heterostructure displays very small variation (of the order of 1 %) when an external *dc* magnetic field (up to 4 T) is superimposed on the time-varying field H_{ac} as compared to the measured value in zero static magnetic field (see **Figure 5.7** [top-left inset]). The room temperature value of the ME voltage coefficient for the BSTO-CFO nanostructure (~315±29 mV cm^{-1} Oe^{-1}) is much higher than the values from macroscopic measurements reported earlier on (1-3) BFO-CFO composites (*Yan et al., 2009; Oh et al., 2010; Amrillah et al., 2017*), (in the range 20-74 mV cm^{-1} Oe^{-1}) and similar to that reported on (1-3) PZT-CFO composite (~390 mV cm^{-1} Oe^{-1}) (*Wan et al., 2007*). The dependence of the magnetoelectric properties of such vertically aligned multiferroic heterostructures on geometrical factors and material parameters are discussed in the following paragraphs.

5.3. Characterization of Vertically Aligned CFO Nanopillar – BTO Matrix Nanocomposites

Metal $CoFe_2$ nanopillar arrays having an average height of ~200 nm and diameter ~90 nm were considered for the fabrication of two BTO-CFO multiferroic nanostructures, schematically illustrated in **Figure 5.8a**. The first BTO-CFO nanocomposite consisted of a BTO matrix/layer structure with total thickness (estimated from SEM images) t_{total}~550 nm (hereinafter BTO_{550}-CFO_{200}) including the BTO top-layer with thickness, $t_{top\text{-}layer}$~300 nm and CFO nanopillars arrays embedded into the BTO structure. The second BTO-CFO nanocomposite consisted of the BTO structure with total thickness, t_{total}~850 nm (referred to as BTO_{850}-CFO_{200}) including 600-nm-thick BTO top-layer on the top of CFO nanopillar arrays. In Section 5.2 the temperature dependence of the magnetoelectric voltage response of the BSTO-CFO nanocomposite, with similar geometric parameters as the BTO_{550}-CFO_{200} nanocomposite, revealed that the ME coupling is somehow dependent on the dielectric properties of the BSTO-CFO nanostructure showing the maximum value of ME coefficient at around Curie temperature of the BSTO matrix, T_C~250K (see **Figure 5.7**). However, the room temperature permittivity reported for the ceramic BTO material, $\varepsilon_{BTO}\sim 1350$, is lower by an order of magnitude than the one for the ceramic BSTO material, $\varepsilon_{BSTO}\sim 1.5 - 2\times 10^4$, (*Mitsui, 1970*). So, to increase the FE contribution in BTO-CFO nanocomposite, thicker BTO structure was prepared, t_{total}~850 nm, while the height of CFO nanopillar arrays remained unchanged h_{pillar}~200 nm.

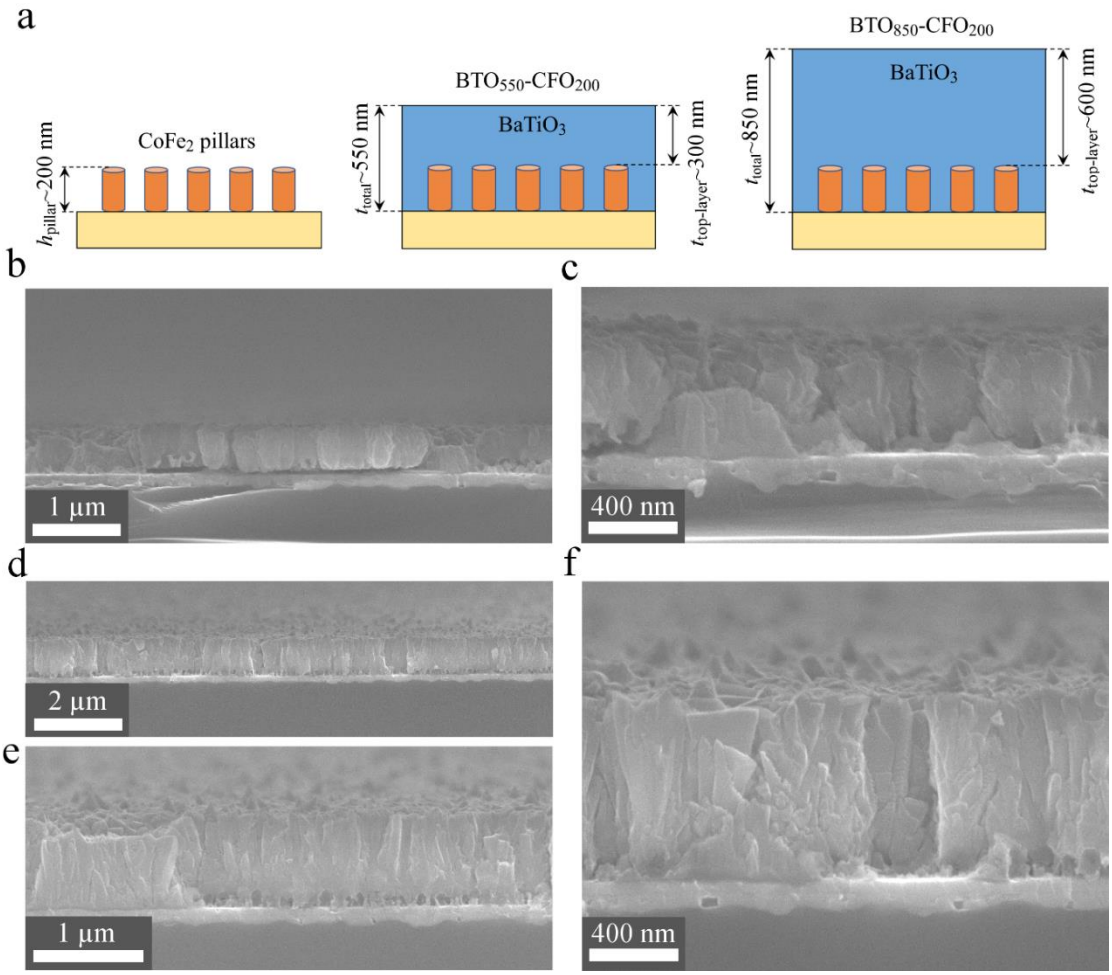

Figure 5.8: (a) Schematic illustration of dimensions for the discussed $CoFe_2$ nanopillar arrays and BTO-CFO multiferroic nanocomposites. SEM images of the tilted cross section view of **(b,c)** BTO_{550}-CFO_{200} and **(d,e,f)** BTO_{850}-CFO_{200} nanocomposites at different magnifications

A tilted-view SEM image (**Figures 5.8b-f**) of the BTO-CFO nanostructures shows that the BTO matrix penetrates the spacing between the CFO nanopillars to form the two-phase columnar structure made of the CFO pillars coated by the BTO shells (**Figures 5.8c,f**). The total thickness of the BTO_{550}-CFO_{200} and BTO_{850}-CFO_{200} nanostructures were about 550 and 850 nm, respectively (**Figures 5.8c** and **5.8e**), which are larger than the sum of the $CoFe_2$ nanopillars height (h_{pillar}~200 nm) and the thickness of BTO top-layers ($t_{top\text{-}layer}$~300 and 600 nm) indicating the volume expansion of the nanopillars. Similar volume expansion was previously for the BSTO-CFO structure (see **Figures 5.2a,d**). The observed microstructure of the BTO_{550}-CFO_{200} nanocomposite (**Figure 5.8c**) is rather similar to the microstructure of the BSTO-CFO nanocomposite discussed in Section 5.2 (see **Figure 5.2d**). Only a shift of all XRD peaks corresponding to the perovskite BTO phase with respect to the XRD peaks of BSTO phase was observed, which is expected due to the difference in lattice parameters of the ceramic BTO and BSTO materials (for BTO a=b=3.99 Å, c=4.03 Å, and for BSTO c=3.96 Å). An average chemical analysis was provided by EDX analysis

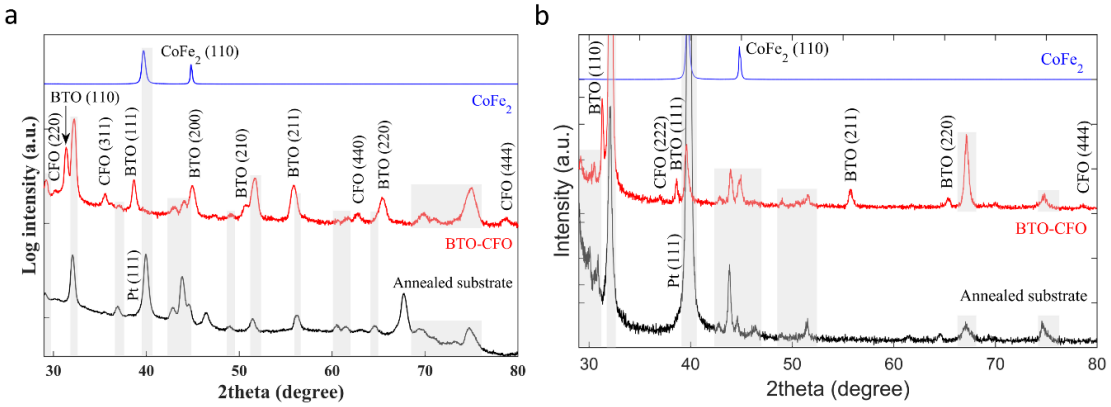

Figure 5.9: In-plane GI-XRD and out-of-plane powder XRD patterns of the vertically aligned $CoFe_2$ nanopillar arrays (blue), the BTO-CFO nanocomposite (red), and the Pt/Ti/Si substrate annealed at ~600 °C (black), respectively

(not shown here) confirming the value of Fe/Co ratio close to 2 in the BTO-CFO nanostructures. As was already mentioned for the BSTO-CFO nanostructure the elemental analysis of the Ba/Ti atomic ratio is not possible using the EDX-HRSEM system due to close energy positions of Ba L (4.464 keV) and Ti K (4.508 keV) lines.

For the BTO-CFO nanostructures like for the BSTO-CFO nanostructure, the *in situ* oxidation approach (during sputtering of FE layers) was used to transform metal $CoFe_2$ nanopillar arrays into the insulating oxide CFO phase, and likewise two techniques XRD and magnetic properties characterization were used to analyse the $CoFe_2$ nanopillars oxidation efficiency. **Figures 5.9a,b** show in-plane GI-XRD and out-of-plane powder XRD patterns of the BTO_{550}-CFO_{200} nanocomposite, the $CoFe_2$ nanopillar arrays (JCPDS # 48-1816), and the Pt/Ti/Si substrate, annealed at ~600 °C. The presence of CFO peaks (220), (311), (440) and (444) (JCPD # 22-1086) on the GI-XRD pattern (**Figure 5.9a**) as well as the appearance of small peaks (222) and (444) on the powder XRD pattern (**Figure 5.9b**) in the BTO_{550}-CFO_{200} diffractogram verifies the oxidation of the metal $CoFe_2$ nanopillar array into the oxide CFO phase during BTO layer sputter deposition. Alike the BSTO-CFO nanocomposite (**Figure 5.3**), the BTO structure in nanocomposite is crystallized into the perovskite structure with random crystalline orientation shown by both GI-XRD and powder XRD.

The magnetic properties of the $CoFe_2$ nanopillar arrays and BTO_{550}-CFO_{200} nanocomposite were analysed by AGM. **Figure 5.10** shows the magnetic hysteresis loops measured at room temperature with the field applied along either the in-plane and out-of-plane directions, where the magnetic moments were normalized by their saturation values. An easy axis of magnetization along in-plane direction (perpendicular to pillars axis) observed for the free-standing $CoFe_2$ nanopillar arrays (**Figure 5.10a**) is less pronounced than the in-plane easy axis observed in the $CoFe_2$ nanopillars used for the BSTO-CFO nanocomposite (see **Figure 5.4a**) suggesting slightly lower packing density of the $CoFe_2$ nanopillar arrays (*Dmytriiev et al., 2013*). After the *in situ* oxidation of $CoFe_2$ nanopillar arrays into the CFO phase forming the BTO_{550}-CFO_{200} nanostructure (**Figure 5.10b**), the coercivities, H_c, in OOP and IP

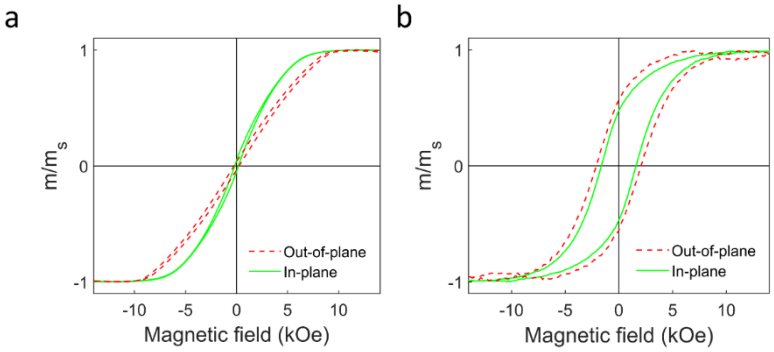

Figure 5.10: Room temperature hysteresis loops along in-plane (solid line) and out-of-plane (dashed line) directions for a vertically aligned $CoFe_2$ nanopillar array (a) and the BTO-CFO multiferroic nanostructure (b). The magnetic moment is normalized to its value in the saturation state

directions increased from ~192 and 80 Oe, to 2.1 and 1.6 kOe, respectively. The remanence-saturation ratio, m_r/m_s, in OOP ~0.04 and in IP ~0.08 directions also increased to m_r/m_s ~0.58 and 0.48, respectively This is associated with large magnetocrystalline anisotropy of the CFO phase, as was previously demonstrated for the BSTO-CFO nanostructure (**Figure 5.4b**). **Figure 5.10b** shows the magnetic hysteresis loops of the $CoFe_2O_4$ nanopillar array embedded in the BTO layer. Consistently the shapes of hysteresis loops of the CFO nanopillar arrays are similar in IP and OOP directions due to the absence of preferential crystalline orientation.

Dielectric properties (capacitance and loss tangent) of the BTO_{850}-CFO_{200} and BTO_{550}-CFO_{200} nanocomposites were measured as a function of temperature, frequency and applied voltage to confirm the ferroelectricity of BTO-CFO nanocomposites and to study the role of top BTO layer's thickness. The pure BTO thin film with thickness of ~400 nm was used as a reference.

Figure 5.11 illustrates the temperature dependence in the range ~80-410 K of capacitance and dielectric losses (at three frequencies 10 kHz, 100 kHz, and 1 MHz) for the pure BTO thin film (**Figures 5.11a,b**), the BTO_{850}-CFO_{200} (**Figure 5.11c,d**) and BTO_{550}-CFO_{200} (**Figure 5.11e,f**) nanocomposites. The pure BTO thin film was deposited on the Pt/Ti/Si substrate that was obtained after chemical dissolution of AAO template resulting in similar interface quality between substrates and FE film and between substrate and the BTO-CFO nanocomposites. The BTO film demonstrates a smoothly increasing capacitance with an increase of temperature (**Figure 5.11a**). However, the maximum in capacitance associated with the phase transition was not observed in this range of temperatures. The dielectric losses of the BTO thin film stay below ~0.02 for the temperature ranging between 80 and 410 K (**Figure 5.11b**).

For the BTO_{850}-CFO_{200} nanocomposite (**Figure 5.11c**), the capacitance smoothly increases when the temperature is raised from 80 to 250 K, similar to the pure BTO thin film (see **Figure 5.11a**). However, above 250 K the capacitance measured at the frequency of ~10 kHz starts to increase rapidly, whereas the capacitance observed at

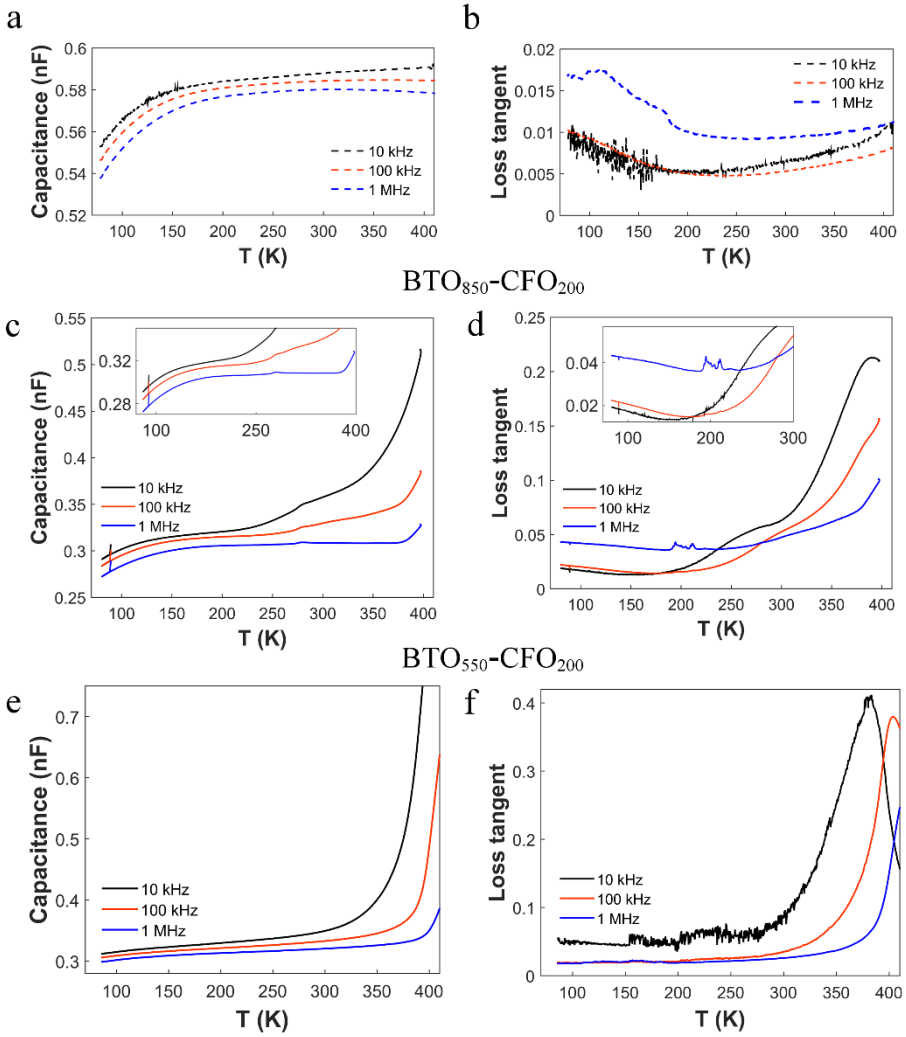

Figure 5.11: Capacitance and dielectric losses as a function of temperature for the BTO thin layer **(a,b)** with thickness ~400 nm deposited on the Pt/Ti/Si substrate obtained after anodization and dissolution of the Al layer, and the BTO_{850}-CFO_{200} **(c, d)** and BTO_{550}-CFO_{200} **(e, f)** nanostructure capacitors

frequencies ~100 kHz and 1 MHz increases only after 350 K. Accordingly, the dielectric losses measured at ~10 kHz showed pronounced peak at ~390 K (**Figure 5.11d**), whose maximum is supposedly shifted to higher temperature as the frequency increases. For the BTO_{550}-CFO_{200} nanocomposite (**Figure 5.11e**), the temperature dependence of capacitance showed similar behaviour as for the BTO_{850}-CFO_{200}, wherein the capacitance measured at three frequencies first slowly increases with increasing temperature, but after temperature overpassed 350 K it starts to increase sharply. The dielectric losses of the BTO_{550}-CFO_{200} nanocomposite at ~300 K (10 kHz) $\tan\delta \sim 0.086$ are higher than the losses observed for the BTO_{850}-CFO_{200} nanocomposites $\tan\delta \sim 0.063$ at ~300 K (10 kHz). It can be assumed that for thicker BTO structure (t_{total}~850 nm) in the BTO_{850}-CFO_{200} nanocomposite the contribution of low permittivity CFO pillar structure is reduced compared to the BTO_{550}-CFO_{200} nanocomposite with thinner BTO structure (t_{total}~550 nm).

Effective permittivity of the reference BTO thin film and BTO-CFO nanocomposite capacitors was estimated using Equation (5.2). In the low temperature range ($T < 200$ K), the permittivity of BTO_{850}-CFO_{200} nanocomposite, corresponding to **Figure 5.11c,** where $t_{total} = 850 \pm 50$ nm (**Figure 5.8f**), top Pt contact diameter, $D = 600$ μm ($S = 0.28 \times 10^{-6}$) is

$$\varepsilon_{BTO_{850}-CFO_{200}} = \frac{0.315 \times 10^{-9} \times (850 \pm 50) \times 10^{-9}}{8.854 \times 10^{-12} \times 0.28 \times 10^{-6}} \sim 107 \pm 6. \quad (5.6)$$

The effective permittivity of BTO_{550}-CFO_{200} nanocomposite ($T < 200$ K), corresponding to **Figure 5.11e**, with $t_{total} = 550 \pm 50$ nm (**Figure 5.8c**), top Pt contact diameter, $D = 600$ μm ($S = 0.28 \times 10^{-6}$) is

$$\varepsilon_{BTO_{550}-CFO_{200}} = \frac{0.321 \times 10^{-9} \times (550 \pm 50) \times 10^{-9}}{8.854 \times 10^{-12} \times 0.28 \times 10^{-6}} \sim 70 \pm 6. \quad (5.7)$$

The effective permittivity of reference BTO thin film ($T \sim 200$ K) with $t_{total} = 400 \pm 50$ nm, top Pt contact diameter, $D = 600$ μm ($S = 0.28 \times 10^{-6}$) is

$$\varepsilon_{BTO_{400}} = \frac{0.581 \times 10^{-9} \times (400 \pm 50) \times 10^{-9}}{8.854 \times 10^{-12} \times 0.28 \times 10^{-6}} \sim 93 \pm 12. \quad (5.8)$$

The effective permittivity of the BTO_{550}-CFO_{200} nanocomposite ($\varepsilon_{BTO_{550}-CFO_{200}} \sim 70 \pm 6$) (**Figure 5.11e**) is lower than the one of the pure BTO_{400} thin film ($\varepsilon_{BTO_{400}} \sim 93 \pm 12$) (**Figure 5.11a**), deposited on the pre-treated Pt/Ti/Si substrate, and lower than the one of BTO_{850}-CFO_{200} nanocomposite ($\varepsilon_{BTO_{850}-CFO_{200}} \sim 107 \pm 6$) (**Figure 5.11c**).

Ferroelectric properties of the BTO-CFO nanocomposites were analysed by conducting the capacitance under applied bias voltage $C(V)$ measurements at 100 kHz to minimize the contribution at low frequency of space charges and associated conductivity mechanisms. For the BTO_{850}-CFO_{200} nanocomposite the capacitance and dielectric losses measured at 250 K show two maxima and an opening of a hysteresis loop (**Figures 5.12a** and **5.12b**) indicating polarization reversal in the BTO_{850}-CFO_{200} nanocomposite. However, when the same measurement was conducted at room temperature, the ferroelectric behaviour of the BTO_{850}-CFO_{200} nanocomposite could be observed only for $C(V)$ dependence, whereas the $tan\delta(V)$ dependence shows a progressive interference of space charge. As for the BTO_{550}-CFO_{200} nanocomposite (**Figures 5.12c** and **5.12d**) when the measurement was performed at 250 K only $C(V)$ dependence showed a small hysteresis with two maxima, while $tan\delta(V)$ dependence did not show the hysteresis. When the temperature was raised to 300 K, $C(V)$ hysteresis disappeared due to the large contribution of the space charge. These results show that

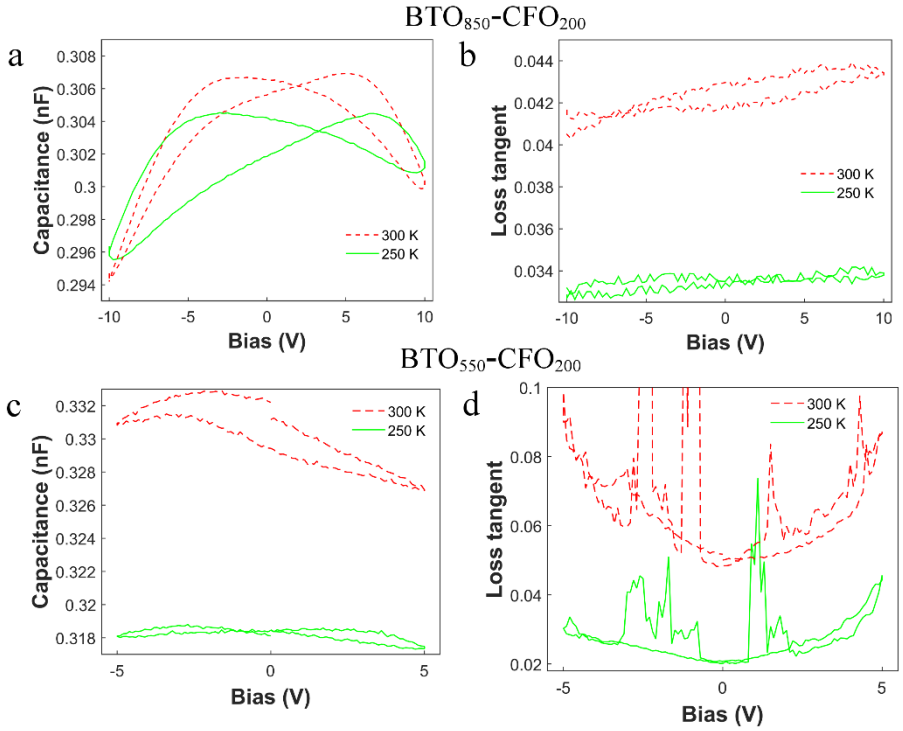

Figure 5.12: Capacitance **(a,c)** and dielectric losses **(b,d)** as a function of bias voltage for the BTO_{850}-CFO_{200} **(a,b)** and BTO_{550}-CFO_{200} **(c,d)** nanostructures at two distinct temperatures, T = 250 K and T = 300K

by increasing the total thickness of BTO structure the dielectric and ferroelectric properties of the BTO-CFO nanostructure can be improved and help to prevent the dissipation of electrical energy through space charges, to overcome barriers in the elastic energies, and to align the polarization in the field direction.

Dynamic magnetoelectric measurements of the magnetoelectric voltage response were performed by the group of Prof. Kristiaan Temst and Dr. Vera Lazenka at Instituut voor Kern- en Stralingsfysica, KU Leuven, Belgium. Direct ME coupling was measured in BTO-CFO nanocomposites as a ME voltage response to *ac* magnetic field, H_{ac}, as a function of temperature or *dc* magnetic field, H_{dc}. We must note that since the considered experimental thickness, t_{total} , is not homogeneous and it was measured from the SEM images (±50 nm), the error bar can reach ~10%.

The temperature dependence of the magnetoelectric coefficient, α_E, in the range 10-300 K for the BTO_{550}-CFO_{200} and BTO_{850}-CFO_{200} nanocomposites is shown in **Figure 5.13a**. The ME voltage coefficient of the BTO_{850}-CFO_{200} nanocomposite increases from ~350±27 mV cm^{-1} Oe^{-1} to ~448±27 mV cm^{-1} Oe^{-1} with temperature increasing from ~10 K to room temperature. However, the results of *dc* magnetic field dependence of α_E for BTO_{850}-CFO_{200} (**Figure 5.13b**) showed a slightly larger room-temperature value without applied *dc* field $\alpha_E \sim 463 \pm 27$ mV cm^{-1} Oe^{-1}. This variation can be attributed to the fact that the *dc* magnetic field measurement (**Figure 5.13b**) was performed before the temperature scan from ~10 to 300 K (**Figure 5.13a**). Thus, the

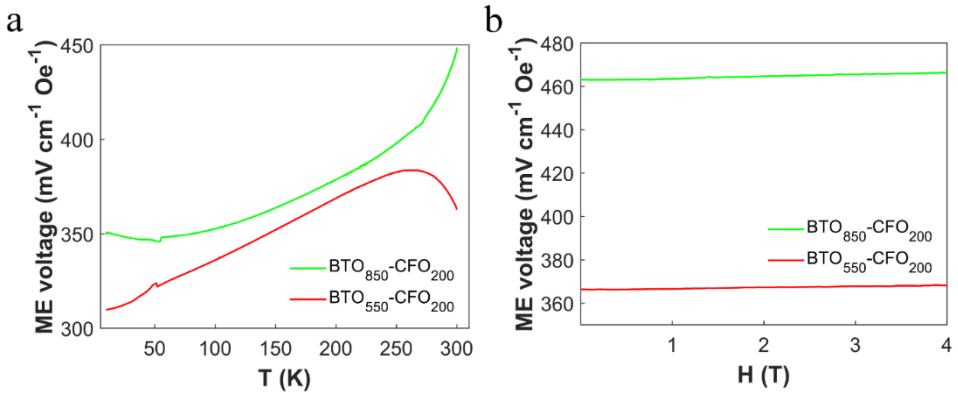

Figure 5.13: (a) Temperature dependence of the ME voltage coefficient for the BTO_{550}-CFO_{200} (red) and BTO_{850}-CFO_{200} (green) nanocomposites. **(b)** Room-temperature variation with external *dc* magnetic field of the ME voltage coefficient for the BTO_{550}-CFO_{200} (red) and BTO_{850}-CFO_{200} (green) nanocomposites

contribution of residual stress, formed after BTO deposition at ~650 °C), was present only for H_{dc} dependence measurement (up to 4T), whereas the temperature dependence was performed after the sample was cooled to ~10 K. The BTO_{550}-CFO_{200} nanostructure with thinner BTO structure at low temperature range shows an increase of α_E from ~310±34 mV cm^{-1} Oe^{-1} to the maximal value ~384±34 mV cm^{-1} Oe^{-1} at ~265 K, then the ME coefficient drops to ~362±34 mV cm^{-1} Oe^{-1} at ~300 K. The peak in the temperature dependence of ME coefficient was aslo observed for the BSTO-CFO nanocomposite with similar dimensions (see **Figure 5.7**). The shape of the $\alpha_E(T)$ for the BSTO-CFO nanocomposite was ascribed to the temperature variation of the dielectric properties (see **Figure 5.5c**), where the maximum of capacitance was observed in the same range of temperature. However, the $C(T)$ dependence of the BTO_{550}-CFO_{200} nanocomposite did not show any peaks around T ~270 K (**Figure 5.11e**).

Although the estimated effective permittivity of the BTO_{850}-CFO_{200} nanocomposite is larger than the permittivity of the BTO_{550}-CFO_{200} nanocomposite (see Equations 5.6 and 5.7), their ME coefficients were quite similar in the range of T~100-250 K (**Figure 5.13a**). So, another critical parameter affecting the ME properties in BTO-CFO nanocomposites can be density of interfaces. In a first attempt, we propose in the present work to consider the ratio h_{pillar}/t_{total} between the height of FM nanopillars, h_{pillar}, and the total thickness of FE matrix/layer structure, t_{total}. The average h_{pillar}/t_{total} ratio was decreased from ~0.36 to 0.23 by increasing t_{total} from ~550 nm (BTO_{550}-CFO_{200}) to ~850 nm (BTO_{850}-CFO_{200}) while maintaining h_{pillar}~200 nm. Previously, theoretical computations using phenomenological thermodynamic theory were reported for the (1-3) type BTO-CFO thin film nanocomposites (see **Figure 2.11**, p. 37). It was shown that the maximum value of ME coefficient corresponds to the optimal volume fraction, f, of the CFO nanopillars between ~0.5 and 0.8. Thus, in the following section we analyse the dependence of ME coefficient on the density of interfaces (h_{pillar}/t_{total}), CFO

nanopillars height (h_{pillar}), and effective permittivity, ε, for both BTO-CFO and BSTO-CFO nanocomposites.

At room temperature, the ME voltage coefficients of both BTO-CFO nanocomposites display very small variation (of the order of 1 %) when an external *dc* magnetic field (up to 4 T) is superimposed on the oscillating field, H_{ac}. The room temperature values of ME voltage coefficient for the BTO_{850}-CFO_{200} and BTO_{550}-CFO_{200} nanocomposites (~463±27 and 366±34 mV cm^{-1} Oe^{-1}, respectively) are in the same range of magnitudes as measured for the BSTO-CFO nanocomposite (~315±29 mV cm^{-1} Oe^{-1}) (see **Figure 5.7**).

5.4 Investigation of Magnetoelectric Coupling in BSTO-CFO and BTO-CFO Vertically Aligned Multiferroic Nanocomposites

We aim to investigate the dependence of the magnetoelectric properties for BSTO-CFO and BTO-CFO multiferroic nanocomposites on geometrical factors such as density of interfaces, h_{pillar}/t_{total}, height of the FM nanopillars, h_{pillar}, and effective permittivity, ε. However, we must precise that the considered experimental parameters, t_{total}, h_{pillar}, and ratio h_{pillar}/t_{total} allow only a qualitative comparison. As a result, the interpretation relating ME coefficient to these geometrical parameters can only provide some trends. We prepared a set of $BSTO_x$-CFO_y and BTO_x-CFO_y nanostructures, where x ~500-1220 nm is the average total thickness, t_{total}, of BSTO and BTO structure, and y ~150-500 nm is the average height, h_{pillar}, of $CoFe_2$ nanopillar arrays before BSTO and BTO deposition. The geometric parameters and physical properties including permittivity, ε, loss tangent, $tan\delta$, and ME voltage coefficient, α_E, of the prepared BSTO-CFO and BTO-CFO nanocomposites are summarized in **Table 5.1**.

Schematic illustrations of the prepared $CoFe_2$ nanopillar arrays and BSTO and BTO nanocomposites including their notations and geometric parameters are shown in **Figure 5.14** (for details see **Table 5.1**).

Figures 5.15a-b show the tilted cross-section view SEM images of the free-sanding and vertically aligned $CoFe_2$ nanopillar arrays used for the fabrication of BSTO-CFO and BTO-CFO nanostructures. Tilted view SEM images on the fabricated BSTO-CFO and BTO-CFO nanocomposites are shown in **Figures 5.15e,g,i,k,m** and **5.15f,h,j,l,n**, respectively. The $BSTO_{550}/BTO_{550}$-CFO_{200} and $BSTO_{1220}/BTO_{1220}$-CFO_{500} nanocomposites have nearly the same ratio h_{pillar}/t_{total}~0.4 as well as the specimens $BSTO_{500}/BTO_{550}$-CFO_{150} and $BSTO_{950}/BTO_{950}$-CFO_{250}, where h_{pillar}/t_{total}~0.3.

Table 5.1: Average geometric parameters of BSTO-CFO and BTO-CFO nanocomposites and corresponding room temperature dielectric and magnetoelectric properties (the largest $\varepsilon_{33}/\varepsilon_0$ and α_E are in bold)

Composites	$CoFe_2$ h_{pillar} nm	FE $t_{top\text{-}layer}$ nm	t_{total} nm	h_{pillar}/t_{total}	$\varepsilon_{33}/\varepsilon_0$ 100 kHz	$tan\delta$ 100 kHz	α_E mV cm^{-1} Oe^{-1}
$BSTO_{500}$-CFO_{150}	150	300	500	**0.3**	**97**±11	0.05	**787**±87
$BSTO_{950}$-CFO_{250}	250	600	950	**0.26**	**163**±8	0.09	**682**±36
$BSTO_{850}$-CFO_{200}	200	600	850	**0.23**	**75**±4	0.08	**506**±30
$BSTO_{550}$-CFO_{200}	200	300	550	0.36	57±5	0.03	315±29
$BSTO_{1220}$-CFO_{500}	500	600	1220	0.41	48±2	0.34	320±13
BTO_{850}-CFO_{200}	200	600	850	**0.23**	**112**±7	0.05	**463**±27
BTO_{550}-CFO_{200}	200	300	550	0.36	50±5	0.04	366±34
BTO_{1220}-CFO_{500}	500	600	1220	0.41	50±2	0.04	211±9
BTO_{500}-CFO_{150}	150	300	500	0.3	46±4	0.05	186±18
BTO_{950}-CFO_{250}	250	600	950	0.26	42±2	0.06	92±5

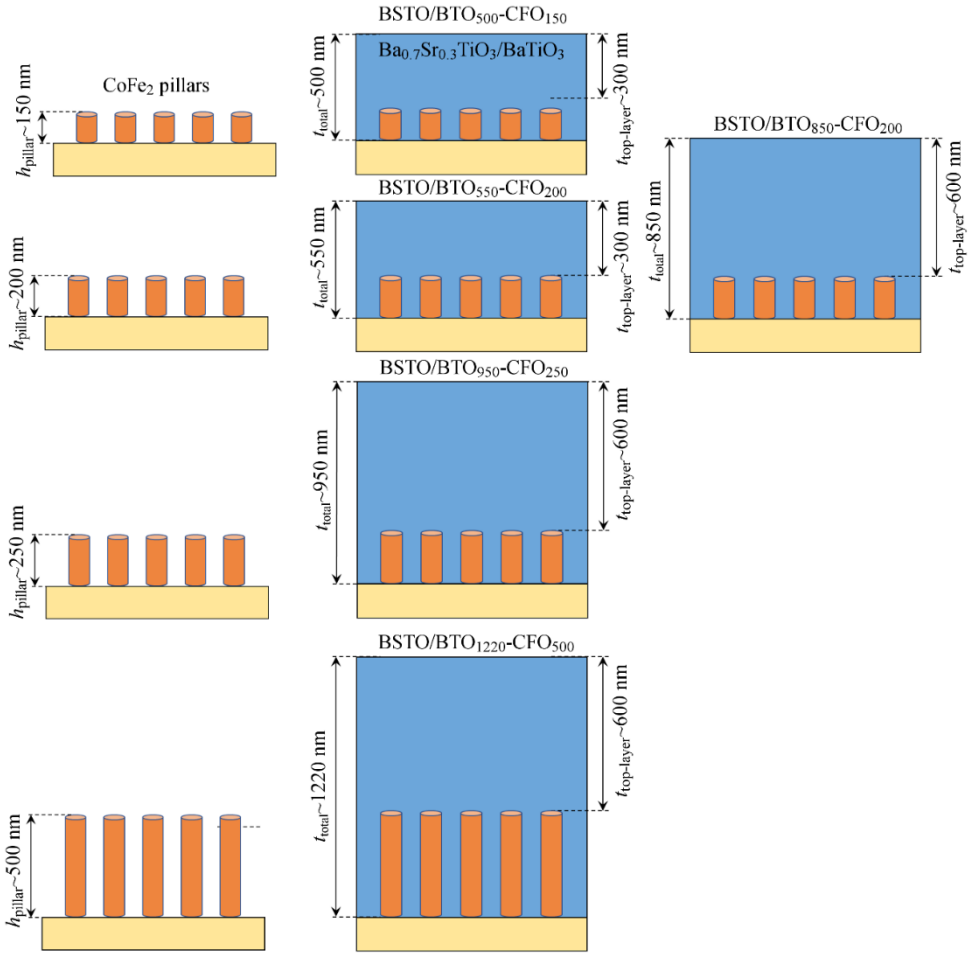

Figure 5.14: Schematic illustration of the prepared CFO nanopillar arrays and corresponding $BSTO_x$-CFO_y and BTO_x-CFO_y nanostructures including their notations (placed above sketches) and geometric parameters (on sides), where *x* is the total thickness of BSTO and BTO structure (equivalent to the thickness of nanocomposite), and *y* is the $CoFe_2$ pillars height before BSTO and BTO deposition

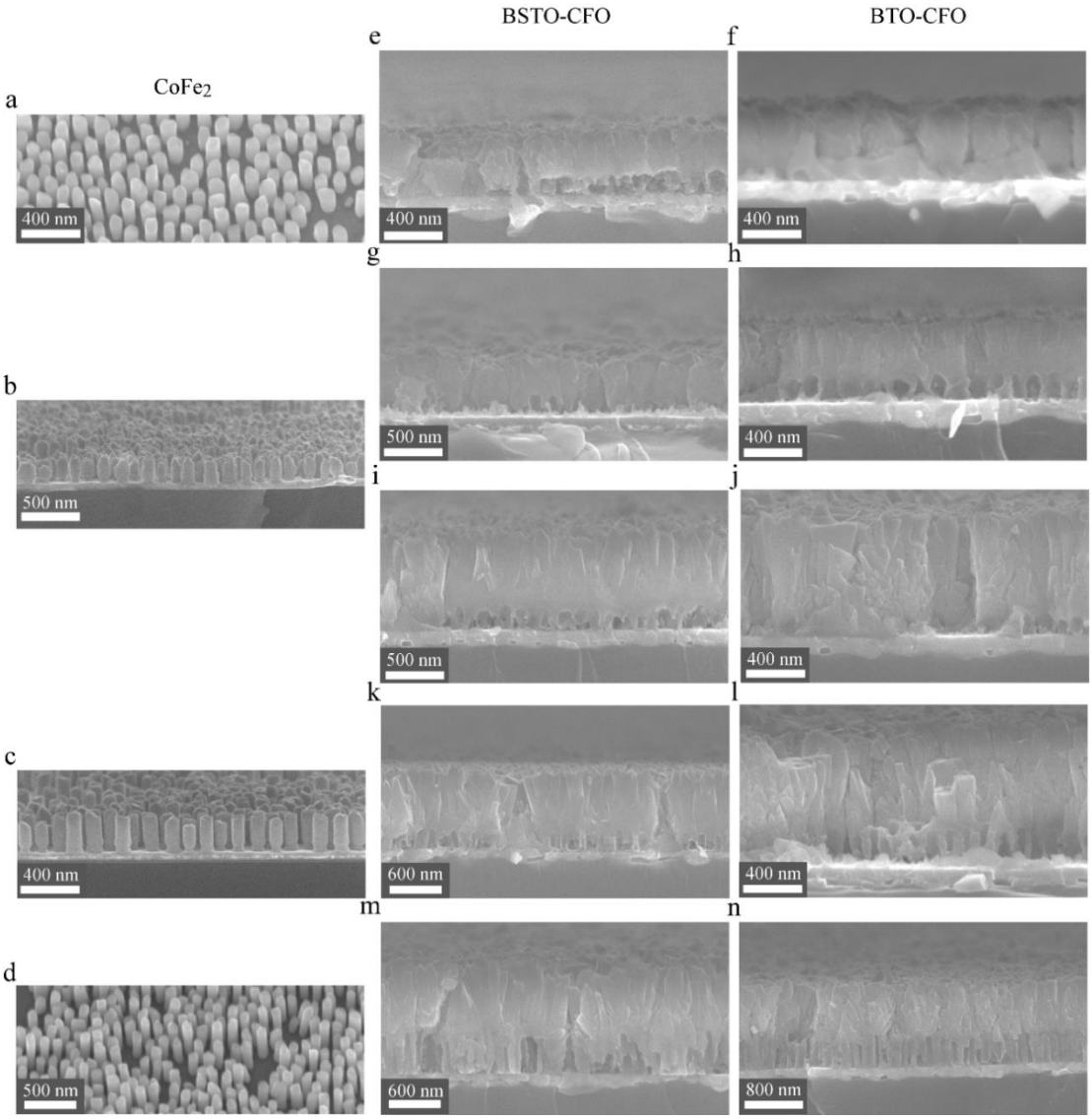

Figure 5.15: Tilted cross-section view SEM images of the vertically aligned $CoFe_2$ nanopillar arrays with average height, h_{pillar}, of **(a)** ~150 nm, **(b)** ~200 nm, **(c)** ~250 nm, and **(d)** 500 nm. **(e-n)** SEM images of the specimens corresponding to a tilted cross-section view on **(e)** $BSTO_{500}$-CFO_{150}, **(f)** BTO_{500}-CFO_{150}, **(g)** $BSTO_{550}$-CFO_{200}, **(h)** BTO_{550}-CFO_{200}, **(i)** $BSTO_{850}$-CFO_{200}, **(j)** BTO_{850}-CFO_{200}, **(k)** $BSTO_{950}$-CFO_{250}, **(l)** BTO_{950}-CFO_{250}, **(m)** $BSTO_{1220}$-CFO_{500}, **(n)** BTO_{1220}-CFO_{500}**,** for details see **Table 5.1** and **Figure 5.14**

The resulting ME voltage coefficients for the BSTO-CFO and BTO-CFO nanocomposites, summarized in **Table 5.1,** were plotted as a function of temperature in the range T ~10-300 K (**Figure 5.16**). The large room temperature α_E value ~787±87 and 682±36 mV cm^{-1} Oe^{-1} were obtained for the $BSTO_{500}$-CFO_{150} and $BSTO_{950}$-CFO_{250}, respectively with similar ratio h_{pillar}/t_{total} ~0.3. However, for the BTO_{550}-CFO_{150} and BTO_{950}-CFO_{250} nanocomposites this h_{pillar}/t_{total} ratio showed the weakest ME coupling α_E ~186±18 and 92±5 mV cm^{-1} Oe^{-1}, respectively.

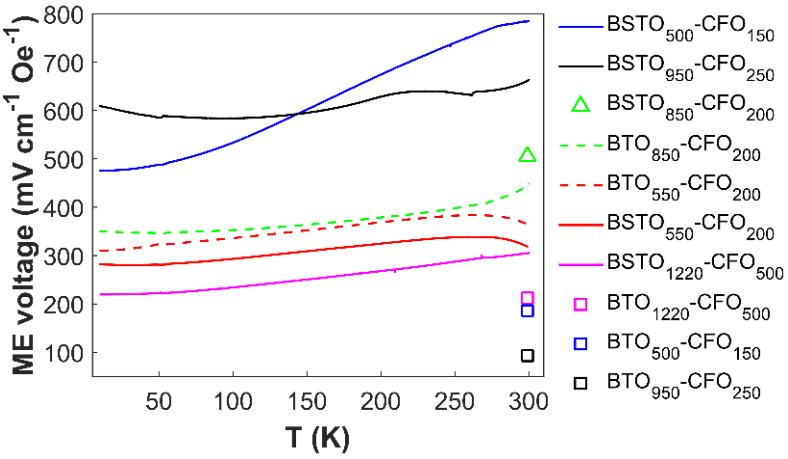

Figure 5.16: Temperature dependence of ME voltage coefficients for the BSTO-CFO and BTO-CFO nanocomposites, where the total thickness of the BSTO and BTO structure, t_{total}, varies between ~500 and 1220 nm, and the height of $CoFe_2$ nanopillars, h_{pillar}, is in the range ~150-500 nm. Solid lines and a triangle corresponds to the results for BSTO-CFO nanocomposites, while broken lines and squares correspond to the results obtained for BTO-CFO nanocomposites. Same colours correspond to the same ratio t_{total}/h_{pillar}.

To analyse the effects that contribute to the ME voltage response in the vertically aligned nanocomposites, the ME voltage response was plotted as a function of h_{pillar}/t_{total} ratio (**Figure 5.17a**), h_{pillar} (**Figure 5.17b**), and effective permittivity of nanocomposites (**Figure 5.17c**), estimated from the measured capacitance data and geometric parameters obtained from SEM images. However, we must precise since the considered experimental thickness, t_{total}, is not homogeneous and it was measured from the SEM images (±50 nm), therefore only a qualitative comparison with the error bar ~10% is proposed when dealing with ε and α_E.

The results for α_E as a function of h_{pillar}/t_{total} ratio (**Figure 5.17a**) show that for the BSTO-CFO system the best two candidates appear to be $BSTO_{500}$-CFO_{150} and $BSTO_{950}$-CFO_{250} nanocomposites with the ratios h_{pillar}/t_{total} close to ~0.3 and 0.26, respectively. However, for the BTO-CFO system the maximum α_E~463±27 mV cm^{-1} Oe^{-1} was observed for the BTO_{850}-CFO_{200} nanocomposite with lower h_{pillar}/t_{total}~0.2. This could be explained by the fact that the room temperature permittivity of BTO is lower compared to the permittivity of $Ba_{0.7}Sr_{0.3}TiO_3$, therefore the optimal combination between effective permittivity and density of interfaces for the BTO-CFO nanocomposites corresponds to the larger total thickness of BTO structure (i.e. lower h_{pillar}/t_{total}~0.2).

The α_E dependence on the h_{pillar} (**Figure 5.17b**) showed that for the BSTO-CFO system an increase of h_{pillar} from ~200 to 250 nm in the $BSTO_{850}$-CFO_{200} and $BSTO_{950}$-CFO_{250} nanocomposites with more or less similar h_{pillar}/t_{total} ratio ~0.23-0.26 results in a small increase of α_E from ~506±30 to 682±36 mV cm^{-1} Oe^{-1}, whereas for BTO-CFO system an increase of h_{pillar} from ~150 to 200 nm in the BTO_{500}-CFO_{150} and BTO_{550}-CFO_{200} nanocomposites with h_{pillar}/t_{total} ratio ~0.3-0.36 results in a large increase of α_E

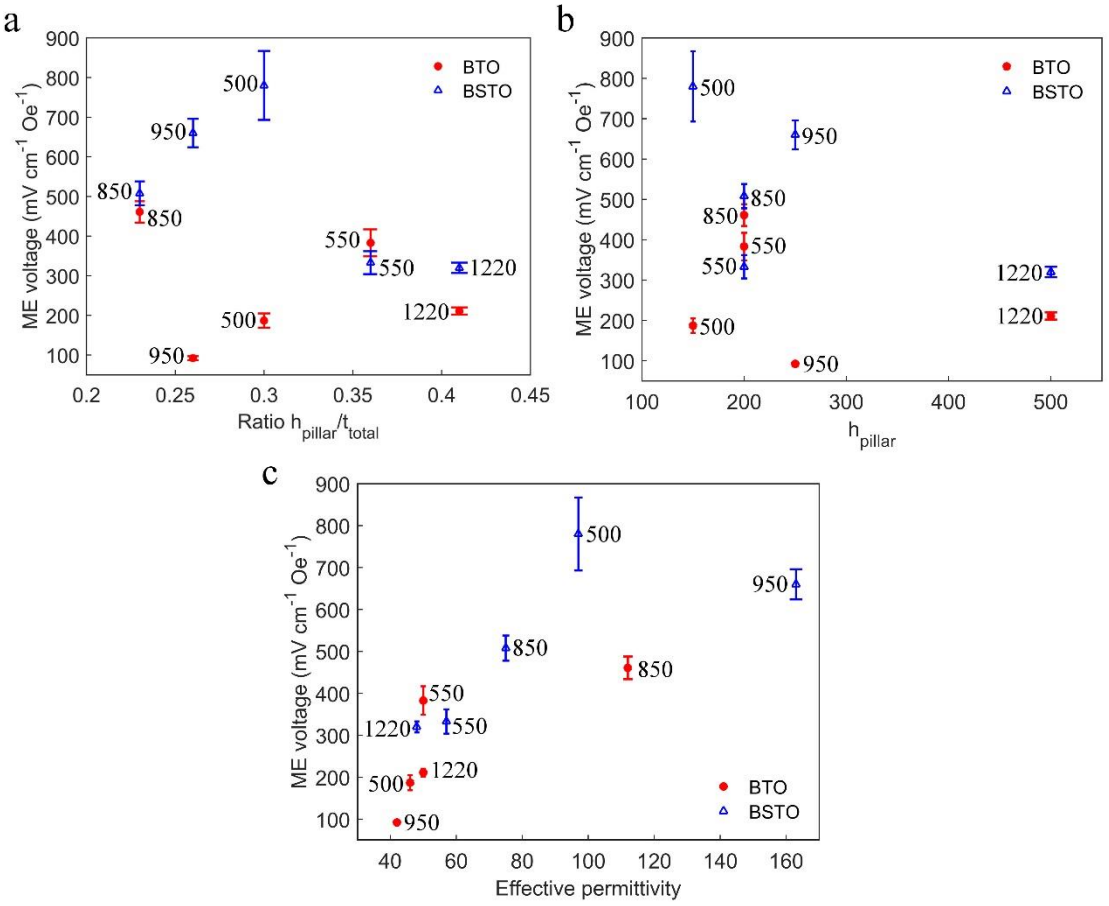

Figure 5.17: Dependence of ME voltage coefficient on **(a)** ratio between the height of $CoFe_2$ nanopillars, h_{pillar}, and the total thickness of the BSTO and BTO structure, t_{total}, **(b)** h_{pillar}, and **(c)** effective permittivity of BSTO-CFO and BTO-CFO nanocomposites, estimated from measured capacitance values using Equation (5.2). The numbers indicated next to symbols indicate the total thickness of the BSTO and BTO structure, equivalent to the thickness of BSTO-CFO and BTO-CFO nanocomposites

from ~186±18 to 366±34 mV cm^{-1} Oe^{-1}. However, the reverse effect was observed in the $BSTO_{500}$-CFO_{150} and $BSTO_{550}$-CFO_{200} nanocomposites, and BTO_{850}-CFO_{200} and BTO_{950}-CFO_{250} nanocomposites (i.e. α_E decreases with h_{pillar} increasing), which is possibly due to the variation of residual stresses and their relaxation behaviour in the BTO-CFO and BSTO-CFO nanocomposites. **Figure 5.17c** shows α_E as a function of effective permittivity of the BSTO-CFO and BTO-CFO nanocomposites. Herein the dependence is consistent for both BSTO-CFO and BTO-CFO nanostructures. Larger ME effect is observed in the nanocomposites, which are more insulating with larger effective permittivity and lower dielectric losses. However, taking into account that the thickness measurement error ~10% (±50 nm) is relatively large, the quantitative analysis using larger number of samples is required to understand the dependence of α_E on h_{pillar} and h_{pillar}/t_{total} ratio.

In future studies, to further understand the key parameters explaining the different α_E behaviours for the BTO-CFO and BSTO-CFO nanostructures, we should consider the residual stress effects, as the dominant contributions for the strain-stress mediated

ME coupling in piezoelectric-magnetostrictive nanostructures on silicon substrates. Previously, it was shown that the residual stress in the ferroelectric fims can lead to the reduction of permittivity (*Shaw et al., 1999*). A BSTO film on a silicon subsrate is under a tensile residual stress, σ. The stress in the plane of the film causes a change in the permittivity measured through the film thickness:

$$\frac{1}{\varepsilon_f} = \frac{1}{\varepsilon_u} - 4Q_{12}\sigma, \tag{5.9}$$

where ε_f is the permittivity of the stressed film, and ε_u the permittivity of the unstressed film, q_{12} is the electrostrictive coefficient. Since $q_{12} < 0$, a residual tensile stress in the film reduces the permittivity. The tensile misfit strain in the films is reported to induce in barium titanate films a transition to a ferroelectric phase in which the polarizaiton axis lies in in-plane direction of the film (*Pertsev et al., 1998*) The films growth by PVD or CVD techniques requires high temperatures, which may increase a stress in the film before cooling, denoted by σ_p. After a temperature drop ΔT, the difference in the thermal expansion coefficients of the film and the substrate, ΔA, leads to a strain $\Delta A \Delta T$. When a voltage is applied across the thickness, the film tends to contract in-plane by a strain quatratic in the electric displacment, $q_{12}d^2$, where d is the electric displacement. Then the constraint of the substrate demands that both the thermal and electrostrictive strains in the film be accomodated by elastic stress. Thus, the residual stress in the film is

$$\sigma = \sigma_p + M_f(\Delta A \Delta T - q_{12}d^2), \tag{5.10}$$

where M_f is the biaxial elastic modulus of the film, which is related to Young's modulus Y_f and Poisson's ratio ν_f by $M_f = Y_f/(1-\nu_f)$. For BSTO $M_f \approx 200$ GPa. The BSTO film has a larger thermal expansion coefficient than the Si substrate, $\Delta A \approx 6 \times 10^{-6}$/K, so that a temperature reduction $\Delta T = 680$ K adds to the film a tensile stress of about 800 MPa. The electrostrictive strain $q_{12}d^2$ is typically below 10^{-3} , resulting in an additional tensile stress less than 200 MPa. The magnitude of stress, σ_p, is affected by the deposition and conditions and is difficult to predict (*Shaw et al., 1999*).

In the present work besides the biaxial in-plane tensile stress generated in the BSTO and BTO structures by the misfit between the thermal expansion coefficients of BSTO and BTO material and Si substrate, the vertically aligned CFO nanopillar arrays also might contribute to the stress state in FE layers. For the CFO material $M_{f\mathrm{CFO}} = 150/(1-0.26) \approx 203$ GPa and for the BTO material $M_{f\mathrm{BTO}} = 118/(1-0.4) \approx 196$ GPa. The BSTO matrix has lower thermal expansion coefficient compared to the CFO phase, by $\Delta A \approx 1.3 \times 10^{-6}/\,\mathrm{K}$, whereas the BTO material posseses lower thermal expansion coefficient than the one of BTO, by $\Delta A \approx 4 \times 10^{-6}$/K, so that a temperature drop of $\Delta T = 630$ K might induce different magnitude of in-plane stress in BTO-CFO and BSTO-CFO nanocomposites. When the *ac* magnetic field is applied

along CFO nanopillar axis, the nanopillars will contract due to the negative magnetrostriction of CFO material and generate in-plane compressive strain in the constituent piezoelectric structure. Therefore, in addition to the relation between α_E to the geometric parameters of nanocomposites studied in the present work, the dependence of α_E on the spontaneous and residual stresses in both phases should be considered carefully.

5.5. Characterization of Vertically Aligned CFO Nanopillar – PZT Matrix Nanocomposites

In this section we report the synthesis and characterization of vertically aligned $PbZr_{0.52}Ti_{0.48}O_3$-$CoFe_2O_4$ (PZT-CFO) nanocomposites. In **Figure 5.18** we remind the fabrication steps of the PZT-CFO vertically aligned multiferroic nanocomposites. These processes were schematically shown in **Figures 3.14** and **3.28** (pp. 87, 109). The $PbZr_{1-x}Ti_xO_3$ material is chosen due to the large piezoelectric coefficient d_{ij} (d_{15} = 494 pC/N, d_{31} = -93.5 pC/N, d_{33} = 223 pC/N) and suitable permittivity $\varepsilon_{33}/\varepsilon_0$ = 800 at x=0.48 corresponding to the morphotropic phase boundary (MPB) (*Jaffe et al., 1971*).

Compared to the BSTO-CFO and BTO-CFO nanocomposites discussed in **Sections 5.2-5.3**, an oxidation of the $CoFe_2$ nanopillars arrays into the CFO spinel phase cannot be implemented *in situ*, i.e. during crystallization of the PZT layer. Therefore, the preparation of PZT-CFO nanostructures implies an additional step of *ex situ* thermal oxidation of the $CoFe_2$ nanopillars. This prevents the interdiffusion during thermal oxidation between nanopillars and hosting template, but on the other hand leads to a change of the surface roughness and increase of the diameter, D_{pillar}, of free-standing CFO nanopillar arrays as shown in **Figure 3.25**, p. 105. We characterize dielectric and magnetic properties and quantify the magnetoelectric coefficient of the fabricated PZT-CFO nanocomposite using similar techniques as for BSTO-CFO and BTO-CFO multiferroic nanostructures discussed in **Sections 5.2-5.3**.

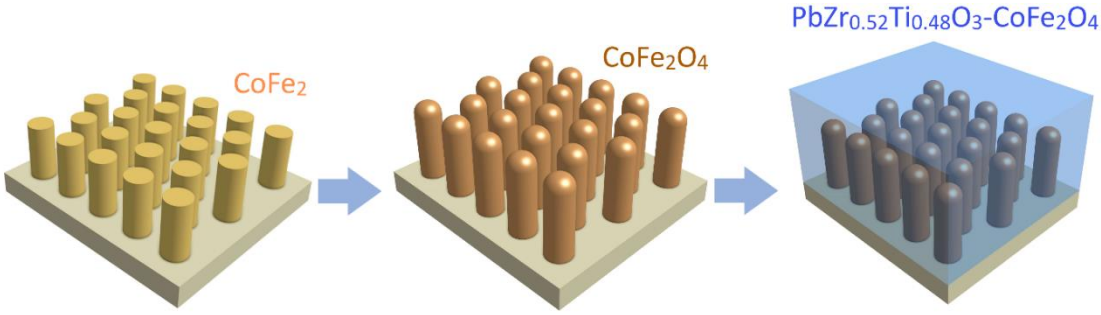

Figure 5.18: Schematic representation of the fabrication process of the vertically aligned $PbZr_{0.52}Ti_{0.48}O_3$-$CoFe_2O_4$ by thermal oxidation of the metal $CoFe_2$ nanopillars into the metal oxide $CoFe_2O_4$ and sol-gel dip-coating deposition of FE $PbZr_{0.52}Ti_{0.48}O_3$ layer on the insulating $CoFe_2O_4$ nanopillar arrays

$PbZr_{0.52}Ti_{0.48}O_3$ Layer Sol-Gel Dip-Coating Deposition on $CoFe_2O_4$ Nanopillar Arrays

The $CoFe_2O_4$ nanopillar arrays with height of ~500 nm were considered (referred to as CFO_{500}). In Sections 5.1 and 5.2 the $CoFe_2$ nanopillars with height of ~200 nm were considered for the fabrication of BSTO-CFO and BTO-CFO nanostructures. The larger height of CFO nanopillars, h_{pillar}~500 nm was considered to further increase the density of interfaces by increasing the h_{pillar}, while maintaining the experimentally observed optimal ratio h_{pillar}/t_{total}~0.3. This could be achieved for the PZT-CFO nanocomposites by using multiple sol-gel dip-impregnations allowing to obtain thicker PZT structures as compared to the BSTO and BTO structures discussed in **Sections 5.2** and **5.3**. Wherein the relatively low ME voltage coefficient ~211-320 mV cm^{-1} Oe^{-1} was obtained for the $BSTO_{1220}$-CFO_{500} and BTO_{1220}-CFO_{500} with large h_{pillar}~500 nm, which could be due to the limited total thickness of BTO and BSTO structures to ~1220 nm and minimum value of h_{pillar}/t_{total}~0.4. Permittivity of the ceramic PZT $\varepsilon_{33}/\varepsilon_0$~800 at room temperature is lower than $\varepsilon_{33}/\varepsilon_0$~1350 and 1.5-2×$10^4$ of ceramic BTO and BSTO, respectively (see **Table 2.4**), but since the piezoelectric coefficient, d_{ij}, of ceramic PZT material is larger than d_{ij} of ceramic BTO or BSTO materials (see **Table 2.4**), larger mechanical strain-stress interaction in the PZT-CFO multiferroic nanocomposites is expected. In addition, by further increasing the density of interfaces in PZT-CFO system by increasing both nanopillars height and FE structure total thickness, the enhanced ME coupling can be achieved. Recently extremely high low-frequency (700 Hz) ME voltage coefficient ~737 V cm^{-1} Oe^{-1} was reported for the FeCoSiB/AlN thin-film nanocomposite (*Greve et al., 2010*) due the large piezoelectric constant of AlN material.

Schematic illustration of the fabricated PZT_{600}-CFO_{500}, PZT_{900}-CFO_{500}, and PZT_{1300}-CFO_{500} nanocomposites is shown in **Figure 5.19a**. Tilted cross-section SEM images of the corresponding PZT-CFO nanostructures are shown in **Figures 5.19b-d**. **Figure 5.19a** shows the SEM images taken at two different magnifications for the PZT_{600}-CFO_{500} nanocomposite, where the PZT layer penetrates the spacing between highly packed CFO nanopillars forming a two-phase columnar structure consisting of the CFO nanopillars embedded into PZT matrix and continuous PZT top-layer with thickness $t_{top\text{-}layer}$ ~100 nm formed on the top of the CFO nanopillars. The total thickness, t_{total}, of the PZT structure and PZT_{600}-CFO_{500} nanocomposite is ~600 nm, which corresponds to the sum of the CFO nanopillars average height, h_{pillar}~500 nm, and PZT top-layer thickness, $t_{top\text{-}layer}$~100 nm. The thickness of the PZT structure was controlled by a multiple dip-coating technique. **Figures 5.19c,d** show the tilted cross-section view SEM images of the PZT_{900}-CFO_{500} and PZT_{1300}-CFO_{500} nanocomposites consisted of two and three PZT top-layers, respectively, prepared by two and three subsequent dip-coating depositions. For the PZT_{900}-CFO_{500} nanostructure the PZT top-layer thickness, $t_{top\text{-}layer}$, was increased after the second PZT deposition from ~100 to ~400 nm, while for the PZT_{1300}-CFO_{500} nanocomposite, $t_{top\text{-}layer}$, was increased after the third deposition

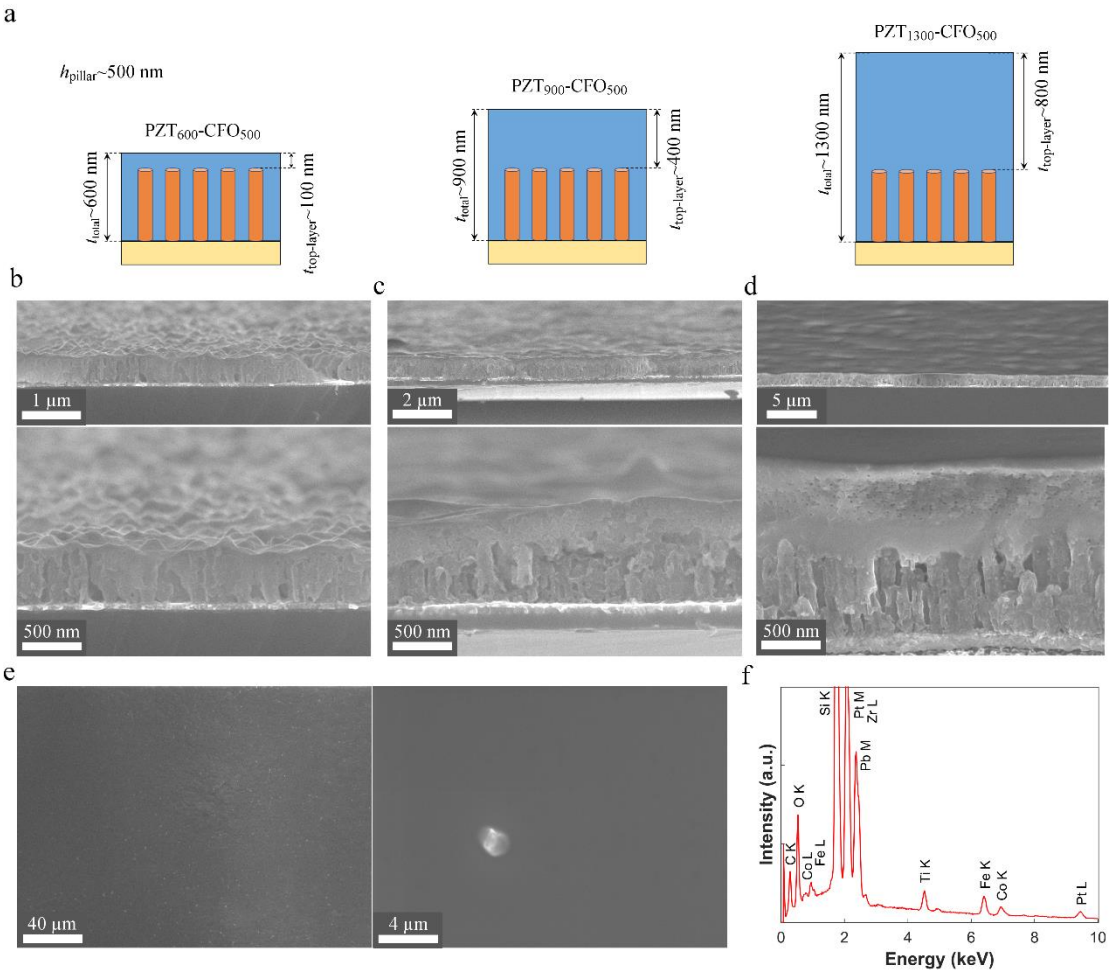

Figure 5.19: (a) Schematic illustration of the PZT-CFO nanocomposites with notations and geometric parameters, every sample was prepared using CFO nanopillar arrays with height, h_{pillar}, of ~500 nm. Tilted-view **(b-d)** and top-view **(e)** SEM images of the **(a)** PZT_{600} -CFO_{500}, **(b)** PZT_{900} -CFO_{500}, and **(c)** PZT_{1300}-CFO_{500} nanostructures with three different thickness obtained by a multi-dip coating technique. **(f)** EDX spectra of the PZT-CFO nanostructure

from ~400 to 800 nm. The average ratio h_{pillar}/t_{total}, was estimated qualitatively from SEM images for the PZT_{600}-CFO_{500}, PZT_{900}-CFO_{500}, and PZT_{1300}-CFO_{500} nanocomposites ~0.83, 0.55 and 0.38, respectively.

The top-view SEM images of the PZT_{600}-CFO_{500} nanocomposite at two magnifications (**Figure 5.19e**) confirm the formation of continuous PZT layer. The average chemical elemental analysis was provided by EDX technique (**Figure 5.19f**) confirming a value of the Fe/Co ratio close to 2 and Pb:Zr:Ti ratio ~111:59:41. A small deviation from the expected Pb:Zr:Ti ratio of 100:52:48 could be caused by the similar excitation energies of Zr L (2.042 eV) and Pt M (2.048) lines in EDX spectrum.

The critical step to achieve PZT-CFO nanostructure without cracking while avoiding formation of pyrochlore phase is clearly the thermal crystallization process of PZT layers. Structural characterizations have been conducted to probe the oxidation efficiency of $CoFe_2$ nanopillar arrays and the crystallization of pyrolyzed amorphous

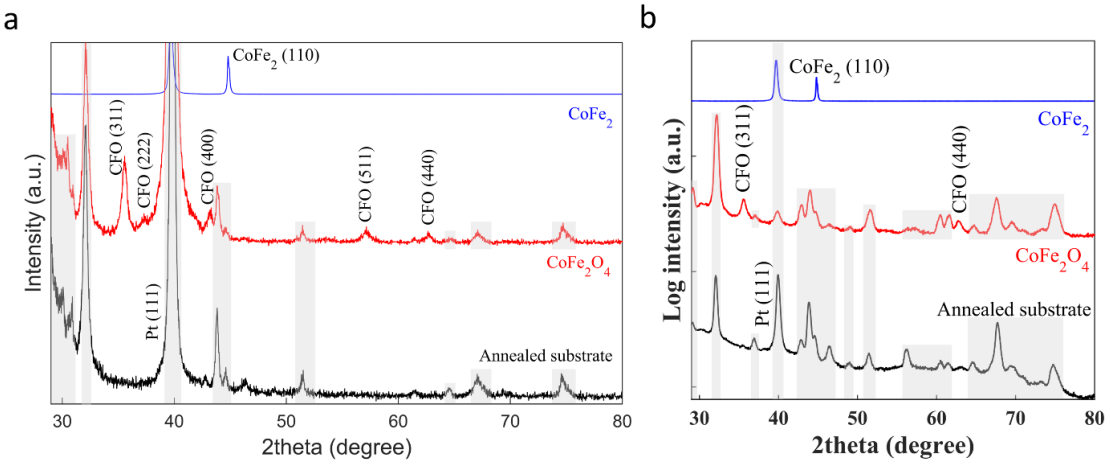

Figure 5.20: Out-of-plane powder XRD **(a)** and in-plane GIXRD **(b)** patterns of the vertically aligned $CoFe_2$ nanopillar arrays (blue), the $CoFe_2O_4$ nanopillar arrays (red), and the Pt/Ti/Si substrate annealed at ~600 °C (black)

PZT layers. **Figures 5.20a,b** show powder XRD and GIXRD patterns of the CFO and $CoFe_2$ nanopillar arrays (JCPDS # 48-1816), and the Pt/Ti/Si substrate annealed at ~600 °C. The oxidation of the $CoFe_2$ nanopillars into the polycrystalline CFO phase at 600 °C for 24 hours was confirmed by XRD through the appearance of CFO peaks (311), (222), (400), (511) and (440) in the powder XRD pattern (**Figure 5.20a**) and (311), (440) peaks in GIXRD pattern in **Figure 5.20b** (JCPD # 22-1086).

The powder X-ray diffraction pattern of the pure PZT thin film and PZT-CFO nanostructure prepared by thermal annealing at 650 °C for 30 min at 5 °C/min heating rate confirm the crystallization of polycrystalline PZT structure with all peaks corresponding to perovskite structure with random crystalline orientation (**Figure 5.21a**). Pt peaks and additional peaks resulting from reactions and associated phase formation during annealing are observed in the XRD pattern of Pt/Ti/Si substrate. **Figure 5.21b** illustrates the powder XRD diffraction pattern of the pure PZT film and PZT-CFO nanostructure prepared using quenching at 650 °C for 1 min. The XRD shows that the ultra-fast thermal shock in quenching process leads to the formation of

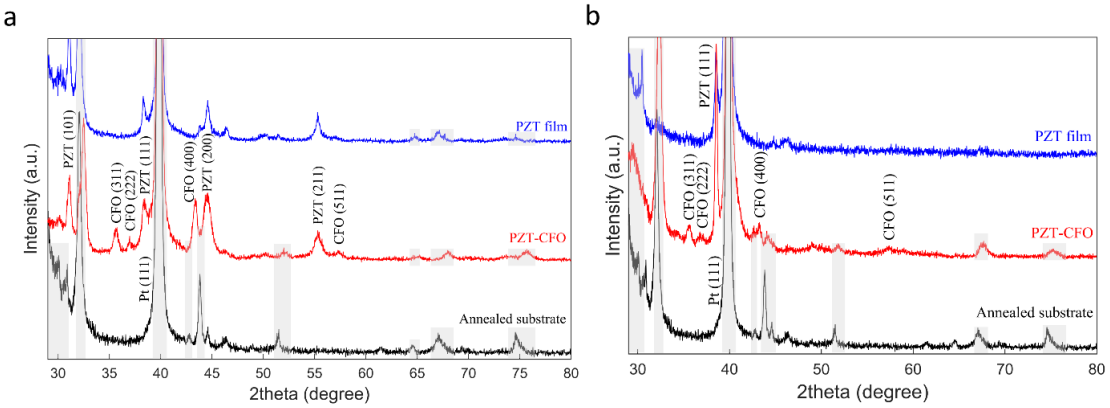

Figure 5.21: Out-of-plane powder XRD patterns of the PZT thin films (blue) and PZT-CFO nanostructures (red) crystallized using thermal annealing **(a)** and quenching **(b)** techniques, and the Pt/Ti/Si substrate annealed at ~600 °C (black)

a polycrystalline PZT layer with preferred alignment of PZT grains along (111) crystallographic direction. Previously it was reported that different temperatures of pyrolysis for the PZT films and PZT-CFO multilayers thin-films lead to different crystal orientation (*Gong et al., 2004*; *He et al., 2008*). For example, the PZT films and PZT-CFO multilayers pyrolyzed at 450 °C and then crystallized using thermal annealing at 700 °C showed a dominant (100) orientation, whereas the pyrolysis treatment at lower temperatures favoured the (111) orientation of the PZT film.

Figures 5.22a,b,c show the normalized magnetic hysteresis loops measured at room temperature with the field applied along the in-plane (perpendicular to pillar axis) and out-of-plane (parallel to pillar axis) directions. **Table 5.2** summarizes the magnetic properties of the $CoFe_2$ and CFO nanopillar arrays and PZT-CFO nanocomposite. For the $CoFe_2$ nanopillar array, the magnetocrystalline anisotropy can be neglected and the effective anisotropy is entirely magnetostatic, as pointed out previously in **Figures 5.4** and **5.10**, pp. 167, 176. **Figure 5.22a** shows the easy axis of magnetization along the in-plane direction, as shape anisotropy, associated with the infinite array of the vertically aligned nanopillars behaving as a whole film, overcomes the uniaxial shape anisotropy along the out-of-plane direction of the individual nanopillars. In addition, this causes the coercivity H_c~158 Oe and remanence-saturation ratio m_r/m_s~0.08 measured in OOP direction become smaller. **Figure 5.22b** shows the magnetic hysteresis curve for the $CoFe_2O_4$ nanopillar array. The shapes of the hysteresis loops are similar in the in-plane and out-of-plane directions. This can be explained by the fact

Table 5.2: Effects of thermal oxidation and PZT layer deposition on magnetic properties of the free-standing $CoFe_2$ nanopillar array

Sample	T_{ox}, °C	Time, h	H_C OOP, Oe	H_C IP, Oe	m_r/m_s OOP	m_r/m_s IP
$CoFe_2$	-	-	158	294	0.09	0.32
CFO	600	24	1997	1470	0.46	0.44
PZT-CFO	650	0.5	2428	2203	0.55	0.54

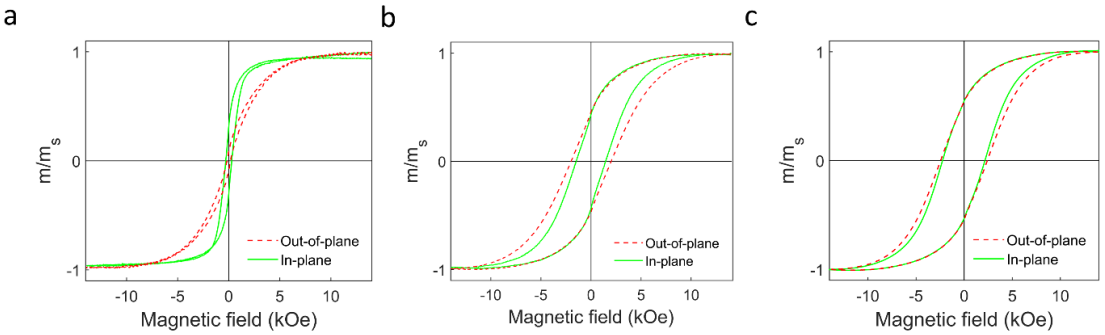

Figure 5.22: Room temperature hysteresis loops along in-plane (solid line) and out-of-plane (dashed line) directions for a vertically aligned $CoFe_2$ nanopillar arrays **(a)**, $CoFe_2O_4$ nanopillar arrays **(b)**, and the PZT-CFO multiferroic nanostructure **(c)**. The magnetic moment is normalized to its value in the saturation state

that the magneto-crystalline anisotropy energy dominates in the CFO nanopillar arrays, and there is no preferred crystallite orientation along the wire axes. Besides, large coercive field (H_c OOP ~2 kOe) have been achieved in the CFO nanopillar array. The observed coercive fields (H_c OOP ~2.4 kOe) and remanence (m_r/m_s OOP ~0.55) of the PZT-CFO nanocomposites are similar to the values obtained for the CFO nanopillar arrays (see **Figure 5.22c**).

Figures 5.23a,b show the thermal variations at three frequencies (10 kHz, 100 kHz, and 1 MHz) of capacitance and dielectric losses for the PZT_{900}-CFO_{500} nanostructure, respectively. The capacitance slightly increases when the temperature is increased from 80 to 400 K, However, to observe the maximum in capacitance associated with the ferroelectric-to-paraelectric phase transition close to 600 K, the measurements should be conducted above 410 K. The dielectric losses showed pronounced peaks (**Figure 5.23b**), whose maximum is shifted to higher temperature as the frequency increases which indicates the dielectric relaxation similar to the dielectric relaxation effects observed for the BSTO-CFO nanocomposite (see **Figures 5.5c**, p. 169).

Effective permittivity of the PZT_{900}-CFO_{500} nanocomposite capacitors was estimated using Equation (5.2). In the low temperature range ($T < 200$ K, 100 kHz), the effective permittivity of PZT_{900}-CFO_{200} nanostructure corresponding to **Figure 5.23a,** where $t_{total} = 900 \pm 50$ nm (**Figure 5.23d**), top Pt contact diameter, $D = 600$ μm ($S = 0.28 \times 10^{-6}$) is

$$\varepsilon_{PZT_{900}-CFO_{500}} = \frac{0.107 \times 10^{-9} \times (900 \pm 50) \times 10^{-9}}{8.854 \times 10^{-12} \times 0.28 \times 10^{-6}} \sim 38 \pm 2. \qquad (5.11)$$

In the low temperature range (T <200 K, 100 kHz), for which the conductivity contribution can be neglected, the effective permittivity of the nanostructure ($\varepsilon_{33}/\varepsilon_0$~38) is lower than the permittivity of the BSTO-CFO and BTO_{550}-CFO_{200} nanostructures $\varepsilon_{33}/\varepsilon_0$~60±6 and 70±6, respectively [see **Equations (5.3)** and **(5.7)**], indicating the poor dielectric properties and high dielectric losses ~0.2 (300 K, 10 kHz) for the PZT-CFO nanocomposite. We have also considered higher volume fraction of low permittivity of CFO pillar phase h_{pillar}/t_{total}~0.55 and the presence of microcracks in the PZT structure,

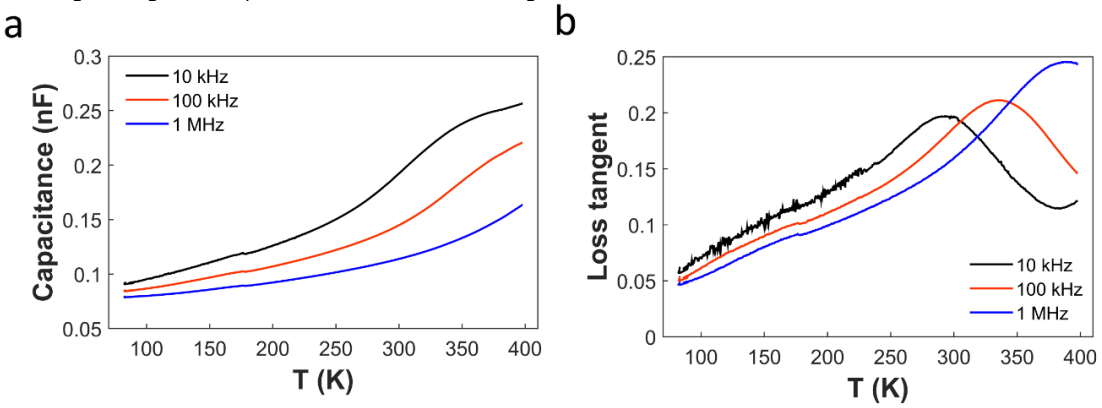

Figure 5.23: Capacitance and dielectric losses as a function of temperature for the PZT-CFO nanostructure with the 300-nm-thick PZT layer formed above the 500-nm-long CFO nanopillars

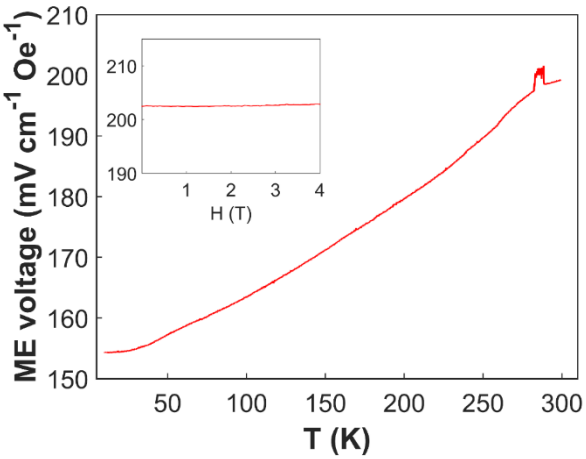

Figure 5.24: Temperature dependence of the ME voltage coefficient for the PZT_{400}-CFO_{500} nanostructure. Room-temperature variation with external dc magnetic field is shown in the top-left inset

which is often observed in FE thin films prepared by sol-gel techniques. The dielectric properties of the PZT_{600}-CFO_{500} and PZT_{1300}-CFO_{500} nanocomposites with corresponding h_{pillar}/t_{total}~0.83 and 0.38, respectively, will be analysed in future studies.

Dynamic magnetoelectric measurements of the ME voltage coefficient were performed by the group of Prof. Kristiaan Temst and Dr. Vera Lazenka at Instituut voor Kern- en Stralingsfysica, KU Leuven, Belgium. Direct ME coupling was tested in PZT_{900}-CFO_{500} nanocomposite with h_{pillar}/t_{total}~0.55 as a ME voltage response to the *ac* magnetic field, H_{ac}, as a function of temperature or *dc* magnetic field, H_{dc}.

The temperature variation of ME voltage coefficient in the range T~10-300 K for the PZT_{900}-CFO_{500} nanocomposite is shown in **Figure 5.24**. The α_E increases by 23% with temperature increasing from 10 K to 300 K. The maximal value of the ME coefficient ~202±12 mV cm^{-1} Oe^{-1} was achieved at room temperature.

At room temperature, the ME voltage coefficient of the PZT_{900}-CFO_{500} nanostructure shows very small variation (of the order of 1 %) when an external *dc* magnetic field (up to 4 T) is superimposed on the *ac* field, H_{ac}, as compared to the measured value in zero static magnetic field (see **Figure 5.24**(top-left inset)). If we consider similar value of h_{pillar}/t_{total} in BSTO-CFO BTO-CFO, and PZT-CFO nanocomposites, then the values of α_E ~320±13 and 211±9 mV cm^{-1} Oe^{-1} corresponding to the $BSTO_{1220}$-CFO_{500} and BTO_{1220}-CFO_{500} nanocomposites, respectively, are quite close to α_E ~202±12 mV cm^{-1} Oe^{-1} of the PZT_{900}-CFO_{500} nanocomposite.

5.6 Conclusions

In this work, we developed an original and efficient pathway for the synthesis of vertically aligned multiferroic nanocomposites. The method allowed the fabrication of regular, dense and free-standing $CoFe_2$ nanopillar arrays by electrodeposition through an anodic aluminium oxide template supported on a Si substrate. Next, $Ba_{0.70}Sr_{0.30}TiO_3$-$CoFe_2O_4$ and $BaTiO_3$-$CoFe_2O_4$ multiferroic nanostructures were grown through direct RF sputtering deposition of a ferroelectric film on the pillar structure, with *in situ* simultaneous oxidation of the ferromagnetic nanopillars, as confirmed by both structural and magnetic characterization. The synthesis approach preserves the morphology of the nanopillars during oxidation, improves the BSTO matrix penetration, and reduces the interface roughness between two constituents. The $BSTO_{500}$-CFO_{200} and BTO_{850}-CFO_{200} multiferroic nanocomposites exhibit strain-mediated ME coupling, whose maximum ME coefficients were measured as ~787±87 and 462±27 mV cm^{-1} Oe^{-1} at room temperature, respectively. The maximum ME coefficient was observed for a ratio between the nanopillars height and total thickness of the ferroelectric structure corresponding to 0.3 and 0.23 for the BSTO-CFO and BTO-CFO nanocomposites, respectively. Also, larger ME voltage coefficients were obtained for the BSTO-CFO and BTO-CFO with larger average effective permittivity that can be tuned by changing the ratio FE/FM.

The PZT-CFO (1-3) pillar based ME nanostructures have been successfully prepared from $CoFe_2O_4$ nanopillar arrays using the sol-gel dip-coating technique. The CFO nanopillars were obtained via an *ex situ* thermal oxidation of the electrodeposited $CoFe_2$ nanopillar arrays after chemical dissolution of the hosting AAO template. The PZT coating solution prepared using the chelate route was successfully modified by increasing boiling point which allowed to obtain crack-free, smooth, and continuous PZT top-layers on top of the CFO nanopillar arrays and to effectively penetrate and fill the space inside the CFO pillar arrays in spite of the fact that the surface roughness morphology and pillars diameter were strongly affected by the *ex situ* thermal oxidation prior to the PZT layer deposition. The PZT_{900}-CFO_{500} multiferroic nanostructure exhibits strain-mediated ME coupling, whose maximum ME coefficients was measured as ~202±12 mV cm^{-1} Oe^{-1} at room temperature. The $BSTO_{1220}$-CFO_{500} and BTO_{1220}-CFO_{500} nanostructures with similar ratio between the nanopillars height and total thickness of FE ~0.4 and similar nanopillars height ~500 nm, showed relatively close values of α_E ~320±13 mV cm^{-1} Oe^{-1} and 211±9 mV cm^{-1} Oe^{-1}, respectively. Further optimization of the sol-gel synthesis technique to improve microstructural properties and physical performance of the PZT-CFO nanostructures such as *in situ* oxidation of the $CoFe_2$ nanopillars during PZT layers crystallization. In future experiments, the dielectric and ME measurements will be conducted for the PZT-CFO nanocomposites with increased total thickness of the PZT structure using multiple dip-coating technique

.

Chapter 6

PZT-CFO Nanocomposites Based on 3D Interconnected Nanowire Networks

In order to increase the density of interfaces and interfacial area between FE and FM phases and thus to optimize the ME coupling of the FM nanowire to the adjacent FE matrix, original multiferroic nanostructures based on 3D interconnected FM nanowires networks were designed. The 3D interconnected $CoFe_2$ nanowire networks with large heights up to 25 µm and small NW diameters, D_{NW}, of 40 and 230 nm enable to fabricate multiferroic nanostructures with large interfacial areas between magnetostrictive and piezoelectric phases. In **Figure 6.1** we remind the preparation steps of the PZT-CFO nanostructures. This process was schematically shown in **Figure 3.29**, p. 111, and described in detail in **Section 3.3** (p. 110). The $CoFe_2$ 3D interconnected NW networks were chosen due to large aspect ratio of nanowires, robustness of self-supported $CoFe_2$ 3D NW network, and near-zero clamping effect.

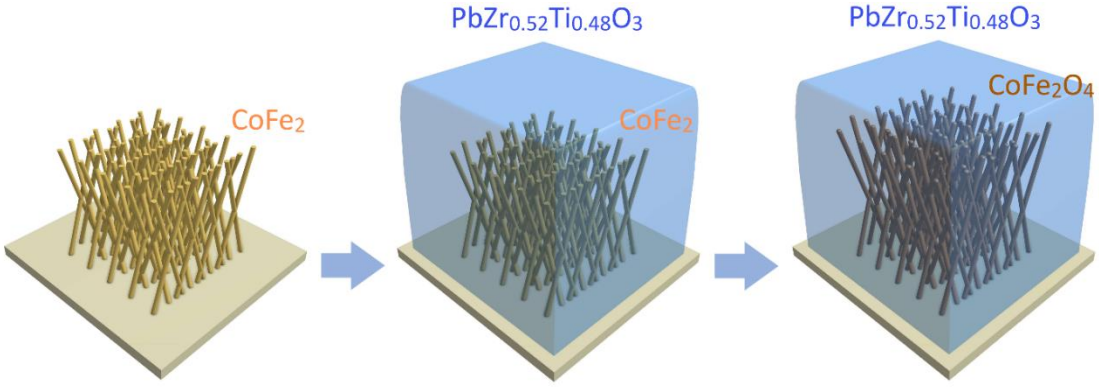

Figure 6.1: Brief illustration of the preparation of $PbZr_{0.52}Ti_{0.48}O_3$-$CoFe_2O_4$ ME system based on 3D interconnected NW network by sol-gel dip coating deposition and crystallization of the PZT thick layer and in-situ oxidation of the $CoFe_2$ NW network followed by the thermal post-annealing to complete the metal $CoFe_2$ NW network oxidation into the $CoFe_2O_4$ phase

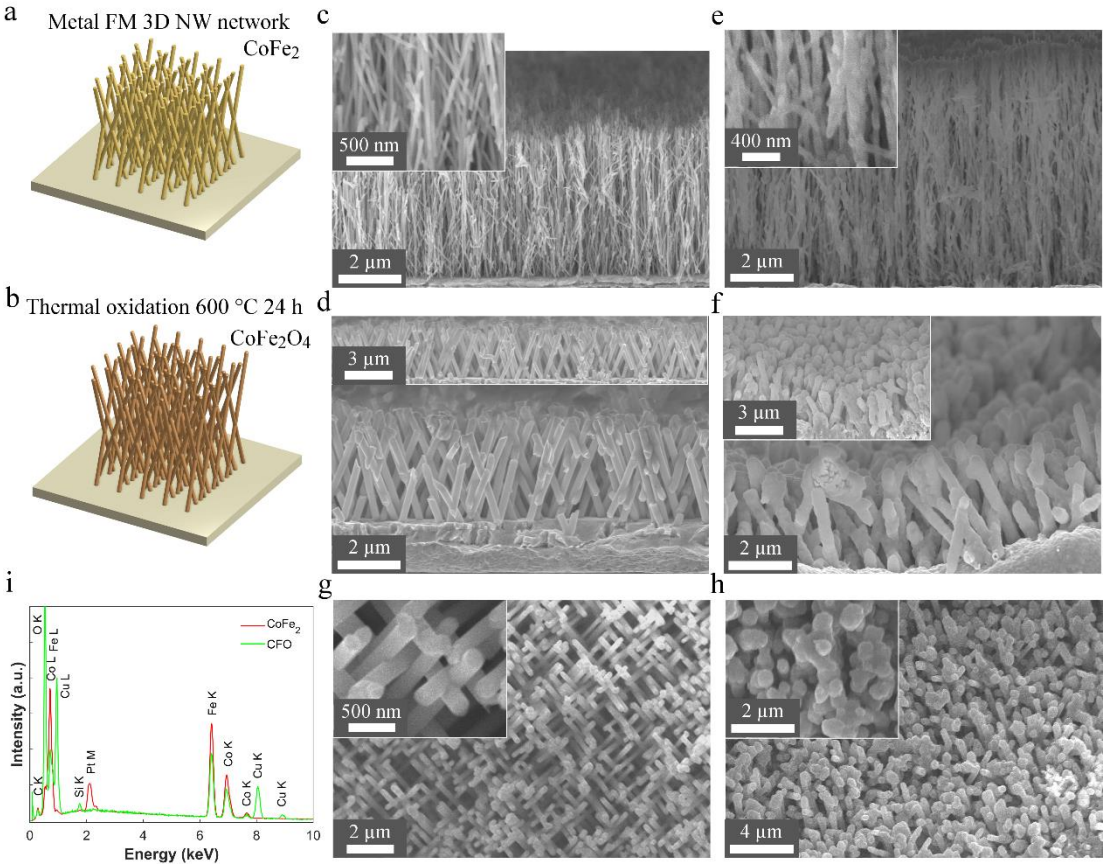

Figure 6.2: Schematic illustration of the $CoFe_2$ and CFO 3D interconnected nanowire networks before **(a)** and after the **(b)** thermal oxidation, respectively. Tilted cross-section view SEM micrographs of the $CoFe_2$ 3D NW networks grown into the **(c)** PC-1 (D_{NW} ~45 nm, α_{tilt} is a range of angles from -45° to +45° to the film's normal) and **(d)** PC-2 (D_{NW} ~230 nm, α_{tilt} is a fixed angle 25° to the film's normal) polymer membranes. Tilted view SEM images of the 3D NW networks shown in **(c)**, **(d)** after the thermal oxidation at 600 °C for 24 h indicating the change of the NWs surface roughness morphology, NW network buckling and increase of NWs diameter **(e,f)**. HRSEM images on the top view of the $CoFe_2$ NW network shown in **(d)** before and after the thermal annealing **(g,h)**. EDX spectra of the $CoFe_2$ (red) and CFO (green) 3D NW networks

The most interesting feature of these 3D nanostructured materials is a significant reduction of the magnetic anisotropy when the magnetic field is applied perpendicular and parallel to the plane of the 3D NW network sample (*Araujo et al., 2015*). This leads to the tunable anisotropy and microwave absorption properties by adjusting the relative orientation of the nanochannels, pore size and composition of material along the length of the nanowire deposited inside the channels.

The oxidation of free-standing $CoFe_2$ 3D interconnected NW networks is critical for the fabrication of PZT-CFO nanocomposites. In order to prepare PZT-CFO nanocomposites an *in situ* oxidation approach was used to transform the $CoFe_2$ 3D NW networks into the CFO phase simultaneously during crystallization of PZT matrix. The sol-gel dip-coating technique was quite efficient in terms of the penetration of PZT solution into the high-density CFO nanopillar arrays (see **Section 5.2**), therefore similar dip-coating sol-gel technique was used to prepare thicker PZT layers on top of the CFO

3D NW networks. However, the conditions of thermal annealing (650 °C for 30 min at 5 °C/min) used to obtain crack-free PZT top-layers for the PZT-CFO nanopillar based nanocomposites is not efficient enough to complete the oxidation process of metal $CoFe_2$ NWs into the CFO spinel phase. Consequently, in addition to the pyrolysis (at 300 °C for 5 min) and PZT crystallization (650 °C for 30 min t 5 °C/min), a post-annealing step (600 °C for 12 hours at 2 °C/min) was added to the process to complete $CoFe_2$ phase oxidation. The efficiency of $CoFe_2$ 3D NW networks oxidation and PZT structures crystallization was analysed using XRD and AGM techniques.

6.1 Thermal Oxidation of Free-Standing $CoFe_2$ 3D NW Networks

In **Figures 6.2a,b** we remind the *ex situ* oxidation process of free-standing $CoFe_2$ 3D NW networks into the CFO phase. Tilted view SEM images of the $CoFe_2$ 3D NW networks with nanowire diameters, D_{NW}, of ~40 and 230 nm, respectively are show in **Figures 6.2c,d**. The geometric parameters used for electrodeposition of 3D NW networks polymer membranes are summarized in **Table 3.11** (p. 112). **Figures 6.2c** and **6.2d** shown the average heights of $CoFe_2$ 3D NW networks, h_{NW}, ~5 and 3.5 μm, respectively. **Figures 6.2e,f** show the tilted view SEM images of the CFO 3D NW networks obtained after the thermal oxidation of the corresponding $CoFe_2$ NW networks in **Figures 6.2c,d**, respectively. An increase of the h_{NW} from ~5 μm to 7.5 μm and D_{NW} from ~40 to 60 nm by ~1.5 times was observed confirming the volume expansion of the $CoFe_2$ network (**Figure 6.2e**). The $CoFe_2$ 3D NW networks shown in **Figure 6.2d** demonstrate an increase of the D_{NW} from ~230 to 370 nm after thermal oxidation as well as an increase of the surface irregularity of nanowires, and 3D NW network buckling due to thermal stresses (**Figures 6.2f**). The ordering and uniform D_{NW}~230 nm for the $CoFe_2$ 3D NW network are shown on the top-view SEM image (**Figure 6.2g**). However, **Figure 6.2h** shows that the thermal oxidation of $CoFe_2$ 3D NW network results in the change of nanowires diameter and morphology, increase of surface roughness, disordering, and network's deformation. Note that by surface roughness we imply an average estimation based on the SEM image. An average elemental analysis of the $CoFe_2$ and CFO 3D NW networks was provided by EDX characterization (**Figure 6.2i**) confirming the values of Fe/Co ratio around 2 both before and after thermal oxidation.

As was previously demonstrated in Chapters 4 and 5, the critical processing step is a thermal oxidation of the $CoFe_2$ metallic phase into the metal oxide CFO insulating phase. Magnetic characterizations have been carried out to confirm the efficiency of oxidation process of $CoFe_2$ 3D NW networks. **Figures 6.3a** and **6.3b** show normalized magnetic hysteresis loops measured at ambient temperature with magnetic field applied along the in-plane direction, i.e. parallel to the plane of 3D NW network (exact direction of magnetic field with respect to nanowire axis is not defined). For the metal

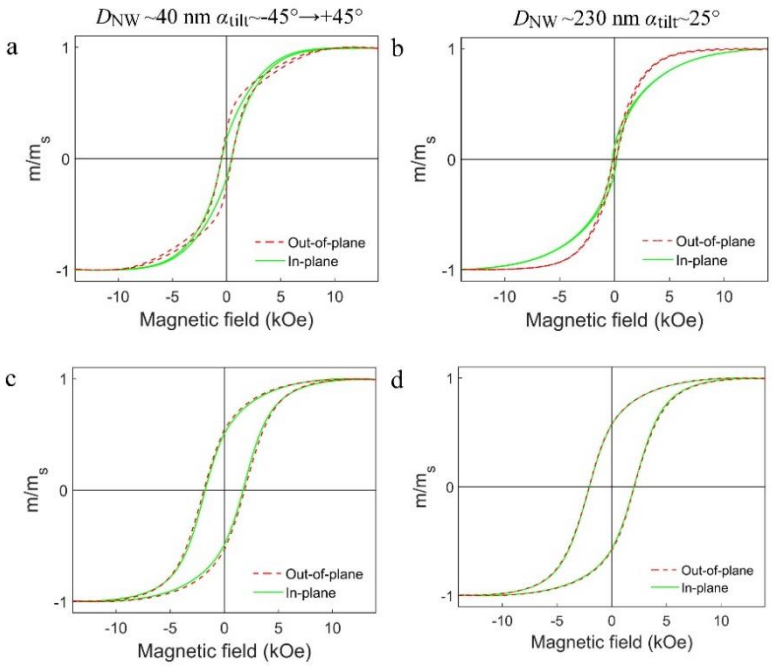

Figure 6.3: Room temperature magnetic loops along in-plane (solid line) and out-of-plane (dashed line) directions for the 3D interconnected $CoFe_2$ nanowire networks with **(a)** NWs diameter D_{NW} ~40 nm and tilt angle with respect to *Z* [001] out-of-plane direction α_{tilt} ~-45°→+45° and **(b)** D_{NW} ~230 nm and α_{tilt} ~25°. **(c,d)** Magnetic hysteresis loops of the CFO 3D interconnected NW networks formed by a thermal treatment at 600 °C for 24 hours using 2 °C/min heating rate of the corresponding $CoFe_2$ 3D NW networks **(a)** and **(b)**, respectively

$CoFe_2$ 3D NW networks the magnetocrystalline anisotropy is relatively small compared to the magnetostatic anisotropy as was pointed out previously for the $CoFe_2$ nanopillar and nanowire arrays (see **Figures 4.6a, 5.4a, 5.10a** and **5.22a**). However, **Figure 6.3a** shows the absence of easy direction of magnetization for the $CoFe_2$ 3D NW networks with D_{NW} ~40 nm and α_{tilt} ~-45°→+45°, which is in contrast with the easy directions of magnetization along IP and OOP observed for the high packing density arrays of free-standing $CoFe_2$ nanopillars (see **Figure 5.4a**, p. 167) and low packing density of $CoFe_2$ nanowires embedded into AAO membrane (**Figure 4.6a**, p. 146), respectively. Whereas for the $CoFe_2$ 3D NW network with D_{NW} ~230 nm and α_{tilt} ~25°, the easy axis of magnetization along the out-of-plane direction is observed (**Figure 6.3b**) as the angle between NWs axis and *Z* [001] OOP direction of magnetization ~25°<45°, while the average angles along *X* [100] and *Y* [010] IP directions > 45°.

Figures 6.3c,d show the magnetic hysteresis loops of the CFO 3D NW networks obtained after thermal oxidation (600 °C for 24 hours at 2 °C/min) of the $CoFe_2$ 3D NW networks corresponding to **Figures 6.3a,b**, respectively. The shapes of the hysteresis loops are similar in the in-plane and out-of-plane directions as was previously observed for the CFO nanopillar arrays (**Figures 5.4b**, **5.10b** and **5.22b**, pp. 167, 176 and 191) and CFO NW arrays surrounded by PZT nanotubes (see **Figure 4.11**, p. 153), indicating the dominant magnetocrystalline anisotropy in the CFO 3D NW

networks associated with large anisotropy constant K_1 ~2.6-3.8×10^6 erg/cm^3 and random crystalline orientation of the CFO nanowires. Additionally, the coercivity H_c increased from ~490 Oe to 1.9 kOe for the $CoFe_2$ 3D NW network with D_{NW} ~40 nm and from 130 Oe to 2.06 kOe for the $CoFe_2$ 3D NW network with D_{NW} ~230 nm, while the ratio m_r/m_s increased from 0.25 to 0.52 and from 0.05 to 0.58, respectively suggesting that the metal $CoFe_2$ phase is transformed into the oxide CFO phase. However, due to the change of 3D NW networks diameter, roughness, morphology and associated networks deformation after thermal oxidation, the dip-coating deposition of continuous and uniform PZT layers cannot be achieved. Therefore, in the following section to prepare PZT-CFO nanocomposites a simple *in situ* oxidation of $CoFe_2$ 3D NW networks during crystallization of PZT matrix is discussed.

6.2 Deposition of $PbZr_{0.52}Ti_{0.48}O_3$ Thick Layers on $CoFe_2$ 3D NW Networks

The direct PZT layers deposition on the metal $CoFe_2$ 3D NW networks is necessary to avoid an increase of nanowires diameter, surface roughness, and 3D NW networks buckling and deformation (see **Figures 6.2e,f,h**). Therefore, the $CoFe_2$ 3D NW networks were oxidized *in situ* during crystallization of the PZT thick layers (650 °C for 30 min at 5 °C/min). To complete the oxidation procedure of metal $CoFe_2$ 3D NW networks into metal oxide $CoFe_2O_4$ phase, a post-annealing treatment (600 °C for 12 hours at 2 °C/min) was conducted after the PZT crystallization step (650 °C for 30 min at 5 °C/min).

As mentioned previously in **Section 3.1.2** (p. 60), the thermal treatment determines the evolution of the microstructure and thus the heating process has to be optimized for the desired PZT layer morphology (density, porosity, grain size etc.). In particular the heating rate and pyrolysis temperature play an important role (*Reaney et al., 1994*; *Brooks et al., 1994*). The low heating rate for solvent evaporation is desirable to prevent cracking. The heating rates in the decomposition and crystallization phase are determined specifically for each system. Typically, thermal treatment of the as-deposited and dried PZT gels is divided into two steps: (a) gel pyrolysis, i.e. simultaneous evaporation of solvents and partial decomposition of organic residues, and (b) further thermal treatment at higher temperatures leading to amorphous or crystalline PZT ceramic layers.

In the first step of pyrolysis, a competition between solvent evaporation perpendicular to the substrate and reticulation parallel to the substrate surface (decomposition of the organic residues) results in shrinkage of the layers and formation of microcracks as shown in **Figure 6.4** (*Gaucher et al., 1992*). Therefore, the coating solution was prepared using an ethylene glycol to increase the boiling point. High boiling point allowed us to start the evaporation of the solvents at lower temperatures

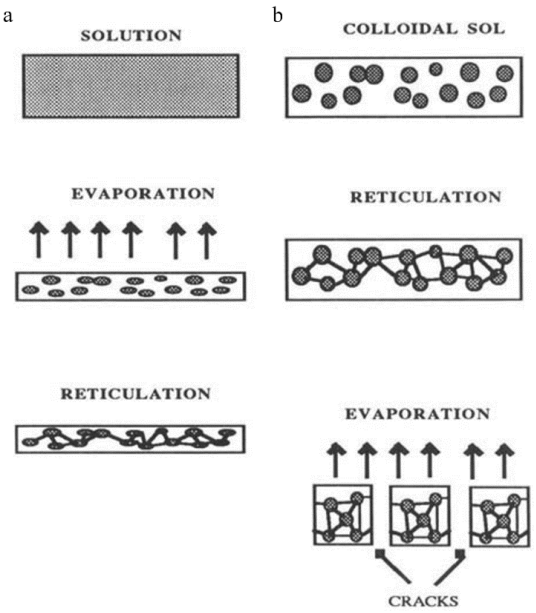

Figure 6.4: Schematic description of the successive steps during drying of sols of equal concentration from MOD **(a)** and sol-gel **(b)** process explaining the formation of cracks for too concentrated sols in sol-gel (from *Gaucher et al., 1992*)

compared to the reticulation decomposition. Thus, the shrinkage of the PZT layer was dominantly in *Z* [001] OOP direction (perpendicular to the substrate) and the parallel reticulation shrinkage was delayed to higher temperatures preventing the formation of microcracks.

In the second step of crystallization and densification, four main processes contribute to densification of PZT layers: (1) capillary contraction, as the solvent and reaction organics are removed from the pore spaces within the layer, creating pressures that drive the collapse of the amorphous network; (2) continued condensation reactions, as residual alkoxy (OR) and hydroxyl (OH) groups are removed from the M-O-M backbone; (3) skeletal densification and structural relaxation as the structure approaches the state that would be characteristic of the metastable liquid; and (4) viscous flow, as further structural rearrangement occur at higher temperature. It was reported (*Schwartz & Narayanan, 2009*; *Brinker & Scherer, 1990*) that the processes determining the densification mainly depend on precursor nature and heating rate used during the crystallization. Beyond the overlap between processes such as organic removal and structural collapse, a number of other processes are in competition with one another during higher heat treatment temperatures including densification, nucleation, grain growth, interfacial reactions, formation and consumption of intermediate phases, diffusion of layer constituents into the substrate and the loss of volatile species. During *in situ* oxidation of metal $CoFe_2$ 3D NW networks, the corresponding volume expansion of nanowires inside PZT layers may induce PZT layers cracking. It was reported that the addition of a higher boiling structural modifier delays organic removal, reduces thermodynamic driving force of crystallization,

resulting in an increased energy barrier for nucleation, and shift of crystallization to a higher temperature, thus supressing the second nucleation event at the layer surface (*Schwartz et al., 1990*). Nucleation at the substrate interface and layer surface was reported to occur simultaneously (*Schwartz et al., 1997*). The nucleation at the substrate occurs first, leading to the growth of columnar grains toward the surface of the film. Subsequently the nucleation at the layer surface occurs with lower nucleation density resulting in large hemispherical grains, that grow toward the substrate and may cause the parallel to substrate shrinkage and formation of microcracks. To prevent the formation of microcracks at the surface of thick layers, high crystallization temperatures and rapid heating can be used to complete the growth of the columnar grains nucleated at the substrate surface before the nucleation at the layer surface takes place.

In the present work to form and crystallize amorphous PZT layers without formation of microcracks at the layer surface, the boiling point of the PZT coating solution was increased by introducing ethylene glycol (see **Figure 3.27**, p. 108), then short pyrolysis was conducted using pre-heated hot plates (for 5 min), the PZT crystallization was conducted at maximum rate (at 5 °C/min) and finally long post-annealing process (for 12 hours) was carried out to complete $CoFe_2$ nanowires oxidation.

Figure 6.5 shows room temperature magnetic hysteresis loop of the $CoFe_2$ 3D NW network with D_{NW} ~40 nm and α_{tilt} ~-45°→+45° (**Figure 6.5a**) and PZT-CFO nanostructure (**Figure 6.5b**). The magnetic properties of the $CoFe_2$ 3D NW network and PZT-CFO nanostructure are summarised in **Table 6.1**.

Table 6.1: Effects of the *in situ* oxidation conditions on magnetic properties of the 3D interconnected $CoFe_2$ NW network with D_{NW} ~40 nm and α_{tilt} ~-45°→+45° and corresponding PZT-CFO nanostructure

Sample (**Figure 6.5**)	T_{ox}, °C	Time, min	Heating rate, °C/min	H_C OOP, Oe	H_C IP, Oe	m_r/m_s OOP	m_r/m_s IP
3D $CoFe_2$	-	-	-	636	521	0.38	0.18
PZT-CFO	300+650+600	5+30+720	5+2	1227	1074	0.41	0.38

For the free-standing $CoFe_2$ 3D NW network a small anisotropy with easy direction of magnetization along *Z* [001] OOP direction perpendicular to the plane of $CoFe_2$ NW network was observed, where larger H_c ~636 Oe and m_r/m_s ~0.38 along OOP direction compared to H_c ~521 Oe and m_r/m_s ~0.18 along IP direction were obtained (**Figure 6.5a**). For the PZT-CFO nanostructure this anisotropy disappears (**Figures 6.5b**) indicating the $CoFe_2$ nanowires oxidation into the CFO phase. The hysteresis loops obtained for the PZT-CFO nanostructure (**Figure 6.5**) and CFO 3D NW networks, obtained by the thermal annealing of the $CoFe_2$ 3D NW networks with similar geometric parameters (D_{NW} ~40 nm and α_{tilt} ~-45°→+45°) (**Figure 6.3c**), are similar. However, *H*c ~1227 Oe and m_r/m_s ~0.41 for the PZT-CFO nanostructure are slightly lower than *H*c ~1900 Oe and m_r/m_s ~0.52 for the CFO 3D NW networks.

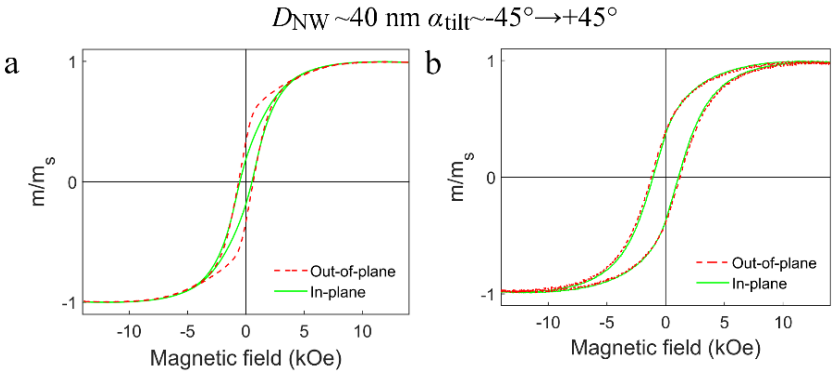

Figure 6.5: Room temperature hysteresis loops along in-plane (solid line) and out-of-plane (dashed line) directions for the 3D interconnected $CoFe_2$ with D_{NW} ~40 nm and α_{tilt} ~-45°→+45° **(a)**, and **(b)** the corresponding PZT-CFO nanostructure prepared using the pyrolysis at 300 °C for 5 min, thermal crystallization at 650 °C for 30 min at 5 °C/min and post-annealing at 600 °C for 12 hours at 2 °C/min

In addition to the magnetic properties measurement to confirm the efficiency of the *in situ* oxidation of $CoFe_2$ 3D NW networks inside PZT layer as well as crystallization of PZT layer, structural XRD characterization was conducted. **Figures 6.6a,b** show out-of-plane powder XRD and in-plane GIXRD patterns, respectively. The oxidation of the $CoFe_2$ phase into a polycrystalline CFO phase was indicated by XRD via the appearance of CFO peaks (220), (311) and (422) in powder XRD pattern and CFO peaks (220), (311) and (400) in GIXRD pattern (JCPDS # 22-1086). The crystallization of PZT layer was also shown by the appearance of PZT peaks (100), (101), (111), (200), and (211) on both powder XRD and GIXRD patterns. The $CoFe_2$ peak (110) can hardly be separated from the Au (200) and PZT (200) peaks, therefore it is difficult to conclude from the XRD observation if the metal $CoFe_2$ phase oxidation was completely transformed into the CFO phase. In future work, the magnetic properties measurement and XRD analysis will be conducted to confirm the *in situ* $CoFe_2$ phase oxidation for the PZT-CFO nanostructure prepared using the $CoFe_2$ 3D NW networks with larger nanowires diameter D_{NW} ~230.

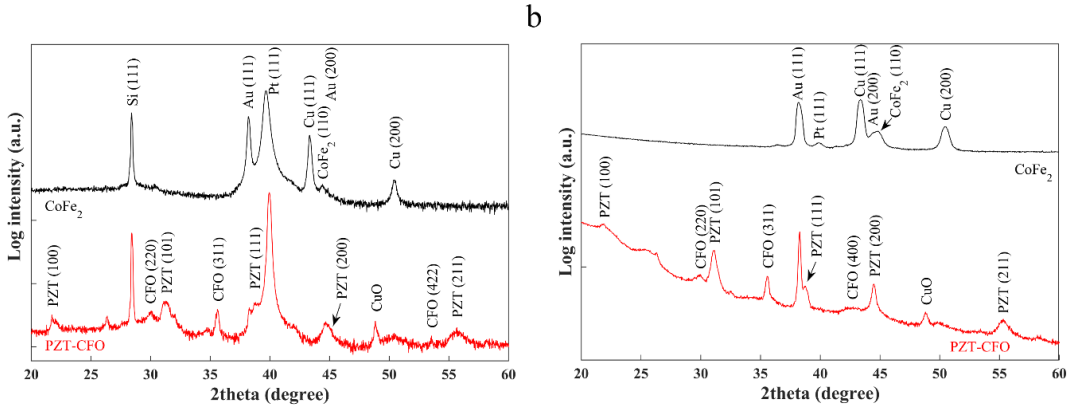

Figure 6.6: Out-of-plane powder XRD **(a)** and in-plane GIXRD **(b)** patterns of the $CoFe_2$ 3D NW network and PZT-CFO 3D nanostructure prepared using thermal crystallization of PZT layer and in-situ oxidation of the $CoFe_2$ 3D NW network at 600 °C for 12 h at 1.5 °C/min heating rate

Figure 6.7a shows the top view SEM image of the $CoFe_2$ 3D NW networks with D_{NW}~230 nm and h_{NW}~3.5 µm. The PZT gel impregnated into the $CoFe_2$ 3D NW networks is shown in **Figures 6.7b**. **Figures 6.7c,d** show the tilted view SEM images of the crack-free PZT-CFO nanostructure after the PZT layer was pyrolyzed and crystallized (650 °C for 30 min at 5 °C/min). **Figures 6.7e,f** show the tilted and top view of the PZT-CFO nanostructure obtained after the post-annealing process (600 °C for 12 hours at 2 °C/min), conducted after the crystallization (650 °C for 30 min at 5 °C/min) to complete the oxidation of the $CoFe_2$ 3D NW networks into the CFO phase. **Figures 6.7e,f** reveals the cracking of the PZT top-layer during after the post-annealing process. These results confirm that the crystallization of PZT thick layers during slow heating (2 °C/min) and long duration (12 hours) results in a formation of microcracks, probably due the 2nd nucleation event occurring at the PZT layer surface which can induce in-plane tensile stresses in layers (see **Figure 3.6**, p. 69). The PZT layer crystallization should be fast enough to complete the initial growth of columnar grains from the substrate towards the layer surface before the beginning of the 2nd nucleation event occurring at the layer surface. Another reason causing the PZT cracking could be the volume expansion of nanowires during *in situ* thermal oxidation, which may also generate large stresses in the PZT layer. Previously it was shown for the vertically

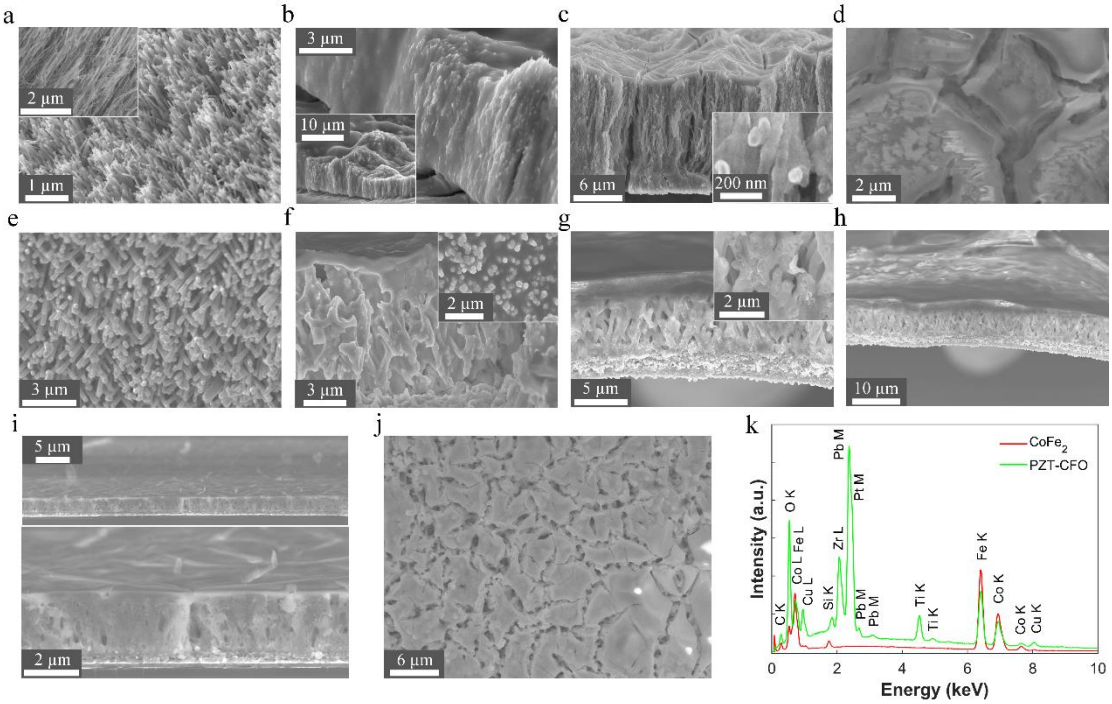

Figure 6.7: Tilted view SEM images on **(a)** 3D interconnected $CoFe_2$ nanowire network with D_{NW} ~230 nm and α_{tilt} ~25°, **(b)** corresponding PZT-$CoFe_2$ 3D nanostructure after sol-gel dip-coating deposition and dehydration of PZT sol, **(c,d)** PZT-CFO nanostructure after simultaneous PZT crystallization and in-situ oxidation of $CoFe_2$ 3D NW network at 650 °C for 30 min at 5 °C/min heating rate, **(e)** PZT-CFO nanostructure after post-annealing at 600 °C for 12 hours at 2 °C/min heating rate. **(f)** Top view SEM micrograph on the corresponding post-annealed at at 600 °C for 12 hours at 2 °C/min PZT-CFO 3D nanostructure shown in **(e). (g)** EDX analysis spectra for the $CoFe_2$ 3D NW network (red) and the PZT-CFO 3D nanostructure (green)

aligned CFO nanopillar arrays that volumetric expansion by 1.5 times takes place during thermal oxidation (**Figures 3.25** and **3.26**, pp. 105-6). An average composition analysis of the $CoFe_2$ 3D NW network and PZT-CFO nanostructure was provided by EDX (**Figure 6.7g**) confirming the value of Fe/Co ratio around 2 and the desired Pb:Zr:Ti ratio of 104:54:46. However, the analysis in this case is more qualitative due to the proximity of excitation energy for Zr L (2.042 keV) and Pt M (2.048 keV) lines in the EDX spectrum.

6.3 Conclusions

To summarize, 3D interconnected $CoFe_2$ nanowire networks with two different nanowire diameters were prepared using pulsed electrodeposition growth inside commercial track-etched polymer membranes. Free-standing $CoFe_2$ 3D NW networks were obtained after chemical dissolution of polymer membranes. *Ex situ* thermal oxidation of the free-standing $CoFe_2$ NW network resulted in a change of the NWs diameter, surface irregularity, roughness, buckling and deformation of the 3D NW networks due to the thermal stress and volumetric expansion of nanowires.

Through the optimization of coating solution, pyrolysis and crystallization, it was possible to obtain a crack-free PZT-CFO nanostructure with *in situ* oxidation of $CoFe_2$ 3D NW networks whose nanowire diameter ~230 nm and height ~3.5 μm. However, in order to complete the oxidation of metal $CoFe_2$ nanowires into the CFO phase inside PZT matrix, additional thermal post-annealing step was conducted, which lead to the PZT layer's cracking. Further optimization of thermal treatment should be made in future work.

The PZT layer's cracking results in large leakage currents, thereby dielectric, ferroelectric and ME voltage measurements are not suitable at this stage. Nevertheless, the strain-mediated ME coupling in the PZT-CFO nanocomposites based on 3D CFO nanowire networks can be probed indirectly. For example, a temperature-dependent magnetization measurement technique was previously used to show a distinct drop in the CFO nanopillars magnetization (~15% of magnetization at a 100-Oe external field) around BTO matrix ferroelectric Curie temperature (~390 K) (*Zheng et al., 2004*). In addition, the ferromagnetic resonance (FMR) measurement can be used to observe voltage-driven shifts in the FMR frequency, reflecting electrically induced change in magnetic anisotropy (*Benatmane et al., 2010; Lou et al., 2008*), or the in-plane and out-of-plane magnetic hysteresis loops can be measured under electric field using superconducting quantum interference device (MPMS, Quantum Design) or VSM/AGM magnetometer to measure the magnetic properties and an electrometer (Keithley) to apply the bias voltage (*Yang et al., 2009*).

Chapter 7

Conclusions and Future Work

In summary, this work was focused on vertically aligned multiferroic nanostructures, so called (1-3) connectivity multiferroic nanocomposites. Different architectures have been designed using the combination of electrodeposition, sol-gel and RF sputtering processes. Our main goal was to enhance the magnetoelectric coupling through an accurate control of interfaces thanks to the optimization of both the geometry of the nanostructures and the different synthesis steps required for each process. The possibility of fabrication and characterisation of the vertically aligned multiferroic nanocomposites, ferroelectric thin films, and ferromagnetic nanowire arrays was provided by the unique collaboration and access to the facilities of IMCN, Université catholique de Louvain, Belgium and ICMCB-CNRS, Université de Bordeaux, France in the framework of IDS-FunMat Doctoral School.

First, PZT-CFO core-shell nanocables have been successfully prepared combining the cost-effective dip-impregnation based on sol-gel chemical solution deposition and pulsed electrodeposition processes. One of the critical points for the preparation of PZT nanotubes to ensure good ferroelectric properties is the nanotube wall thickness. The wall thickness of PZT nanotubes was increased by increasing the number of sol-gel dip-impregnations to three. The thermal treatment required to transform metal $CoFe_2$ phase into the insulating $CoFe_2O_4$ spinel phase is a key step with respect to the interdiffusion phenomena between AAO membrane, PZT shells, and $CoFe_2$ nanowires. We demonstrated that PZT nanotubes act as an efficient diffusion barrier between the $CoFe_2$ nanowires and AAO template. We overcame the thermal constraints and demonstrated the benefit of a global lowering of the processing temperature to preserve both architecture and structural integrity of this complex system.

Magnetic properties of the PZT-$CoFe_2$ and PZT-CFO core-shell nanocables show that for the PZT-$CoFe_2$ system packing density and corresponding dipolar coupling of $CoFe_2$ nanowire arrays can be reduced by increasing the surrounding PZT nanotube thickness, as for the PZT-CFO core-shell nanocables the magnetocrystalline anisotropy

is dominant leading to the isotropic hysteresis behaviour regardless of the direction of applied magnetic field.

We investigated the local ferroelectric properties of nanotubes and core-shell nanocables by PFM polarization switching. The measured PFM phase change in the PZT nanotube was ~170° while the voltage was switched from -5 to +5 V, as for the PZT-CFO core-shell nanocables the phase variation was ~180° with the voltage changed from -6 to +6 V.

We also developed an original and efficient pathway for the synthesis of vertically aligned multiferroic nanocomposites based on electrodeposition and RF sputtering deposition. The method allowed the fabrication of regular, dense, and free-standing $CoFe_2$ nanopillar arrays by electrodeposition through an anodic aluminium oxide template supported on a Si substrate. Next, $Ba_{0.70}Sr_{0.30}TiO_3$-$CoFe_2O_4$ and $BaTiO_3$-$CoFe_2O_4$ multiferroic nanostructures were obtained through direct RF sputtering deposition of a ferroelectric film on the pillar structure, with *in situ* simultaneous oxidation of the metallic ferromagnetic nanopillars, as confirmed by both structural and magnetic characterizations. The synthesis approach preserves the morphology of the nanopillars during oxidation, improves the BSTO matrix penetration, and reduces the interface roughness between the two constituents. ME coefficient of different nanocomposites were measured, the highest values were obtained for the BSTO-CFO and BTO-CFO multiferroic nanostructures exhibiting strain-mediated ME coupling of about ~787 and 463 mV cm^{-1} Oe^{-1} at room temperature, respectively. In a first attempt, we tried to correlate the ME coefficient to the ratio between nanopillars height and total thickness of the ferroelectric structure and to the effective permittivity of FE component.

The $PbZr_{0.52}Ti_{0.48}O_3$-$CoFe_2O_4$ (1-3) nanopillar arrays based ME nanostructures have been successfully prepared from $CoFe_2O_4$ nanopillar arrays using sol-gel dip-coating technique. The CFO nanopillars were obtained via an *ex situ* thermal oxidation of the electrodeposited $CoFe_2$ nanopillar arrays after chemical dissolution of the hosting AAO template. The PZT coating solution, prepared using the chelate route, was successfully modified by increasing boiling point which allowed to obtain crack-free, smooth, and continuous PZT top-layers on top of the CFO nanopillar arrays and to enable efficient penetration and filling of the space inside CFO pillar arrays in spite of the strongly affected surface roughness morphology and pillars diameter by *ex situ* thermal oxidation. The PZT_{900}-CFO_{500} multiferroic nanostructures exhibit strain-mediated ME coupling, whose maximum magnetoelectric coefficients was measured as ~202 mV cm^{-1} Oe^{-1} at room temperature.

Finally, the design of nanocomposite based on 3D interconnected $CoFe_2$ nanowire networks was proposed. The 3D nanowire networks with two different nanowire diameters were prepared using pulsed electrodeposition into porous commercial track-etched polymer membranes. Free-standing $CoFe_2$ 3D NW networks were obtained after chemical dissolution of polymer membranes. *Ex situ* thermal oxidation of the free-

standing $CoFe_2$ 3D NW networks resulted in a change of the nanowires diameter, surface irregularity, roughness, and deformation of the 3D NW networks due to the thermal stress and volumetric expansion of 3D NW networks. Through the optimization of coating solution, pyrolysis and crystallization, it was possible to obtain a crack-free PZT-CFO nanostructure but with incomplete $CoFe_2$ phase *in situ* oxidation. In order to complete the oxidation of metallic $CoFe_2$ nanowires into the CFO phase inside PZT matrix, additional thermal post-annealing step was conducted, which led to the PZT layer's cracking.

Further optimization of sol-gel synthesis technique and thermal treatment should be conducted in future work to improve microstructural properties and physical performance of the PZT-CFO nanocomposites. In addition, it is important to optimize the sol-gel deposition of PZT layers in order to make it compatible with *in situ* oxidation of metallic $CoFe_2$ nanopillar arrays and 3D interconnected nanowire networks during crystallization of PZT layers.

In future experiments, the total thickness of PZT structure should be increased using multiple dip-coating technique in order to obtain the optimal range of density of interfaces and improve their dielectric and ME properties. In addition, another configuration of electrodes can be tested, that is in-plane geometry, which possibly can reduce the contribution of CFO conductivity and space charges relaxation trapped in the interfaces. Also, this electrode geometry is attractive for the ME coefficient measurement in transverse geometry, which is important for multiferroic materials consisting of magnetic phases with negative magnetostriction. The observed large dielectric losses ($\tan\delta$ ~0.2-0.4) is still one of the main issues. To solve this problem the packing density of magnetic nanopillar arrays should be reduced to improve the penetration of ferroelectric layers using sputter deposition. For the PZT-CFO nanocomposites thermal oxidation of free-standing nanopillar array led to the increase of nanopillars diameter and packing density, thus $CoFe_2$ *in situ* oxidation approach should be used for sol-gel crystallization of PZT layers.

Larger ME effect was observed for the more insulating nanocomposites with larger value of effective permittivity. However, the measurement error bar of nanostructures thickness and nanopillars height using SEM is too large ~10% (±50 nm), therefore to quantitatively analyze the dependence of magnetoelectric coefficient on nanocomposite's geometric parameters such as nanopillars height and ratio between this heigth and total thickness of ferroelectric phase, TEM measuremet of geometric parameters and a larger number of samples are required.

Additional effects such as residual stress should be considered to properly highlight the key parameters. This could be one of the topics for future studies. Residual stresses in vertically aligned multiferroic nanocomposites can affect the ME coupling and dielectric properties. As a perspective the dependence of ME coupling on the residual stress can be studied on both micro- and macro-scale using TEM evaluation of crystal lattice parameters and free-standing cantilever technique (*Banerjee et al., 2014*),

respectively. When we consider nanostructures, their properties can differ from the bulk. For example, the dielectric properties of bulk CFO $\varepsilon \sim 10$ could be affected by non-stoichiometry of CFO nanowires, which can affect the global dielectric performance of multiferroic nanocomposite. Thus, in future work to analyse local non-stoichiometry of elements and affinity in nanowires, we should use TEM/EDX technique.

To conduct the surface roughness analysis, AFM technique can be used. For the nanowires surface analysis, they need to be collected on the substrate in horizontal position, whereas for the vertically aligned nanopillar based nanocomposites the AFM can be used directly to scan the top surface of nanocomposite.

The main issue for the PZT-CFO nanocomposites based on 3D interconnected nanowire networks is cracking, which does not allow to conduct dielectric, ferroelectric and ME voltage experiments. In future work, indirect magnetoelectric measurement techniques could be used including the temperature-dependent magnetization measurement technique to show a distinct drop in the CFO nanopillars magnetization (~15% of magnetization at a 100-Oe external field) around ferroelectric layer Curie temperature (*Zheng et al., 2004*). In addition, the ferromagnetic resonance (FMR) measurement can be conducted to observe voltage-driven shifts in the FMR frequency, reflecting electrically induced change in magnetic anisotropy (*Benatmane et al., 2010; Lou et al., 2008*), or the in-plane and out-of-plane magnetic hysteresis loops can be analyzed under electric field using superconducting quantum interference device (MPMS, Quantum Design) (*Zavaliche et al., 2005*) or VSM/AGM magnetometer to measure the magnetic properties and an electrometer (Keithley) to apply the bias voltage (*Yang et al., 2009*).

For future technology applications of magnetoelectric nanocomposites such as magnetic/electric fields sensors, gyrators, actuators and energy harvesting, the vital element is magnetic-to-electric conversion capabilities (i.e. ME susceptibility). Generally, to obtain larger power conversion in piezomagnetic-piezoelectric based multiferroic devices, both the power coupling coefficient and the mechanical quality factor must be large (*Palneedi et al., 2016*). For these applications the PZT-CFO nanocomposites with larger surface area such as core-shell PZT-CFO nanocables and 3D nanowire networks based nanostructures are more promising. However, for the nanoscale applications such multi-state logic devices, spintronics, MERAM and writing/reading heads, to increase the data storage capacity the device miniaturization is important (*Scott, 2007; Bibes & Barthélémy, 2008*). Thus, the vertically aligned multiferroic nanocomposites based on vertically aligned nanopillar arrays with relatively nanopillars height are more applicable.

One of most interesting features of these 3D nanostructured materials is a significant reduction of the magnetic anisotropy when the magnetic field is applied perpendicular and parallel to the plane of the 3D NW network sample leading to the tunable anisotropy and microwave absorption properties by tuning the geometry, i.e.

the relative orientation of the nanochannels, pore size and composition of material along the length of the nanowire deposited inside the channels (*Araujo et al., 2015*). Multiferroic nanocomposites based on 3D interconnected NW networks with electrically tunable magnetic anisotropy can be used as picotesla sensitivity magnetoelectric magnetometer (*Dong et al., 2003; Zhai et al., 2006*), electrostatically tunable magnetic microwave signal processing devices like resonators (*Fetisov & Srinivasan, 2006*), phase shifters (*Ustinov et al., 2007*), and filters (*Pettiford et al., 2007*) as well as energy harvesting cantilever (*Onuta et al., 2011*). Electrostatic control of magnetization will lead to new magnetic devices that are fast, compact and energy efficient.

Bibliography

Adachi, M., Matsuzaki, T., Yamada, T., Shiosaki, T. & Kawabata, A. *Jap. J. Appl. Phys*. **26**, 550 (1987).

Ahn, C. H., Rabe, K. M. & Triscone, J.-M. Ferroelectricity at the Nanoscale: Local Polarization in Oxide Thin Films and Heterostructures. *Science* **303**, 488-491 (2004).

Allibe, J. Fusil, S., Bouzehouane, K., Daumont, C., Sando, D., Jacquet, E., Deranlot, C., Bibes, M. & Barthélémy, A. Room temperature electrical manipulation of giant magnetoresistance in spin valves exchange-biased with BiFeO3. *Nano Lett*. **12**, 1141–1145 (2012).

AlMawlawi, D., Coombs, N. & Moskovits, M. *J. Appl. Phys*. **70**, 4421-4425 (1991).

Amrillah, T., Bitla, Y., Shin, K., Yang, T., Hsieh, Y. H., Chiou, Y. Y., Liu, H. J., Do, T. H., Su, D., Chen, Y.-C., Jen, S.-U., Chen, L.-Q., Kim, K. H., Juang, J. Y. & Chu, Y. H. Flexible multiferroic bulk heterojunction with giant magnetoelectric coupling via van der waals epitaxy *ACS Nano* **11**, 6122-30 (2017).

Andrew, J. S., Starr, J. D. & Budi, M. A. K. *Scr. Mater*. **74**, 38-43 (2014).

Antohe, V.-A. *pH Sensitive Capacitive Detectors Based on Localized Nanowire Arrays*, PhD thesis. (Université catholique de Louvain, Louvain-la-Neuve, Belgium, 2012).

Aoyama, T. Yamauchi, K.,, Iyama, A.,, Picozzi, S.,, Shimizu, K. & Kimura, T. Giant spin-driven ferroelectric polarization in TbMnO3 under high pressure. *Nat. Commun*. **5,** 4927 (2014).

Araujo, E., Encinas, A., Velázquez-Galván, Y., Martínez-Huerta, J. M., Hamoir, G., Ferain, E. & Piraux, L. *Nanoscale* **7**, 1485 (2015).

Arima, T. Ferroelectricity induced by proper-screw type magnetic order. *J. Phys. Soc. Japan* **76**, 073702 (2007).

Ascher, E. Higher-order magnetoelectric effects. *Philos. Mag*. **17**, 149–157 (1968).

Assink, R. & Schwartz, R. *Chem Mater* 5, 511 (1993).

Astrov, D. N. The magnetoelectric effect in antiferromagnetics. *Sov. Phys. JETP*, **11**, 708–709, (1960).

Baji, A., Mai, Y-M., Yimnirum, R. & Unruan, S. *RSC Adv*. **4**, 55217-55223 (2014).

Banerjee, N., Houwman, E. P., Koster, G. & Rijnders, G. Fabrication of piezodriven, free-standing, all-oxide heteroepitaxial cantilevers on silicon. *APL Mater*. **2**, 096103 (2014)

Barone, P. & Picozzi, S. Mechanism and origin of multiferroicity. *C. R. Phys.* **16**, 143-152 (2015)

Batra, I. P. & Silverman, B. D. Thermodynamic stability of thin ferroelectric films. *Solid State Commun.* **11**, 291-294 (1972).

Becher, C., Maurel, L., Aschauer, U., Lilienblum, M., Magén, C., Meier, D., Langenberg, E., Trassin, M., Blasco, J., Krug, I. P., Algarabel, P. A., Spaldin, N. A., Pardo, J. A., Fiebig, M. Strain-induced coupling of electrical polarization and structural defects in SrMnO3 films. *Nat. Nanotechnol*. **10**, 661–665 (2015).

Bellaiche, L., Garcia, A. & Vanderbilt, D. *Phys. Rev. Lett.* **84**, 5427 (2000).

Benedek, N. A. & Fennie, C. J. Hybrid improper ferroelectricity: a mechanism for controllable polarization-magnetization coupling. *Phys. Rev. Lett*. **106**, 107204 (2011).

Benatmane, N., Crane, S. P., Zavaliche, F., Ramesh, R. & Clinton, T. W. Voltage-dependent ferromagnetic resonance in epitaxial multiferroic nanocomposites. *Appl. Phys. Lett*. **96**, 082503 (2010).

Bernal, A., Tselev, A., Kalinin, S. & Bassiri-Gharb, N. *Adv. Mater*. **24**, 1160 (2012).

Bharadwaja, S. S. N., Olszta, M., Trolier-McKinstry, S., Li, X., Mayer, T. S. & Roozenboom, F. *J. Am. Ceram. Soc*. **89**, 2695 (2006).

Bhattachargee, S., Bousquet, E. & Ghosez, P. Engineering Multiferroism in $CaMnO_3$. *Phys. Rev. Lett.* **102**, 117602 (2009).

Bhushan, B. *Springer Handbook of Nanotechnology*. 2 edn., (Berlin Heidelberg New York: Springer-Verlag, 2004).

Bibes, M. & Barthélémy, A. Multiferroics: towards a magnetoelectric memory. *Nat. Mater*. **7**, 425–426 (2008).

Bichurin, M. I., Petrov, V. M. & Srinivasan, G. Theory of low-frequency magnetoelectric coupling in magnetostrictive-piezoelectric bilayers. *Phys. Rev. B* **68** 054402 (2003).

Bousquet, E. & Cano, A., Non-collinear magnetism in multiferroic perovskites. *J. Phys. Condens. Matter* **28**, 123001 (2016).

Boyle, T. J., Dimos, D., Schwartz, R. W., Alam, T. M., Sinclair, M. B. & Buchheit, C. D. *J. Mater. Res*. **12**, 1022 (1997).

Bozorth, R. M. *J. Appl. Phys*. **8**, 575 (1937).

Bozorth, R. M., Tilden, E. F. & Williams, A. J. *Phys. Rev.* **99**, 1788 (1955).

Brinker, C. J. & Scherer, G. W. *Sol-gel science: the physics and chemistry of sol-gel processing*. (Boston: Academic, 1990).

Brooks, K. G., Reaney, I. M., Klissurska, R., Huang, Y., Bursill, L. & Setter, N. Orientation of rapid thermally annealed lead zirconate titanate thin films on (111) Pt substrates. *J. Mater. Res*. **9**, 2540–2553 (1994).

Brown Jr., W. F., Hornerich, R.M. & Shtrikman, S. Upper bound on the magnetoelectric susceptibility. *Phys. Rev*., **168**, 574–576 (1968).

Buschow, K. H. J. *Handbook of Magnetic Materials*, Vol. 19., 129-229 (Oxford, UK: Elsevier B.. 2011).

Budd, K. D., Dey, S. K., Payne, D. A. *Brit. Ceram. Soc. Proc* **36**, 107 (1985).

Buessem, W. R., Cross, L. E. & Goswami, A. K. *J. Am. Ceram. Soc*. **49**, 33 (1966).

Carlier, D. & Ansermet, J.-P. *J. Electrochem. Soc*. **153**, C277-C281 (2006).

Catalan, G. Magnetocapacitance without magnetoelectric coupling. *Appl. Phys. Lett.* **88**, 102902 (2006).

Chen, C. P., Tang, M. H., Lv, X. S., Tang, Z. H. & Xiao, Y. G. *Appl. Phys. Lett*. **101**, 212902 (2012).

Chen, H. T., Hong, L. & Soh, A. K. *J. Appl. Phys*. **109**, 094102 (2011).

Chen, J., Wang, Y. & Deng, Y. *J. Alloys Compd.* **552**, 65-69 (2013).

Cheng, Y., Zou, B., Yang, J., Wang, C., Liu, Y., Fan, X., Zhu, L., Wang, Y., Ma, H. & Cao, X. *CrystEngComm* **13**, 2268-2272 (2011).

Cheong, S.-W. & Mostovoy, M., *Nat. Mater*. **6**, 13 (2007).

Chikazumi, S. *Physics of Magnetism*, 153-155 (Hoboken: Wiley, 1964).

Chinnasamy, C. N., Jeyadevan, B., Shinoda, K., Tohji, K., Djayaprawira, D. J., Takahashi, M., Joseyphus, R. J. & Narayanasamy, A. *Appl. Phys. Lett*. **83**, 2862-2864 (2003).

Choi, H. K., Aimon, N. M., Kim, D. H., Sun, X. Y., Gwyther, J., Manners, I. & Ross, C. A. *ACS Nano* **8**, 9248 (2014).

Choi, J., Nielsch, K., Reiche, M., Wehrspohn, R.B. & Gösele, U. *J. Vac. Sci. Technol. B*, **21**, 763-766 (2003).

Chu, S. Z., Wada, K., Inoue, S., Isogai, M. & Yasumori, A. *Adv. Mater*. **17**, 2115–2119 (2005).

Chu, Y. H., Zhao, T., Cruz, M. P., Zhan, Q., Yang, P. L., Martin, L. W., Huijben, M., Yang, C. H., Zavaliche, F., Zheng, H. & Ramesh, R. Ferroelectric size effects in multiferroic $BiFeO_3$ thin films. *Appl. Phys. Lett.* **90**, 252906 (2007).

Chu, Y.-H., Martin, L. W., Holcomb, M. B., Gajek, M., Han, S. J., He, Q., Balke, N., Yang, C. H., Lee, D., Hu, W., Zhan, Q., Yang, P. L., Fraile-Rodríguez, A., Scholl, A., Wang, S. X., Ramesh, R. Electric-field control of local ferromagnetism using a magnetoelectric multiferroic. *Nat. Mater*. **7**, 478–482 (2008).

Chu, Z. Shi, H., Shi, W., Liu, G., Wu, J., Yang, J. & Dong, S. Enhanced resonance magnetoelectric coupling in (1-1) connectivity composites. *Adv. Mater*. 1606022 (2017).

Coeuré, P., Guinet, F., Peuzin, J. C., Buisson, G. & Bertaut, E. F. Ferroelectric properties of hexagonal orthomanganites of yttrium and rare earths. *Proc. Int. Meet. Ferroelectr.* (Prague, 1966).

Cohen, R. E. Origin of ferroelectricity in perovskite oxides. *Nature* **358**, 136–138 (1992a).

Cohen, R. E. & Krakauer, H. Electronic-structure studies of the differences in ferroelectric behavior of $BaTiO_3$ and $PbTiO_3$. *Ferroelectrics* **136**, 65–83 (1992b).

Cohen, R. E. Theory of ferroelectrics: A vision for the next decade and beyond. *J. Phys. Chem. Solids* **61**, 139–146 (2000).

Comes, R., Liu, H., Khokhlov, M., Kasica, R., Lu, J. & Wolf, S. A. *Nano Lett*. **12**, 2367 (2012).

Cox, D. E., Noheda, B., Shirane, G., Uesu, Y., Fujishiro, J. & Yamada, Y. *Appl. Phys. Lett.* **79**, 400 (2001).

Cullity, B. D. *Elements of X-Ray Diffraction*, 2nd ed. (Reading, MA: Addison-Wesley, 1978).

Cullity, B. D. & Graham, C. D. *Introduction to magnetic materials*. 2nd edn.,Hanzo, L. ed. (Hoboken, NJ: A John Wiley & Sons, Inc.) pp 141-83 (2009).

Czichos H., Saito T. & Smith L. *Springer Handbook of Metrology and Testing*, 2nd ed. (Heidelberg: Springer-Verlag, 2011).

da Câmara Santa Clara Gomes, T., De La Torre Medina, J., Lemaitre, M. & Piraux, L. *Nanoscale Research Lett*. **11**, 466 (2016a).

da Câmara Santa Clara Gomes, T., De La Torre Medina, H., Velazquez-Galvan, Y. G., Martınez-Huerta, J. M., Encinas, A. & Piraux, L. *J. Appl. Phys*. **120**, 043904 (2016b).

da Câmara Santa Clara Gomes, T., De La Torre Medina, H., Velazquez-Galvan, Y. G., Martınez-Huerta, J. M., Encinas, A. & Piraux, *IEEE Transactions on Magnetics* **53**, 7959106 (2017).

Damodaran, A. R., Clarkson, J. D., Hong, Z., Liu, H., Yadav, A. K., Nelson, C. T., Hsu, S.-L., McCarter, M. R., Park, K.-D., Kravtsov, V., Farhan, A., Dong, Y., Cai, Z., Zhou, H., Aguado-Puente, P., García-Fernández, P., Íñiguez, J., Junquera, J., Scholl, A., Raschke, M. B., Chen, L.-Q., Fong, D. D., Ramesh, R. & Martin, L. W. *Nat. Mater.* **16**, 1003 (2017)

Darques, M., Encinas, A., Vila, L. & Piraux, L. *J. Phys. D: Appl. Phys*. **37**, 1411 (2004).

Dawber, M., Rabe, K. & Scott, J. F. Physics of ferroelectric thin film oxides. *Rev. Mod. Phys.* **77**, 1083-1130 (2005).

De Groot, J., Mueller, T., Rosenberg, R. A., Keavney, D. J., Islam, Z., Kim, J. W. &Angst, M. Charge order in LuFe2O4: an unlikely route to ferroelectricity. *Phys. Rev. Lett*. **108**, 187601 (2012).

De La Torre Medina, J. *Magnetic Anisotropy and Dipolar Interaction in Arrays of Magnetic Nanowires*. PhD thesis. (Université catholique de Louvain, Louvain-la-Neuve, Belgium, 2009).

Dekkers, M., Nguyen, M. D., Steenwelle, R., te Riele, P. M., Blank, D. H. A. & Rijndersa, G. *Appl. Phys. Lett*. **95**, 012902 (2009).

Deng, C., Zhang, Y., Ma, J., Lin, Y. & Nan, C.-W. Magnetic-electric properties of epitaxial multiferroic NiFe2O4–BaTiO3 heterostructure. *J. Appl. Phys*. **102**, 074114 (2007).

Deng, C., Zhang, Y., Ma, J., Lin, Y. & Nan, C.-W. *Acta Mater*. **56** 405-12 (2008).

Deng, C. Y., Zhang, Y., Ma, J., Lin, Y. H. & Nan, C. W. Magnetoelectric effect in multiferroic heteroepitaxial BaTiO3-NiFe2O4 composite thin films. *Acta Materialia* **56**, 405–412 (2008).

Dey, S. K., Budd, K. D., Payne, D. A. *IEEE Trans UFFC* **35**, 80 (1988).

Dmytriiev, O., Al-Jarah, U. A. S., Gangmei, P., Kruglyak, V. V., Hicken, R. J., Mahato, B. K., Rana, B., Agrawal, M., Barman, A., Mátéfi-Tempfli, M., Piraux, L. & Mátéfi-Tempfli, S. Static and dynamic magnetic properties of densely packed magnetic nanowire arrays. *Phys. Rev. B* **87**, 174429 (2013).

Dong, S. X., Li, J. F. & Viehland, D. *Appl. Phys. Lett.* **83**, 2265 (2003).

Dong, S., Li, J.-F. & Viehland, D. *J. Appl. Phys*. **95** 2625-30 (2004).

Dong, S., Liu, J.-M., Cheong, S.-W. & Ren, Z. *Adv. Phys*. **64**, 519-626 (2015).

Duan, C.-G., Jaswal, S. S. & Tsymbal, E. Y. Predicted magnetoelectric effect in Fe/BaTiO3 multilayers: ferroelectric control of magnetism. *Phys. Rev. Lett.* **97**, 047201 (2006).

Dzyaloshinskii, I. E. A thermodynamic theory of "weak" ferromagnetism of antiferromagnetics. *J. Phys. Chem. Solids* **4**, 241–255 (1958).

Dzyaloshinskii, I. E.. On the magneto-electrical effect in antiferromagnets. *Sov. Phys. JETP*, **10**, 628–629, (1960).

Ebihara, K., Takahashi, H. & Nagayama, M., *J. Met. Finish. Soc. Jap*. **33**, 4 (1982).

Ederer, C. & Spaldin, N. A. Weak ferromagnetism and magnetoelectric coupling in bismuth ferrite. *Phys. Rev. B* **71**, 060401 (2005).

Ederer, C. & Spaldin, N. A. Electric-field-switchable magnets: the case of BaNiF4. *Phys. Rev. B* **74**, 020401 (2006).

Eerenstein, W., Mathur, N. D. & Scott, J. F. *Nature* **442**, 759-765 (2006).

Elbaile, L., Crespo, R. D., Vega, V. & Garcia, J. A. Magnetostatic interaction in Fe-Co nanowires. *J. Nanomater*. **2012**, 1 (2012).

Engin, R. & Fitzgerald, A. G. *J. Mater. Sci*. **8**, 169 (1973).

Encinas-Oropesa, A., Demand, M., Piraux, L., Huynen, I. & Ebels, U. Dipolar interactions in arrays of nickel nanowires studied by ferromagnetic resonance *Phys. Rev. B* **63**, 104415 (2001).

Esmaeily, A. S., Venkatesan, M., Razavian, A. S. & Coey, J. M. D. Diameter-modulated ferromagnetic CoFe nanowires. *J. Appl. Phys*. **113**, 17A327 (2013).

Fang, Z., Lu, S. G., Li, F., Datta, S., Zhang, Q. M. & El Tahchi, M. *Appl. Phys. Lett*. **95**, 11-13 (2009).

Fe, L., Norga, G. J., Wouters, D. J., Maes, H. E. & Maes, G. *J. Mater. Res*. **19**, 2499 (2001).

Feng, M., Wang, J.-J., Hu, J.-M., Wang, J., Ma, J., Li, H.-B., Shen, Y., Lin, Y.-H., Chen, L.-Q. & Nan, C.-W. Optimizing direct magnetoelectric coupling in Pb(Zr,Ti)O3/Ni multiferroic film heterostructures. *Appl. Phys. Lett*. **106**, 072901 (2015).

Fennie, C. J. & Rabe, K. M. Ferroelectric transition in YMnO3 from first principles. *Phys. Rev. B* **72**, 100103 (2005).

Fennie, C. J. & Rabe, K. M., Magnetic and electric phase control in epitaxial EuTiO3 from first principles. *Phys. Rev. Lett*., **97**, 267602 (2006).

Ferain, E & Legras, R. Nucl. Instrum. *Methods Phys. Res. Sect. B: Beam Interactions with Material and Atoms* **208**, 115-122 (2003).

Fetisov, Y. K. & Srinivasan, G. *Appl. Phys. Lett.* **88**, 143503 (2006).

Fiebig, M., Fröhlich, D., Kohn, K., Leute, St., Lottermoser, Th., Pavlov, V. V. & Pisarev, R. V. Determination of the magnetic symmetry of hexagonal manganites by second harmonic generation. *Phys. Rev. Lett.* **84**, 5620–5623 (2000).

Fiebig, M., Eremenko, V. & Chupis, I. E. Proceedings of the 5th International Workshop on Magnetoelectric Interaction Phenomena in Crystals (Kluwer, Dordrecht 2004).

Fiebig, M. Revival of the magnetoelectric effect. *J. Phys. D: Appl. Phys*. **38**, R123-152 (2005).

Fiebig, M., Lottermoser, T., Meier, D. & Trassin, M. *Nature Reviews Materials* **1**, 16046 (2016).

Fischer, P. & Polomska, M. J., *Phys. C Solid State* **13**, 1931(1980).

Fleisher, R.L. Price, P.B. & Walker, R.M. *Nuclear Tracks in Solids: Principles and Applications*. (Berkley: University of California Press, 1975).

Folen, V. J. Landolt-Börnstein, vol. 3, part 4b, Magnetic and Other Properties of Oxides and Related Compounds, Hellwege, K.-H. & Hellwege, A.M. eds. (Berlin, Heidelberg, New York: Springer, 1970).

Fong, D. D., Stephenson, G. B., Streiffer, S. K., Eastman, J. F., Auciello, O., Fuoss, P. H. & Thompson, C. *Science* **304**, 1650 (2004).

Fong, D. D., Kolpak, A. M., Eastman, J. A., Streiffer, S. K., Fuoss, P. H., Stephenson, G. B., Thompson, C., Kim, D. M., Choi, K. J., Eom, C. B., Grinberg, I. & Rappe, A. M. Stabilization of Monodomain Polarization in Ultrathin $PbTiO_3$ Films. *Phys. Rev. Lett.* **96**, 127601 (2006).

Fournier-Bidoz, S., Kitaev, V., Routkevich, D., Manners, I. & Ozin, G. A. *Adv. Mater*. **16**, 2193- 2196 (2004).

Fu, B., Lu, R., Gao, K., Yang, Y. & Wang, Y. *EPL* **2112**, 27002 (2015).

Fukushima, J., Kodaira, K. & Matsushita, T. *J. Mater. Sci*. **19**, 595 (1984).

Gamburg, Y. D. & Zangari, G. *Theory and Practice of Metal Electrodeposition*. (New York Dordrecht Heidelberg London: Springer, 2011).

Gao, X., Liu, L., Birajdar, B., Ziese, M., Lee, W., Alexe, M. & Hesse, D. *Adv. Funct. Mater*. **19**, 3450-3455 (2009).

Gao, X., Rodriguez, B. J., Liu, L., Birajdar, B., Pantel, D., Ziese, M., Alexe, M. & Hesse, D. Microstructure and properties of well-ordered multiferroic Pb(Zr,Ti)O3/CoFe2O4 nanocomposites *ACS Nano* **4** 1099-107 (2010).

Gao, P., Zhang, Z., Li, M., Ishikawa, R., Feng, B., Liu, H.-J., Huang, Y.-L., Shibata, N., Ma, X., Chen, S., Zhang, J., Liu, K., Wang, E.-G., Yu, D., Liao, L., Chu, Y.-H. & Ikuhara, Y. Possible absence of critical thickness and size effect in ultrathin perovskite ferroelectric films. *Nat. Commun.* **8**, 15549 (2017).

Garcia-Castro, A. C., Spaldin, N. A., Romero, A. H. & Bousquet, E. Geometric ferroelectricity in fluoroperovskites. *Phys. Rev. B* **89**, 104107 (2014).

Gaucher, P., Faure, S. P. & Barboux, P. *Integr. Ferroelectrics* **1**, 353-62 (1992).

George, M., Nair, S. S., Malini, K. A., Joy, P. A. & Anantharaman, M. R. Finite size effects on the electrical properties of sol–gel synthesized CoFe2O4 powders: deviation from Maxwell–Wagner theory and evidence of surface polarization effects. *J. Phys. D: Appl. Phys*. **40**, 1593-602 (2007).

Ghemes, A., Dragos-Pinzaru, O., Chiriac, H., Lupu, N., Grigoras, M., Shore, D., Stadler, B. & Tabakovic, I. *J. Electrochem. Soc*. **164**, D13 (2017).

Ghosez, P. & Rabe, K. M. Microscopic model of ferroelectricity in stress-free $PbTiO_3$ ultrathin films. *Appl. Phys. Lett.* **76**, 2767 (2000).

Glavic, A., Becher, C., Voigt, J., Schierle, E., Weschke, E., Fiebig, M. & Brückel, T. Stability of spin-driven ferroelectricity in the thin-film limit: coupling of magnetic and electric order in multiferroic TbMnO3 films. *Phys. Rev. B* **88**, 054401 (2013).

Gong, W., Li, J.-F., Chu, X., Gui, Z. & Li L. *Jpn. J. Appl. Phys.* **42**, L 1459 (2003).

Gong, W., Li, J. F., Chu, X. C. & Li, L. T. *J. Eur. Ceram. Soc*. **24**, 2977 (2004).

Greve, H., Woltermann, E., Quenzer, H.-J., Wagner, B. & Quandt, E. Giant magnetoelectric coefficients in (Fe90Co10)78Si12B10-AlN thin film composites. *Appl. Phys. Lett*. **96**, 182501 (2010).

Gruverman, A., Auciello, O. & Tokumoto, H. *Annu. Rev. Mater. Sci*. **28**, 101 (1998).

Gust, M. C., Momoda, L. A. & MeCartney, M. L. Microstructure and crystallization behavior of sol-gel prepared BaTiO3 thin films. *Mater. Res. Soc. Symp. Proc*. **346,** 649–653 (1994).

Haeni, J. H. Irvin, P., Chang, W., Uecker, R., Reiche, P., Li, Y. L., Choudhury, S., Tian, W., Hawley, M. E., Craigo, B., Tagantsev, A. K., Pan, X. Q., Streiffer, S. K., Chen, L. Q., Kirchoefer, S. W., Levy, J. & Schlom, D. G. Room-temperature ferroelectricity in strained SrTiO3. *Nature* **430**, 758–761 (2004).

Han, J .K., Kim, J. & Bu, S. D. *J. Appl. Phys*. **112**, 034106 (2012).

He, H.-C., Ma, J., Wang, J. & Nan, C.-N. *J. Appl. Phys*. **103**, 034103 (2008).

He, H. C., Ma, J., Lin, Y. H. & Nan, C. W. Enhanced magnetoelectric properties in Pb(Zr,Ti)O3-CoFe2O4 layered thin films with LaNiO3 as a buffer layer. *J. Phys. D: Appl. Phys*. **42**, 095008 (2009).

Heron, J. T., Schlom, D. G. & Ramesh, R. Electric field control of magnetism using BiFeO3-based heterostructures. *Appl. Phys. Rev*. **1**, 021303 (2014a).

Heron, J. T., Bosse, J. L,, He, Q., Gao, Y., Trassin, M., Ye, L., Clarkson, J. D., Wang, C., Liu, J., Salahuddin, S., Ralph, D. C., Schlom, D. G., Iñiguez, J., Huey, B. D. & Ramesh, R. Deterministic switching of ferromagnetism at room temperature using an electric field. *Nature* **516**, 370–373 (2014b).

Hill, N. A. *J. Phys. Chem. B* **104**, 6694 (2000).

Hill, N. A. Density functional studies of multiferroic magnetoelectrics, *Annu.Rev. Mater. Res*. **32**, 1–37 (2002).

Hoffmann, S., Hasenkox, U., Waser, R., Jia, C. L & Urban, K. *Mater. Rec. Soc. Symp. Proc*. **479**, 9 (1997).

Hong, S., Woo, J., Shin, H., Jeon, J. U., Pak, Y. E., Colla, E. L., Setter, N., Kim, E. & No, K. *J. Appl. Phys*. **89**, 1377-1386 (2001).

Hu, J.-M., Duan, C.-G., Nan, C.-W. & Chen, L.-Q. *NPJ Computational Materials* **3**, 18 (2017).

Hua, Z. H., Chen, R. S., Li, C. L., Yang, S. G., Lu, M., Gu, B. X. & Du, Y. W., *J. Alloys Compd*. **427**, 199-203 (2007).

Hua, Z., Yang, P., Huang, H., Wan, J., Yu, Z.-Z., Yang, S., Lu, M., Gu, B. & Du, Y. *Mater. Chem. Phys.* **107**, 541-546 (2008).

Hur, N., Park, S., Sharma, P. A., Ahn, J. S., Guha, S., Cheong, S. W. Electric polarization reversal and memory in a multiferroic material induced by magnetic fields. *Nature* **429**, 392–395 (2004).

Hutchinson, J. W. & Suo, Z., Hutchinson, J. W., Wu, T. Y. eds. *Advances in applied mechanics*. (New York: Academic, 1991).

Ikeda, N., Ohsumi, H., Ohwada, .K, Ishii, K., Inami, T., Kakurai, K., Murakami, Y., Yoshii, K., Mori, S., Horibe, Y. & Kitô, H., Ferroelectricity from iron valence ordering in the charge-frustrated system LuFe2O4. *Nature* **436**, 1136–1138 (2005).

Ishidate, T., Abe, S., Takahashi, H., Moeri, N. Phase diagram of $BaTiO_3$. *Phys. Rev. Lett.* **78**, 2397 (1997).

Islam, R. A. & Priya, S. *c*

Islam, R. A. & Priya, S. *J. Mater. Sci* **44**, 5935-5938 (2009).

Imai, A., Cheng, X., Xin, H. L., Eliseev, E. A., Morozovska, A. N., Kalinin, S. V., Takahashi, R., Lippmaa, M., Matsumoto Y. & Nagarajan, V. *ACS Nano* **7**, 11079 (2013).

Jaffe, B., Cook Jr, W. R. & Jaffe, H. *Piezoelectric Ceramics*. (London, UK: Academic Press, 1971).

Jenkins, R. & Snyder, R. L. *Introduction to X-Ray Powder Diffractometry*. (New York, NY: John Wiley, 1996).

Jesse, S., Baddorf, A. P. & Kalinin *Appl. Phys. Lett*. **88**, 062908 (2006).

Jessensky, O., Muller, F. & Gosele, U. *J. Electrochem. Soc*. **145**, 3735-3740 (1998).

Ji, G., Tang, S., Xu, B., Gu, B. & Du, Y. *Chem. Phys. Lett*. **379**, 484-489 (2003)

Ji, R., Cao, C., Chen, Z. & Yao, R Synthesis of crystalline $CoFe_x$ nanowire arrays through high voltage pulsed electrochemical deposition. *J. Magn. Magn. Mat***. 363**, 95 (2014).

Ji, Y & Lin, Y. Nanostructural Thin Film Development with Chemical Solution Deposition. In: Lin, Y. & Chen, X., editors. Advanced Nano Deposition Methods. (Wiley-VCH Verlag GmbH &Co., 159-177, 2016).

Jian, G., Shao, H., Zhang, C., Yan, C., Zhao, N., Song, B. & Wong, C. P. *J. Magn. Magn. Mater*. **449**, 263 (2018).

Jing, P., Du, J., Jin, C., Wang, J., Pan, L., Li, J. & Liu, Q. *J. Mater. Sci*. **51**, 885-892 (2016).

Johnson, S. H., Finkel, P., Leaffer, O. D., Nonnenmann, S. S., Bussmann, K. & Spanier, J. E. *Appl. Phys. Lett*. **99**, 182901 (2011).

Johnson, R. D., Chapon, L. C., Khalyavin, D. D., Manuel, P., Radaelli, P. G. & Martin, C. *Phys. Rev. Lett*. **108** 067201 (2012).

Johnson, R. D. & Radaelli, P. G. Diffraction studies of multiferroics. *Annu. Rev. Mater. Res*. **44**, 269–298 (2014).

Jonker, G. H. Analysis of the semiconducting properties of cobalt ferrite. *J. Phys. Chem. Solids* **9**, 165-75 (1959).

Jooss, C., Wu, L., Beetz, T., Klie, R. F., Beleggia, M., Schofield, M. A., Schramm, S., Hoffmann, J., & Zhu, Y. Polaron melting and ordering as key mechanisms for colossal resistance effects in manganites. *Proc. Natl Acad. Sci. USA* **104**, 13597–13602 (2007).

Jung, J.-S., Lim, J.-H., Choi, K.-H., Oh, S.-L., Kim, Y.-R., Lee, S.-H., Smith, D.A., Stokes, K. L., Malkinski, L. & O'Connor, C. J. *J. Appl. Phys.* **97**, 10F306 (2005).

Junguera, J & Ghosez, P. *Nature* **422**, 506 (2003).

Jurca, I. S., Viart, N., Mény, C., Ulhaq-Bouillet, C., Panissod, P. & Pourroy, G. Structural study of $CoFe_2/CoFe_2O_4$ multilayers. *Surface Science* **529**, 215 (2003a).

Jurca, I. S., Meny, C., Viart, N., Ulhaq-Bouillet, C., Panissod, P. & Pourroy, G. Growth, structure and morphology of $CoFe_2/CoFe_2O_4$ multilayers. *Thin Solid Films* **444**, 58-63 (2003b).

Kalpat, S. & Uchino, K. *J. Appl. Phys*. **90**, 2703 (2001).

Katsura, H., Nagaosa, N. & Balatsky, A. V. Spin current and magnetoelectric effect in noncollinear magnets. *Phys. Rev. Lett.* **95**, 057205 (2005).

Kawai, S. & Ueda, R. *J. Electrochem. Soc*. **122**, 32-36 (1975).

Khomskii, D. *Physics* **2**, 20 (2009).

Kim, B., Park, S., McCarthy, T. J. & Russell, T. P. *Small* **3**, 1869-1872 (2007).

Kim, J., Yang, S. A., Choi, Y. C., Han, J. K., Jeong, K. O., Yun, Y. J., Kim, D. J., Yang, S. M., Yoon, D., Cheong, H., Chang, K.-S., Noh, T. W. & Bu, S. D. *Nano Lett*. **8**, 1813-1818 (2008).

Kim, Y. S., Kim, D. H., Kim, J. D., Chang, Y. J., Noh, T. W., Kong, J. H., Char, K., Park, Y. D., Bu, S. D., Yoon, J.-G. & Chung, J.-S. Critical thickness of ultrathin ferroelectric $BaTiO_3$ films. *Appl. Phys. Lett*. **86**, 102907 (2005).

Kimura, T., Goto, T., Shintani, H., Ishizaka, K., Arima, T. & Tokura, Y. *Nature* **426**, 55 (2003).

Kimura, T. Spiral magnets as magnetoelectrics. *Annu. Rev. Mater. Res*. **37**, 387–413 (2007).

Kingon, A. I. & Srinivasan, S. *Nat. Mater*. **4**, 233 (2005).

Kirchhof, C., Krantz, M., Teliban, I., Jahns, R., Marauska, S., Wagner, B., Knöchel, R., Gerken, M., Meyners, D. & Quandt, E. Giant magnetoelectric effect in vacuum. *Appl. Phys. Lett*. **102**, 232905 (2013).

Klee, M., Eusemann, R., Waser, R. & BrandH. Van Hal, W. *J. Appl. Phys*. **72**, 1566 (1992).

Kozuka, H. Stress Evolution and Cracking in Sol-Gel-Derived Thin Films. In: Klein, L., editor. Handbook of Sol-Gel Science and Technology. Switzerland: Springer International Publishing (2016).

Kretschmer, R. & Binder, K. *Phys. Rev. B* **20**, 1065 (1979).

Krishnan, R. & Thompson, C. V. *Adv. Mater*. **19**, 988-992 (2007).

Kumar, A., Scott, J. F., Katiyar, R. S., *Appl. Phys. Lett*. **99**, 062504 (2011).

Lahtinen, T. H. E., Franke, K. J. A. & van Dijken, S. Electric-field control of magnetic domain wall motion and local magnetization reversal. *Sci. Rep*. **2**, 258 (2012).

Lage, E., Urs, N. O., Röbisch, V., Teliban, I., Knöchel, R., Meyners, D., McCord, J. & Quandt, E. Magnetic domain control and voltage response of exchange biased magnetoelectric composites. *Appl. Phys. Lett*. **104**, 132405 (2014).

Landau, L. D. & Lifshitz, E. M. *Electrodynamics of Continuous Media*, 2nd edn. (Oxford, UK: Pergamon Press, 1984).

Lakeman, C. D. E., Xu, Z. & Payne, D. A. *J. Mater. Res*. **10**, 2042 (1995).

Lazenka V V, Zhang G, Vanacken J, Makoed I I, Ravinski A F and Moshchalkov V V J. Phys. D: Appl, Phys. 45 125002 (2012).

Lebeugle, D., Colson, D., Forget, A., Viret, M., Bonville, P., Marucco, J. F. & Fusil, S., *Phys. Rev. B* **76**, 024116 (2007).

Lee, J. H., Fang, L., Vlahos, E., Ke, X., Jung, Y. W., Kourkoutis, L. F., Kim, J. W., Ryan, P. J., Heeg, T., Roeckerath, M., Goian, V., Bernhagen, M., Uecker, R., Hammel, P. C., Rabe, K. M., Kamba, S., Schubert, J., Freeland, J. W., Muller, D. A., Fennie, C. J., Schiffer, P., Gopalan, V., Johnston-Halperin, E. & Schlom, D. G. A strong ferroelectric ferromagnet created by means of spin–lattice coupling. *Nature* **466**, 954–958 (2010).

Lee, W., Ji, R., Gosele, U. & Nielsch, K. *Nat. Mater*. **5**, 741-747 (2006).

Lee, W., Nielsch, K. & Gosele, U. *Nanotech*. **18**, 475713 (2007).

Lee, W., Han, H., Lotnyk, A., Schubert, M. A., Senz, S., Alexe, M., Hesse, D., Baik, S. & Gösele *Nat. Nanotech*. **3**, 402 (2008).

Levin, I., Li, J., Slutsker, J. & Roytburd, L. *Adv. Mater*. **18**, 2044 (2006).

Li, A. P., Müller, F., Birner, A., Nielsch, K. & Gösele, U. *J. Appl. Phys*. **84**, 6023 – 6026 (1998a).

Li, F., Zhang, L. & Metzger, R. M. *Chem. Mater*. **10**, 2470-2480 (1998b).

Li, J., Wang, J., Wuttig, M., Ramesh, R., Wang, N., Ruette, B., Pyatakov, A. P., Zvezdin, A. K. & Viehland, D., *Appl. Phys. Lett*. **84**, 5261 (2004).

Li, J., Levin, I., Slutsker, J., Provenzano, V., Schenck, P. K., Ramesh, R., Ouyang, J. & Roytburd, A. L. *Appl. Phys. Lett*. **87**, 072909 (2005a).

Li, Y. L., Cross, L. E. & Chen, L. Q. *J. Appl. Phys*. **98**, 064101 (2005b).

Li, Y. X., Wang, Z. C., Yao, J. J., Yang, T. N., Wang, Z. G., Hu, J. M., Chen, C. L., Sun, R., Tian, Z. P., Li, J. F., Chen, L. Q. & Viehland, D. Magnetoelectric quasi-(0-3) nanocomposite heterostructures. *Nature Communications* **6**, 6680 (2015a).

Li, J., Li, J.-F., Yu, Q., Chen, Q. N. & Xie, S. *J. Materiomics* **1**, 3-21 (2015b).

Liang, W., Li, Z., Bi, Z., Nan, T., Du, H., Nan, C.-W., Chen, C., Jia, Q. & Lin, Y. Role of the interface on the magnetoelectric properties of BaTiO3 thin films deposited on polycrystalline Ni foils. *J. Mater. Chem.* C **2**, 708–714 (2014).

Lichtensteiger, C., Triscone, J.-M., Junquera, J. & Ghosez, P. Ferroelectric and Tetragonality in Ultrathin $PbTiO_3$ Films. *Phys. Rev. Lett.* **94**, 047603 (2005).

Lide, D. R. *CRC Handbook of Chemistry and Physics*. 86th ed. (Boca Raton, FL: Taylor and Francis, 2006).

Lilienblum, M., Lottermoser, T., Manz, S., Selbach, S. M., Cano, A. & Fiebig, M., Ferroelectricity in the multiferroic hexagonal manganites. *Nat. Phys.* **11**, 1070–1074 (2015).

Liu, N. W., Datta, A., Liu, C. Y. & Wang, Y. L. *Appl. Phys. Lett*. **82**, 1281-1283 (2003).

Liu, G., Nan, C.-W., Xu, Z. K. & Chen, H. *J Phys. D: Appl. Phys*. **38**, 2321 (2005).

Liu, G. & Nan, C.-W. & Sun, J. Coupling interaction in nanostructured piezoelectric/magnetostrictive multiferroic complex films. *Acta Mater*. **54** 917 (2006).

Liu, M., Li, X., Imrane, H., Chen, Y., Goodrich, T., Cai, Z., Ziemer, K. S., Huang, J. Y. & Sun, N. X. *Appl. Phys. Lett*. **90**, 152501 (2007).

Liu, B., Sun, T., He, J. & Dravid, V. P. Sol-Gel-Derived Epitaxial Nanocomposite Thin Films with Large Sharp Magnetoelectric Effect. *ACS Nano* **4**, 6836 (2010).

Liu, X., Li, M., Hu, Z., Zhu, Y., Dong, S. & Zhao, X. *Mater. Lett*. **82**, 57-60 (2012a).

Liu, X. L., Li, M. Y., Wang, J., Hu, Z. Q., Zhu, Y. D. & Zhao, X. Z. *Appl. Phys. A* **108**, 829-834 (2012b).

Livage, J., Henry, M. & Sanchez, C. *Prog. Solid St. Chem*. **18**, 259 (1988).

Livage, J., Henry, M., Jolivet, J. P. & Sanchez, C. Chemical synthesis of fine powders. *Mater. Res. Soc. Bull*. **15**, 18–25 (1990).

Lobo, R. P. S. M., Mohallem, N. D. S. & Moreira, R. L. Grain-size effects on diffuse phase transitions of sol-gel prepared barium titanate ceramics. *J. Am. Ceram. Soc*. **78**, 1343-6 (1995).

Londoño-Calderón, C. L., Moscoso-Londoño, O., Muraca, D., Arzuza, L., Carvalho, P., Pirota, K. B., Knobel, M., Pampillo, L. G. & Martínez-García, R. *Nanotechnology* **28**, 245605 (2017).

Lorenz, M., Hirsch, D., Patzig, C., Hoche, T., Hohenberger, S., Hochmuth, H., Lazenka, V., Temst, K. & Grundman, M. *ACS Appl. Mater. Interfaces* **9**, 18956 (2017).

Lottermoser, T., Lonkai, T., Amann, U., Hohlwein, D., Ihringer, J. & Fiebig, M. *Nature* **430**, 541 (2004).

Lou, J., Reed, D., Pettiford, C., Liu, M., Han, P., Dong, S. & Sun, N. X. Giant microwave tunability in FeGaB/lead magnesium niobite-lead titanate multiferroic composites. *Appl. Phys. Lett.* **92**, 262502 (2008).

Lu, R. E., Chang, K. G., Fu, B., Shen, Y. J., Xu, M. W., Yang, S., Song, X. P., Liu, M. & Yang, Y. D. *J. Mater. Chem. C* **2**, 8578-8584 (2014).

Luo, H., Yang, H., Bally, S. A., Ugurlu, O., Jain, M., Hawley, M. E., McCleskey, T. M., Burrell, A. K., Bauer, E., Civale, L., Holesinger, T. G. & Jia, Q. *J. Am. Chem. Soc*. **129**, 14132 (2007).

Luo, Y., Szafraniak, I., Zakharov, N., Nagarajan, V., Seinhart, M, Wehrspohn, R. B., Wendorff, J. H., Ramesh, R. & Alexe, M. *Appl. Phys. Lett*. **83**, 440 (2003).

Ma, Y. G., Cheng, W. N., Ning, M. & Ong, C. K. Magnetoelectric effect in epitaxial Pb(Zr0.52Ti0.48)O3/La0.7Sr0.3MnO3 composite thin film. *Applied Physics Letters* **90**, 152911 (2007a).

Ma, J., Shi, Z. & Nan, C. W. Magnetoelectric properties of composites of single Pb (Zr,Ti)O3 rods and Terfenol-D/Epoxy with a single-period of 1-3-type structure. *Adv. Mater*. **19**, 2571–2573 (2007b).

Ma, J., Hu, J. M., Li, Z. & Nan, C.-W. *Adv. Mater*. **23**, 1062 (2011).

MacManus-Driscoll, J. L., Zerrer, P., Wang, H. Y., Yang, H., Yoon, J., Fouchet, A., Yu, R., Blamire, M. G. & Jia, Q. X. *Nat. Mater*. **7** 314 (2008).

Maki, K., Soyama, N., Mori, S. & Ogi, K. Lowering of crystallization temperature of sol-gel derived Pb(Zr, Ti)O_3 thin films. *Integrated Ferroelectrics* **30**, 193-202 (2000)

Maksymovych, P. Huijben, M., Pan, M., Jesse, S., Balke, N., Chu, Y.-H., Chang, H. J., Borisevich, A. Y., Baddorf, A. P., Rijnders, G., Blank, D. H. A., Ramesh, R. & Kalinin, S. V. Ultrathin limit and dead-layer effects in local polarization switching of $BiFeO_3$. *Phys. Rev. B.* **85**, 014119 (2012).

Mallet, J., Yu-Zhang, K., Mátéfi-Tempfli, S., Mátéfi-Tempfli, M. & Piraux, L. *J. Phys. D: Appl. Phys*, **38**, 909 (2005).

Martí, X., Sánchez, F., Hrabovsky, D., Fabrega, L., Ruyter, A., Fontcuberta, J. & Laukhin, V. Exchange biasing and electric polarization with YMnO3. *Appl. Phys. Lett*. **89**, 032510 (2006).

Martin, L. W., Crane, S. P., Chu, Y.-H., Holcomb, M. B., Gajek, M., Huijben, M., Yang, C.-H., Balke, N. & Ramesh, R. *J. Phys.: Condens. Matter*, **20**, 434200 (2008).

Martinez, R., Kumar, A., Palai, R., Srinivasan, G. & Katiyar, R. S. Observation of strong magnetoelectric effects in Ba0.7Sr0.3TiO3/La0.7Sr0.3MnO3 thin film heterostructures. *J. Appl. Phys.* **111**, 104104 (2012).

Maruyama, K., Kondo, M., Singh, S. K. & Ishiwara, H. *FUJITSU Sci. Tech. J*. **43**, 502-507 (2007).

Masuda, H. & Fukuda, K. *Science* **268**, 1466–1468 (1995).

Masuda, H.; Yamada, H; Satoh, M.; Asoh, H.; Nakao, M. & Tamamura, T. *Appl. Phys. Lett*., **71**, 2770-2772 (1997a).

Masuda, H., Hasegwa, F. & Ono, S. J. Electrochem. Soc. 144, L127-L130 (1997b).

Mátefi-Tempfli, S. *Leading Edge Nanotechnology Research Developments: Nanostructures Grown Via Electrochemical Template Methods*. Nanotechnology Science and Technology (New York: Nova Science, 2008).

Mátefi-Tempfli, S., Mátefi-Tempfli, M., Vlad, A., Antohe, V. & Piraux, L. *J. Mater. Sci.: Mater. Electron.*, **20**, 249-254 (2009a).
Mátéfi-Tempfli, S., Mátéfi-Tempfli, M. & Piraux, L. *Appl. Phys. A*. **96,** 603-608 (2009b).
Mattox, D. M. *Handbook of Physical Vapor Deposition (PVD) Processing*. (New Jersey: Noyes Publications, 1998).
Mattsson, L., Le Page, Y. H. & Ericson, F. *Thin Solid Films* **198**, 149-156 (1991).
McDannald, A., Staruch, M., Sreenivasulu, G., Cantoni, C., Srinivasan G. & Jain, M. *Appl. Phys. Lett.* **102**, 122905 (2013).
McDannald, A., Ye, L., Cantoni, C., Sreenivasulu, G., Srinivasan G., Huey, B D. & Jain, M. *Nanoscale* **9**, 3246-3251 (2017).
Megaw, H. D. Origin of ferroelectricity in barium titanate and other perovskite-type crystals. *Acta Crystallogr*. **5**, 739–749 (1952).
Mehta, R. R., Silverman, B. D. & Jacobs, J. T. Depolarization fields in thin ferroelectric films. *J. Appl. Phys.* **44**, 3379 (1973).
Menoret, C., Kiat, J. M., Dkhil, B., Dunlop, M., Dammak, H. & Hernandez, O. Structural evolution and polar order in Sr1-xBaxTiO3. *Phys. Rev. B* **65**, 224104 (2002).
Meyer, B., Vanderbilt, B.D., Ab initio study of ferroelectric domain walls in PbTiO3. *Phys. Rev. B* **65**, 104111 (2002).
Mitsui, T. Landolt-Börnstein, vol. 3, part 16a1, Ferroelectrics and Related Substances, Hellwege, K.-H. & Hellwege, A.M. eds. (Berlin, Heidelberg, New York: Springer, 1981).
Mishina, E.D., Vorotilov, K. A., Vasil'ev, V. A., Sigov, A. S., Ohta, N. & Nakabayashi, S. *J. Exp. Theor. Phys*. **95**, 502 (2002).
Molegraaf, H. J. A., Hoffman, J., Vaz, C. A. F., Gariglio, S., van der Marel, D., Ahn, C. H. & Triscone, J.-M. Magnetoelectric effects in complex oxides with competing ground states. *Adv. Mater*. **21**, 3470–3474 (2009).
Moreau, J. M., Michel, C., Gerson, R. & James, W. J., *J. Phys. Chem. Solids* **32** 1315 (1971).
Mori, K & Wuttig, M. *Appl. Phys. Lett.* **81**, 100-101 (2002).
Morrison, F. D., Luo, Y., Szafraniak, I., Nagarajan, V., Wehrspohn, R. B., Steinhart, M., Wendorff, J. H., Zakharov, N. D., Mishina, E. D., Vorotilov, K. A., Sigov, A. S., Nakabayashi, S., Alexe, M., Ramesh, R. & Scott, J. F. Rev. *Adv. Mater. Sci.* **4**, 114-122 (2003).
Mostovoy, M. Ferroelectricity in spiral magnets. *Phys. Rev. Lett*. **96**, 067601 (2006).
Muench, F., Sun, L., Kottakkat, T., Antoni, M., Schaefer, S., Kunz, U., Molina-Luna, L., Duerrschnabel, M., Kleebe, H.-J., Ayata, S., Roth, C. & Ensinger, W., *ACS Appl. Mater. Interfaces* **9**, 771 (2017).
Murphy, S. R. & Rao, T. S. *Phys. Status Solidi* **90**, 631 (1985).
Myung, N. V., Lim, J., Fleurial, J.-P., Yun, M., West, W. & Choi, D. *Nanotech*. **15**, 833-838 (2004).
Nagarajan, V., Prasertchoung, S., Zhao, T., Zheng, H., Ouyang, J., Ramesh, R., Tian, W., Pan, X. Q., Kim, D. M., Eom, C. B., Kohlstedt, H. & Waser, R. *Appl. Phys. Lett*. **84**, 5225-5227 (2004).
Nan, C.-W. Magnetoelectric effects in composites of piezoelectric and piezomagnetic phases. *Phys. Rev. B* **50**, 6082 (1994).
Nan, C.-W., Liu, G., Lin, Y. & Chen, H. Magnetic-field-induced electric polarization in multiferroic nanostructures. *Phys. Rev. Lett*. **94**, 197203 (2005).
Nan, C.-W., Bichurin, M. I., Dong, S., Viehland, D. & Srinivasan, G. *J. Appl. Phys*. **103**, 031101 (2008).
Nan, C.-W. *Magnetoelectricity in Composites*. Bichurin, M. I. & Viehland, D. eds. (Singapore: Pan Stanford Publishing Pte. Ltd., 2012).
Narayanan, T. N., Mandal, B. P., Tyagi, A. K., Kumarasiri, A., Zhan, X., Hahm, M. G., Anantharaman, M. R., Lawes, G. & Ajayan, P. M. *Nano Lett.* **12**, 3025-3030 (2012).

Newnham, R. E., Kramer, J. J., Schulze, W. A. & Cross, L. E. Magnetoferroelectricity in Cr2BeO4. *J. Appl. Phys*. **49**, 6088–6091 (1978).

Nielsch, K., Choi, J., Schwirn, K., Wehrspohn, R. B. & Gosele, U. *Nano Lett*. **2**, 677-680 (2002).

Nishio, K., Yanagishita, T., Hatakeyama, S., Maegawa, H. & Masuda H. *J. Vac. Sci. Technol. B*, **26**, L10-L12 (2008).

Noheda, B., Cox, D. E., Shirane, G., Gonzalo, J. A., Cross, L. E. & Park, S. E. *Appl. Phys. Lett.* **74**, 2059 (1999).

Noheda, B. & Cox, D. E. *Phase Transitions* **79**, 5 (2006).

Nonnenmann, S. S., Gallo, E. M., Coster, M. T., Soja, G. R., Johnson, C. L., Joseph, R. S. & Spanier, J. E. *Appl. Phys. Lett*. **95**, 232903 (2009).

Nonnenmann, S. S., Leaffer, O. D., Gallo, E. M., Coster, M. T. & Spanier, J. E. *Nano Lett.* **10**, 542-546 (2010).

Nourmohammadi, A., Bahrevar, M. A. & Hietschold, M. *J. Alloys Compd*. **473**, 467-472 (2009).

O'Dell, T. H. *The Electrodynamics of Continuous Media* (North-Holland, 1970).

O'Sullivan, J.P. & Wood, G.C. *Proc. Roy. Soc. Lond*., **200**, 5071-5076 (1970).

Ojha, S., Nunes, W. C., Aimon, N. & Ross, C. A. *ACS Nano* **10**, 7657 (2016).

Oh, Y. S., Crane, S., Zheng, H., Chu, Y. H., Ramesh, R. & Kim, K. H. Quantitative determination of anisotropic magnetoelectric coupling in BiFeO3–CoFe2O4 nanostructures *Appl. Phys. Lett*. **97**, 052902 (2010).

Ohgai, T., Hoffer, X., Gravier, L. & Ansermet, J.-Ph. *J. Appl. Electrochem*. **34**, 1007-1012 (2004).

Palneedi, H., Annapureddy, V., Priya, S. & Ryu, J. *Actuators* **5**, 9 (2016).

Palneedi, H. Maurya, D., Kim, G. Y., Annapureddy, V., Noh, M. S., Kang, C. Y., Kim, J. W., Choi, J. J., Choi, S. Y., Chung, S. Y., Kang, S. L., Priya, S. & Ryu, J. Unleashing the full potential of magnetoelectric coupling in film heterostructures. *Adv. Mater*. **29**, 1605688 (2017a).

Palneedi, H., Yeo, H. G., Hwang, G.-T., Annapureddy, V., Kim, J.-W., Choi, J.-J., Trolier-McKinstry, S. & Ryu, J. *APL Mater.* **5**, 096111 (2017b).

Park, C.-S., Ryu, J., Choi, J.-J., Park, D.-S., Ahn, C.-W. & Priya, S. *Jpn. J. Appl. Phys*. **48**, 080204 (2009).

Park, J. H., Jang, H. M., Kim, H. S., Park, C. G. & Lee, S. G. *Appl. Phys. Lett*. **92**, 062908 (2008).

Parker, C. B., Maria, J.-P. & Kingon, A. I. Temperature and thickness dependent permittivity of (Ba,Sr)TiO3 thin films. *Appl. Phys. Lett*. **81**, 340-2 (2002).

Parkhutik, V. P. & Shershulsky, V. I. *J. Phys. D: Appl. Phys.* **25**, 1258-1263 (1992).

Patil, D., Kim, J. H., Chai, Y. S., Nam, J. H., Cho, J. H., Kim, B. I. & Kim, K. H. Large longitudinal magnetoelectric coupling in NiFe2O4-BaTiO3 laminates. *Applied Physics Express* **4**, 073001 (2011).

Pauling, L. *Phys. Rev*. **54**, 899 (1938).

Peng, C. Y., Liu, C. Y., Liu, N. W., Wang, H. H., Datta, A. & Wang, Y. L. *J. Vac. Sci. Technol. B*, **23**, 559-562 (2005).

Pham-Huu, C., Keller, N., Estournes, C., Ehret, G., Greneche, J. M. & Ledoux, M. *J. Phys. Chem. Chem. Phys*. **5**, 3716-3723 (2003).

Periklina, T. M., Smirnovskaya, E. M., Cherkezyan, S. & Lyamina, O. I. *Kristallografiya* **29**, 169 (1984).

Pertsev, N. A., Zembilgotov, A. G. & Tagantsev, A. K. *Phys. Rev. Lett*. **80**, 1988 (1998).

Pettiford, C., Dasgupta, S., Lou, J., Yoon, S. D. & Sun, N. X. *IEEE Trans. Magn.* **43**, 3343 (2007).

Piraux, L., George, J. M., Despres, J. F., Leroy, C., Ferain, E., Legras, R., Ounadjela, K. & Fert, A. *Appl. Phys. Lett*. **65**, 2484 (1994).

Pirouzfar, A. & Ebrahimi, S. A. S. *J. Magn. Magn. Mater*. **370**, 1-5 (2014).

Polli, A. D., Lange, F. F. & Levi, C. G. Metastability of the fluorite, pyrochlore and perovskite structures in the PbO-ZrO2-TiO2 system. *J. Am. Ceram. Soc*. **83**, 873–881 (2000).

Prasad, S. & Paul, A. *Appl. Phys. Lett*. **90**, 233114 (2007).

Pyatakov, A. P. & Zvezdin, A. K. Magnetoelectric and multiferroic media. *Physics-Uspekhi* **55**, 557 (2012).

Qin, L., Jones, G. A., Shen, T. H., Grundy, P. J., Li, W. X. & Abrams, K. *J. Mater. Lett*. **64**, 2685-2687 (2010).

Rabe, K., Dawber, M., Lichtensteiger, C., Ahn, Ch. H. & Triscone, J.-M. *Physics of Ferroelectrics*. 1–14. (Berlin Heidelberg: Springer Verlag, 2007).

Ramazani, A., Almasi-Kashi, M., Golafshan, E. & Arefpour, M. Magnetic behavior of as-deposited and annealed CoFe and CoFeCu nanowire arrays by ac-pulse electrodeposition. *J. Cryst. Growth* **402**, 42 (2014).

Ramesh, R. & Spaldin, N. A. *Nat. Mater*. **6**, 21-29 (2007).

Reaney, I. M., Brooks, K., Klissurska, R., Pawlaczyk, C. & Setter, N. Use of transmission electron microscopy for the characterization of rapid thermally annealed, solution-gel, lead zirconate titanate films. *J. Am. Ceram. Soc.* **77**, 1209–1216 (1994).

Reimer, L. & Kohl, H. *Transmission Electron Microscopy: Physics of Image Formation*. (New York, NY, USA: Springer, 2008).

Robinson, A. P., Burnell, G., Hu, M. & MacManus-Driscoll, J. L. *Appl. Phys. Lett*., **91**, 143123-143125 (2007).

Roeder, R. K. & Slamovich, E. B. Measuring the critical thickness of thin metalorganic precursor films. *J. Mater. Res*. **14**, 2364–2368 (1999).

Rushchanskii, K. Z., Kamba, S., Goian, V., Vaněk, P., Savinov, M., Prokleška, J., Nuzhnyy, D., Knížek, K., Laufek, F., Eckel, S., Lamoreaux, S. K., Sushkov, A. O., Ležaić M., & Spaldin, N. A. *Nat. Mater*. **9**, 649–654 (2010).

Ryu, H., Murugavel, P., Lee, J. H., Chae, S. C. & Noh, T. W. Magnetoelectric effects of nanoparticulate Pb(Zr0.52Ti0.48)O3–NiFe2O4Pb(Zr0.52Ti0.48)O3–NiFe2O4 composite films *Appl. Phys. Lett*. **89**, 102907 (2006).

Ryu, J., Priya, S., Uchino, K & Kim, H. E. *J. Electroceram*. **8**, 107-119 (2012).

Ryu, S., Park, J. H. & Jang, H. M. Magnetoelectric coupling of [00l]- oriented Pb(Zr0.4Ti0.6)O3-Ni0.8Zn0.2Fe2O4 multilayered thin films. *Applied Physics Letters* **91**, 142910 (2007).

Saito, E., Huang, Y., Kosec, M., Bell, A. & Settter, N. *Appl. Phys. Lett*. **65**, 2678 (1994).

Sakai, H., Fujioka, J., Fukuda, T., Okuyama, D., Hashizume, D., Kagawa, F., Nakao, H., Murakami, Y., Arima, T., Baron, A. Q. R., Taguchi, Y. & Tokura, Y., Displacement-type ferroelectricity with off-center magnetic ions in perovskite Sr1 − xBaxMnO3. *Phys. Rev. Lett*. **107**, 137601 (2011).

Sallagoity, D., Elissalde, C., Majimel, J., Berthelot, R., Chung, U. C., Penin, N., Maglione, M., Antohe, V. A., Hamoir, G., Abreu Araujo, F. & Piraux, L., *J. Mater. Chem. C* **3**, 107-111 (2015a).

Sallagoity, D. *Synthèse et étude d'hétérostructures diélectrique/magnétique dans des membranes d'alumine nanoporeuses*, PhD thesis. (Université de Bordeaux, Pessac, France, 2015b).

Sallagoity, D., Elissalde, C., Majimel, J., Maglione, M., Antohe, V. A., Araujo, F. A., Pereira de Sá, P. M., Basov, S. and Piraux, L. Synthesis of dense arrays of multiferroic CoFe2O4–PbZr0.52Ti0.48O3 core/shell nanocables *RSC Advances* **6**, 106716-22 (2016).

Sando, D. Agbelele, A., Rahmedov, D., Liu, J., Rovillain, P., Toulouse, C., Infante, I. C., Pyatakov, A. P., Fusil, S., Jacquet, E., Carrétéro, C., Deranlot, C., Lisenkov, S., Wang, D., Le Breton, J. M., Cazayous, M., Sacuto, A., Juraszek, J., Zvezdin, A. K., Bellaiche, L., Dkhil, B., Barthélémy, A. & Bibes, M. Crafting the magnonic and spintronic response of BiFeO3 films by epitaxial strain. *Nat. Mater*. **12**, 641–646 (2013).

Sando, D., Barthélémy, A. & Bibes, M. BiFeO3 epitaxial thin films and devices: past, present and future. *J. Phys. Condens. Matter* **26**, 473201 (2014).
Sangmanee, M & Maensiri, S. *Appl. Phys. A* **97**, 167-177 (2009).
Schileo, G. *Prog. Solid State Chem.* **41**, 87-98 (2013).
Schmid, H. *Ferroelectrics* **62**, 317 (1994).
Schmid, H. Magnetoelectric effects in insulating magnetic materials. *Proceedings of the SPIE* **4097**, 12-24 (2000).
Schmid, H. *Ferroelectrics* **252**, 41 (2001).
Schmitz-Antoniak, C., Schmitz, D., Borisov, P., de Groot, F. M. F., Stienen, S., Warland, A., Krumme, B., Feyerherm, R., Dudzik, E., Kleemann, W. & Wende, H. Electric in-plane polarization in multiferroic CoFe2O4/BaTiO3 nanocomposite tuned by magnetic fields. *Nature Communications* **4**, 2051 (2013).
Schneller, T., Waser, R., Kosec, M. & Payne, D. *Chemical Solution Deposition of Functional Oxide Thin Films* (Springer-Verlag, Wien, 2013).
Schwartz, R. W., Lakeman, C. D. E. & Payne, D. A. The effects of hydrolysis conditions, and acid and base additions, on the gel-to-ceramic conversion in sol-gel derived PbTiO3. *Mater. Res. Soc. Symp. Proc*. **180**, 335–340 (1990).
Schwartz, R. W., Voigt, J. A., Tuttle, B. A., Payne, D. A. Comments on the effects of solution precursor characteristics and thermal processing conditions on the crystallization behavior of sol-gel derived PZT thin films. *J. Mater. Res*. **12**, 444-456 (1997).
Schwartz, R. W., Schneller, T. & Waser, R. Chemical solution deposition of electronic oxide films. *CR Chimie* **7**, 433–461 (2004).
Schwartz, R. W. & Narayanan, M. *Chemical solution deposition – basic principles, Solution processing of inorganic materials*. Mitzi, D. ed. 33–76. (New York, NY: Wiley, 2009).
Scott, J. F. *Ferroelectric Thin Films and Thin Film Devices, Ferroelectric Ceramics*. Setter, N. & Colla, E. L., eds. (Basel, Boston, Berlin: Birkhäuser Verlag, 1993).
Scott, J. F. Data storage: multiferroic memories. *Nat. Mater*. **6**, 256–257 (2007a).
Scott, J. F. *Science* **315**, 954 (2007b).
Scott, J. F., Fan, H. J., Kawasaki, S., Banys, J., Ivanov, M., Krotkus, A., Macutkevic, J., Blinc, R., Laguta, V. V., Cevc, P., Liu, J. S. & Kholkin, A. L. *Nano Lett.* **8**, 4404 (2008).
Seifert, A., Lange, F. F. & Speck, J. S. Epitaxial growth of $PbTiO_3$ thin films on (001) $SrTiO_3$ from solution precursors. *J. Mater. Res*. **10**, 680–691 (1995).
Sergienko, I. A. & Dagotto, E. Role of the Dzyaloshinskii–Moriya interaction in multiferroic perovskites. *Phys. Rev. B* **73**, 094434 (2006).
Shaw, T. M., Suo, Z., Huang, M., Liniger, E., Laibowitz, R. B. & Baniecki, J. D. *Appl. Phys. Lett*. **75**, 2129 (1999).
Shaw, T. M., Trolier-McKinstry, S. & McIntyre, P. C. *Ann. Rev. Mater. Sci.* **30**, 263-298 (2000).
Shen, J., Cong, J., Chai, Y., Shang, D., Shen, S., Zhai, K., Tian, Y. & Sun, Y., Nonvolatile Memory Based on Nonlinear Magnetoelectric Effect. *Phys. Rev. Appl.* **6**, 021001 (2016).
Shi, D.-W., Javed, K., Ali, S. S., Chen, J.-Y., Li, P.-S., Zhao, Y.-G. & Han, X.-F. *Nanoscale* **6**, 7215-7220 (2014).
Shimada, T., Wang, X., Kondo, Y. & Kitamura, T. *Phys. Rev. Lett*. **108**, 067601 (2012).
Slauter, J. C. *J. Appl. Phys*. **8**, 385 (1937).
Slonczewski, J. C. Origin of magnetic anisotropy in cobalt-substituted magnetite. *Phys. Rev.* **110**, 1341 (1958).
Slutsker, J., Levin, I., Li, J., Artemev, A. & Roytburd, A. L. *Phys. Rev. B* **73** 184127 (2006).
Smit, J. & Wijn, H. P. J. Physical Properties of Ferrites. *Advances in Electronics and Electronic Physics* **6**, 69-136 (1954).
Son, J. Y., Lee, J.-H., Song, S., Shin, Y.-H. & Jang, H. M. *ACS Nano* **7**, 5522-5529 (2013).
Sourmail, T. *Prog. Mater. Sci*. **50**, 816 (2005).
Spaldin, N. & Fiebig, M. *Science* **309**, 391-392 (2005).

Spaldin, N. A., *Introduction to magnetic materials*, 2nd edn. (Cambridg, UK: Cambridge Univ. Press, 2010).

Spanier, J. E., Kolpak, A. M., Urban, J. J., Grinberg, I., Ouyang, L., Yun, W. S., Rappe, A. M. & Park, H. *Nano Lett*. **6**, 735-739 (2006).

Sporn, D., Merklein, S., Grond, W., Seifert, S., Wahl, S. & Berger, A. Sol-gel processing of perovskite films. *Microelectron. Eng*. **29**, 161–168 (1995).

Srinivasan, G., Rasmussen, E. T., Levin, B. J. & Hayes, R. Magnetoelectric effects in bilayers and multilayers of magnetostrictive and piezoelectric perovskite oxides. *Physical Review B* **65**, 134402 (2002).

Srinivasan, G. *Annu. Rev. Mater. Res*. **40**, 153-178 (2010).

Srolovitz, D. J. & Safran, S. A. Capillary instabilities in thin films. Part I energetics and part II kinetics. *J. Appl. Phys*. **60**, 247–260 (1986).

Stemmer, S., Streiffer, S. K., Ernst, F., Rühle, M., Atomistic structure of 90° domain walls in ferroelectric PbTiO3 thin films, *Philos. Mag. A* **71**, 713–724 (1995).

Stognij, A., Novitskii, N., Sazanovich, A., Poddubnaya, N., Sharko, S., Mikhailov, V., Nizhankovski, V., Dyakonov, V. & Szymczak. H. Ion-beam sputtering deposition and magnetoelectric properties of layered heterostructures $(FM/PZT/FM)_n$, where FM—Co or $Ni_{78}Fe_{22}$. *The European Physical Journal Applied Physics* **63**, 21301 (2013).

Stoner, E. C. *Philos. Mag.* **15**, 1018 (1933).

Stratulat, S. M., Lu, X., Morelli, A., Hesse, D., Erfurth, W. & Alexe, M. *Nano Lett.* **13**, 3884 (2013).

Sun, C., Luo, J., Wu, L. & Zhang, J. *ACS Appl. Mater. Interfaces* **2**, 1299-1302 (2010).

Sun, Z. & Kim, H. K. *Appl. Phys. Lett*. **81**, 3458-3460 (2002).

Tachiki, M. Origin of magnetocrystalline anisotropy energy in cobalt ferrite, *Prog. Theor. Phys*. **23**, 1055 (1960).

Tagantsev, A. K. & Stolichnov, I. A. *Appl. Phys. Lett*. **74**, 1326-1328 (1999).

Tagantsev, A. K., Sherman, V. O., Astafiev, K. F., Venkatesh, J. & Setter, N. Ferroelectric materials for microwave tunable applications. *J. Electroceram*. **11**, 5-66 (2003).

Tang, C., Bang, J., Stein, G. E., Fredrickson, G. H., Hawker, C. J., Kramer, E. J., Sprung, M. & Wang, *J. Macromolecules* **41**, 4328-4339 (2008).

Tang, D., Zeng, Z., Zhou, Q., Su, S., Hu, D., Li, P., Lin, X., Gao, X., Lu, X., Wang, X., Jin, M., Zhou, G., Zhang, Z. & Liu, J. *RSC Adv.* **7**, 29096-29102 (2017).

Takahashi, H. & Nagayama, M. *Corrosion Science* **18**, 911-925 (1978).

Taylor, D. V. & Damjanovic, D. *Appl. Phys. Lett*. **76**, 1615 (2000).

Teague, J. R., Gerson, R. & James, W. *J Solid State Commun*. **8**, 1073 (1970).

Tenne, D. A., Xi, X. X., Li, Y. L., Chen, L. Q., Soukiassian, A., Zhu, M. H., James, A. R., Lettieri, J., Schlom, D. G., Tian, W. & Pan, X. Q. *Phys. Rev. B* **69**, 174101 (2004).

Tenne, D. A., Turner, P., Schmidt, J. D., Biegalski, M., Li, Y. L., Chen, L. Q., Soukiassian, A., Trolier-McKinstry, S., Schlom, D. G., Xi, X. X., Fong, D. D., Fuoss, P. H., Eastman, J. A., Stephenson, G. B., Thompson, C. & Streiffer, S. K. Ferroelectricity in Ultrathin $BaTiO_3$ Films: Probing the Size Effect by Ultraviolet Raman Spectroscopy. *Phys. Rev. Lett.* **103**, 177601 (2009).

Terada, N., Glazkova, Y. S. & Belik, A. A. Differentiation between ferroelectricity and thermally stimulated current in pyrocurrent measurements of multiferroic $M Mn_7O_{12}$ (M = Ca, Sr, Cd, Pb). *Phys. Rev. B* **93**, 155127 (2016).

Tu, Y., Calzada, M. L., Phillips, N. J. & Milne, S. J. *J. Amer. Ceram. Soc*. **79**, 441 (1996).

Tybell, T., Ahn, C. H. & Triscone, J.-M. *Appl. Phys. Lett*. **75**, 856-858 (1999).

Ustinov, A., Srinivasan, G. & Kalinikos, B. A. *Appl. Phys. Lett.* **90**, 031913 (2007).

Valencia, S., Crassous, A., Bocher, L., Garcia, V., Moya, X., Cherifi, R. O., Deranlot, C., Bouzehouane, K., Fusil, S., Zobelli, A., Gloter, A., Mathur, N. D., Gaupp, A., Abrudan, R., Radu, F., Barthélém, A. & Bibes, M. Interface-induced room-temperature multiferroicity in $BaTiO_3$. *Nat. Mater*. **10**, 753–758 (2011).

Van Aken, B. B., Palstra, T. T. M., Filippetti, A. & Spaldin, N. A. The origin of ferroelectricity in magnetoelectric $YMnO_3$. *Nat. Mater*. **3**, 164–170 (2004).

Van den Brink, J. & Khomskii, D. I. Multiferroicity due to charge ordering. *J. Phys. Condens. Matter* **20**, 434217 (2008).

Van Run, A. M. J. G., Terrell, D. R. & Scholing, J. H. *J. Mater. Sci*. **9**, 1710-1714 (1974).

Van Suchtelen, J. Product properties: a new application of composite materials. *Philips Res. Rep*. **27**, 28 (1972).

Vasudevan, R. K., Balke, N., Maksymovych, P., Jesse, S. & Kalinin, S. V. *Appl. Phys. Rev*. **4**, 021302 (2017).

Vest, R. W. & Xu, J. *IEEE Trans. UFFC* **35**, 711 (1988).

Vlad, A. *Advanced Fabrication of Nanowire Arrays and Three-Dimensional Nanostructures*, PhD thesis. (Université catholique de Louvain, Louvain-la-Neuve, Belgium, 2009).

Vlad, A., Antohe, V.-A., Martínez-Huerta, J. M., Fearin, E., Gohy, J.-F. & Piraux, L. *J. Mater. Chem. A* **4**, 1603 (2016).

Wan, J.-G., Wang, X. W., Wu, Y. J., Zeng, M., Wang Y., Jiang, H., Zhou, W. Q., Wang, G. H. & Liu, J.-M. *Appl. Phys. Lett*. **86**, 122501 (2005).

Wan, J.-G., Weng, Y., Wu, Y., Li, Z., Liu, J.-M. & Wang, G. Controllable phase connectivity and magnetoelectric coupling behavior in $CoFe_2O_4$–$Pb(Zr,Ti)O_3$ nanostructured films *Nanotechnology* **18**, 465708 (2007).

Wang, J., Neaton, J. B., Zheng, H., Nagarajan, V., Ogale, S. B., Liu, B., Viehland, D., Vaithyanathan, V., Schlom, D. G., Waghmare, U. V., Spaldin, N. A., Rabe, K. M., Wuttig, M. & Ramesh, R., Epitaxial $BiFeO_3$ multiferroic thin film heterostructures. *Science*, **299**, 1719 (2003).

Wang, J., Zhang, Y., Ma, J., Lin, Y. & Nan, C. W. Magnetoelectric behavior of BaTiO3 films directly grown on CoFe2O4 ceramics. *J. Appl. Phys*. **104**, 014101 (2008).

Wang, F., Huang, H. & Yang, S. *J. Eur. Ceram. Soc*. **29**, 1387-1391 (2009).

Wang, Y., Hu, J., Lin, Y. & Nan, C.-W. *NPG Asia Mater*. **2**, 61-68 (2010).

Wang, Z., Yan, L., Yang, Y., Li, J. F., Das, J., Geiler, A. L., Yang, A., Chen, Y., Harris, V. G., Viehland, D. Magnetoelectric Effect in Crystallographically Textured BaTiO3 Films Deposited on Ferromagnetic Metallic Glass Foils. *J. Appl. Phys.* **109**, 034102 (2011a).

Wang, Y. J. Gray, D., Berry, D., Gao, J., Li, M., Li, J. & Viehland, D. An extremely low equivalent magnetic noise magnetoelectric sensor. *Adv. Mater*. **23**, 4111–4114 (2011b).

Wang, Z. G., Yang, Y. D., Viswan, R., Li, J. F. & Viehland, D. Giant electric field controlled magnetic anisotropy in epitaxial $BiFeO_3$-$CoFe_2O_4$ thin film heterostructures on single crystal $Pb(Mg_{1/3}Nb_{2/3})_{0.7}Ti_{0.3}O_3$ substrate. *Applied Physics Letters* **99**, 043110 (2011c).

Wang, W. W., Zhao, J., Wang, W., Gai, Z., Balke, N., Chi, M., Lee, H. N., Tian, W., Zhu, L., Cheng, X., Keavney, D. J., Yi, J., Ward, T. Z., Snijders, P. C., Christen, H. M., Wu, W., Shen, J. & Xu, X., Room-temperature multiferroic hexagonal $LuFeO_3$ films. *Phys. Rev. Lett*. **110**, 237601 (2013a).

Wang, J., Li, Z., Shen, Y., Lin, Y. & Nan, C. W. Enhanced magnetoelectric coupling in $Pb(Zr_{0.52}Ti_{0.48})O_3$ film-on-$CoFe_2O_4$ bulk ceramic composite with $LaNiO_3$ bottom electrode. *J. Mater. Sci*. **48**, 1021–1026 (2013b).

Wang, Z., Zhang, Y., Wang, Y., Li, Y., Luo, H., Li, J. & Viehland, D. *ACS Nano* **8**, 7793 (2014a).

Wang, J., Xu, T., Shimada, T., Wang, X., Zhang, T.-Y., Kitamura, T. *Phys. Rev. B* **89**, 144102 (2014b).

Weiss, P. *J. Phys*. **6**, 661 (1907).

Wiegelmann, H., Jansen, A. G. M., Wyder, P., Rivera, J.-P. & Schmid, H. Magnetoelectric effect of Cr_2O_3 in strong static magnetic fields. *Ferroelectrics* **162**, 141-146 (1994).

Wen, Z., Li, C., Wu, D., Li, A. & Ming, N. Ferroelectric-field-effect-enhanced electroresistance in metal/ferroelectric/semiconductor tunnel junction. *Nat. Mater*. **12**, 617-621 (2013).

Wu, W., Wong, K. H., Choy, C. L. & Zhang, Y. H. *Appl. Phys. Lett*. **77**, 3441-3443 (2000).

Wu, T., Zurbuchen, M. A., Saha, S., Wang, R.-V., Streiffer, S. K. & Mitchell, J. F. Observation of magnetoelectric effect in epitaxial ferroelectric film/manganite crystal heterostructures. *Phys. Rev. B* **73**, 134416 (2006).

Wu, Z., Niu, P., Yang, B. & Yu, R. *Appl. Phys. A* **105**, 177-181 (2011).

Wu, H., Chai, G., Zhou, T., Zhang, Z., Kitamura, T. & Zhou, H. *J. Appl. Phys*. **115**, 114105 (2014).

Xiang, C., Zhang, X., Li, J., Chu, Y. & Shen, X. *Chem. Phys. Lett*. **576**, 39-43 (2013).

Xiao, Z. L., Han, C. Y., Welp, U., Wang, H. H., Kwok, W. K., Willing, G. A., Hiller, J. M., Cook, R. E., Miller, D. J. & Crabtree, G. W. *Nano Lett.* **2**, 1293-1297 (2002).

Xie, S. H., Li, J. Y., Qiao, Y., Liu, Y. Y., Lan, L. N., Zhou, Y. C. & Tan, S. T. *Appl. Phys. Lett*. **92**, 062901 (2008a).

Xie, S. H., Li, J. Y., Liu, Y. Y., Lan, L. N., Jin, G. & Zhou, Y. C. *J. Appl. Phys*. **104**, 024115 (2008b).

Xie, S., Ma, F., Liu Y. & Li, J. *Nanoscale* **3**, 3152-3158 (2011).

Xie, Y., Ou, Y., Ma, F., Yang, Q., Tan, X. & Xie, S. *Nanosci. Nanotechnol. Lett*. **5**, 546-551 (2013).

Xu, S. & Shi, Y. *J. Phys. D: Appl. Phys*. **42**, 085301 (2009).

Yadav, A. K., Nelson, C. T., Hsu, S. L., Hong, Z., Clarkson, J. D., Schlepuetz, C. M., Damodaran, A. R., Shafer, P., Arenholz, E., Dedon, L. R., Chen, D., Vishwanath, A., Minor, A. M., Chen, L. Q., Scott, J. F., Martin, L. W. & Ramesh, R. Observation of Polar Vortices in Oxide Superlattices. *Nature* **530**, 198−201 (2016).

Yan, F., Chen, G., Lu, L., Finkel, P. & Spanier, J. E. *Appl. Phys. Lett*. **103**, 042906 (2013).

Yan, L., Yang, Y., Wang, Z., Xing, Z., Li, J. & Viehland, D. *J. Mater. Sci*. **44**, 5080-5094 (2009).

Yan, L., Wang, Z. G., Xing, Z. P., Li, J. F. & Viehland, D. Magnetoelectric and multiferroic properties of variously oriented epitaxial $BiFeO_3$-$CoFe_2O_4$ nanostructured thin films. *Journal of Applied Physics* **107**, 064106 (2010).

Yan, L., Zhuo, M., Wang, Z., Yao, J., Haberkorn, N., Zhang, S., Civale, L., Li, J., Viehland, D. & Jia, Q. X. Magnetoelectric Properties of Flexible $BiFeO_3$/Ni Tapes. *Appl. Phys. Lett*. **101**, 012908 (2012).

Yan, L. H., Liang, W. Z., Liu, S. H., Huang, W. & Lin, Y. *Integr. Ferroelectr*. **131**, 82 (2011).

Yang, S. G., Li, T., Huang, L. S., Tang, T., Zhang, J. R., Gu, B. X., Du, Y. W., Shi, S. Z. & Lu, Y. N. *Phys. Lett. A* **318**, 440-444 (2003).

Yang, J. J., Zhang, Y. G., Tian, H. F., Luo, L. B., Zhang, H. Y., He, Y. J. & Luo, H. S. Electric field manipulation of magnetization at room temperature in multiferroic $CoFe_2O_4$/$Pb(Mg_{1/3}Nb_{2/3})_{0.7}Ti_{0.3}O_3$ heterostructures. *Appl. Phys. Lett.* **94**, 212504 (2009).

Yang, Y., Infante, I. C., Dkhil, B. & Bellaiche, L. Strain effects on multiferroic $BiFeO_3$ films. *C. R. Phys*.**16**, 193–203 (2015).

Yao, F., Xu, L., Lin, B. & Fu, G.-D., *Nanoscale* **2**, 1348-1357 (2010).

Yao, L., Pan, Z., Zhai, J. & Chen, H. H. D. *Nanoscale* **9**, 4255 (2017).

Yi, G., Wu, Z. & Sayer, M. *J. Appl. Phys*. **64**, 2717 (1988).

Yokoyama, S., Honda, Y., Morioka, H., Asano, G., Oikawa, T., Iijima, T., Matsuda, H. and Funakubo, H. *Jpn. J. Appl. Phys.* **42**, 5922 (2003).

Yourdkhani, A., Caruntu, D., Vopson, M. & Caruntu G. *CrystEngChomm*. **19**, 2079-2088 (2017).

Yuan, J. J., Zhao, Q., Xu, Y. S., Liu, Z. G., Du, X. B. & Wen, G. H. *J. Magn. Magn. Mater*. **321**, 2795-2798 (2009).

Zavaliche, F., Zheng, H., Mohaddes-Ardabili, L., Yang, S. Y., Zhan, Q., Shafer, P., Reilly, E., Chopdekar, R., Jia, Y., Wright, P., Schlom, D. G., Suzuki, Y. & Ramesh, R. Electric field-induced magnetization switching in epitaxial columnar nanostructures. *Nano Lett*. **5** 1793-6 (2005).

Zavaliche, F., Zhao, T., Zheng, H., Straub, F., Cruz, M. P., Yang, P. L., Hao, D. & Ramesh, R. Electrically assisted magnetic recording in multiferroic nanostructures. *Nano Letters* **7**, 1586–1590 (2007).

Zhai, J., Xing, Z., Dong, S. X., Li, J. F. & Viehland, D. *Appl. Phys. Lett.* **88**, 062510 (2006).

Zhang, X. Y., Zhao, X., Lai, C. W., Wang, J., Tang, X. G. & Dai, J. Y. *Appl. Phys. Lett*. **85**, 4190-4192 (2004).

Zhang, J. X., Li, Y. L., Schlom, D. G., Chen, L. Q., Zavaliche, F., Ramesh, R. & Jia Q. X. Phase-field model for epitaxial ferroelectric and magnetic nanocomposite thin films. *Appl. Phys. Lett*. **90** 052909 (2007).

Zhang, Y., Deng, C., Ma, J., Lin, Y. & Nan, C.-W. Enhancement in magnetoelectric response in CoFe2O4-BaTiO3 heterostructure. *Appl. Phys. Lett*. **92**, 062911 (2008).

Zhang, S., Zhao, Y. G., Li, P. S., Yang, J. J., Rizwan, S., Zhang, J. X., Seidel, J., Qu, T. L., Yang, Y. J., Luo, Z. L., He, Q., Zou, T., Chen, Q. P., Wang, J. W., Yang, L. F., Sun, Y., Wu, Y. Z., Xiao, X., Jin, X. F., Huang, J., Gao, C., Han, X. F. & Ramesh, R. Electric-Field Control of Nonvolatile Magnetization in $Co_{40}Fe_{40}B_{20}/Pb(Mg_{1/3}Nb_{2/3})0.7Ti_{0.3}O_3$ Structure at Room Temperature. *Phys. Rev. Lett.* **108**, 137203 (2012).

Zhang, X. Tang, D., Huang, K., Hu, D., Zhang, F., Gao, X., Lu, X., Zhou, G., Zhang, Z. & Liu, J. Nanoscale Research Letters **11**, 225 (2016).

Zheng, H, Wang, J., Lofland, S. E., Ma, Z., Mohaddes-Ardabili, L., Zhao, T., Salamanca-Riba, L., Shinde, S. R., Ogale, S. B., Bai, F., Viehland, D., Jia, Y., Schlom, D. G., Wuttig, M., Roytburd, A. & Ramesh, R. *Science* **303**, 661-663 (2004).

Zheng, H., Straub, F., Zhan, Q., Yang, P.-L., Hsieh, W.-K., Zavaliche, F., Chu, Y.-H., Dahmen, U. & Ramesh, R. *Adv. Mater*. **18**, 2747-2752 (2006).

Zhigalina, O. M., Mishina, E. D., Sherstyuk, N. E., Vorotilov, K. A., Vasiljev, V. A., Sigov, A. S., Lebedev, O. I., Grigoriev, Yu. V., de Santo, M. P., Barberi, R. & Rasing, Th. *Ferroelectrics* **336**, 247 (2006).

Zhu, Q., Xie, Y., Zhang, J., Liu, Y., Zhan, Q., Miao, H. & Xie, S. *J. Mater. Res.* **29**, 657-664 (2014).

Zhuang, X., Leung, C. M., Sreenivasulu, G., Gao, M., Zhang, J., Srinivasan, G., Li, J. & Viehland, D. Upper limit for power conversion in magnetoelectric gyrators. *Appl. Phys. Lett.* **111**, 163902 (2017).

Zighem, F., Maurer, T., Ott, F. & Chaboussant, G. *J. Appl. Phys*. **109**, 013910 (2011).

List of Figures

List of Tables

List of Symbols & Abbreviations

(1-3) – Connectivity of 1D nanostructures embedded into 3D matrix
(2-2) – Connectivity of multi-layered 2D nanostructures
(0-3) – Connectivity of nanoparticles distributed within 3D matrix
AAO – Anodic aluminium oxide
ac – Alternating current
AF – Antiferromagnetic
AFD – Antiferrodistortive distortion
AFE – Antiferroelectric
AFM – Atomic Force Microscopy
AGM - Alternating Gradient Magnetometer
ALD – Atomic layer deposition
B – Magnetic induction
BF - Bright-field
BFO – $BiFeO_3$
BSTO – $BaSr_{0.7}Ti_{0.3}O_3$
BTO – $BaTiO_3$
c – Elastic stiffness
C – Capacitance
CFO – $CoFe_2O_4$
CSD – Chemical solution deposition
d – Piezoelectric coefficient
D - Diameter
D_{cell} – Alumina cell size or inter-pore distance
D_{pillar} – Nanopillars diameter
dc – Direct current
DSO – $DyScO_3$
ϵ – Strain
E – Electric field
E_a – Activation energy
E-beam – Electron beam
ECD – Electrochemical deposition
EDTA – Ethylenediaminetetraacetic acid

EDX – Electron Diffraction X-ray Spectrometry
EG – Ethylene glycol
f – Volume fraction
F - Faraday constant
FE – Ferroelectric
FE_y^x – *x* index is crystallization temperature [°C] and *y* index is total thickness [nm]
FIB - Focused ion beam
FM – Ferromagnetic
FM_y^x – Index *x* is oxidation temperature [°C] and index *y* is nanopillars height [nm]
FMR – Ferromagnetic resonance
FRAM – Ferroelectric Random-Access Memory
GI-XRD – Grazing Incidence X-ray configuration
h – Height
H – Magnetic field
H_{eff} – Effective magnetic field
HR-SEM – High-Resolution Scanning Electron Microscopy
HR-TEM – High-Resolution Transmission Electron Microscopy
I – Electric current
K_1 – Magnetocrystalline anisotropy constant
L – Length
L*A*MO - $La_{1-x}A_xMnO_3$ (*A* = Ca, Se, Ba, Co)
LAO – $LaAlO_3$
m – Magnetic moment
M – Magnetization
MBE – Molecular beam epitaxy
MD – Magnetodielectric
ME – Magnetoelectric
MERAM – Magnetoelectric random-access memory
MFM – Magnetic Force Microscopy
MPB – Morphotropic phase boundary
MPMS – Magnetic property measurement system
MR – Magnetoresistive
n – Volume concentration
N_p – Number of pores
NC - Nanocable
NFO – $NiFe_2O_4$
NT – Nanotube
NW – Nanowire
P – Polarization
P_{AAO} – Porosity
P_{NW} – Packing factor

PC – Polycarbonate
PED – Pulsed electron deposition
PEI – Polyethyleneimine
PFM – Piezo-Response Force Microscopy
PLD – Pulsed laser deposition
PMN-PT – $(PbMg_{1/3}Nb_{2/3}O_3)_{1-x}$-$(PbTiO_3)_x$
ppm - Parts per million
PPMS – Quantum Design Physical Property Measurement System
PTO – $PbTiO_3$
PVD – Physical vapour deposition
PVP – Polyvinylpyrrolidone
PZN-PT - $(PbZn_{1/3}Nb_{2/3}O_3)_{1-x}$-$(PbTiO_3)_x$
PZT – $PbZr_{1-x}Ti_xO_3$
q – Piezomagnetic coefficient
Q – Charge
R – Radius
RTA – Rapid thermal annealing
s – Slope
S – Surface area
SAED – Selected-area electron-diffraction
SDS – Sodium dodecyl sulfate
SE – Secondary electron
SEM –Scanning Electron Microscopy
SQUID – Superconducting Quantum Interference Device
SRO – $SrRuO_3$
SS-PFM - Switching spectroscopy piezoresponse force microscopy
STEM – Scanning-tunnelling electron microscopy
STO – $SrTiO_3$
t – Thickness
$t_{top\ layer}$ – Thickness of a ferroelectric top layer above nanopillars
t_{total} – Total thickness of a nanocomposite
T – Temperature
T_C – Curie temperature
T_N – Néel temperature
$tan\delta$ – Dielectric loss tangent
TEM – Transmission Electron Microscopy
Terfenol-D – $Tb_{1-x}Dy_xFe_2$
V - Voltage
VSM – Vibration sample magnetometry
XRD – X-ray Diffraction
Y_f – Young's modulus

Z - Charge
α – Linear magnetoelectric coefficient/susceptibility
β – Bilinear magnetoelectric coefficient/susceptibility
γ – Bilinear magnetoelectric coefficient/susceptibility
ε – Permittivity
ε_0 – Free space or vacuum permittivity
ε – Permittivity
θ – Angle (degree)
k – Dielectric constant
k_B – Boltzmann constant
λ – Magnetostriction coefficient
μ – Permeability
μ_0 – Free space or vacuum permeability
ν_f - Poisson's ratio
ρ – Density
σ – Stress
τ_{Al} – Amount of residual aluminium
Φ – Thermodynamic potential
χ – Susceptibility
ω - Frequency

Parts of this thesis have been published in the following journal articles:

Sallagoity, D., Elissalde, C., Majimel, J., Antohe, V. A., Abreu Araujo, F., Pereira de Sá, P. M., Basov, S and Piraux, L. "Synthesis of Dense Arrays of Multiferroic $CoFe_2O_4$-$PbZr_{0.52}Ti_{0.48}O_3$ Core/Shell Nanocables" RSC Advances 6, 106716 (2016).

Basov, S., Elissalde, C., Simon, Q., Maglione, M., Castro-Chavarria, C., Herrison de Beauvoir, T., Payan, S., Temst, K., Lazenka, V., Antohe, V. A. Pereira de Sá, P. M., Sallagoity, D. and Piraux, L. "Simple Synthesis and Characterization of Vertically Aligned $Ba_{0.7}Sr_{0.3}TiO_3$-$CoFe_2O_4$ Multiferroic Nanocomposites from $CoFe_2$ Nanopillar Arrays" Nanotechnology 28, 475707 (2017).